METAL NANOPARTICLES IN THERAPEUTIC AND SENSOR APPLICATIONS

AMIT SINGH

BIOCHEMICAL SCIENCES DIVISION
NATIONAL CHEMICAL LABORATORY
PUNE – 411 008
INDIA

DECEMBER 2006

Metal Nanoparticles in Therapeutic and Sensor Applications

THESIS SUBMITTED TO

UNIVERSITY OF PUNE

FOR THE DEGREE OF

DOCTOR OF PHILOSOPHY

IN

BIOTECHNOLOGY

BY

AMIT SINGH

BIOCHEMICAL SCIENCES DIVISION
NATIONAL CHEMICAL LABORATORY
PUNE – 411 008
INDIA

DECEMBER 2006

to everyone who made a difference in my life….

my parents, teachers and friends

CERTIFICATE

This is to certify that the work discussed in the thesis entitled **"METAL NANOPARTICLES IN THERAPEUTIC AND SENSOR APPLICATIONS"** by **AMIT SINGH**, submitted for the degree of *Doctor of Philosophy in Biotechnology* was carried out under my supervision at the Biochemical Sciences and the Materials Chemistry Divisions of the National Chemical Laboratory, Pune, India. Such materials as have been obtained by other sources have been duly acknowledged in this thesis. To the best of my knowledge, the present work or any part thereof, has not been submitted to any other University for the award of any other degree or diploma.

Date:
Place: Pune

Dr. (Mrs.) Mala Rao
(Research Guide)

CERTIFICATE

This is to certify that the work discussed in the thesis entitled **"METAL NANOPARTICLES IN THERAPEUTIC AND SENSOR APPLICATIONS"** by **AMIT SINGH**, submitted for the degree of *Doctor of Philosophy in Biotechnology* was carried out under my joint supervision at the Biochemical Sciences and the Materials Chemistry Divisions of the National Chemical Laboratory, Pune, India. Such materials as have been obtained by other sources have been duly acknowledged in this thesis. To the best of my knowledge, the present work or any part thereof, has not been submitted to any other University for the award of any other degree or diploma.

Date:
Place: Pune

Dr. Murali Sastry
(Research Co-Guide)

DECLARATION

I hereby declare that the work incorporated in this thesis entitled **"METAL NANOPARTICLES IN THERAPEUTIC AND SENSOR APPLICATIONS"** submitted for the degree of *Doctor of Philosophy in Biotechnology* has been carried out by me at the Biochemical Sciences and the Materials Chemistry Divisions of the National Chemical Laboratory, Pune, India under the joint supervision of Dr. (Mrs.) Mala Rao and Dr. Murali Sastry. Such materials as have been obtained by other sources have been duly acknowledged in this thesis. The work is original and has not been submitted in part or full by me for award of any other degree or diploma in any other University.

Date:
Place: Pune

Amit Singh
(Research Student)

Acknowledgement

The work presented in this thesis would not have been possible without my close association with many people who were always there when I needed them the most. I take this opportunity to acknowledge them and extend my sincere gratitude for helping me make this Ph.D. thesis a possibility.

I would like to start with the person who made the biggest difference in my life, my mentor, Dr. Murali Sastry. He has been there, in front of my eyes for last three and a half years, motivating and inspiring every bit of me towards new possibilities in life. He has been a living role model to me, taking up new challenges every day, tackling them with all his grit and determination and always thriving to come out victorious. It's his vigor and hunger to perform in adverse situation, which has inspired me to thrive for excellence and nothing less. During my initial days with the group, I was apprehensive about my decision to join an alien field, where things were new to me. Dr. Sastry came to my rescue with his intelligent ideas, thought provoking discussions and comprehensive understanding to help me sail through the initial fumbling. His attitude of living every moment as it comes, making serendipitous observation and converting them to new possibilities, correlating ideas and understanding the obvious has helped me come a long way and will always guide me in future. He made me realized what I had only heard, "When the going gets tough, the tough get going". I will never find words to tell what I owe to him, and if I start doing it, I would not know where to stop…thanks for everything Sir…to me, professionally, you are "perfection personified".

My special words of thanks should also go to my research guide, Dr. Mala Rao, for always being so kind, helpful and motivating. She has taught me another aspect of life, that, "goodness can never be defied and good human beings can never be denied". She has always been there for me with her motherly hand whenever I needed it the most. Her constant guidance, cooperation and support has always kept me going ahead. I owe a lot of gratitude to her for always being there for me and I feel privileged to be associated with a person like her during my life.

I express my heart-felt gratitude to Dr. Absar Ahmad for his constant motivation and support during the course of my thesis. I enjoyed the personal discussion with him and the time I spent with him during festive seasons. My sincere thanks to Dr. B.L.V. Prasad for being with me as an elderly figure through out. His scientific inputs, personal helps and friendly nature has always made me feel at ease with him and I could always look back on him for any support during my course of Ph.D. I also gratefully acknowledge Dr. Satish Ogale for his constant advises, friendly nature and elderly support, which made a lot of difference to me. The constant motivation and support from Mrs. Suguna Adhyanthaya and Dr. Pankaj Poddar is also gratefully acknowledged.

I would like to acknowledge all the teachers I learnt from since my childhood, I would not have been here without their guidance, blessing and support. My special thanks to Dr. Sitaramam, Department of Biotechnology, University of Pune, for being another role model for me. I feel privileged to be his student once, a feeling that every student of his will second.

I extend my sincere word of thanks to Mrs. Renu Pasricha, who has always been there, more as a friend than a scientist. I would never be able to pay back the love and affection showered upon by her. The work done with her as a co-worker has taught me how a person can succeed in achieving what seems impossible to begin with…thanks you Mam for everything. I would also like to extend my love to Kanika and Aneesh, her kids, who have been so close to me and have helped me revive the child hidden in me.

My acknowledgement will never be complete without the special mention of my lab seniors who have taught me the lab culture and have lived by example to make me understand the hard facts of life. I would like to acknowledge Dr. Anand Gole, Dr. Ashvani Kumar, Dr. Debabrata, Dr. Sumant, Dr. Anita Dr. Senthil, Dr. Ankamwar, Kannan and Shankar for all their support and motivation during the initial days of my stay in the lab. My special words of gratitude to Kannan and Shankar for all their personal and professional help that they have extended to me throughout.

My heartfelt thanks to my fellow labmates, Hrushikesh, Ambarish, Tanushree, Atul, Vipul, Sourabh, Minakshi, Prathap, Deepti, Sanjay, Imran, Anil, Priyanka, Virginia, Umesh, Sudarshan, Baisakhi and Ramaya for always being there and bearing with me the good and bad times during my wonderful days of Ph.D. If I have missed out a name from the bunch of guys that we were together during all these days, it is on purpose. I would like to acknowledge Akhilesh and Vinod separately for being a friend before a labmate. Our association goes a long way since days of post graduation and they have been with me ever since then as a friend, a companion, a roommate and lab mate. Thank you dear for being with me in ups and downs of life during last 6 years. I also acknowledge my roommate of 2 years and friend, Rasesh Parikh, for keeping a healthy atmosphere and bearing with me all these days. The discussion and suggestions from him were always valuable to me. My special thanks to Sourabh, Manasi, Prathap and Deepti for correcting my thesis chapters on short notices. I would like to thank my other friends from NCL who have been a source of moral support to me and have extended their helping hands without fail. I would also like to thank all my seniors and juniors from Department of biotechnology, University of Pune, for all the love that they have showered upon me. I could not have asked for more than what I got from them.

I would like to acknowledge my other friends for their moral support and motivation, which drives me to give my best. Rajendra, Raghvendra, Awadesh, Vijay, Pradeep, Sanjay, Umesh, Kishore, Sanjeev, Manish, Himanshu, Nitin…the list is endless…thanks to one and all. My special gratitude to Ankur and Sushanth for being with me in thicks and thins of life, I find myself lucky to have friends like them in my life.

I would like to thank Ravi Shukla and Dr. R.R. Bhonde for their valuable support and collaboration in shaping up this thesis in its present form. I don't imagine any better collaboration than what I had with them. My special thanks to Ravi for his constant support and brotherly affection during this course of time.

I am grateful to many people in the Center for Materials Characterization, NCL who have assisted me in the course of this work. My sincere thanks to Dr. S. R. Sainkar, Dr. M. Bhadbhade, Mrs. R. Pasricha, Mr. A. B. Gaikwad, Dr. Patil and Dr. A. B. Mandale for making the facilities available during the research work. I would also like to acknowledge Minakshi, Manasi and Sanjay for their assistance with AFM measurements.

During the course of my work, I had the pleasure of working with several project students, Vijay, Kapil, Anubhav, Abhijeet and Shantesh. Their assistance during the presented work is gratefully acknowledged.

My thanks to the staff of Physical Chemistry division for their innumerable help. A special word of gratefulness to Mr. Deepak and Mr. Punekar who have gone out of way to help me with several official matters.

I am grateful to Dr. S. Sivaram, Director NCL, and Dr. S. Pal, Head, Physical Chemistry Division, NCL for giving me an opportunity to work in this institute and making the facilities available for carrying out research.

I acknowledge the Council of Scientific and Industrial Research (CSIR), Government of India for providing me with the necessary funding and fellowship to pursue research at NCL.

I thank the Almighty for giving me the strength and patience to work through all these years so that today I can stand proud with my head held high.

Finally, I would like to acknowledge the people who mean world to me, my parents, uncle-aunty, my brothers and sisters. I extend my respect to my parents, my paternal and maternal grand parents and all elders to me in the family. I don't imagine a life without their love and blessings. Thank you mom, dad, uncle and aunty for showing faith in me and giving me liberty to choose what I desired. I consider myself the luckiest in the world to have such a supportive family, standing behind me with their love and support.

Amit Singh.

Table of Contents

Chapter I

Introduction

This chapter is an introduction to the thesis discussing general methods of metal nanoparticle synthesis, their properties, assembly and various applications of nanoparticles in different fields. The chapter sums up the previous reports on the use of nanostructures for thin film fabrication and chemical vapor sensing. A part of the chapter discusses various attempts that have been made to study the biocompatibility of nanostructures. Towards the end, we discuss the lay out of the thesis.

1.1 Introduction.

Miniaturization is a concept nurtured by nature since the process of evolution and with time, the control of biological processes at small length scales has become immaculate. The origin of the field of nanoscience and nanotechnology has primarily been a motivation to mimic the programmed synthesis and manipulation of materials at similar length scale, an art perfected by nature. Richard Feynaman was the visionary who first drew attention towards this possibility in his speech titled "There's plenty of room at the bottom" [1]. Since then, several significant achievements have been made towards the process of miniaturization, even though control at complexity levels manifested by biological systems is still a dream. Figure 1.1 sums the success of the man in competition to nature on fabrication of material at small scale routinely. Two different approaches have been undertaken to achieve this goal, which are "top-down" [2] and "bottom up" [3].

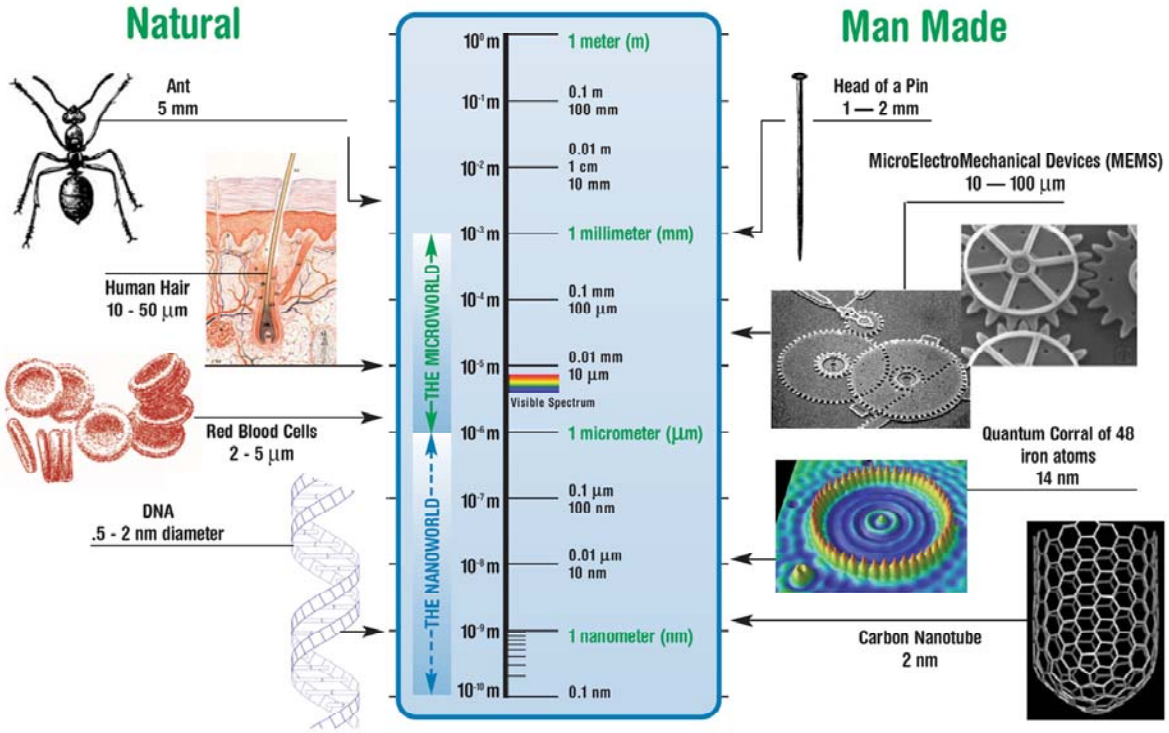

Figure 1.1 *Picture showing the relative size scale of various miniaturized natural and man made material. [Courtesy: Josh Wolfe's report on Nanotechnology, www.forbeswolfe.com.]*

The top-down approach thrives on the principle that large sized objects can be chiseled to obtain smaller objects. Humans have been following this approach since the beginning of civilization and with time, this art has been mastered to achieve size limits of

submicron levels. However, physical constraints limit the application of this approach to achieve nano-domain precision. Thus, the bottom-up approach has taken over where small-scale objects can be assembled to build up larger sized materials for various applications. This includes the synthesis of nanostructures of desired characteristics, their self-assembly and eventual formation of larger sized particles.

1.2 Historical Perspective:

Exposure of mankind to the nano-world is not new and the history of noble metal colloids has been reported in ancient literature. History claims that Moses, the great physician, gave the first recipe for colloidal gold [4]. The verses 19 and 20 in the book "Exodus" mention the preparation of the first colloidal gold. According to verse 20,

"And he took the [golden] calf which they had made, and burnt it in the fire, and ground it to powder, and strewed it upon the water, and made the children of Israel drink of it."

The mention above indicates that the potential of noble metal colloidal suspension in therapeutics has been realized since ancient time. The great German physician and alchemist, Paracelsus (1493-1541) had once quoted, "*Of all Elixirs, Gold is supreme and the most important for us, for it can keep the body indestructible. Drinkable gold will cure all illnesses, it renews and restores*" [5]. Aurum potable (drinking gold) and luna potable (drinking silver) have been considered as elixirs by the alchemist since 1570 [6]. The optical properties of colloidal gold and silver have specially drawn attention due to their absorption maxima in the visible region of the electromagnetic spectrum, which leads to colored colloidal suspension. In 1818, Jeremias Benjamin Richters gave an explanation for the different colors seen in drinkable gold indicating that the pink or purple color was due to finest degree of subdivision while yellow color arises due to the aggregation of very fine particles [7].

In earlier days, colloidal gold and silver has been used as colorant [8]. The colorant in glasses, "Purple of Cassius", is a colloid with heterocoagulation of gold nanoparticles and tin oxide [4b]. Similarly, the Lycurgus cup of fourth century AD, which looks green in reflected and red in transmitted light, has been reported to contain colloidal gold and silver [9]. In 1857, Faraday reported the preparation of deep red colored solution of gold nanoparticles by the reduction of aqueous chloroaurate ions using phosphorus in CS_2 [10]. This probably was

the first rationalized report on the purposeful synthesis of colloidal gold nanoparticles. Soon thereafter, the term colloid was coined by Thomas Graham (1861) for suspended particles in liquid medium [11] and was categorized to be in the size range 1 nm to few μm. However, Norio Taniguchi gave the term 'nanotechnology' [12] for the colloidal particles, which have at least one dimension of the length scale of 1-100 nm. Ever since the report of Faraday, several different approaches have been developed towards the synthesis of colloidal noble metal nanoparticles by physical, chemical and biological routes.

1.3 Synthesis of metal nanoparticles.

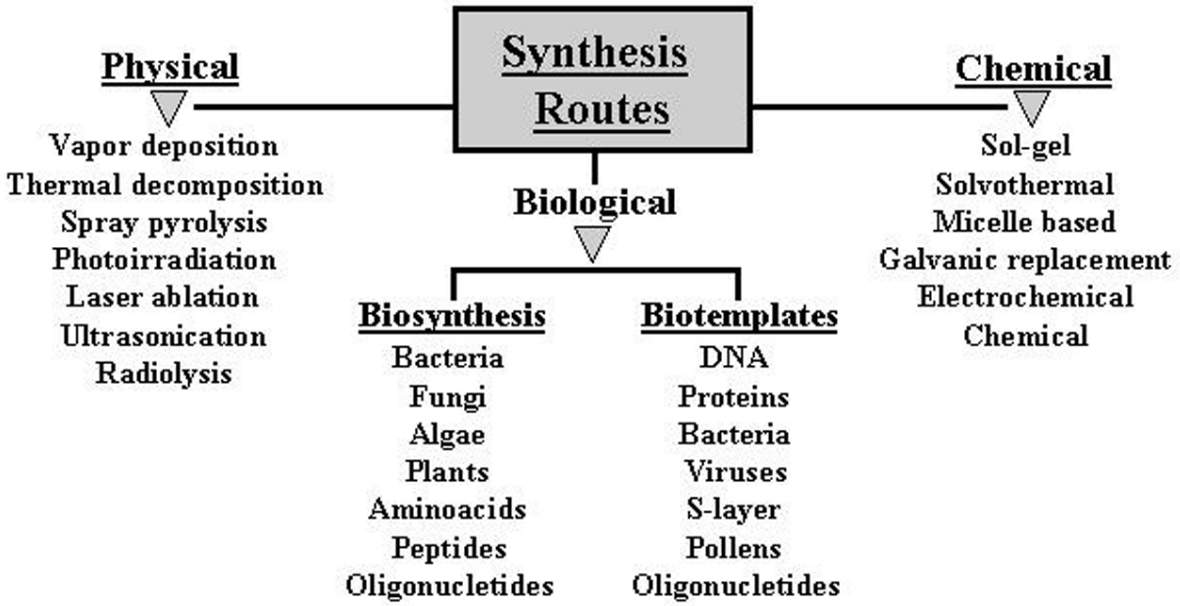

Figure 1.2 *Flowchart showing the various approaches undertaken for synthesis of metal nanostructures.*

The flow chart in Figure 1.2 summarizes some of the major attempts made towards the synthesis of noble metal nanoparticles. The physical routes mainly include vapor deposition [13], thermal decomposition [14], spray pyrolysis [15], photoirradiation [16], laser ablation [17], ultrasonication [18], radiolysis [19] and solvated metal atom dispersion [20]. However, chemical methods for synthesis of metal nanoparticles have been more popular and have gained wide acceptance. Some of the common chemical routes include sol-gel method [21], solvothermal synthesis [22], micelles based synthesis [23] and galvanic replacement reaction [24]. Chemical reduction has been the most popular route towards synthesis of metal nanostructures due to easy protocols and the exquisite shape and size control provided by this method. The control of size, shape, stability and the assembly of nanoparticles have been

achieved by using different capping agents, solvents and templates. Various types of capping agents have been used ranging from ions [25] to polymeric molecules [26] and even biomolecules [27]. Ever since the first report by Brust et al. [28] for the synthesis of monolayer-protected clusters (MPCs), several advances have been made in this field and a variety of capping agents have been used to prepare MPCs [29] soluble in non-polar organic as well as polar solvents. Although water has been used primarily for synthesis protocols, several reports on use of organic solvents [17a, 30], ionic liquids [26g, 31] and super critical fluids [32] are also available. Similarly, different templates such as micelles [33], polymers [34], mesoporous materials [35], carbon nanotubes (CNTs) [36], biomolecules [37] and microorganisms [38] have been used for the synthesis of nanoparticles on the surface or in confined spaces.

Although, over the past several decades, physical and chemical methods have dominated the synthesis of nanostructures, recently considerable attention has been paid towards the use of biological systems. Biological systems have been known to fabricate intricate structures at the micro and nano scales with precise control in normal environmental conditions. The exquisite siliceous exoskeletons of the diatoms and radilarians [39] and calcareous structures synthesized by the coccoliths [40] are micro scale materials, which have attracted tremendous interest. Besides, magnetite particles found in the magnetosomes [41] of the magnetic bacteria [42] are a wonderful example of functional nanomaterials that helps the microorganism to navigate in the earth's geomagnetic field. This fact has lured scientists to understand the underlying mechanisms used by the biological systems and thus, explore the biomimetic approach towards synthesis of nanomaterials. Significant work has been done to study diatoms and sponges to elucidate the molecular mechanism of silicification [43] and the involved biomolecules have been found to be two major poly-cationic peptides, silaffins [44] and silicateins [45] along with some other peptides like frustulins [46] and pleuralins [47] (formerly known as HF-extracted proteins, or HEPs). Similarly, the presence of magnetic nanoparticles have also been reported in several eukaryotic biological systems such as Euglena algae [48], dinoflagellates [49], salmon [50], trout [51], carrier pigeons [52], army ants [53] and even in the human brain [54]. Ever since these discoveries were made, biological systems have been exploited tremendously for synthesis and assembly of nanoparticles. One of the reports that opened up the gates for the

use of biological systems for the synthesis of nanomaterials was a report by Klaus et al. [55] on the synthesis of silver nanoparticles in the periplasmic space of the bacteria *Pseudomonas stutzeri* AG259. Till date, several bacteria [56], S-layer bacteria [57], fungi [58], algae [59] and plant systems [60] have been used for the synthesis of nanomaterials of different shapes, sizes and compositions.

1.4 Properties of metal nanoparticles.

During the course of this miniaturization, it has been observed that materials exhibit some exotic properties in the nanometer regime, which are significantly different from their bulk counterparts. The following section briefly discusses the changes in the properties of the metals of nanometer size.

1.4.1 Lattice parameters.

Earlier reports have documented that the lattice parameter of metals is inversely proportional to the particle size [61]. This reduction in the size can be explained according to the theoretical model given by Vermaak et al. [62] where the lattice parametre reduction has been interpreted in terms of the surface stress caused by the reduction in the particle size. It is well known that the surface energy of the nanoparticles increase with the decreasing size of the nanoparticles due to the large percentage of the atoms exposed to the surface. This increase in the surface energy induces a stress that leads to the elastic contraction of the lattice parameter. Qi et al. [63] have introduced another model to calculate the lattice parameter of metal nanoparticles based on the shape dependence by introducing a shape factor to their previous model for spherical nanoparticles [64]. Thus, by minimizing the sum of the surface energy and the elasticity energy, a formula could be obtained to calculate the lattice parameter of anisotropic metal nanoparticles.

1.4.2 Melting point.

The melting point of the nanocrystals has a direct relation with the size of the nanoparticles i.e. smaller is the size of a nanoparticle; lower will be the melting point [65]. The surface atoms in the solid phase are coordinatively unsaturated and thus high amount of surface energy is associated with them. It is important to understand that the surface energy is always lower in the liquid phase as compared to the solid phase. The bonding geometry in the solid phase causes stepped surfaces with the edges and corners of high-energy atoms. The process of melting starts from the surface and thus, the nanoparticle system is much more

stable in the liquid phase due to reduced surface energy [66]. A dramatic decrease in the melting point is observed in the nanoparticles that are smaller than 3-4 nm in size [67].

1.4.3 Catalytic property.

Catalysis is a surface phenomenon and for a given material, the available surface area directly governs catalytic efficiency. It is well known that with decrease in the size of particles for a given volume of material, the number of atoms at the surface (surface area) increases tremendously. Thus, the reduction in the size of the particles renders them excellent catalysts [68]. The unique surface structure, electronic structure, high surface area and lower work function make nanoparticles attractive candidates for homogenous catalysis in solution or heterogeneous catalysis on a solid support. The best example could be gold that is known to be a noble metal in its bulk state but has been shown to be an excellent catalyst as nanoparticles for the oxidation of carbon monoxide [7b, 69]. It has also been shown that the catalytic efficiency is also strongly dependent on the shape of the nanostructures. The reactants show a preferential adsorption towards some faces of a catalyst [70], which can be exploited to improve the performance of the catalytic property of a nanostructure by controlling the shape. Similarly, tremendous amount of work has also been done to show that the bimetallic nanoparticles can also be used as a good and improved catalyst [71].

1.4.4 Optical property.

Optical properties have specifically gained an indispensable status in the study of the noble metal nanostructures. This is due to the fact that they show size, shape and composition dependent absorption profile in the visible region of the spectrum, owing to their surface plasmon characteristics [72]. Mie theory describes the light absorption characteristic of spherical metal nanoparticles [72a], which shows that in the size range 3 to 10 nm, the absorption does not depend strongly on the size of the particle. This is due to the fact that the higher order terms in the Mie formula become insignificant in this size range. Thus, only the dipole term becomes relevant, which depends only on the total metal concentration and not the size of the particles. The absorption spectrum of particles in a given solvent can be calculated from the optical constants of the bulk metal [73]. The absorption coefficient, α ($mol^{-1}Lcm^{-1}$) can be calculated according to the relation

$$\alpha = \frac{18\pi}{\ln 10} \frac{10^5}{\lambda} \frac{Mn_0^3}{\rho} \frac{\varepsilon_2}{\left(\varepsilon_1 + 2n_0^2\right) + \varepsilon_2^2} \quad \ldots\ldots\ldots (1.1)$$

where λ is the wavelength of light, M and ρ are the molecular weight and density of the metal, n_o is the refractive index of the solvent and ε_1 and ε_2 are the real and imaginary parts of the dielectric constant of the metal. For particles smaller than the mean free path of the electrons, the absorption profile is explained using corrected values of ε_2 [73]

$$\varepsilon_2 = \varepsilon_{2(bulk)} + \left(\omega_p^2 / \omega^3\right)\left(V_F / R\right) \quad \text{.....(1.2)}$$

where ω is the frequency of light, ω_p the plasmon frequency, V_F the electron velocity at the Fermi level and R the particle radius (R/V_F, mean time of the free movement of the electrons). The plasmon frequency can be expressed as following

$$\omega_P = \frac{Ne^2}{m\varepsilon_0} \quad \text{.....(1.3)}$$

where N is the concentration of free electrons in the metal, e is charge on one electron and m is the effective mass of an electron [72c]. In order to satisfy the resonance condition with the incident light, ε_1 should be twice the negative value of dielectric constant of the medium,

$$\varepsilon_1 = -2\varepsilon_m \quad \text{.....(1.4)}$$

Gold and silver nanoparticles have a transverse plasmon absorption in the visible region of electromagnetic radiation, which is due to collective coherent excitation of conduction-band electrons on interaction with the incoming electromagnetic radiation [74]. The movement of the electrons under the influence of electric field vector of the incident light leads to a dipole oscillations across the particle sphere. The positive polarization charge acts as a restoring force, which causes the electrons to oscillate. Thus, the electron density within the surface layer, the thickness of which is about equal to the screening length of a few angstroms, oscillate whereas the density in the interior of the particle remains constant ("surface plasmon"). Therefore, any change in the electron density of this surface layer will lead to changes in the plasmon absorption [75]. Higher order modes become more dominant with increasing particle size, causing the plasmon absorption band to red shift and resulting in increased bandwidth. In the case of larger particles, the light cannot polarize the nanoparticles homogeneously and retardation effects lead to the excitation of higher order modes. Within the size range of 25 nm, the nanoparticles can be treated within the dipolar

approximation and the absorption profile is independent of the particle size. Though, it has been reported that below the size limit of 10 nm the particles start showing size dependence of the plasmon resonance band and ultimately disappear for particles of size less than 2 nm. This is attributed to the decreasing validity of the free electron gas model assumption [74,75].

Gans extended the Mie theory within the dipole approximation to explain the optical absorption of the cylindrical and oblate nanoparticles [76]. The plasmon resonance for nanorods shows two bands; the high energy band for the out of plane transverse plasmon resonance and the low energy band corresponding to the in-plane longitudinal plasmon resonance along the axis of the nanorods. The transverse plasmon band shows a linear relation with the aspect ratio (ratio of length to width of nanorods) and the dielectric constant of the medium [74,75]. With an increase in the aspect ratio, the energy separation between the two plasmon bands also increases [77]. Similarly, triangular nanoparticles also show two absorption bands corresponding to the transverse and longitudinal plasmon resonance. In certain cases, another peak in between the two plasmon peaks has also been reported which has been attributed to the in-plane quadrupole mode of plasmon resonance [78]. Several attempts have been made towards successful synthesis of anisotropic metal nanostructures such as rods [79], disks [80], triangular prisms [60g, 81], multipods [82], cubes [83] and nanoshells [84] and their optical properties have been studied.

1.4.5 Electronic property.

The electrical conductivity of bulk metal is dependent on the band structure and mobility of the electrons. The expression for mobility of an electron is given as,

$$\mu = \frac{e.\lambda}{4\pi\varepsilon_0 m_e V_F} \qquad \text{..... (1.5)}$$

where λ is the mean free path of the electron between two successive collisions, m_e being effective mass of electron in the lattice, V_F the speed of electron (Fermi speed) and ε_0 the dielectric constant of the medium. The collective motion of electrons in the bulk phase obeys Ohm's law [85]. However, when the size of the metal approaches the nanometer scale, the finite size leads to unique electronic properties and Ohm's law is not necessarily obeyed.

When an electron is transferred to a particle, its Coulomb energy increases ($E_C=e^2/2C$, C being capacitance of the particle). The thermal motion of the atoms (phonon) within the

particle can cause a change in charge and the Coulomb energy, resulting in uncontrolled electron tunneling. Thus, in order to obtain a single electron tunneling process, the thermal energy of the particle should be less than the Coulomb energy ($kT<<E_C$). Addition of a charge to the particle causes building up of a voltage (V=e/C), which results in a tunneling current ($I=V/R_T$ where R_T is the tunneling resistance).

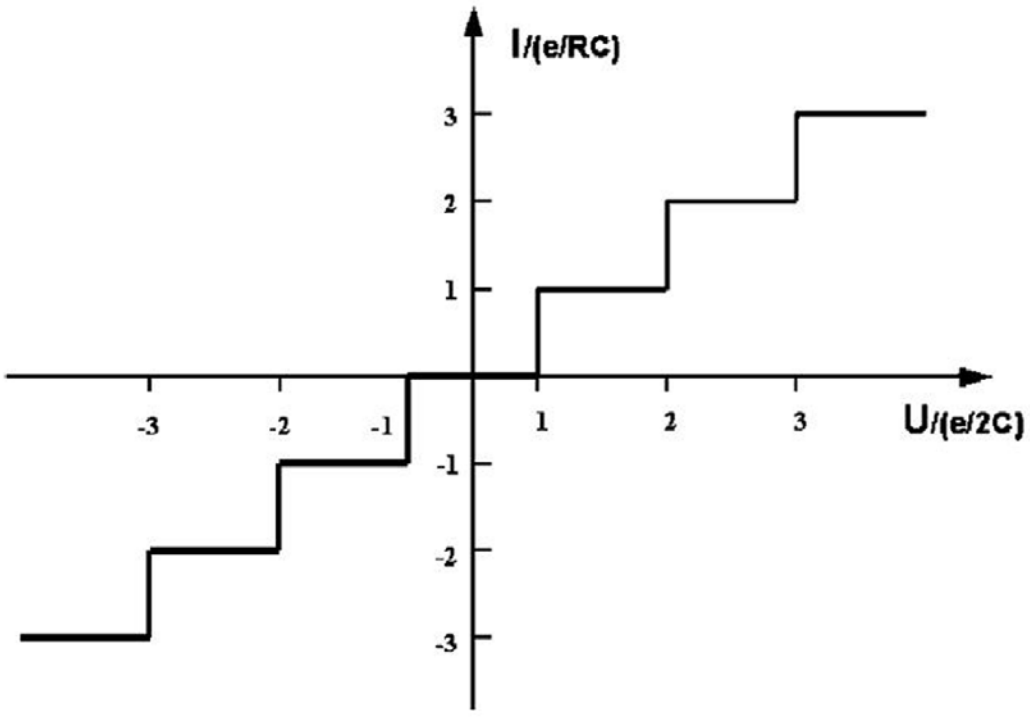

Figure 1.3 *I-V plot of ideal single electron transport showing Coulomb blockade as step function [75].*

A particle does not show current upto a voltage (V=±e/2C), the phenomenon known as Coulomb blockade. Thus, an external voltage above this value leads to the tunneling of the electron since the Coulomb energy is compensated. The repeated single electron tunneling in such cases result in an idealized "stair-case" (Figure 1.3) where the height of the stair, ΔI corresponds to e/RC while the width of the stair, ΔV is e/2C. This behavior is caused by the extremely small capacitance of the particles, which can store charge by the addition or removal of the charge. It is due to the presence of this small capacitance in the particles, which renders them extremely sensitive to the neighboring charges [86] and thus find application in fabricating sensor materials. A nanoparticle in a medium with a dielectric constant, ε, will have capacitance which will be a function of its size i.e.

$$C(r) = 4\pi\varepsilon_0 r \qquad \ldots\ldots\ldots (1.6)$$

The energy required to add a single charge to a nanoparticle can be given by the expression,

$$E_C = \frac{e^2}{2C(r)} \qquad \ldots\ldots\ldots (1.7)$$

The tunneling of a single charge on to the nanoparticles can be observed in the condition where $k_BT < E_C$ for all single nanoparticle devices or across the particle [87] on a conducting surface during STM measurement [86a, 88].

The electrical charge transport in discontinuous metal nanoparticles film/cluster depends on two factors: the charging energy (E_{ch}), which is determined by the capacitance of the particles and the tunnel coupling between the particles, which is a function of the distance between the nanoparticles. The tunneling current has been found to be dependent on the separation between the particles (x) and the barrier height, φ (work function). It can be expressed as

$$I \alpha e^{\frac{-2x}{\hbar\sqrt{2m\varphi}}} \qquad \ldots\ldots\ldots (1.8)$$

The electrical behavior of such films has been extensively studied in the past [89] and it has been shown that the activation energy for charge transport in such 3-D nanoparticles arrangement depends simply on the separation between the nanoparticles rather than the chemical nature of the molecule between them [90]. The temperature dependent electron conduction in such systems have been seen to follow the Arrhenius type activated electron tunneling behavior which follows the following relation [91],

$$\sigma(T) = \sigma_0 . e^{\frac{-E_A}{k_B . T}} \qquad \ldots\ldots\ldots (1.9)$$

where E_A is the activation energy, k_B is the Boltzmann's constant and T is the temperature. This shows the characteristic hopping transport between nearest neighboring particles. The activation energy (E_A) becomes temperature dependent when the measuring temperature is decreased and at very low temperatures, the conductivity follows the variable-range hopping (VRH) model given by Mott [92],

$$\sigma(T) = \sigma_0 . e^{\left(\frac{-T_0}{T}\right)^{\gamma}} \quad \text{..... (1.10)}$$

where γ=1/(D+1) in D dimensions of the conduction path. Though γ is expected to have the value equal to ¼ for 3D nanoparticles, its value is mostly found to be ½ (D=1) for compact metal-cluster compounds. The temperature range, where the nearest-neighbor hopping to variable-conduction hopping transition is observed, has been found to be dependent on the particle size and the degree of disorder.

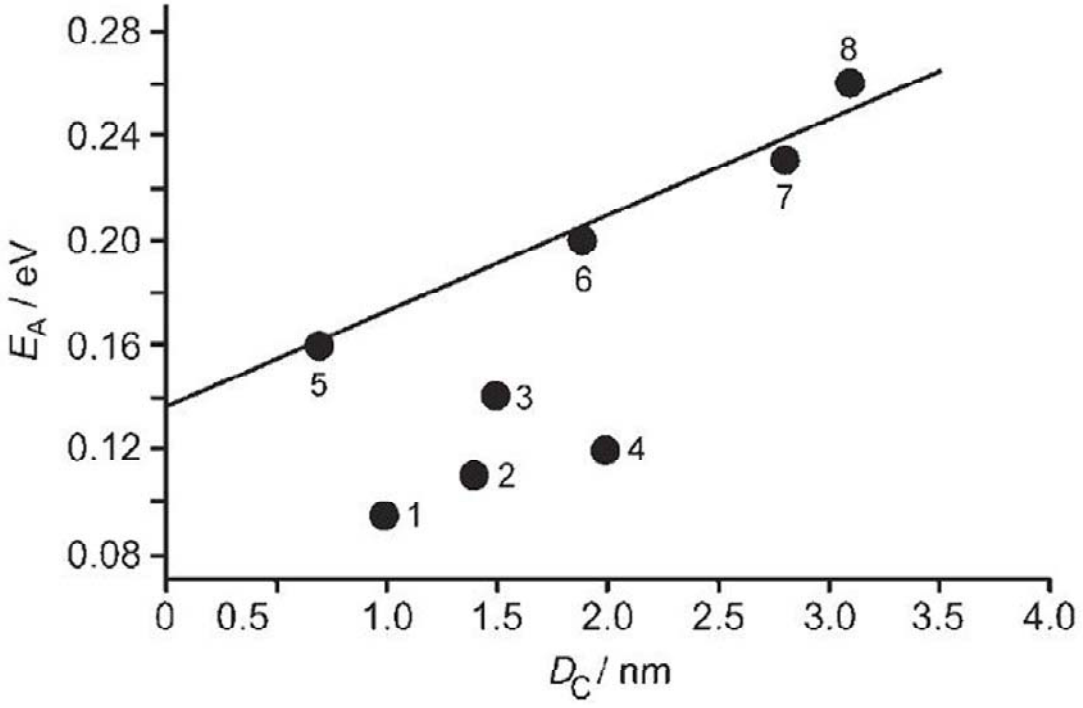

Figure 1.4 *Activation energies (E_A) vs interparticle distance (D_C) for the covalently (1-4) and non-covalently (5-8) organized system [93].*

The dependence of the electrical conductivity of such 3D nanoparticles assembly on temperature and applied electric field has been studied using several theoretical models for electron hopping to finally confirm that the experimental results could be explained by thermally activated stochastic multiple site hopping process. However, at higher temperatures, nearest-neighbor hopping dominates [94]. It is important to understand that at low temperatures, the number of charge carriers participating in the hopping process is independent of the temperature where as at higher temperatures, where k_BT term becomes comparable to the charging energy (E_{ch} is determined by the capacitance of the particles and

thus is particle size and interparticle space dependent) of the metal nanoparticle, further thermally excited charge carriers participate in the hopping process. It has also been shown that for room temperature measurements, where Arrhenius-type thermal activation exists, the nearest-neighbor hopping is a strong function of the interparticle spacing when the particle size is fixed [91]. The plot in Figure 1.4 shows that with increasing interparticle distance, the activation energy for hopping increases linearly. This can be explained from the fact that the interparticle capacitance will decrease with increasing interparticle spacing when the other geometric and dielectric parameters are kept constant. However, the limitation to this relation has to be realized that the spacer molecules should not be covalently attached to the particle surface and they should not have delocalized π-electron system in their termini. In cases where the covalently linked spacer with delocalized π-electron system enables the electron transfer, the activation energy of the system drops, depending on the electronic structure and length of the molecule (Figure 1.4, data points 1,2,3,4).

Wuelfing, Murray and coworkers have proposed that the cell constant, i.e. the geometry parameter of the sample, must be known precisely in order to discriminate between a temperature-independent tunneling and the thermally activated over-barrier process [95]. They have suggested an Arrhenius-type activated tunneling model to describe the transport phenomenon through a 3D network of ligand-stabilized gold nanoparticles. The relation governing this phenomenon is given as,

$$\sigma(\delta,T) = \sigma_0 .e^{-\beta\delta} .e^{\frac{-E_A}{k_B T}} \quad \text{..... (1.11)}$$

where β is the electron tunneling coefficient, δ is the average interparticle distance and the expression $\sigma_0 . e^{-\beta\delta}$ gives the conductivity when $k_BT >> E_A$. The first term in the above expression gives the electron tunneling between particles through the ligand shell and depends exponentially on the length of the surface capping molecule as long as the Fermi level of the particles lies between the highest occupied molecular orbital (HOMO)-lowest unoccupied molecular orbital (LUMO) gap of the capping molecule. Recently it has also been shown that the partial resonant tunneling through the conjugated portion of the interconnecting molecules, the electrical property of the 3D-linked gold nanocluster

assemblies can be tuned [96]. The second exponential term in the expression gives the activation energy for the charge transport.

Thus, in general, it can be concluded that the electrical conduction within the 3D nanoparticle assemblies depends on the particles size, the interparticle spacing as well as the nature of the capping agent and its electronic structure. So, selective adsorption of gas molecules on such hybrid nano-assemblies can be easily exploited to fabricate chemiresistors for sensing chemical vapors.

1.4.6 Biocompatibility.

One of the important aspects in the study of nanoscience and nanotechnology is to assess the cytotoxicity levels of nanoparticles in living systems. Nanoparticles have been used for various biological applications and otherwise [97]. They have found potential future in the fields of biodiagonostics [98], therapeutics [99], drug delivery [100], bioimaging [101], immunostaining [102] and biosensing [103]. Thus, it becomes an important issue to study the short and long term effect of size, shape, and surface functional groups on the bioavailability, uptake, subcellular distribution, metabolism, and degradation of these different nanostructures. Some attempts have been made towards this aim and studies have been undertaken to address these issues with carbon nanostructures [104], CdSe quantum dots [105] and gold nanoparticles [106]. Gold nanoparticles have specially been extensively studied for their cytotoxicity effects because it is a noble metal and has been exploited for various applications in the field of biomedical science. Sastry et al. [106g] have studied the uptake of gold nanoparticles by mammalian cells by pinocytosis and its compartmentalization in lysosomal bodies. They have shown that the chemically synthesized (sodium borohydride reduced) gold nanoparticles do not show any visible cytotoxicity to the human cell lines till 100 μM concentration. They report upto 85% of cell viability even after 72 h of exposure of the human cells to the gold nanoparticles. These reports clearly suggest that the gold nanoparticles are biocompatible and thus, are useful candidates for various applications in nanomedicine.

1.5 Nanoparticle assembly.

Metal nanoparticles have been assembled on different substrates into ordered arrangement using several approaches. The rationale behind assembling of the nanoparticles on a substrate depends largely on the nature of the substrate.

1.5.1 Assembly on a glass substrate.

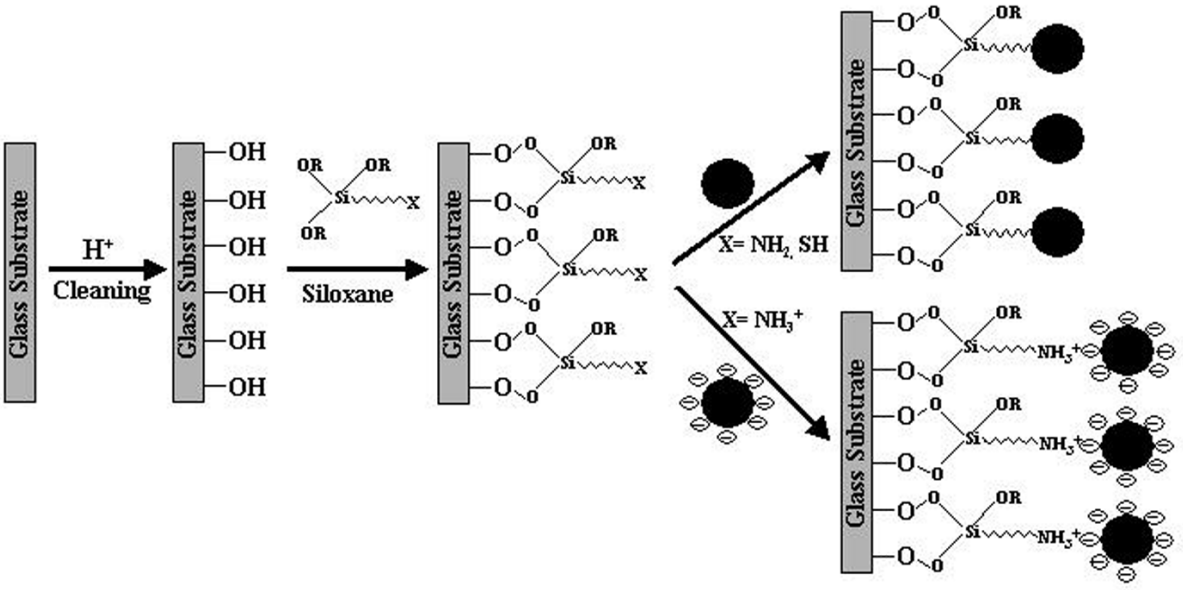

Figure 1.5 *Schematic showing the assembly of nanoparticle on glass by surface modification.*

Glass substrates can be conducting (such as indium-doped tin oxide or 'K' Glass) or non-conducting (quartz or soda glass). The surface of the substrate in such cases should be clean in order to have maximum number of free –OH groups and this is often achieved by washing the substrate in piranha solution or aqua regia. The substrate is often functionalized by silane [107] or siloxanes [108] groups in order to achieve strong binding of the nanoparticles to the surface. Some of the techniques to achieve the fabrication of these assemblies can be enlisted as photolithography [109], sedimentation [110], electrostatic-induced crystallization [111], convective self-assembly [112], physical confinement [113], chemical vapor deposition [114], dielectrophoresis [115] and Langmuir-Blodgett deposition [116].

1.5.2 Assembly on a metal substrate.

The assembly of nanoparticles on a metal substrate is similar to the methods followed for glass substrates. In the case of gold as a substrate, the surface is often modified by functionalized alkanethiols [117] to allow its covalent attachment to the gold, while the other end bears another moiety such as another thiol [118], amine [119] or carboxylic acid [120], which coordinates with the nanoparticle surface. Similarly, aluminium surface can be easily functionalized by the use of carboxylic acid for assembly of nanoparticles [121]. Electrically

conducting substrates also open up the possibility of assembling the nanoparticles on the substrate electrophoretically [122]. The surface of the substrate here is first functionalized by thiols to reduce the surface charge following which, the particles are deposited at the anodic electrode under application of low potential.

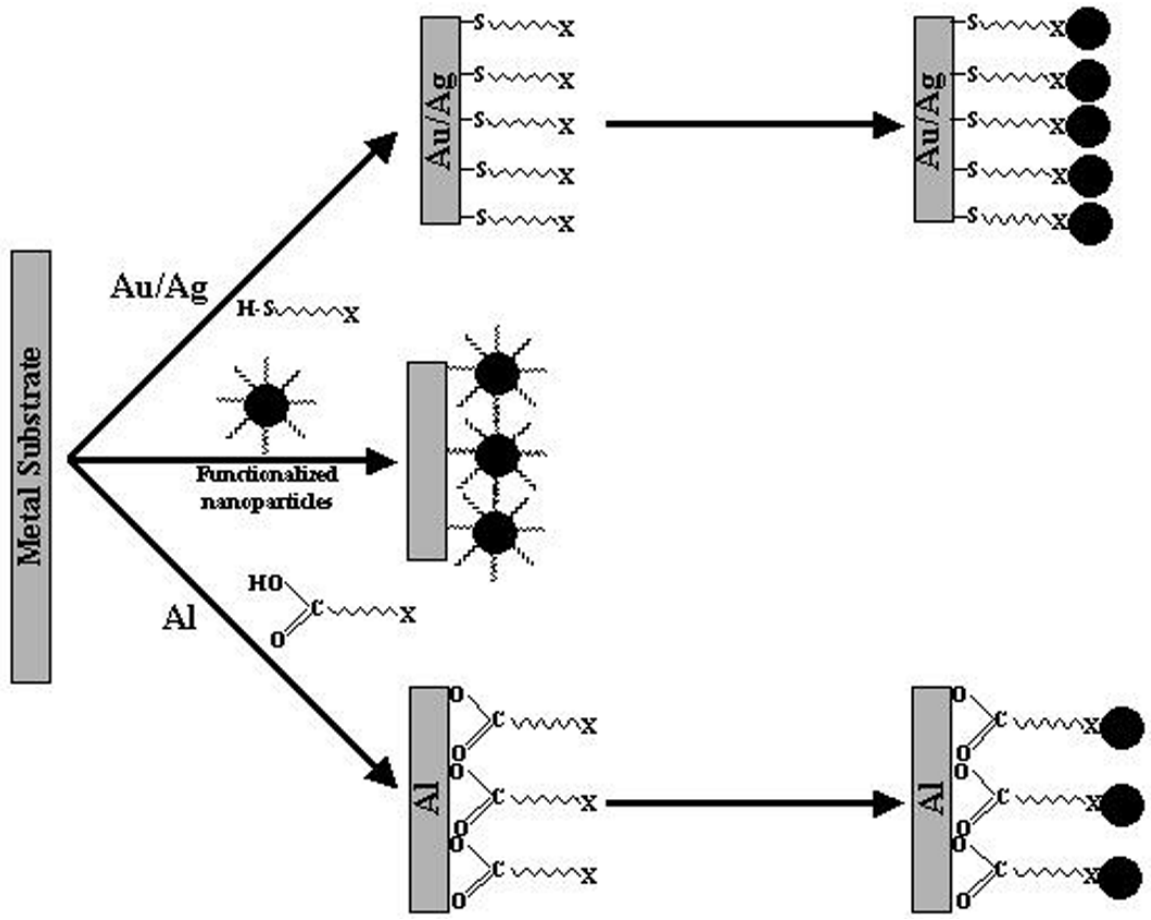

Figure 1.6 *Schematic showing the assembly of nanoparticle on metal surface by metal surface or nanoparticle modification.*

1.5.3 Assembly on carbon substrates.

Electrochemical deposition is the most popular method for assembly of the nanoparticles on a carbon substrate. This process follows the electrochemical reduction of the metal salt of on the surface of the substrate, formation of primary ad-atom and the subsequent growth process of the nanocrystals [123]. Controlling the deposition conditions such as salt concentration and applied potential can control the overall surface area, size, density and the surface texture of the formed nanocrystallites [124]. Similarly, carbon nanotubes have been used for electrostatic assembly of metal nanoparticles [125]. A review by Wildgoose et al.

summarizes the various electrochemical, chemical and physical routes adopted for the assembly of metal nanoparticles on carbon nanotubes and the application of the nanocomposites thus formed [126].

1.5.4 Assembly on polymer substrates.

Polymers have been used as a template for assembling nanoparticles mainly by electrostatic attraction. Generally, anionic colloidal particles are assembled onto the cationic polymers and viceversa, leading to the formation of multilayer composite structure in a stepwise manner. Several polyelectrolytes such as poly (diallyldimethylammonium) (PDDA) [127], poly (allylamine hydrochloride) (PAH) [128], polyaniline [129] and poly (Phenylene-pyridyl) dendrimers [130] have been used to assemble metal nanostructures. The advantage of these nanocomposites is that the polymer layer thickness can be easily controlled and the colloidal layer can be maintained at a desired distance from each other. Thus, such nanocomposites hold great promises for application in fabricating nano-devices. Sastry et al. have reported the use of polyurethane microspheres to immobilize gold nanoparticles on the surface to form nanocomposites, which has been shown to find application as scaffold for enzyme immobilization [131].

1.5.5 Assembly on other substrates.

One of the growing challenges in the field of nanotechnology is the development of bio-nano hybrid systems for several applications. One of the most exploited biological templates is DNA (deoxy ribonucleic acid), which has been used as substrate for assembling metal nanostructures [132]. Sastry et al. have shown that the preferential binding of nucleotide bases to gold nanoparticles is in the order of Cytosine> Guanine> Adenine> Thymine [133]. DNA-inorganic hybrids can be prepared by two approaches: 1) use of the duplex DNA as a physical template to immobilize nanoparticles leading to the formation of the hybrid system and, 2) use of single strand DNA-functionalized nanoparticles for sequence specific hybridization to obtain the assembly of the attached nanoparticles. DNA template has been used to grow wires of DNA-inorganic hybrid materials and the electrical conductivity has been studied [134]. It was shown that the threshold voltage for electrical conduction could be controlled by varying the amount of silver deposited on the DNA surface and such controls will open up a new area for nanocircuitry for future nano-scale electronic devices. Other than DNA, several other biological materials such as peptides

[135], lipids [136], immunoglobulin [137], viruses [138] and microorganisms [139] have also been used as template to assemble metal nanoparticles on their surface.

1.6 Motivation of the work.

The introduction given towards the beginning of this chapter clearly indicates that metal nanoparticles find application in wide-ranging fields. Reduction in size leads to a change in the physical, chemical, optical, electronic and catalytic properties of the material, which are otherwise considered intensive in nature [140]. It is this change in the properties that has driven us to exploit metal nanomaterials for various applications. The importance of metal nanostructures is evident from the various aspects that are being pursued towards their potential applications. They have been exploited for applications such as catalysis [7b, 68-69, 141], fuel cells [142], heavy metal detection [143], photonic band-gap materials [144], single electron transistors [145], non-linear optical devices [146] and surface-enhanced Raman spectroscopy [147]; besides the biological applications enlisted above [97-103]. The work presented in this thesis emphasizes on the use of metal nanoparticles on a substrate for resistive chemical vapor sensing as well as solution based detection of mercury. A detailed account of the previous research in the field of chemical vapor sensors is discussed in the following section. Further more, an attempt has also been made to assess the biocompatibility of biogenic gold nanotriangles and their internalization process inside the cell. This thesis focuses mainly on the following aspects:

1) Assembly of metal nanoparticles on hard substrates for chemical vapor sensing.
2) Assembly of metal nanoparticles on soft template for chemical vapor sensing.
3) Use of anisotropic metal nanostructures for solution based mercury detection.
4) Cytotoxicity studies and probing of internalization of biogenic anisotropic gold nanotriangles in human cells.

1.7 Metal nanostructures in chemical vapor sensing.

Development of a sensor to detect and monitor a variety of gases and vapors, including toxic and explosive gases, humidity and odors is a key area of research. A sensor element has to transform the chemical information in the gases or vapors into an analytically manageable signal by virtue of a chemical or physical reaction of the gas with the sensing material. Several such sensors that have been reported in the past are calorimetric sensors [148], electrochemical cells [149], gas-sensitive field-effect transistors [150], acoustic wave

transistors [151], quartz crystal microbalances [152] and chemiresistors. Among these, chemiresistors (resistive gas sensing elements) are the one that are most commonly applied. The earlier attempts towards fabrication of chemiresistors were focused on the use of metal oxides, which change their electrical resistance on exposure to an oxidizing or reducing gas.

Brattein and Bardeen for the first time reported this phenomenon of change in resistance for Ge [153], which was confirmed by Heiland a little later [154]. Further attempts by Seiyama et al. [155] and Taguchi [156] lead to the fabrication of the first gas-sensing elements. Since them, extensive efforts have been made to improve upon the parameters such as sensitivity, selectivity, stability and the response and recovery time, which are considered to be vital for performance of a chemiresistor. Besides the use of metal oxides, metal nanostructures embedded in an organic matrix have also been exploited as potential vapor and gas sensors [157]. In such nanocomposite systems, the metal nanoparticles impart electrical conductivity while the organic matrix provides the selective binding site for the analyte molecules on exposure.

The *sensitivity (S)* of a sensor is defined as the ability to detect a given concentration of the analyte in the environment and is usually expressed as the slope of the output signal y (e.g. resistance change in the case of a chemiresistor) as a function of the concentration x of that particular gas [158]. It can be given as

$$S = \frac{dy}{dx} \qquad \ldots\ldots\ldots (1.12)$$

Similarly, *selectivity (Q)* of a sensor is its ability to discriminate the analyte in question in a mixture of gases and is usually defined by the sensor's cross sensitivity to all the other gases which occur at same concentration x as the analyte. It can be shown as

$$Q = \frac{\frac{dy}{dx'}}{\frac{dy}{dx}}.100 \qquad \ldots\ldots\ldots (1.13)$$

The response (or recovery) time of a sensor is defined as the time taken by the sensor to give 90% of the saturation output signal from the point at which the pulse of the analyte is switched on (or off).

Wohltjen and Snow, for the first time, reported the use of metal nanoparticles (film of 2 nm gold nanoparticles capped with octanethiol) for fabrication of a chemiresistor to show

quick, sensitive and reversible response towards toluene, tetrachloroethene, 1-propanol and water vapor [157a]. They showed that the electronic conduction between the particles (hopping/tunneling) is affected by the adsorption of vapors into the interparticle organic phase. Since then, several other attempts have been made to improve upon the selectivity of such metal nanoparticle films by introducing chemical functionalities into the organic matrix [157b-d,g]. Vossmeyer and co-workers used gold nanoparticles organic dendrimer nanocomposites for preparation of sensors [157d,e]. They exploited the well-understood host-guest chemistry of the dendrimers to develop sensitive nanocomposites for vapor sensing. This approach was novel due to the fact that the polyfunctionalized dendrimers could be easily used for layer-by-layer assembly of gold nanoparticles on their surface to obtain desired thickness and interparticle distance. In yet another report, they studied the use of gold nanoparticles poly (propyleneimine) dendrimer based chemiresistor for vapor-sensing applications. Here, they used different generation dendrimers to show that the resistivity of the films increase exponentially with increasing generation of the dendrimers. They showed that the film was sensitive towards exposure to toluene, 1-propanol and water vapor. It was also observed that the sensitivity of the film towards the two organic molecules increased with increasing dendrimer size while it was unchanged to water vapor. This was explained based on the assumption that the site of interaction of the organic molecules to the nanocomposite is different to that of the water vapor; the organic molecules are solvated within the interior compartment of the dendrimer while water vapor interact with the surface amine groups only. The same group also reported the use of Pt and Au nanoparticles cross linked with nonanedithiols based chemiresistors for sensitive detection of CO and NH_3 vapor [159].

The exact mechanism of the ability of an analyte to change the electronic conductivity is not fully understood at present. In the case of nanocomposites, it is speculated that the swelling of the film due to the incorporation of the vapor into the organic matrix leads to increase in the tunneling resistance of the film. However, in cases where the analyte directly binds to the metal nanoparticles, the exact explanation is difficult to realize. However, Gregor'ev et al. have shown that in the nanocomposites of poly (p-xylene) with lead, copper or palladium, the uptake of an electron donor analyte (e.g. ammonia, alcohols, water) tends to decrease the work function for charge transport [160], in turn decreasing the

potential barrier and thus increasing the conductivity. On the other hand, electron accepting analytes (e.g. hydrogen, dichlorobutane) increase the electron work function, resulting in an increase in the potential barrier and consequent decrease in the tunneling current [161]. They assume that the adsorption of the analyte on the nanocomposite change the fractal characteristic of the composite as well as the work function for charge transport.

1.8 Outline of the thesis.

The work presented in this thesis deals with the potential application of metal nanoparticles in chemical vapor sensing and as optical beacons for detection of mercury in water samples. Biogenic gold nanotriangles have been used to fabricate conducting film onto quartz substrate to find application in chemical vapor sensing. Similarly, transmetallation approach has been undertaken to fabricate bimetallic conducting film on quartz substrate for detecting ammonia and carbon di oxide vapors. In another approach, spider silk has been used as an active scaffold for immobilization of gold nanoparticles on the surface for sensitive detection of polar vapors based on their polarity. The anisotropy of the biogenic gold nanotriangles has been exploited to develop a methodology for ultra-low level solution based detection of mercury in water samples. Recently, biological synthesis has been considered as an eco-friendly and green approach for obtaining nanostructures. However, no attempt has been made to study the biocompatibility of these biologically synthesized nanostructures for their cytotoxicity levels and biocompatibility. A part of this thesis tries to address this issue by using lemon grass reduced gold nanotriangles for biocompatibility studies.

The ***Second Chapter*** gives an account of instruments and experimental characterization techniques such as UV-visible-NIR Spectroscopy, Transmission Electron Microscopy (TEM), Scanning Electron Microscopy (SEM) and Energy Dispersive Analysis of X-Rays (EDAX), Atomic Force Microscopy (AFM), Phase Contrast Microscopy, X-ray Photoelectron Spectroscopy (XPS), High Current Source Measurement Conductivity Meter, X-ray diffraction (XRD), Flow cytometry and enzyme linked immunosorbent assay (ELISA) that have been used to characterized samples during the course of this thesis. The physical principals of all these instruments have been discussed to illustrate their importance in characterization of nanomaterials.

The ***Third chapter*** describes the fabrication of conducting films onto a solid support using the biologically synthesized gold nanotriangles by a simple drop coating method. The electrical conductivity of the films has been studied as a function of number of coats showing a trend in the resistance drop. Further, it has been shown that a film of very high conductivity can be obtained by a simple annealing process, by keeping the film at 200° C for three cycles of one hour each. It has been shown that these films can find an application in sensing polar vapors such as methanol where a nine orders of magnitude increase in conductivity is observed on exposure where as weakly polar chloroform vapor shows little response. A part of this chapter has been used to report the fabrication of highly porous bimetallic film of Ag-Au onto a solid support by using the transmetallation reaction. These bimetallic films have been formed by using varying concentrations of chloroauric acid ($HAuCl_4$) and the electrical conductivity measurement in each case has been performed. Further, it is discussed that these porous films can be of importance in sensing chemical vapors like carbon di oxide and ammonia, where the exposure to these vapors shows three to four orders of magnitude increase in conductivity.

The ***Fourth chapter*** describes the use of soft active template like spider silk to reduce and subsequently immobilize gold nanoparticles onto their surface. SEM imaging and EDAX analysis confirm the presence of gold on the surface of spider silk. It has also been shown that by varying the initial concentration of the gold salt, the degree of decoration of the spider silk can be varied. Besides, we have also performed electrical conductivity studies on the nanogold-spider silk bioconjugate and the activation energy for conduction has been calculated. Further, the chapter also describes the application of this bioconjugate in sensing polar vapors, exploiting the property of spider silk to contract in polar environment reversibly. It has also been shown in this work that the nanogold-spider silk bioconjugate gives varying response to different vapors based on the polarity of the respective vapor and thus can be used to detect gases on the basis of their polarity. Further, control experiments have been done using silkworm silk fibers, which do not show any change in conductivity on exposure to these vapors, as they have not been reported to show any such contraction mechanism on exposure to such vapors.

The ***Fifth chapter*** illustrates the use of the biologically synthesized gold nanotriangles to develop an easy but highly sensitive protocol to detect mercuric ions in

water samples. Mercury has been known for a long time to have a strong tendency to amalgamate gold. This property has been exploited in this work where mercuric ions have been reduced in the presence of the gold nanotriangles to facilitate amalgamation. In this lab, we have shown earlier that anisotropic gold nanotriangles show a very strong absorbance in the NIR region besides characteristic peak in visible[9]. It has been observed that on the amalgamation of these gold nanotriangles by mercury, the NIR absorbance of the triangular gold nanoparticles is decreased drastically at higher concentrations of mercuric ions and shows significant change even at concentration as low as 10^{-18} M. The TEM imaging also corroborates the observed UV-vis-NIR spectra of the gold nanotriangles on exposure to different concentrations of mercuric ions. AFM and HRTEM measurements have been done to illustrate the underlying mechanism causing the change in the absorption properties of these nanotriangles in presence of mercury.

The ***Sixth chapter*** discusses the study of the dose and time dependent cytotoxicity effect and limit of the biologically synthesized gold nanotriangles onto the cancerous (RAW & MCF-7) and non-cancerous (NIH3T3) animal cell lines. We find that these nanotriangles do not show much toxicity to the animal cells even at high concentrations compared to the chemically synthesized spherical nanoparticles as well as the precursor salt of gold. Further ELISA studies have been done to show stress induced cytokine response of the animal cells when they are exposed to the gold nanotriangles. Further, microscopic imaging has been done to confirm that these nanoparticles are indeed internalized inside the macrophages cells using a phase contrast microscope. Thus, it has been illustrated that these biologically synthesized gold nanotriangles are not toxic to animal cells even at high concentrations and thus can serve as an excellent candidates for use in hyperthermic treatment of cancer cells owing to their tunable strong absorbance in the NIR region. Its internalization inside the animal cells also open up area of drug and gene delivery using these nanotriangles.

The ***Seventh chapter*** includes a brief summary of the work presented in the thesis and emphasizes on the possible further research in this area.

1.9 References.

1) Feynman, R. P. *Eng. Sci.* **1960**, *23*, 22.
2) September issue of Scientific American, **2001**.

3) (a) Whitesides, G.M. *Small*, **2005**, *1*, 172. (b) Fendler, J. H.; Meldrum, F.C. *Adv. Mater*. **1995**, *7*, 607. (c) Schmid, G. *Chem. Rev.* **1992**, *92*, 1709.
4) http://www.colloidalgold.com/history.htm
5) http://www.horusmedia.de/2001-aurum/aurum-en.php
6) (a) Antonii, F. Panacea Aurea–Auro Potabile, Bibliopolio Frobeniano, Hamburg, **1618**. (b) Kunckels, J. Nuetliche Observationes oder Anmerkungen von Auro und ArgentoPotabili, Schutzens, Hamburg **1676**. (c) Helcher, H. H. Aurum Potabile oder Gold Tinstur, J. Herbord Klossen, Breslau and Leipzig **1718**. (d) Lloyd, J.U. *Elixirs and Flavoring Extracts: Their History, Formulae, and Methods of Preparation*, **1892**, New York: William Wood and Company.
7) (a) Ostwald, W. *Kolloid Z.***1909**, *4*, 5. (b) Daniel, M.; Astruc, D. *Chem. Rev.* **2004**, *104*, 293.
8) Fulhame, Mrs. *An Essay on Combustion with a View to a New Art of Dying and Painting*; J. Cooper: London, **1794**.
9) (a) Savage, G. *Glass and Glassware*, Octopus Book, London **1975**. (b) Wagner, F.E.; Haslbeck, S.; Stievano, L.; Calogero, S.; Pankhurst, Q.A.; Martinek, K.-P. *Nature* **2000**, *407*, 691. (c) Turkevich, J. *Gold Bull.* **1985**, *18*, 86.
10) Faraday, M. *Philos. Trans.* **1857**, *147*, 145.
11) Graham, T. *Philos. Trans. R. Soc*. **1861**, *151*, 183.
12) Taniguchi, N. 1974. On the Basic Concept of 'Nano-Technology'. In: *Proceedings of the international conference on production engineering. Tokyo, Part II,* Japan Society of Precision Engineering, 1974: 18-23: Tokyo: JSPE.
13) (a) Wegner, K.; Walker, B.; Tsantilis, S.; Pratsinis, S.E. *Chem. Eng. Sci.* **2002**, *57*, 1753. (b) Choi, C.J.; Tolochko, O.; Kim, B.K. *Mater. Lett.* **2002**, *56*, 289. (c) Wang, Z.H.; Choi, C.J.; Kim, J.C.; Kim, B.K.; Zhang, Z.D. *Mater. Lett.* **2003**, *57*, 3560. (d) Oha, S.; Choi, C.; Kwon, S.; Jin, S.; Kim, B.; Park, J. *J. Magn. Magn. Mater.* **2004**, *280*, 147. (e) Chevallier, J. *Thin Solid Films* **1977**, *40*, 223. (f) Perekrestov, V.I. *Tech. Phys. Lett.* **2005**, *31*, 830.
14) (a) Wang, Y.; Zhang, L.; Meng, G.; Liang, C.; Wang, G.; Sun, S. *Chem.Commun.* **2001**, 2632. (b) Teng, X.; Black, D.; Watkins, N.J.; Gao, Y.; H. Yang, *Nano Lett.* **2003**, *3*, 261. (c) Wang, Y.; Herricks, T.; Xia, Y. *Nano Lett.* **2003**, *3*, 1163. (d) Hou, Y.; Kondoh, H.;

Kogure, T.; Ohta, T. Chem. Mater. **2004,** *16,* 5149. (e) Lee, D.K.; Kang, Y.S. *ETRI Journal* **2004**, *26*, 252.

15) (a) Kim, J.H.; Germer, T.A.; Mulholland, G.W.; Ehrman, S.H. *Adv. Mater.* **2002**, *14*. 518. (b) Mädler, L.; Kammler, H.K.; Mueller, R.; Pratsinis, S.E. *J. Aerosol Sci.* **2002**, *33*, 369. (c) Okuyama, K.; Lenggoro, I.W. *Chem. Eng. Sci.* **2003**, *58*, 537. (d) Mueller, R.; Mädler, L.; Pratsinis, S.E. Chem. Eng. Sci. 2003, 58, 1969. (e) Suh, W.H.; Suslick, K.S. *J. Am. Chem. Soc.* **2005**, 127, 12007.

16) (a) Zhou, Y.; Wang, C.Y.; Zhu, Y.R., Chen, Z.Y. *Chem. Mater.* **1999**, *11*,2310. (b) Li, H.X.; Lin, M.Z.; Hou, J.G. *J. Crystal Growth* **2000**, *212*, 222. (c) Mallick , K.; Wang , Z.L.; Pal, T. *J. Photochem. Photobiol. A* **2001**, *140*, 75. (d)Chen, W.X.; Lee, J.Y.; Liu, Z. *Chem. Commun.* **2002**, 2588. (e) Mandal, M.; Kundu, S.; Ghosh, S.K.; Pal, T. *Bull. Mater. Sci.* **2002**, *25*, 509. (f) Jin, R.; Cao, Y.C.; Hao, E.; Métraux, G.S.; Schatz, G.C.; Mirkin, C.A. *Nature* **2003**, *425*, 487. (g) Yin, H.; Yamamoto, T.; Wada, Y.; Yanagida, S. *Mater. Chem. Phys.* **2004**, *83*, 66. (h) Zhua, H.; Zhang, C.; Yin, Y. *J. Crystal Growth* **2004**, *270*, 722. (i) Kimling, J.; Maier, M.; Okenve, B.; Kotaidis, V.; Ballot, H.; Plech, A. *J. Phys. Chem. B* **2006,** *110,* 15700. (j) Sakamoto, M.; Tachikawa, T.; Fujitsuka, M.; Majima, T. Langmuir, **2006**, *22,* 6361. (k) Jia, H.; Xu, W.; An, J.; Li, D.; Zhao, B. *Spectrochimica Acta A* **2006**, *64*, 956. (l) Itakura, T.; Torigoe, K.; Esumi, K. *Langmuir* **1995**,*11*, 4129. (m) Ershov, B. G.; Henglein, A. *J. Phys. Chem.* **1993**, *97*, 3434. (n) Gutierrez, M.; Henglein, A. *J. Phys. Chem.* **1993**, *97*, 11368. (o) Torigoe, K.; Esumi, K. *Langmuir* **1993**, *9*, 1664. (p) Torigoe, K.; Esumi, K. *Langmuir* **1992**, *8*, 59. (q) Esumi, K.; Matsuhisa, K.; Torigoe, K. *Langmuir* **1995**, *11*, 3285. (r) Marignier, J. L.; Belloni, J.; Delcourt, M. 0.; Chevalier, J. P. *Nature* **1985**, *317*, 344.

17) (a) Amendola, V.; Polizzi, S.; Meneghetti, M. *J. Phys. Chem. B* **2006,** *110,* 7232. (b) Amendola, V.; Rizzi, G.A.; Polizzi, S.; Meneghetti, M. *J. Phys. Chem. B* **2005**, *109*, 23125. (c) Balchev, I.; Minkovski, N.; Marinova, Ts.; Shipochka, M.; Sabotinov, N. *Mater. Sci. Eng. B* **2006**, *135*, 108. (d) Becker, M.F.; Brock, J.R.; Cai, H.; Henneke, D.E.; Keto, J.W.; Lee, J.; Nichols, W.T.; Clicksman, H.D. *Nanostruct. Mater.* **1998**, *10*, 853. (e) Mafuné, F.; Kohno, J.; Takeda, Y.; Kondow, T. *J. Phys. Chem. B* **2000,** *104,* 9111. (f) Mafuné, F.; Kohno, J.; Takeda, Y.; Kondow, T. *J. Phys. Chem. B* **2000**, *104*, 8333. (g) Mafuné, F.; Kohno, J.; Takeda, Y.; Kondow, T.; Sawabe, *J. Phys. Chem. B* **2001**, *105*,

5114. (h) Mafuné, F.; Kohno, J.; Takeda, Y.; Kondow, T. *J. Phys. Chem. B* **2002**, *106*, 7575. (i) Zhu, X.P.; Suzuki, T.; Nakayama, T.; Suematsu, H.; Jiang, W.; Niihara, K. *Chem. Phys. Lett.* **2006**, *427*, 127. (j) Cai, H.; Chaudhary, N.; Lee, J.; Becker, M.F.; Brock, J.R.; Keto, J.W. *J. Aerosol Sci*. **1998**, *5/6*, 627.

18) (a) Chen, W.; Cai, W.; Lei, Y.; Zhang, L. *Mater. Lett.* **2001**, *50*, 53. (b) Chen, W.; Cai, W.; Zhang, L.; Wang, G.; Zhang, L. *J. Colloid Interface Sci.* **2001**, *238*, 291. (c) Dhas, N.A., Raj, C.P., Gedanken, A. *Chem. Mater.* **1998,** *10,* 1446. (d) Fujimoto, T.; Terauchi, S.; Umehara, H.; Kojima, I.; Henderson, W. *Chem. Mater.* **2001,** *13,* 1057. (e) Fujimoto, T.; Mizukoshi, Y.; Nagata, Y.; Maeda, Y.; Oshima, R. Scripta Mater. 2001, 44, 2183. (f) Nemamcha, A.; Rehspringer, J.; Khatmi, D. *J. Phys. Chem. B* **2006,** *110,* 383. (g) Okitsu, K.; Mizukoshi, Y.; Bandow, H.; Yamamoto, T.A.; Nagata, Y.; Maeda, Y. *J. Phys. Chem. B* **1997,** *101,* 5470. (h) Pol, V.G.; Grisaru, H.; Gedanken, A. *Langmuir* **2005,** *21,* 3635. (i) Salkar, R.A.; Jeevanandam, P.; Aruna, S.T.; Koltypin, Y.; Gedanken, A. *J. Mater. Chem.* **1999**, *9*, 1333. (j) Su, C.; Wu, P.; Yeh, C. *J. Phys. Chem. B* **2003,** *107,* 14240. (k) Suslick, K.S.; Fang, M.; Hyeon, T. *J. Am. Chem. Soc.* **1996,** *118,* 11960. (l) Wu, C.; Mosher, B.P.; Zeng, T. *Chem. Mater.* **2006**, *18*, 2925.

19) (a) Kurihara, K.; Kizing, J.; Stenius, P.; Fender, J. H. *J. Am. Chem.Soc.* **1983**, *105*, 2574. (b) Mulvaney, P.; A. Henglein, *J. Phys. Chem.* **1990**, *94*, 4182. (c) Joshi, S.S.; Patil, S.F.; Iyer, V.; Mahumuni, S. Nanostruct. Mater. **1998**, *7*, 1135. (d) Henglein, A.; Meisel, D. Langmuir **1998,** *14,* 7392. (e) Gachard, E.; Remita, H.; Khatouri, J.; Keita, B.; Nadjo, L.; Belloni, J. *New J. Chem.* **1998**, 1257. (f) Henglein, A.; Giersig, M. *J. Phys. Chem. B* **1999,** *103,* 9533. (g) Dimitrijevic, N.M.; Bartels, D.M.; Jonah, C.D.; Takahashi, K.; Rajh, T. *J. Phys. Chem. B* **2001,** *105,* 954. (h) Doudna, C.M.; Bertino, M.F.; Blum, F.D.; Tokuhiro, A.T.; Lahiri-Dey, D.; Chattopadhyay, S.; Terry, J. *J. Phys. Chem. B* **2003**, *107,* 2966.

20) (a) S.I. Stoeva, B.L.V. Prasad, S. Uma, P.K. Stoimenov, V. Zaikovski, C.M. Sorensen, K.J. Klabunde, *J. Phys. Chem. B* **2003,** *107,* 7441. (b) Ponce, A.A.; Klabunde, K.J. *J. Mol. Catal.*2005, 225, 1. (c) Smetana, A.B.; Klabunde, K.J.; Sorensen C.M. *J. Colloid Interface Sci.* **2005**, *284*, 521. (d) Klabunde, K. J.; Timms, P. S.; Skell, P. S.; Ittel, S. *Inorg. Synth.* **1979**, *19*, 59. (e) Davis, S. C.; Klabunde, K. J. *Chem. Rev.* **1982**, *82*, 153.

(f) Stoeva, S.; Klabunde, K.J.; Sorensen, C.M.; Dragieva, I. *J. Am. Chem. Soc.* **2002**, *124*, 2305.

21) (a) Armelao, L.; Bertoncello, R.; De Dominicis, M. *Advanced Materials* **1997**, *9*, 736. (b) Devarajan, S.; Bera, P.; Sampath, S. *J. Colloid Interface Sci.* **2005**, *290*, 117. (c) Shukla, S.; Seal, S. Nanostruct. Mater. 1999, 11, 1181.

22) (a) Gao, F.; Lu, Q.; Komarneni, S. *Chem. Mater.* **2005,** *17,* 856. (b) Rosemary, M.J.; Pradeep, T. *J. Colloid Interface Sci.* **2003**, *268*, 81.

23) (a) Bronstein, L.M.; Chernyshov, D.M.; Timofeeva, G.I.; Dubrovina, L.V.; Valetsky, P.M.; Obolonkova, E.S.; Khokhlov, A.R. *Langmuir* **2000**, *16*, 3626. (b) Bronstein, L.M.; Sidorov, S.N.; Valetsky, P.M.; Hartmann, J.; Cölfen, H.; Antonietti, M. *Langmuir* **1999**, *15*, 6256. (c) Lee, C.-L.; Wan, C.-C.; Wang, Y.-Y. *Adv. Funct. Mater.* **2001**, *11*, 344.

24) (a) Sun, Y.; Xia, Y. *J. Am. Chem. Soc.* **2004**, *126*, 3892 (b) Sun, Y.; Mayers, B. T.; Xia, Y. *Adv. Mater.* **2003**, *15*, 641 (c) Sun, Y.; Xia, Y. *Nano Lett.* **2003**, *3*, 1569 (d) Jin, Y.; Dong, S. *J. Phys. Chem. B* **2003,** *107,* 12902 (e) Sun, Y.; Mayers, B.T.; Xia, Y. *Nano Lett.* **2002**, *2*, 481 (f) Chen, J.; Saeki, F.; Wiley, B.J.; Cang, H.; Cobb, M.J.; Li, Z.Y.; Au, L.; Zhang, H.; Kimmey, M.B.; Li, X.D.; Xia, Y. *Nano Lett.* **2005**, *5*, 473. (g) Shukla, S.; Priscilla, A.; Banerjee, M.; Bhonde, R.R.; Ghatak, J.; Satyam, P.V.; Sastry, M. *Chem. Mater.* **2005**, *17*, 5000. (h) Liang, H.-P., Guo, Y.-G., Zhang, H.-M., Hu, J.-S., Wan, L.-J.,. Bai, C.-L *Chem. Commun.* **2004**, 1496.

25) (a) Cliffel, D. E.; Zamborini, F. P.; Gross, S. M.; Murray, R. W. *Langmuir* **2000**, *16*, 9699. (b) Yonezawa, T.; Onoue, S.; Kimizuka, N. *Langmuir* **2000**, *16*, 5218. (c) Thomas, K.G.; Zajicek, J.; Kamat, P.V. *Langmuir* **2002,** *18,* 3722.

26) (a) Henhar, R.S.; Norstern, T.B.; Rotello, V.M. *Adv. Mater.* **2005**, *17*, 657. (b) Cheng, J.; Teply, B.A.; Sherifi, I.; Sung, J.; Luther, G.; Gu, F.X.; Levy-Nissenbaum, E.; Radovic-Moreno, A.F.; Langer, R.; Farokhzad, O.C. *Biomaterials* **2007**, *28*, 869. (c) Hoppe, C.E.; Lazzari, M.; Pardiñas-Blanco, I.; López-Quintela, M.A. *Langmuir* **2006,** *22,* 7027. (d) Qian, X.F.; Yin, J.; Feng, S.; Liu, S.H.; Zhu, Z.K. *J. Mater.Chem.* **2001**, *11*, 2504. (e) Sidorov, S.N.; Bronstein, L.M.; Valetsky, P.M.; Hartmann, J.; Cölfen, H.; Schnablegger, H.; Antonietti, M. *J. Colloid Interface Sci.* **1999**, *212*, 197. (f) Xiong, Y.; Washio, I.; Chen, J.; Cai, H.; Li, Z.–Y.; Xia, Y. *Langmuir* **2006,** *22,* 8563. (g) Mu, X.; Evans, D.G.; Kou, Y. *Catal. Lett.* **2004**, *97*, 151.

27) (a) Selvakannan, PR.; Mandal, S.; Phadtare, S.; Pasricha, R.; Sastry, M. *Langmuir* **2003,** *19,* 3545. (b) Selvakannan, PR.; Mandal, S.; Phadtare, S.; Gole, A.; Pasricha, R.; Adyanthaya, S.D.; Sastry, M. *J. Colloid Interface Sci.* **2004**, *269*, 97. (c) Zhong, Z.; Patskovskyy, S.; Bouvrette, P.; Luong, J.H.T.; Gedanken, A. *J. Phys. Chem. B* **2004,** *108,* 4046. (d) Huang, Y.-F.; Lin, Y.-W.; Chang, H.-T. *Nanotechnology* **2006**, *17*, 4885. (e) Naka, K.; Itoh, H.; Tampo, Y.; Chujo, Y. *Langmuir* **2003,** *19,* 5546. (f) Fan, J.; Chen, S.; Gao, Y. *Colloids Surf. A* **2003**, *28*, 199. (g) Fujiki, Y.; Tokunaga, N.; Shinkai, S.; Sada, K. *Angew. Chem. Int. Ed.* **2006**, *45*, 4764. (h) Aubin-Tam, M.; Hamad-Schifferli, K *Langmuir* **2005,** *21,* 12080. (i) You, C.-C., De, M., Han, G., Rotello, V.M. *J. Am. Chem. Soc.* **2005**, *127*, 12873. (j) Bhargava, S.K.; Booth, J.M.; Agrawal, S.; Coloe, P.; Kar, G. *Langmuir* **2005,** *21,* 5949. (k) Sanyal, A.; Mandal, S.; Sastry, M. *Adv. Funct. Mater.* **2005**, *15*, 273. (l) Selvakannan, PR.; Swami, A.; Srisathiyanarayanan, D.; Shirude, P.S.; Pasricha, R.; Mandale, A.B.; Sastry, M. *Langmuir* **2004,** *20,* 7825. (m) Joshi, H.; Shirude, P.S.; Bansal, V.; Ganesh, K.N.; Sastry, M. *J. Phys. Chem. B* **2004,** *108,* 11535.

28) Brust, M.; Walker, M.; Bethell, D.; Schiffrin, D. J.; Whyman, R. *J. Chem. Soc., Chem. Commun*. **1994**, 801.

29) (a) Ye, H.; Scott, R. W. J.; Crooks, R. M. *Langmuir* **2004**, *20*, 2915. (b) Yee, C.; Scotti, M.; Ulman, A.; White, H.; Tafailovich, M.; Sokolov, J. *Langmuir* **1999**, *15*, 4314. (c) Hasan, M.; Bethell, D.; Brust, M. *J. Am. Chem. Soc.* **2002**, *124*, 1132. (d) Brust, M.; Stuhr-Hansen, N.; Norgaard, K.; Christensen, J. B.; Nielsen, L. K.; Bjornholm, T. *Nano Lett.* **2001**, *1*, 189. (e) Rautaray, D.; Kumar, P. S.; Wadgaonkar, P. P.; Sastry, M. *Chem. Mater.* **2004**, *16*, 988. (f) Kumar, A.; Mandal, S.; Selvakannan, P. R.; Pasricha, R.; Mandale, A. B.; Sastry, M. *Langmuir* **2003**, *19*, 6277. (g) Templeton, A. C.; Chen, S.; Gross, S. M.; Murray, R.W.*Langmuir* **1999**, *15*, 66. (h) Templeton, A. C.; Cliffel, D. E.; Murray, R. W. *J. Am. Chem. Soc.* **1999**, *121*, 7081. (i) Wuelfing, W. P.; Gross, S. M.; Miles, D. T.; Murray, R.W. *J. Am.Chem. Soc*. **1998**, *120*, 12696. (j) Schaff, T. G.; Knight, G.; Shaffigulin, M. N.; Borkman, R. F.; Whetten, R. L. *J. Phys. Chem. B* **1998**, *102*, 10643. (k) Brust, M.; Fink, J.; Bethell, D.; Schiffrin, D. J.; Kiely, C. J. *J. Chem. Soc., Chem. Commun*. **1995**, 1655. (l) Johnson, S. R.; Evans, S. D.; Brydson, R. *Langmuir* **1998**, *14*, 6639. (m) Chen, S.; Kimura, K. *Langmuir* **1999**, *15*, 1075. (n) Shon, Y. S.; Wuelfing, W. P.; Murray, R. W. *Langmuir* **2000**, *17*, 1255. (o) Huang, J.; He, C.;

Liu, X.; Xiao, Y.; Mya, K. Y.; Chai, J. *Langmuir* **2004**, *20*, 5145. (p) Huang, J.; Liu, Z.; Liu, X.; He, C.; Chow, S.Y.; Pan, J. *Langmuir* **2005,** *21,* 699. (q) Schmid, G.; Lehnert, A. *Angew. Chem. Int. Ed. Engl.* **1989**, *28*, 780. (r) Schmid, G. *Chem. Rev.* **1992**, *92*, 1709. (s) Naka, K.; Yaguchi, M.; Chujo, Y. *Chem. Mater.* **1999**, *11*, 849. (t) Leff, D.V.; Brandt, L.; Heath, J.R. *Langmuir* **1996**, *12*, 4723. (u) Brown, L.O.; Hutchison, J.E. *J. Phys. Chem. B.* **2001**, *105*, 8911. (v) Stevenson, K.A.; Muralidharan, G.; Maya, L.; Wells, J.C.; Barhen, J.; Thundat, T. *J. Nanosci. Nanotech.* **2002**, *2*, 397. (w) Murakoshi, K.; Nakato, Y. *Adv. Mater.* **2000**, *12*, 791.

30) (a) Brust, M.; Fink, J.; Bethell, D.; Schiffrin, D. J.; Kiely, C. J. *J. Chem. Soc., Chem. Commun*. **1995**, 1655. (b) Knecht, M.R.; Garcia-Martinez, J.C.; Crooks, R.M. *Langmuir* **2005,** *21,* 11981. (c) Cardenas-Trivino, G.; Klabunde, K. J.; Dale, E. B. *Langmuir* **1987**, *3*, 986. (d) Mandal, S.; Das, A.; Srivastava, R.; Sastry, M. *Langmuir* **2005,** *21,* 2408. (e) Schlotterbeck, U.; Aymonier, C.; Thomann, R.; Hofmeister, H.; Tromp, M.; Richtering, W.; Mecking, S. *Adv. Funct. Mater.* **2004**, *14*, 999. (f) Cozzoli, P.D.; Comparelli, R.; Fanizza, E.; Curri, M.L.; Agostiano, A.; le Laub, D. *J. Am. Chem. Soc.* **2004**, *126*, 3868.

31) (a) Kim, K.-S.; Demberelnyamba, D.; Lee, H. *Langmuir*, **2004**, *20*, 556. (b) Wang, Y.; Yang, H. *Chem. Commun.* **2006**, 2545. (c) Zhao, D.; Fei, Z.; Ang, W.H.; Dyson, P.J. *Small* **2006**, *2*, 879. (d) Scheeren, C.W.; Machado, G.; Teixeira, S.R.; Morais, J.; Domingos, J.B.; Dupont, J. *J. Phys. Chem. B* **2006,** *110,* 13011.

32) (a) Sun, Y.; Riggs, J.E.; Rollins, H.W.; Guduru, R. *J. Phys. Chem. B* **1999,** *103,* 77. (b) Cason, J.P.; Roberts, C.B. *J. Phys. Chem. B* **2000**, *104,* 1217. (c) Cason, J.P.; Khambaswadkar, K.; Roberts, C.B. *Ind. Eng. Chem. Res.* **2000,** *39,* 4749. (d) Ohde, H.; Hunt, F.; Wai, C.M. *Chem. Mater.* **2001,** *13,* 4130. (e) N.Z. Clarke, C. Waters, K.A. Johnson, J. Satherley, D.J. Schiffrin, *Langmuir* **2001,** *17,* 6048. (f) Morley, K.S.; Marr, P.C.; Webb, P.B.; Berry, A.R.; Allison, F.J.; Moldovan, G.; Brown, P.D.; Howdle, S.M. *J. Mater.Chem.***2002**, *12*, 1898. (g) X.-R. Ye, Y. Lin, C. Wang, M.H. Engelhard, Y. Wang, C.M. Wai, *J . Mater. Chem.***2004**, *14*, 908. (h) Morley, K.S.; Licence, P.; Marr, P.C.; Hyde, J.R.; Brown, P.D.; Mokaya, R.; Xia, Y.; Howdle, S.M. *J. Mater. Chem.* **2004**, *14*, 1212. (i) Esumi, K.; Sarashina, S.; Yoshimura, T. *Langmuir* **2004,** *20,* 5189. (j) Hou, Z.; Theyssen, N.; Brinkmann, A.; Leitner, W. *Angew. Chem. Int. Ed.* **2005**, *44*,

1346. (k) Sun, Z.; Fu, L.; Liu, Z.; Han, B.; Liu, Y.; Du, J. *J. Nanosci. Nanotechnol.* **2006**, *6*, 691.

33) (a) Bronstein, L.; Krämer, E.; Berton, B.; Burger, C.; Förster, S.; Antonietti, M. *Chem. Mater.* **1999,** *11,* 1402. (b) Jana, N.R. *Small* **2005**, *1*, 875. (c) Pileni, M.P. *Supramol. Sci.* **1998**, *5*, 321. (d) Pileni, M.P.; Ninham, B.W.; Gulik-Krzywicki, T.; Tanori, J.; Lisiecki, I.; Filankembo, A. *Adv. Mater.* **1999**, *11*, 1358. (e) Pileni, M.P.; Gulik-Krzywicki, T.; Tanori, J.; Filankembo, A.; Dedieu, J.C. *Langmuir* **1998,** *14,* 7359.

34) (a) Balogh, L.; Valluzzi, R.; Laverdure, K.S.; Gido, S.P.; Hagnauer, G.L.; Tomalia, D.A. *J. Nano. Res.* **1999**, *1*, 353. (b) Zhao, M.; Crooks, R.M. *Angew. Chem. Int. Ed.* **1999**, *38*, 364. (c) Chechik, V.; Zhao, M.; Crooks, R.M. *J. Am. Chem. Soc.* **1999,** *121,* 4910. (d) Zhao, M.; Sun, L.; Crooks, R.M. *J. Am. Chem. Soc.* **1998,** *120,* 4877. (e) Niu, Y.; Crooks, R.M. *Chem. Mater.* **2003,** *15,* 3463. (f) Scott, R.W.J.; Wilson, O.M.; Crooks, R.M. *J. Phys. Chem. B* **2005,** *109,* 692.

35) (a) Fukuoka, A.; Higuchi, T.; Ohtake, T.; Oshio, T.; Kimura, J.; Sakamoto, Y.; Shimomura, N.; Inagaki, S.; Ichikawa, M. *Chem. Mater.* **2006,** *18,* 337. (b) Fukuoka, A.; Araki, H.; Sakamoto, Y.; Sugimoto, N.; Tsukada, H.; Kumai, Y.; Akimoto, Y.; Ichikawa, M. *Nano Lett.* **2002**, *2*, 793. (c) Fukuoka, A.; Araki, H.; Kimura, J.; Sakamoto, Y.; Higuchi, T.; Sugimoto, N.; Inagaki, S.; Ichikawa, M. *J. Mater. Chem.* **2004**, *14*, 752. (d) Joo, S.H.; Choi, S.J.; Oh, I.; Kwak, J.; Liu, Z.; Terasaki, O.; Ryoo, R. *Nature* **2001**, *412*, 169.

36) (a) Chen, P.; Wu, X.; Lin, J.; Tan, K.L. *J. Phys. Chem. B.* **1999**, *103*, 4559. (b) Quinn, B.M.; Dekker, C.; Lemay, S.G. *J. Am. Chem. Soc.* **2005**, *127*, 6146. (c) Guo, D.J.; Li, H.L. *J. Colloid Interface Sci.* **2005**, *286*, 274. (d) Qu, J.; Shen, Y.; Qu, X.; Dong, S. *Chem. Commun.* **2004**, 34. (e) Day, T.M.; Unwin, P.R.; Wilson, N.R.; Macpherson, J.V. *J. Am. Chem. Soc.* **2005**, 127, 10639. (f) Govindaraj, A.; Satishkumar, B.C.; Nath, M.; Rao, C.N.R. *Chem. Mater.* **2000,** *12,* 202. (g) Kyotani, T.; Tsai, L.; Tomita, A. *Chem. Commun*. **1997**, 701. (h) Pradhan, B.K.; Kyotani, T.; Tomita, A. Chem. Commun. *1999*, 1317. (i) Sloan, J.; Wright, D.M.; Woo, H.-G.; Bailey, S.; Brown, G.; York, A.P.E.; Coleman, K.S.; Hutchison, J.L.; Green, M.L.H. *Chem. Commun.* **1999**, 699.

37) (a) Wong, K.K.W.; Douglas, T.; Gider, S.; Awschalom, D.D.; Mann, S. *Chem. Mater.* **1998**, *10*, 279. (b) He, J.; Kunitake, T. *Chem. Mater.* **2004,** *16,* 2656. (c) Mark, S.S.;

Bergkvist, M.; Yang, X.; Angert, E.R.; Batt, C.A. Biomacromolecules **2006,** *7*, 1884. (d) Willner, I., Baron, R., Willner, B. *Adv. Mater.* **2006**, *18*, 1109. (e) Zhu, H.; John, G.; Wei, B. *Chem. Phys. Lett.* **2005**, *405*, 49. (f) Klem, M.T.; Willits, D.; Solis, D.J.; Belcher, A.M.; Young, M.; Douglas, T. *Adv. Funct. Mater.* **2005**, *15*, 1489.

38) (a) Pollmann, K.; Merroun, M.; Raff, J.; Hennig, C.; Selenska-Pobell, S. *Lett. Appl. Microbiol.* **2006**, *43*, 39. (b) Douglas, T.; Young, M. *Nature* **1998**, *393*, 152. (c) Konishi, Y.; Tsukiyama, T.; Ohno, K.; Saitoh, N.; Nomura, T.; Nagamine, S. *Hydrometallurgy* **2006**, *81*, 24. (d) Nam, K.T.; Kim, D.-W.; Yoo, P.J.; Chiang, C.-Y.; Meethong, N.; Hammond, P.T.; Chiang, Y.-M.; Belcher, A.M. *Science* **2006**, *312*, 885. (e) Lee, S.-K.; Yun, D.S.; Belcher, A.M. *Biomacromolecules* **2006,** *7*, 14. (f) Peelle, B.R.; Krauland, E.M.; Wittrup, K.D.; Belcher, A.M. *Langmuir* **2005,** *21,* 6929. (g) Reiss, B.D.; Mao, C.; Solis, D.J.; Ryan, K.S.; Thomson, T.; Belcher, A.M. *Nano. Lett.* **2004**, *4*, 1127.

39) (a) Mann, S. *Nature*, **1993**, *365*, 499. (b) Oliver, S.; Kupermann, A.; Coombs, N., Lough, A.; Ozin, G.A. *Nature*, **1995**, *378*, 47. (c) Kröger, N.; Deutzmann, R.; Sumper, M., *Science*, **1999**, *286*, 1129.

40) Young, J.R.; Davis, S.A.; Bown, P.R.; Mann, S. *J. Struct. Biol.* **1999**, *126***,** 195.

41) Balkwill, D.; Marata, D.; Blakemore, R.P. *J. Bacteriol.* **1980**, *141*, 1399.

42) (a)Lovley, D.R.; Stolz, J.F.; Nord, G.L.; Phillips, E.J.P. *Nature*, **1987**, *330*, 252. (b) Spring, H.; Schleifer, K.H. *Sys. Appl. Microbiol*. **1995**, *18*, 147. (c) Dickson, D.P.E. *J. Magn. Magn. Mater.* **1999**, *203*, 46.

43) (a) Mann, S. *Angew. Chem. Int. Ed.* **2000**, *39*, 3392. (b) Hecky, R.E.; Mopper, K.; Kilham, P.; Degans, E.T. *Mar. Biol.* **1973**, *19*, 323. (c) Nakajima, T.; Volcani, B.E. *Science* **1969**, *164*, 1400. (d) Swift, D.; Wheeler, A. *J. Phycol.* **1992**, *28*, 202.

44) (a) Kröger, N.; Deuzmann, R.; Sumper, M. *Science* **1999**, *286*, 1129. (b) Kröger, N.; Deuzmann, R.; Sumper, M. *J. Biol. Chem.* **2001**, *276*, 26066. (c) Kröger, N.; Deuzmann, R.; Bergsdorf, C.; Sumper, M. *Proc. Natl. Acad. Sci. USA* **2000**, *97*, 14133.

45) (a) Shimizu, K.; Cha, J.; Stucky, G.D.; Morse, D.E. *Proc. Natl. Acad. Sci. USA* **1998**, *95*, 6234. (b) Cha, J.; Shimizu, K.; Zhou, Y.; Christiansen, S. C.; Chmelka, B. F.; Stucky, G. D.; Morse, D. E. *Proc. Natl. Acad. Sci. USA* **1999**, *96*, 361.

46) Kroger, N.; Bergsdorf, C.; Sumper, M. *Eur. J. Biochem.* **1996**, *239*, 259.

47) (a) Kroger, N.; Wetherbee, R. *Protist* **2000**, *151*, 263. (b) Kroger, N.; Lehmann, G.; Rachel, R.; Sumper, M. *Eur. J. Biochem.* **1997**, *250*, 99.

48) Torres de Araujo, F.F.; Pires, M.A.; Frankel, R.B.; Bicudo, C.E. M. *Biophys. J.* **1986**, *50*, 375.

49) Bazylinski, D.A.; Frankel, R.B. *Biomineralization* (Ed.: E. Baeuerlein), Wiley-VCH, Weinheim 2000, p. 41-43.

50) Mann, S.; Sparks, N. H.; Walker, M. M.; Kirschvink, J. L. *J. Exp. Biol.* **1988**,*140*, 35.

51) (a) Walker, M.M.; Diebel, C.E.; Haugh, C.V.; Pankhurst, P.M.; Montgomery, J.C.; Green, C.R. *Nature* **1997**, *390*, 371. (b) Diebel, C.E.; Proksch, R.; Green, C.R.; Neilson, P.; Walker, M.M. *Nature* **2000**, *406*, 299.

52) Hanzlik, M.; Heunemann, C.; Holtkamp-Rötzler, E.; Winklhofer, M.; Petersen, N.; Fleissner, G. *Biometal*, **2000**, *13*, 325.

53) Acosta-Avalos, D.; Wajnberg, E.; Oliveira, P. S.; Leal, I.; Farina, M.; Esquivel, D. M. *J. Exp. Biol.* **1999**, *202*, 2687.

54) (a) Kirschvink, J.L.; Kobayashi-Kirschvink, A.; Woodford, B.J. *Proc. Natl. Acad. Sci USA* **1992**, *89*, 7683; b) Dobson, J.; Grassi, P.P. *Brain Res. Bull.* **1996**, *39*, 255. c) Schultheiss-Grassi, P.P.; Wessiken, R.; Dobson, J. *Biochem. Biophys. Acta* **1999**, *1426*, 212. d) Schultheiss-Grassi, P.P.; Dobson, J. *BioMetals* **1999**, *12*, 67.

55) Klaus, T.; Joerger, R.; Olsson, E.; Granqvist, C.G. *Proc. Natl. Acad. Sci. USA* **1999**, *96*, 13611.

56) (a) Ahmad, A.; Senapati, S.; Khan, M.I.; Kumar, R.; Sastry, M. *Langmuir* **2003**, *19*, 3550. (b) Ahmad, A.; Senapati, S.; Khan, M.I.; Ramani, R.; Srinivas, V.; Sastry, M. *Nanotechnology* **2003**, *14*, 824. (c) Beveridge, T.J.; Murray, R.G.E. *J. Bacteriol* **1980**, *141*, 876. (d) Beveridge, T.J.; Hughes, M.N.; Lee, H.; Leung, K.T.; Poole, R.K.; Savvaidis, I.; Silver, S.; Trevors, J.T. *Adv. Microb. Physiol.* **1997**, *38*, 178. (e) Joerger, R.; Klaus, T.; Granqvist C.-G. Adv. Mater. **2000**, *12*, 407. (f) Klaus-Joerger, T.; Joerger, R.; Olsson, E.; Granqvist, C.-G. *Trends Biotechnol.* **2001**, *19*, 15. (g) Konishi, Y.; Nomura, T.; Tsukiyama, T.; Saitoh, N. *Trans. Mater. Res. Soc. Jpn.* **2004**, *29*, 2341.

57) (a) Pum, D.; Sleytr, U.B. *Trends Biotechnol.* **1999**, *17*, 8. (b) Sleytr, U.B.; Messner, P.; Pum, D.; Sara, M. *Angew. Chem. In.t Ed.* **1999**, *38*, 1035.

58) (a) Mukherjee, P.; Ahmad, A.; Mandal, D.; Senapati, S.; Sainkar, S.R.; Khan, M.I.; Ramani, R.; Parischa, R.; Ajayakumar, P.V.; Alam, M.; Sastry, M.; Kumar, R. *Angew. Chem. Int. Ed.* **2001**, *40*, 3585. (b) Mukherjee, P.; Senapati, S.; Mandal, D.; Ahmad, A.; Khan, M.I.; Kumar, R.; Sastry, M. *Chembiochem* **2002**, *3*, 461. (c) Kowshik, M.; Ashtaputre, S.; Kharrazi, S.; Vogel, W.; Urban, J.; Kulkarni, S.K.; Paknikar, K.M. *Nanotechnology* **2003**, *14*, 95. (d) Mukherjee, P.; Ahmad, A.; Mandal, D.; Senapati, S.; Sainkar, S.R.; Khan, M.I.; Ramani, R.; Parischa, R.; Ajayakumar, P.V.; Alam, M.; Sastry, M.; Kumar, R. *Angew. Chem. Int. Ed.* **2001**, *40*, 3585. (e) Mukherjee, P.; Ahmad, A.; Mandal, D.; Senapati, S.; Sainkar, S.R.; Khan, M.I.; Parischa, R.; Ajayakumar, P.V.; Alam, M.; Kumar, R.; Sastry, M. *Nano. Lett.* 2001, 1, 515. (f) Senapati, S.; Ahmad, A.; Khan, M.I.; Sastry, M.; Kumar, R. *Small* **2005**, *1*, 517.

59) Hosea, M.; Greene, B.; Mcpherson, R.; Henzl, M.; Alexander, M.D.; Darnall, D.W. *Inorg. Chim. Acta.* **1986**, *123*, 161.

60) (a) Gardea-Torresdey, J.L.; Parsons, J.G.; Gomez, E.; Peralta-Videa, J.; Troiani, H.E.; Santiago, P.; Yacaman, M.J. *Nano Lett.* **2002**, *2*, 397. (b) Gardea-Torresdey, J.L.; Gomez, E.; Peralta-Videa, J.R.; Parsons, J.G.; Troiani, H.; Yacaman, M.J. *Langmuir* **2003,** *19,* 1357. (c) Shankar, S.S.; Rai, A.; Ahmad, A.; Sastry, M. *J. Colloid Interface Sci.* **2004**, *275*, 496. (d) Shankar, S.S.; Ahmad, A.; Sastry, M. *Biotechnol. Prog.* **2003,** *19,* 1627. (e) Armendariz, V.; Herrera, I.; Peralta-Videa, J.R.; Jose-Yacaman, M.; Troiani, H.; Santiago, P.; Gardea-Torresdey, J.L. *J. Nano. Res.* **2004**, *6*, 377. (f) Ankamwar, B.; Damle, C.; Ahmad, A.; Sastry, M. *J. Nanosci. Nanotech.* **2005**, *5*, 1665. (g) Shankar, S.S.; Rai, A.; Ankamwar, B.; Singh, A.; Ahmad, A.; Sastry, M. *Nat. Mater.* **2004**, *3*, 482.

61) (a) Berry, C.R. *Phys. Rev.* **1952**, *88*, 596. (b) Wasserman, H.J.; Vermaak, J.S. *Surf. Sci.* **1970**, *22*, 164. (c) Wasserman, H.J.; Vermaak, J.S. *Surf. Sci.* **1972**, *32*, 168. (d) Apai, G.; Hamilton, J.F. *Phys. Rev. Lett.* **1979**, *43*, 165. (e) Montano, P.A.; Schulze, W.; Tesche, B.; Shenoy, G.K.; Morrison, T.I. *Phys. Rev. B* **1984**, *30*, 672. (f) Solliard, C.; Flueli, M. *Surf. Sci.***1985**, *156*, 487. (g) Montano, P.A.; Zhao, J.; Ramanathan, M.; Shenoy, G.K.; Schulze, W.; Urban, J. *Chem. Phys. Lett.* **1989**, *164*, 126. (h) Montano, P.A.; Shenoy, G.K.; Alp, E.E.; Schulze, W.; Urban, J. *Phys. Rev. Lett.* **1986**, *56*, 2076.

62) (a) Mays C.W.; Vermaak, J.S.; Kuhlmann-Wilsdorf, D. *Surf. Sci.* **1968**, *12*, 128. (b) Vermaak, J.S.; Mays C.W.; Kuhlmann-Wilsdorf, D. *Surf. Sci.* **1968**, *12*, 134.

63) Qi, W.H.; Wang, M.P. *J. Nano. Res.* **2005**, *7*, 51.

64) Qi, W.H.; Wang, M.P.; Su, Y.C. J. Mater. Sci. Lett. **2002**, *21*, 877.

65) (a) Buffat, P.; Borel, J.-P. *Phys. Rev. A* **1976**, *13*, 2287. (b) Castro, T.; Reifenberger, R.; Choi, E.; Andres, R.P. *Phys. Rev. B* **1990**, *42*, 8548. (c) Beck, R.D.; St. John, P.; Homer, M.L.; Whetten, R.L. *Science* **1991**, *253*, 879. (d) Martin, T.P.; Naher, U.; Schaber, H.; Zimmermann, U. *J. Chem. Phys.* **1994**, *100*, 2322.

66) (a) Couchman, P.R.; Jesser, W.A. *Nature* **1977**, *269*, 481. (b) Ercolessi, F.; Andreoni, W.; Tosatti, E. *Phys. Rev. Lett.* **1991**, *66*, 911.

67) Alivisatos, A. P. *J. Phys. Chem.* **1996**, *100*, 13226.

68) (a) Lewis. L.N. *Chem. Rev.***1993**, *93*, 2693. (b) Astruc, D.; Lu, F.; Aranzaes, J.R. *Angew. Chem. Int. Ed.* **2005**, *44*, 7852.

69) (a) Haruta, M.; Daté M. *Appl. Catal. A* **2001**, *222*, 427. (b) Zhong, C.J., Maye, M.M. *Adv. Mater*. **2001**, *13*, 1507.

70) (a) Wang, Z.L.; Ahmad, T.S.; El-Sayed, M.A. *Surf. Sci.,* **1997**, *380*, 302. (b) Narayanan, R.; El-Sayed, M.A. *Nano Lett.* **2004**, *4*, 1343. (c) Narayanan, R.; El-Sayed, M.A. *J. Phys. Chem. B* **2004**, *108*, 5726.

71) (a) Heemeier, M.; Carlsson, A.F.; Naschitzki, M.; Schmal, M.; Bäumer, M.; Freund, H.-J. *Angew. Chem. Int. Ed.* **2002**, *41*, 4073. (b) He, J.; Ichinose, I.; Kunitake, T.; Nakao, A.; Shiraishi, Y.; Toshima, N. *J. Am. Chem. Soc.* **2003**, *125*, 11034.

72) a) Mie, G. *Ann. Phys*. **1908**, *25*, 377. b) Greighton, J.A.; Eadon, D.G. *J. Chem. Soc. Faraday Trans.* **1991**, *87*, 3881. c) Mulvaney, P. *Langmuir* **1996**, *12*, 788.

73) Johnson, P.B.; Christy, R.W. *Phys. Rev. B* **1972**, *6*, 4370.

74) Link, S; El-Sayed, M.A. *Annu. Rev. Phys. Chem.***2003**, *54*, 331.

75) Burda, C.; Chen, X.; Narayanan, R.; El-Sayed, M.A. *Chem. Rev.* **2005**, *105*, 1025.

76) Gans, R. *Ann. Phys.* **1915**, *47*, 270.

77) (a) van der Zande, B.M.I.; Bohmer, M.R.; Fokkink, L.G.J.; Schonenberger, C. *J. Phys. Chem. B* **1997**, *101*, 852. (b) Yu, Y.Y.; Chang, S.S.; Lee, C.L.; Wang, C.R.C. *J. Phys. Chem. B* **1997**, *101*, 6661.

78) Millstone, J.E.; Park, S.; Shuford, K.L.; Qin, L.; Schatz, G.C.; Mirkin, C.A. *J. Am. Chem. Soc.* **2005**, *127*, 5312.

79) (a) Busbee, B D.; Obare, S.O.; Murphy; C.J *Adv. Mater.* **2003**, *15*, 414. (b) Chang, S.-S.; Shih, C.-W.; Chen, C.-D.; Lai, W.-C.; Wang, C.R.C. *Langmuir* **1999**, *15*, 701. (c) Chemseddine, A.; Moritz, T. *Eur. Inorg. Chem.* **1999**, 235. (d) Jana, N.R.; Gearheart, L.; Murphy, C.J. *Chem. Commun.* **2001**, 617. (e) Kim, F.; Song, J.H.; Yang, P. *J. Am. Chem. Soc.* **2002**, *124*, 14316. (f) Tang, Z.; Kotov, N.A.; Giersig, M. *Science* **2002**, *297*, 237. (g) Xia, Y.N.; Yang, P.D.; Sun, Y.G.; Wu, Y.Y.; Mayers, B.; Gates, B.; Yin, Y.D.; Kim, F.; Yan, Y.Q.; *Adv. Mater.* **2003**, *15*, 353.

80) (a) Chen, S.; Fan, Z.; Carroll, D.L. *J. Phys. Chem. B* **2002**, *106*, 10777. (b) Hao, E.; Kelly, K.L.; Hupp, J.T.; Schatz, G.C. *J. Am.Chem. Soc.* **2002**, *124*, 15182. (c) Maillard, M.; Giorgio, S.; Pileni, M.-P. *Adv. Mater.* **2002**, *14*,1084. (d) Puntes, V.F.; Zanchet, D.; Erdonmez, C.K.; Alivisatos, A.P. *J. Am. Chem. Soc.* **2002**, *124*, 12874. (e) Maillard, M.; Huang, P.; Brus, L. *Nano Lett.* **2003**, *3*, 1611.

81) (a) Jin, R.; Cao, Y.; Mirkin, C.A.; Kelly, K.L.; Schatz, G.C.; Zheng, J.G. *Science* **2001**, *294*, 1901. (b) Chen, S.; Carroll, D.L. *Nano Lett.* **2002**, *2*, 1003. (b) I. Pastoriza-Santos, L.M. Liz-Marźan, *Nano Lett.* **2002**, *2*, 903. (c) Y. Sun, B. Mayers, Y. Xia, *Nano Lett.* **2003**, *3*, 675. (d) Yang, J.; Fendler, J.H. *J. Phys. Chem* **1995**, *99*, 5505. (e) Jin, R.; Cao, Y.; Hao, E.; Metraux, G.; Schatz, G.C.; Mirkin, C.A. *Nature* **2003**, *425*, 487.

82) (a) Lee, S.-M.; Jun, Y.-W.; Cho, S.N.; Cheon, J. *J. Am. Chem.Soc.* **2002**, *124*, 11244. (b) Chen, S.; Wang, Z.L.; Ballato, J.; Foulger, S.H.; Carroll, D.L. *J. Am. Chem. Soc.* **2003**, *125*, 16186. (c) Manna, L.; Milliron, D.J.; Meisel, A.; Scher, E.C.; Alivisatos, A.P. *Nature Mater.* **2003**, *2*, 382. (d) Manna, L.; Scher, E.C.; Alivisatos, A.P. *J. Am. Chem.Soc.* **2000**, *122*, 12700. (e) Hao, E.; Bailey, R.C.; Schatz, G.C.; Hupp, J.T.; Li, S. *Nano Lett.* **2004**, *4*, 327.

83) (a) Sun, Y.; Xia, Y. *Science* **2002**, *298*, 2139. (b) Ahmadi, T.S.; Wang, Z.L.; Green, T.C.; Henglein, A.; El-Sayed, M.A. *Science* **1996**, *272*, 1924.

84) (a) Oldenburg, S.J.; Jackson, J.B.; Westcott, S.L;. Halas, N.J. *Appl. Phys. Lett.* **1999**, *75*, 897. (b) Jackson, J.B.; Halas, N.J. *J. Phys. Chem. B* **2001**, *105*, 2743. (c) Graf, C.; Blaaderen, A.v. *Langmuir* **2002**, *18*, 524. (d) Pordan, E.; Nordlander, P. *Nano Lett.* **2003**,

3, 543. (e) Oldenburg, S.J.; Averitt, R.D.; Westcott, S.L.; Halas, N.J. *Chem. Phys. Lett.* 1998, *288*, 243. (f) Jin, Y.; Dong, S. *J. Phys. Chem. B* **2003**, *107*, 12902.

85) Schmid, G. *Metals: In Nanoscale Materials in Chemistry*; (Ed. Klabunde, K.J.), Wiley-Interscience: New York, **2001**, *Chapter 2*, 15.

86) (a) Andres, R.P.; Bein, T.; Dorogi, M.; Feng, S.; Jenderson, J.I.; Kubiak, C.P.; Mahoney, W.; Osifchin, R.G.; Reifenverger, R. *Science* **1996**, *272*, 1323. (b) Chen, S.; Ingram, R.S.; Hostetler, M.J.; Pietron, J.J.; Murray, R.W.; Schaaff, T.G.; Khoury, J.T.; Alvarez, M.M.; Whetten, R.L. *Science*, **1998**, *280*, 2098.

87) (a) Klein, D.L.; McEuen, P.L.; Katari, J.E.B.; Roth, R.; Alivisatos, A.P. *Appl. Phys. Lett.* **1996**, *68*, 2574. (b) Black, C.T.; Ralph, D.C.; Tinkham, M. *Phys. Rev. Lett.* **1996**, *76*, 688.

88) Ingram, R.S.; Hostetler, M.J.; Murray, R.W.; Schaaff, T.G.; Khoury, J.T.; Whetten, R.L.; Bigioni, T.P.; Guthrie, D.K.; First, P.N. *J. Am. Chem. Soc.* **1997**, *119*, 9279.

89) (a) Schön, G.; Simon, U. *Colloid Polym. Sci.* **1995**, *273*, 101. (b) Schön, G.; Simon, U. *Colloid Polym. Sci.* **1995**, *273*, 202.

90) Simon, U.; G. Schön, *Handbook of Nanostructured Materials and Nanotechnology* (Ed.: H. S. Nalwa), Academic Press **2000**, *Vol. 3*, 131.

91) Torma, V.; Vidoni, O.; Simon, U.; Schmid, G. *Eur. J. Inorg. Chem.* **2003**, 1121.

92) Mott, N.F. *Philos. Mag.* **1969**, *19*, 835.

93) Schmid, G.; Simon, U. *Chem. Commun.* **2005**, 697.

94) (a) Dyre, J.C.; *Phys. Rev. B* **1993**, *47*, 9128. (b) Dyre, J.C. *Phys. Rev. B* **1994**, *49*, 11709.

95) (a) Wuelfing, W.P.; Green, S.J.; Pietron, J.J.; Cliffel, D.E.; Murray, R.W. *J. Am. Chem. Soc.* **2000**, *122*, 11465. (b) Wuelfing, W.P.; Murray, R.W. *J. Phys. Chem. B* **2002**, *106*, 3139.

96) Wessels, J.M.; Nothofer, H.-G.; Ford, W.E.; von Wrochem, F.; Scholz, F.; Vossmeyer, T.; Schroedter, A.; Weller, H.; Yasuda, A. *J. Am. Chem. Soc.* **2004**, *126*, 3349.

97) (a) Glomm, W.R. *J. Dispersion Sci. Technol.* **2005**, *26*, 389. (b) Salata, O.V. *J. Nanobiotechnology* **2004**, *2*, 3. (c) West, J.L.; Halas, N.J. *Curr. Opin. Biotechnol.* **2000**, *11*, 215. (d) Katz, E.; Willner, I. *Angew. Chem. Int. Ed.* **2004**, *43*, 6042.

98) Rosi, N.L.; Mirkin, C.A. *Chem. Rev.* **2005,** *105*, 1547.

99) (a) Shaw III, C.F. *Chem. Rev.* **1999,** *99,* 2589. (b) Pissuwan, D.; Valenzuela, S.M.; Cortie, M.B. *Trends Biotechnol.* **2006**, *24*, 62.

100) (a) Emerich, D.F.; Thanos, C.G. *Biomol. Eng.* **2006**, *23*, 171. (b) Niemeyer C.M. *Angew. Chem. Int. Ed.* **2001**, *40*, 4128. (c) Sanford, J.C.; Smith, F.D.; Russell, J.A. *Methods Enzymol.* **1993**, *217*, 483.

101) (a) Sharma, P.; Brown, S.; Walter, G.; Santra, S.; Moudgil, B. *Adv. Colloid Interface Sci.* **2006**, *123-126*, 471. (b) Bielinska, A.; Eichman, J.D.; Lee, I.; Baker, J.R., Jr.; Balogh, L. *J. Nanopart. Res.* **2002**, *4*, 395.

102) Roth, J. *Histochem. Cell Biol.* **1996**, *106*, 1.

103) Olofsson, L.; Rindzevicius, T.; Pfeiffer, I.; Kall, M.; Hook, F. *Langmuir* **2003**, *19*, 10414.

104) (a) Warheit, D.B.; Laurence, B.R.; Reed, K.L.; Roach, D.H.; Reynolds, G.A.; Webb, T.R. *Toxicol. Sci.* **2004**, *77*, 117. (b) Lam, C.W.; James, J.T.; McCluskey, R.; Hunter, R.L. *Toxicol. Sci.* **2004**, *77*, 126. (c) Kam, N.W.S.; Jessop, T.C.; Wender, P.A.; Dai, H. *J. Am. Chem. Soc.* **2004**, *126*, 6850.

105) (a) Ballou, B.; Lagerholm, B.C.; Ernst, L.A.; Bruchez, M.P.; Waggoner, A.S.; Larson, D.R.; Zipfel, W.R.; Williams, R.M.; Clark, S.W.; Wise, F.W.; Webb, W.W.; Wu, X.; Liu, H.; Liu, J.; Haley, K.N.; Treadway, J.A.; Larson, J.P.; Ge, N.; Peale, F. *Bioconjugate Chem.* **2004**, *15*, 79. (b) Derfus, A.M.; Chan, W.C.; Bhatia, S.N. *Nano Lett.* **2004**, *4*, 11. (c) Larson, D.R.; Zipfel, W.R.; Williams, R.M.; Clark, S.W.; Bruchez, M.P.; Wise, F.W.; Webb, W.W.; Wu, X.; Liu, H.; Liu, J.; Haley, K.N.; Treadway, J.A.; Larson, J.P.; Ge, N.; Peale, F. *Science* **2003**, *300*, 1434. (d) Wu, X.; Liu, H.; Liu, J.; Haley, K.N.; Treadway, J.A.; Larson, J.P.; Ge, N.; Peale, F.; Bruchez, M.P. *Nat. Biotechnol.* **2003**, *21*, 41.

106) (a) Thomas, M.; Klibanov, A.M. *Proc. Natl. Acad. Sci. USA* **2003**, *100*, 9138. (b) Tkachenko, A.G.; Xie, H.; Coleman, D.; Glomm, W.; Ryan, J.; Anderson, M.F.; Franzen, S.; Feldheim, D.L. *J. Am. Chem. Soc.* **2003**, *125*, 4700. (c) Tkachenko, A.G.; Xie, H.; Liu, Y.; Coleman, D.; Ryan, J.; Glomm, W.; Shipton, M.K.; Franzen, S.; Feldheim, D.L. *Bioconjugate Chem.* **2003**, *14*, 482. (d) Hillyer, J.F.; Albrecht, R.M. *J. Pharm. Sci.* **2001**, *90*, 1927. (e) Tsoli, M.; Kuhn, H.; Brandau, W.; Esche, H.; Schmid, G. *Small* **2005**, *1*, 841. (f) Connor, E.E.; Mwamuka, J.; Gole, A.; Murphy, C.J.; Wyatt, M.D. *Small* **2005**, *1*, 325. (g) Shukla, R.; Bansal, V.; Chaudhary, M.; Basu, A.; Bhonde, R.R.; Sastry, M. *Langmuir* **2005,** *21,* 10644.

107) (a) Musick, M.D.; Keating, C.D.; Keefe, M.H. and Natan, M.J. *Chem. Mater.* **1997**, *9*, 1499. (b) Brown, K.R.L.; Lyon, A.; Fox, A.P.; Reiss, B.D. and Natan, M.J. *Chem. Mater.* **2000**, *12*, 314.

108) Doron, A.; Katz, E. and Willner, I. *Langmuir* **1995**, *11*, 1313.

109) (a) Dressick, W.J.; Dulcey, C.S.; Georger Jr, J.H. and Calvert, J.M. *Chem. Mater*. **1993**, *5*, 148. (b) Vargo, T.G.; Gardella Jr, J.A.; Calvert, J.M. and Chen, M.S. *Science* **1993**, *262*, 1711.

110) Blaaderen, A.V.; Ruel, R. and Wiltzius, P. *Nature* **1997**, *385*, 321.

111) (a) Decher, G *Science* **1997**, *277*, 1232 (b) Zheng, H.; Lee, I.; Rubner, M.F. and Hammond, P.T. *Adv. Mater.* **2002**, *14*, 569 (c) Hua, F.; Shi, J.; Lvov, Y. and Cui, T. *Nano Lett.* **2002**, *2*, 1219.

112) (a) Ye, Y.H.; LeBlanc, F.; Hache, A. and Truong, V. *Appl. Phys. Lett*. **2001**,*78*, 52 (b) Zhang, J.; Alsayed, A.; Lin, K.H..; Sanyal, S.; Zhang, F.; Pao, W.J.; Balagurusamy, V.S.; Heiney, P.A. and Yoah, A.G. *Appl. Phys. Lett.* **2002,** *81*, 3176 (c) Prevo, B.G.; Fuller III, J.C. and Velev, O.D. *Chem. Mater.* **2005**, *17*, 28.

113) (a) Yin, Y.; Lu, Y.; Gates, B. and Xia, Y. *J. Am. Chem. Soc.* **2001**, *123*, 8718 (b) Yang, S.M. and Ozin, G.A. *Chem. Commun.***2000**, 2507.

114) (a) Jeon, N.L.; Uzzo, R.G.; Xia, Y.; Mrksich, M. and Whitesides, G.M. *Langmuir* **1995**, *11*, 3024 (b) Potochnik, S.J.; Pehrsson, P.E.; Hsu, D.S.Y. and Calvert, J.M. *Langmuir* **1995**, *11*, 1841.

115) (a) Hermanson, K.D.; Lumsdon, S.O.; Williams, J.P.; Kaler, E.W.; Velev, O.D. *Science* **2001**, *294*, 1082. (b) Bhatt, K.H.; Velev, O.D. Chem. Mater. *Langmuir* **2004,** *20,* 467. (c) Velev, K.H.; Bhatt, K.H. *Soft Matter* **2006**, *2*, 738.

116) (a) Sastry, M.; Gole, A.; Patil, V. *Thin Solid Films* **2001**, *384*, 125. (b) Sastry, M.; Mayya, K.S. *J. Nano. Res.* **2000**, *2*, 183. (c) Swami, A.; Kumar, A.; Selvakannan, PR; Mandal, S.; Sastry, M. *J. Colloid Interface Sci.* **2003**, *260*, 367. (d) Sastry, M.; Rao, M.; Ganesh, K.N. *Acc. Chem. Res.* **2002,** *35*, 847.

117) Xu, J.; Li, H.-L. *J. Colloid Interface Sci.* **1995**, *176*, 138.

118) Sarathy, K.V.; Thomas, P.J.; Kulkarni, G.U.; Rao, C.N.R. *J. Phys. Chem. B* **1999**, *103*, 399.

119) Zhu, T.; Zhang, X.; Wang, J.; Fu, X.; Liu, Z. *Thin Solid Films* **1998**, *327-329*, 595.

120) Rizza, R.; Fitzmaurice, D.; Hearne, S.; Hughes, G.; Spoto, G.; Ciliberto, E.; Kerp, H.; Schropp, R. *Chem. Mater.* **1997**, *9*, 2969.

121) Bandyopadhyay, K.; Patil, V.; Vijayamohanan, K.; Sastry, M. *Langmuir* **1997**, *13*, 5244.

122) (a) Teranishi, T.; Hosoe, M.; Tanaka, T.; Miyake, M. *J. Phys. Chem. B.* **1999**, *103*, 3818. (b) Teranishi, T.; Miyake, M.; Hosoe, M. *Adv. Mater.* **1997**, *9*, 65. (c) Giersig, M.; Mulvaney, P. *Langmuir* **1993**, *9*, 3408. (d) Giersig, M.; Mulvaney, P. *J. Phys. Chem.* **1993**, *97*, 6334.

123) (a) Milchev, A.; Vassileva, E.; Kertov, V. *J. Electroanal. Chem.* **1980**, *107*, 323. (b) Milchev, A.; Vassileva, E *J. Electroanal. Chem.* **1980**, *107*, 337. (c) Gunawardena, G.; Hills, G.; Montenegro, I.; Scharifker, B.; *J. Electroanal. Chem.* **1982**, *138*, 225. (d) Gunawardena, G.; Hills, G.; Montenegro, I. *J. Electroanal. Chem.* **1982**, *138*, 241. (e) Gunawardena, G.; Hills, G.; Montenegro, I.; Scharifker, B.; *J. Electroanal. Chem.* **1982**, *138*, 255. (f) Quinn, B.M., Dekker, C., Lemay, S.G. *J. Am. Chem. Soc.* **2005**, *127*, 6146.

124) Finot, M.O.; Braybrook, G.D.; McDermott, M.T. *J. Electroanal. Chem.* **1999**, *466*, 234.

125) (a) Correa-Duarte, M.A., Liz-Marzán L.M. *J. Mater. Chem.* **2006**, *16*, 22. (b) Correa-Duarte, M.A.; Pérez-Juste, J.; Sánchez-Iglesias, A.; Giersig, M.; Liz-Marzán, L.M. *Angew. Chem. Int. Ed.* **2005**, *44*, 4375.

126) Wildgoose, G.G.; Banks, C.E.; Compton, R.G. *Small* **2006**, *2*, 182.

127) Cassagneau, T.; Fendler, J.H. J. Phys. Chem. B **1999,** *103,* 1789.

128) Feldheim, D.L.; Grabar, K.C.; Natan, M.J.; Mallouk, T.E. *J. Am. Chem. Soc.* **1996,** *118,* 7640.

129) Kovtyukhova, N.I.; Ollivier, P.J.; Martin, B.R.; Mallouk, T.E.; Chizhik, S.A.; Buzaneva, E.V.; Gorchinskiy, A.D. *Chem. Mater.* **1999,** *11,* 771.

130) Shifrina, Z.B.; Rajadurai, M.S.; Firsova, N.V.; Bronstein, L.M.; Huang, X.; Rusanov, A.L.; Muellen, K. *Macromolecules* **2005,** *38,* 9920.

131) Phadtare, S.; Kumar, A.; Vinod, V.P.; Dash, C.; Palaskar, D.V.; Rao, M.; Shukla, P.G.; Sivaram, S.; Sastry, M. *Chem. Mater.* **2003**, *15*, 1944.

132) (a) Mirkin, C.A.; Letsinger, R.L.; Mucic, R.C.; Storhoff, J.J. *Nature* **1996**, *382*, 607. (b) Sastry, M.; Kumar, A. *Appl. Phys. Lett.* **2001**, *78*, 2943. (c) Loweth, C.J.; Caldwell, W.B.; Peng, X.; Alivisatos, A.P.; Schultz, P.G. *Angew. Chem. Int. Ed.* **1999**, *38*, 1808. (d) Patolsky, F.; Ranjit, K.T.; Lichtenstein, A.; Willner, I. *Chem.Commun.*, **2000**, 1025.

(e) Taton, A.T.; Mucic, R.C.; Mirkin, C.A.; Letsinger, R.L. *J. Am. Chem. Soc.* **2000**, *122*, 6305. (f) Niemeyer, C.M.; Simon, U. *Eur. J. Inorg. Chem.* **2005**, 3641. (g) Storhoff, J.J.; Mirkin, C.A. *Chem. Rev.* **1999**, *99*, 1849.

133) Gourishankar, A.; Shukla, S.; Ganesh, K.N.; Sastry, M. *J. Am. Chem. Soc.* **2004**, *126*, 13186.

134) Braun, E.; Eichen, Y.; Sivan, U.; Ben-Yoseph, G. *Nature* **1998**, *391*, 775.

135) (a) Fu, X.; Wang, Y.; Huang, L.; Sha, Y.; Gui, L.; Lai, L.; Tang, Y. *Adv. Mater.* **2003**, *15*, 902. (b) Naik, R.R.; Stringer, S.J.; Agarwal, G.; Jones, S.E.; Stone, M.O. *Nat. Mater.* **2002**, *1*, 169. (c) Wong, M.S.; Cha, J.N.; Choi, K.-S.; Deming, T.J.; Stucky, G.D. *Nano Lett.* **2002**, *2*, 583.

136) Burkett, S.L.; S. Mann, *Chem. Commun.* **1996**, 321.

137) Yang, J.; Mayer, M.; Kriebel, J.K.; Garstecki, P.; Whitesides, G.M. *Angew. Chem. Int. Ed.* **2004**, *43*, 1555.

138) (a) Lee, S.-W.; Lee, S.K.; Belcher, A.M. *Adv. Mater.* **2003**, *15*, 689. (b) Dujardin, E.; Peet, C.; Stubbs, G.; Culver, J.N.; Mann, S. *Nano Lett.,* **2003**, *3*, 413. (c) Slocik, J.M.; Naik, R.R.; Stone, M.O.; Wright, D.W. *J. Mater. Chem.* **2005**, *15*, 749.

139) (a) Li, Z.; Chung, S.-W.; Nam, J.-M.; Ginger, D.S.; Mirkin, C.A. *Angew. Chem. Int. Ed.* **2003**, *42*, 2306. (b) Berry, V.; Rangaswamy, S.; Saraf, R.F. *Nano Lett.* **2004**, *4*, 939. (c) Berry, V.; Saraf, R.F. *Angew. Chem. Int. Ed.* **2005**, *44*, 6668. (d) He, Y.; Yuan, J.; Su, F.; Xing, X.; Shi, G. *J. Phys. Chem. B* **2006,** *110,* 17813. (e) Rosi, N.L.; Thaxton, C.S.; Mirkin, C.A. *Angew. Chem. Int. Ed.* **2004**, *43*, 5500.

140) Thomas, J.M. *Pure Appl. Chem.,* **1988**, *60*, 1517.

141) Roucoux, A.; Schulz, J.; Patin, H. *Chem. Rev.* **2002,** *102,* 3757.

142) Fichtner, M. *Adv. Eng. Mater.* **2005**, *7*, 443.

143) (a) Kim, Y.; Johnson, R.C.; Hupp, J.T. *Nano Lett.* **2001**, *1*, 165. (b) Liu, J.; Lu, Y. *J. Am. Chem. Soc.* **2004**, *126*, 12298. (c) Obare, S.O.; Hollowell, R.E.; Murphy, C.J. *Langmuir* **2002**, *18*, 10407.

144) Moran, C.E.; Steele, J.M.; Halas, N.J. *Nano Lett.* **2004**, *4*, 1497.

145) a) Simon, U. In *Nanoparticles: From Theory to Application*, Schmid, G., Ed. Wiley-VCH, Weinheim, **2004**. b) *Nanomaterials: Synthesis, Properties, and Applications*,

edited by A. S. Edelstein and R. C. Cammarata (Institute of Physics Publishing, Bristol, U.K., **1996**).

146) a) Maier, S.A.; Brongersma, M.L.; Kik, P.G.; Meltzer, S.; Requicha, A.A.G.; Atwater, H.A. *Adv. Mater.* **2001**, *13*, 1501. b) Maier, S.A.; Brongersma, M.L.; Kik, P.G.; Atwater, H.A. *Phys. Rev. B*, **2002**, *65*, 193408. c) Wang, Y. *Acc. Chem. Res.* **1991**, *24*, 133. (b) Yoffe, A.D. *Adv. Phys.* **1993**, *42*, 173.

147) Li, X.; Xu, W.; Zhang, J.; Jia, H.; Yang, B.; Zhao, B.; Li, B.; Ozaki, Y. *Langmuir* **2004**, *20*, 1298.

148) Debeda, H.; Rebiere, D.; Pistre, J.; Menil, J. *Sens. Actuators B* **1995**, *27*, 297.

149) Brailsford, A.D.; Yussouff, M.; Logothetis, E.M. *Technical Digest of the 4th International Meeting on Chemical Sensors* (Ed.: Yamazoe, N.), Japan Association of Chemical Sensors, Tokyo, **1992**.

150) Ostrik, B; Fleischer, M.; Meixner, H.; Kohl, D. *Sens. Actuators B* **2000**, *68*, 197.

151) Lucklum, R.; Hauptmann, P. *Sens. Actuators B* **2000**, *70*, 30.

152) Chang, S.M.; Kim, Y.H.; Kim, J.M.; Chang, Y.K. *Mol. Cryst. Liq. Cryst.* **1995**, *267*, 405.

153) Brattein, W.H.; Bardeen, J. *Bell Syst. Tech. J.* **1953**, *32*, 1.

154) Heiland, G. *Z. Phys.* **1954**, *138*, 549.

155) (a) Seiyama, T.; Kato, A.; Fujiishi, K.; Nagatami, M. Anal. Chem. 1962, 34, 1502. (b) Seiyama, T.; Kagawa, S. *Anal. Chem.* **1966**, *38*, 1069.

156) Taguchi, N. Patent 45-38200, **1962**.

157) (a) Wohltjen, H.; Snow, A.W. *Anal. Chem.* **1998**, **70**, 2856. (b) Evans, S.D.; Johnson, S.R.; Cheng, Y.L.; Shen, T. *J. Mater. Chem.* **2000**, *10*, 183. (c) Han, L.; Daniel, D.R.; Mayer, M.M.; Zhong, C.-J. *Anal. Chem.* **2001**, *73*, 4441. (d) Krasteva, N.; Besnard, I.; Guse, B.; Bauer, R.E.; Muellen, K.; Yasuda, A.; Vossmeyer, T. *Nano Lett.* **2002**, *2*, 551. (e) Vossmeyer, T.; Guse, B.; Besnard, I.; Bauer, R.E.; Muellen, K.; Yasuda, A. *Adv. Mater.* **2002**, *14*, 238. (f) Zamborini, F.P.; Leopold, M.C.; Hicks, J.F.; Kulesza, P.J.; Malik, M.A.; Murray, R.W. *J. Am. Chem. Soc.* **2002**, *124*, 8958. (g) Zhang, H.-L.; Evans, S.D.; Henderson, J.R.; Miles, R.E.; Shen, T.-H. *Nanotechnology* **2002**, *13*, 439. (h) Grate, J.W.; Nelson, D.A.; Skaggs, R. *Anal. Chem.* **2003**, *75*, 1868. (i) Krasteva, N.; Guse, B.; Besnard, I.; Yasuda, A.; Vossmeyer, T. *Sens. Actuators B* **2003**, *92*, 137.

158) Kohl, C.-D. *"Electronic Noses" in Nanoelectronics and Information Technology,* (Ed.: R. Waser), Wiley-VCH, Berlin, **2005**, 835.

159) Joseph, Y.; Guse, B.; Yasuda, A.; Vossmeyer, T. *Sens. Actuators B* **2004**, *98*, 188.

160) (a) Asscher, M.; Rosenzweig, *Z. J. Vac. Sci. Technol. A* **1991**, *9*, 1913. (b) Grigor'ev, E.I.; Vorontsov, P.S.; Zav'yalov, S.A.; Chvalun, S.N. *Tech. Phys. Lett.* **2002**, *28*, 845.

161) Wilker, S.; Henning, D.; Lober, R. *Phys. Rev. B* **1994**, *50*, 2548.

Chapter II

Characterization Techniques

This chapter discusses the basic working principle of the various characterization techniques, which were used during the course of the presented work.

2.1 Introduction.

The work presented in this thesis emphasizes on the application of metal nanostructures in the following aspects: 1) fabrication of conducting metallic film on a solid substrate and its application in chemical vapor sensing, 2) immobilization on to a soft active template for chemical vapor sensing, 3) solution based mercuric ion detection and 4) cytotoxicity and cell internalization studies of biologically synthesized gold nanotriangles. Various characterization techniques such as UV-visible spectroscopy, Transmission Electron Microscopy (TEM), Scanning Electron Microscopy (SEM), Energy dispersive microanalysis (EDAX), Atomic force microscopy (AFM), Phase contrast microscopy, X-ray photoelectron spectroscopy (XPS), Current source measurement unit, X-ray diffraction (XRD), Flow cytometry and Enzyme linked immunosorbent assay (ELISA) have been used for characterization while pursuing these work. This chapter is devoted to explain the basic principles and the techniques used for characterization.

2.2 UV-vis-NIR spectroscopy.

Basic principles:

Absorption spectroscopy in the different regions of electromagnetic spectrum has been an important tool to the analyst since a long time [1]. Any molecular system possesses three types of energy namely electronic (E_{ele}), vibrational (E_{vib}) and rotational (E_{rot}) with decreasing magnitude in same order for a system. Absorption of energy leads to transition of electron from ground state to excited state. The absorption peak thus obtained is broad, smooth and never very sharp due to the fact that the electronic absorption is accompanied with a corresponding change in the vibrational and rotational energies as well. The relationship between the energy absorbed in an electronic transition and the frequency, ν, wavelength, λ and wavenumber, $\bar{\nu}$ of the radiation producing the transition is

$$\Delta E = h\nu = hc/\lambda = h.\ \bar{\nu}.c$$

where, h is Planck's constant, c is the velocity of light and ΔE is the energy absorbed in an electronic transition in a molecule from a low-energy state (ground state) to a high energy state (excited state). The position of absorption maxima for a molecule depends on the difference in the energy of the ground state level to that of excited state; larger the difference between the energies, higher is the frequency of absorption and thus smaller will be the wavelength. Absorption band shows two important characteristic; position of the band which

depends on the energy difference between electronic level and intensity which depends on the interaction between the radiation and electronic system as well as on the energy difference between the ground and excited state. A convenient expression, which relates the absorbance with the path length that the radiation travels within the system and the concentration of the species, can be derived from the Lambert-Beer law and is given as,

$$A = a.b.c \qquad \ldots\ldots\ldots(2.1)$$

where A is measured absorbance, a is the absorptivity, b is the path length and c is the concentration of the analyte.

In the presented work, UV-vis-NIR spectroscopy has been used to study the optical properties of gold nanotriangles in solution and for the film on quartz substrate. Besides, an attempt has been made to understand the changes in the optical properties of gold nanotriangles by the process of amalgamation to elucidate its application in optical detection of mercuric ions in aqueous system. These measurements were done on JASCO V570 UV/VIS/NIR spectrophotometer operated at a resolution of 1 nm.

2.3 Transmission electron microscope (TEM).

Basic Principles:

TEM works on the principle similar to that of an optical microscope with the key difference that it uses electrons and not photons as the source. The uncertainty principle sets a fundamental limit on the spatial resolution while using a beam of particles with de Broglie wavelength. Thus, smaller the wavelength of the source, higher will be the resolution of the system. In the transmission electron microscopy, much smaller wavelength electrons (0.03 Å) are used instead of photons (λ> 1000 Å) providing much higher resolution. During TEM analysis, a thin sample is bathed with a collimated beam of accelerating electrons uniformly over the illuminated area. Electrons being charged in nature, can be easily deflected using an external electric or magnetic field and can be accelerated using external potential. As the electrons travel through the sample, they are either scattered or are transmitted unaffected through the sample. The probability of scattering is described in terms of the interaction cross-section or the mean free path and can be elastic or inelastic. This results into an non-uniform distribution of electrons in the beam that comes out of the sample, which contains all the structural information of the sample [2].

The scattered (diffracted) electrons deflected away from the optical axis of the microscope are blocked using an aperture and thus the transmitted electron beam generates a contrast on the fluorescent screen depending on its varying intensity. In the case of nanomaterials, the crystalline structures interact with the electron beam mainly by diffraction rather than absorption, though the intensity of the transmitted beam depends largely on the density and thickness of the material though which it passes. The intensity of the diffraction thus depends on the orientation of the planes of atom in the crystal relative to the electron beam. Angular distribution of electrons due to diffraction can be viewed in the form of scattering patterns, usually called diffraction patterns, and spatial distribution of electrons can be observed as contrast in images of the sample. Figure 2.1 shows the layout of the various components of a transmission electron microscope.

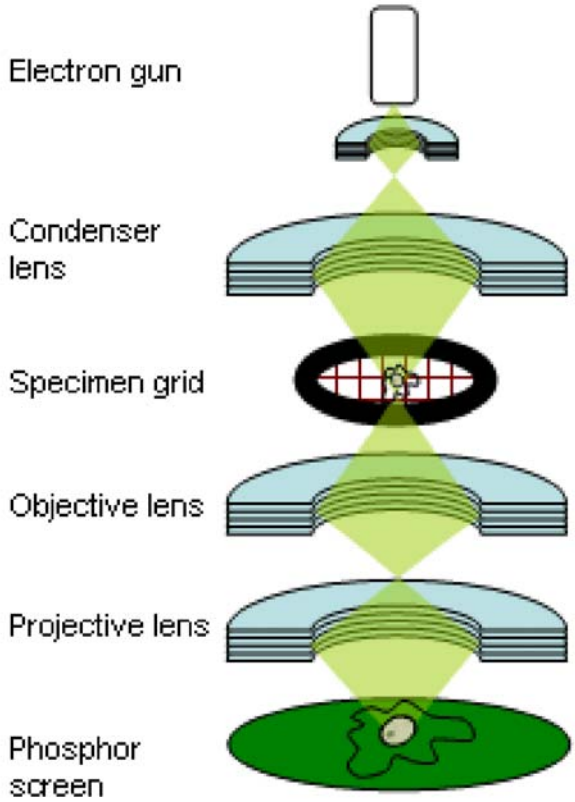

Figure 2.1 *Diagram showing the various components of a TEM [3].*

The transmitted electron beam strikes the fluorescent screen and generates an image with varying contrast. The darker areas with higher contrast are those from where fewer electrons have been transmitted due to high density or thickness of the sample while the areas

of lower contrast show the areas in the sample, which have less density or thickness, and thus more number of transmitted electrons are present.

In the present study, TEM has been used for analysing the shape and size of the gold nanotriangles synthesized using lemon grass broth and tyrosine reduced silver nanoparticles. TEM analysis has also been used to visualise the change in the morphology of the gold nanotriangles on exposure to the metallic mercury in varying concentration. Besides, the transmetallation on the surface of silver nanoparticles has been followed using different concentrations of chloroaurate ions by TEM analysis. This particular work has been done by first making a thin film of silver nanoparticles on to the copper TEM grid, which was then exposed to different concentrations of chloroaurate ions for the transmetallation to take place. In another part of the thesis, the gold nanostructure prepared by ex-surface reduction of chloroaurate ions by silkworm silk were visualised using TEM imaging. The TEM measurements were done on a JEOL model 1200EX instrument operated at an accelerating voltage of 80 kV. High resolution transmission electron microscopy (HRTEM) of the gold triangular and hexagonal particles samples prepared on carbon coated grids were carried on a Technai G^2 F-30 model operated at an accelerating voltage of 300 kV.

2.4 Scanning electron microscope (SEM).

Basic Principles:

Scanning electron microscope is an extremely useful tool for the study of the surface of the sample because it offers a better resolution than the optical microscope. It uses electrons emitted from tungsten or Lanthanum hexaboride (LaB_6) thermionic emitters for the visualisation of surface of the sample. The filament is heated resistively by a current to achieve a temperature between 2000-2700 K. This results in an emission of thermionic electrons from the tip over an area about 100 μm x 150 μm. The electron gun generates electrons and accelerates them to energy in the range 0.1 – 30 keV towards the sample [4]. A series of lenses focus the electron beam on to the sample where it interacts with the sample to a depth of approximately 1 μm. Figure 2.2 shows the components of a scanning electron microscope [5].

When the electron beam impinges on the specimen, many types of signals are generated and any of these can be displayed as an image. The two signals most often used to generate SEM images are secondary electrons (SE) and backscattered electrons (BSE). Most

of the electrons are scattered at large angles (from 0^o to 180^o) when they interact with the positively charged nucleus. These elastically scattered electrons usually called 'backscattered electrons' (BSE) are used for SEM imaging. Some electrons are scattered in-elastically due to the loss in kinetic energy upon their interaction with orbital shell electrons. Incident electrons may knock off loosely bound conduction electrons out of the sample. These are secondary electrons (SE) and along with backscattered electrons are widely used for SEM topographical imaging. Both SE and BSE signals are collected when a positive voltage is applied to the collector screen in front of detector. When a negative voltage is applied on the collector screen only BSE signal is captured because the low energy SEs are repelled. Electrons captured by the scintillator/ photomultiplier are then amplified and used to form an image in the SEM [6].

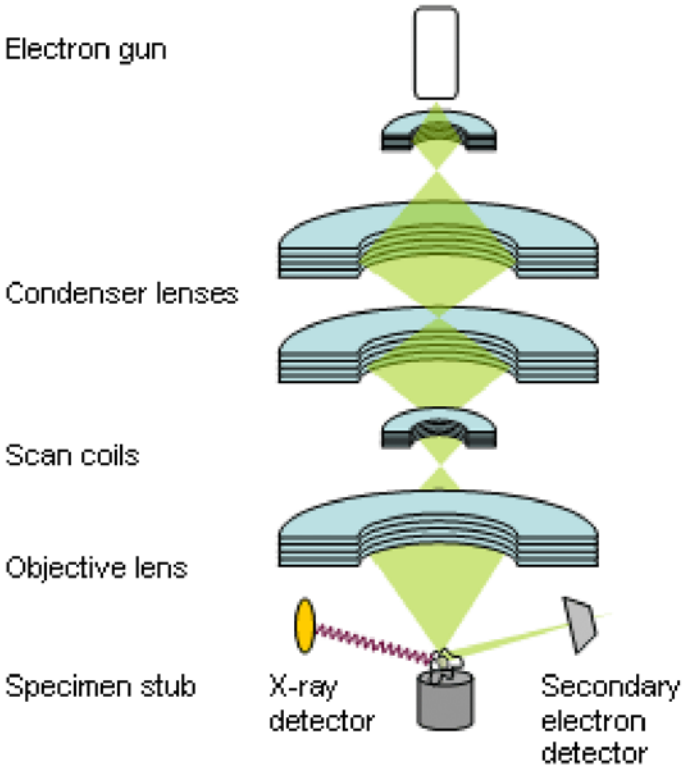

Figure 2.2 *Diagram showing the various components of a SEM [5].*

When the electron beam knocks off the inner shell electron, electron from higher energy levels drop to lower energy levels resulting into emission of Auger electrons, which are used to draw information of the chemical composition of the sample. This technique is called as Auger electron spectroscopy (AES). The emission can also be in the form of photons known as X-ray photons and have high energy, which are used for the compositional

analysis of the sample. This technique is known as energy dispersive analysis of X-ray (EDAX) and is used extensively to study the elemental composition of the sample.

In the presented work, SEM has been used to study the microstructure of the gold nanotriangles film on the substrate as a function of number of coats and after annealing the film by heating. Besides, tyrosine reduced silver film and the bimetallic film formed by transmetallation have also been characterized by using SEM. As a part of the thesis, the spider silk fibre and the nanogold-spider silk bioconjugate has been visualised under SEM to confirm the reduction and immobilization of gold nanoparticles on the surface of the spider silk fibre. EDAX analysis has been used to confirm the bimetallic nature of Ag-Au film and the presence of gold nanoparticles on the surface of spider silk in the nanogold-spider silk bioconjugate. A Leica Stereoscan-440 instrument equipped with a Phoenix energy dispersive analysis of X-rays (EDAX) attachment was used for all the measurements.

2.5 Atomic force microscope (AFM).

Basic Principles:

Atomic force microscopy is a revolutionary sophisticated technique for the study of the topology of a sample in x, y as well as z direction. It utilizes a sharp tip at the end of cantilever that moves over the sample in a raster scan and bends in response to the force between the tip and the sample. Initial AFM was equipped with a scanning tunnelling microscope at the end of the cantilever to monitor its bending, but now, an optical lever technique is employed for the purpose, as shown in the Figure 2.3. As the cantilever bends,

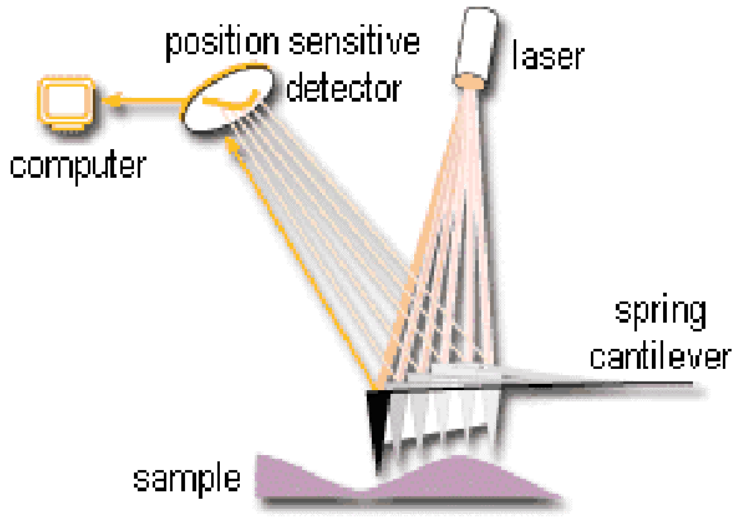

Figure 2.3 *Diagram showing the working of and AFM cantilever [7].*

light from the laser is reflected onto the split photo-diode. The difference in the signal is used as a measure of bending of the cantilever. The bending of the cantilever obeys the Hooke's law for small displacements and so the force between the tip and the sample can be calculated. A device made of piezo-electric ceramic in the form of a tube scanner is used to control the movement of the tip or the sample. The scanner is capable of sub-angstrom level resolution in the x, y or z direction, z being the direction perpendicular to the sample.

The AFM can be operated in two modes namely, with feedback control mode and without feedback control mode. The feedback control mode works at a constant force between the tip and the sample where the piezo which moves sample (or the tip) responds to any change in the force between the sample and tip and alters the separation between the two to restore the original value of force. This measurement is known as height mode measurement and enables reliable topographical analysis of the sample. When the feedback control mode is off, the measurement is performed at constant height (deflection mode), which is useful in high-resolution analysis of the samples that are extremely flat. AFM incorporates several refinements such as sensitive detection, flexible cantilever, sharp tips, high resolution precise tip-sample positioning and force feedback, which enables it to achieve atomic level resolution. Since the imaging process uses the force of interaction of the atoms on the tip to that of the sample, AFM is used for imaging even the non-conducting samples.

AFM measurements can be performed in contact, tapping or non-contact modes, the difference being the extent of tip-sample interaction during the measurement. Contact mode AFM is the most commonly used method where the tip remains in close contact with the sample during the process of scanning. The force of interaction between the tip and the sample lies in the repulsive regime in the intermolecular force curve. Contact mode AFM provides 3-dimensional information of the sample non-destructively with 1.5 nm lateral and 0.05 nm vertical resolution. Tapping mode is generally used for imaging soft and poorly immobilized samples. The tip is oscillated at its resonating frequency and positioned over the sample so that it contacts the sample for a short time interval during oscillation. In the non-contact mode, the tip is oscillated at a distance from the sample so that the two are no longer in contact.

In this thesis, all the AFM imaging has been done in contact mode. This technique was used to study the thickness range of the gold nanotriangles synthesized by lemon grass reduction. AFM has also been used to study the microstructure of gold nanotriangles film as a function of the number of coats and heat treatment cycles. Besides, AFM has been used here to image the clean spider silk fibre in order to measure its height to ascertain that spider silk can be separated into thin fibrils by acid treatment. The gold nanotriangles treated with different concentration of metallic mercury were also analysed by AFM in order to ascertain that the process of amalgamation do not impart any change in the thickness of gold nanotriangles. AFM imaging was also done for the human cell exposed to gold nanotriangles in order to study the topological change during the process. The AFM measurements were done in the contact mode on a VEECO Digital Instruments multimode scanning probe microscope equipped with a Nanoscope IV controller at a scan rate of 5.086 Hz.

2.6 Phase contrast microscope.

Basic Principles:

Phase contrast microscopy finds application in generating high contrast image of the unstained transparent specimens such as living cells, microorganisms, thin tissue slices, lithographic patterns, and sub-cellular particles (such as nuclei and other organelles). It imparts contrast to the biological sample by transforming the phase difference of light, due to the difference in the refractive index between different sub-cellular systems, into difference in the amplitude of light. When a light ray passes through a sample with areas of different optical paths, it is retarded in phase even though the amplitude of the light remains same. Since the human eyes cannot distinguish phase difference, the information is lost. Phase contrast microscope converts this phase difference into amplitude difference to generate the contrast visible to human eye. The various components of a phase contrast microscope have been shown in the Figure 2.4.

A phase contrast has two unique components namely the “phase plate” which retards the incoming light to ¼ of wavelength in a centered, ring shaped area at the back focal plane of the objective lens and a matching “phase annulus” in the condenser consisting of a clear ring on a black field. The matching phase plate and annulus allows the direct unmodified light to pass through and be retarded by ¼ of wavelength. Since the intensity of the diffracted light will be diminished slightly due to the absorption by the sample, a neutral density

coating on top of the phase ring attenuates undiffracted, background light to balance total illumination. The light ray interacting with the sample diffract away from and do not impinge on to the phasing area of the phase plate but are focused by the objective on the image plane. It is due to this difference in the optical path of the light interacting and non-interacting with the sample that retards the refracted wave by ¼ of wavelength in phase. Light that does not interact with the specimen is collected by the objective, passed through the phase plate ring, and is retarded exactly ¼ of wavelength. Since the phase shift is not detectable to human eye, the resulting image on the image plane in the microscope appears as a normal bright background.

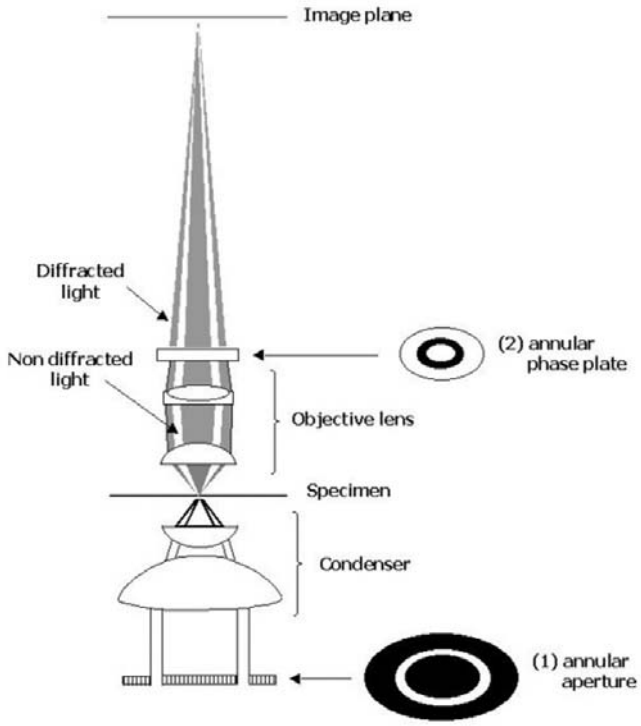

Figure 2.4 *Schematic showing different components of a phase contrast microscope [7].*

Contrarily, the light passing through the specimen gets scattered due to edges and irregularities causing retardation in phase. The diffracted light diverges from the specimen filling the back focal plane of the objective and is resolved on the image plane in the microscope. The undiffracted and diffracted light interacts at the image plane causing wave interference. In negative phase contrast, a constructive interference occur between the two at the image plane resulting into bright areas depending on the difference in the refractive index within the specimen against the background of the undiffracted light. In the presented work,

an inverted phase contrast microscope has been used where the specimen is positions at the top and the source of light comes from the bottom. Such an arrangement makes the visualization of the living animal cells in culture medium easier. Here, the cancerous and non-cancerous animal cells have been studied in the absence and presence of gold nanotriangles in various different concentrations. The tool has been used to make cell counts for cytotoxicity analysis and visual imaging to ascertain the internalization of gold nanotriangles by the animal cells.

2.7 X-ray photoelectron spectroscopy (XPS).

Basic Principles:

XPS is a surface sensitive technique, which is used extensively for the compositions and oxidation state analysis of the sample. It is also know as Electron Spectroscopy for Chemical Analysis (ESCA) due to the fact that it give an accurate quantitative information of the surface of the sample. XPS uses X-ray of a characteristic energy to excite electrons from orbitals in atoms. It is based on the concept of photoelectric effect. In photoelectron spectroscopy, a monochromatic source of X-ray (i.e. fixed energy governed by the relation E=hν) to knock off inner core electron from the atoms constituting the sample resulting into ionization. The kinetic energy of the emitted electron can be calculated using a suitable electrostatic or electromagnetic analyzer and thus the spectrum of the sample could be recorded as a function of number of electrons of one energy emitted per unit time.

A simplistic approach to understand will be from the equation 2.6 showing the ionization process of an element A.

$$\mathbf{A + h\nu = A^{+} + e^{-}} \qquad \text{…… (2.6)}$$

According to the law of conservation of energy,

$$\mathbf{E\,(A) + h\nu = E\,(A^{+}) + E\,(e^{-})} \qquad \text{…… (2.7)}$$

Since the entire energy of the emitted electron will be kinetic energy (KE), equation 2.7 can be rearranged as follows,

$$\mathbf{KE = h\nu - [E\,(A^{+}) - E\,(A)]} \qquad \text{…… (2.8)}$$

The term in the square bracket represents the energy difference between the ionized and the atomic state of an atom, known as the binding energy (BE), which is characteristic for an atom. The equation 2.8 is thus simplified to

$$\mathbf{KE = h\nu - BE} \qquad \text{…… (2.9)}$$

The binding energy is measured with respect to the fermi energy level in solids and thus equation 2.9 is modified incorporating the work function (ϕ) term for the solids.

$$\mathbf{KE = h\nu - BE - \phi} \quad \ldots\ldots\ldots (2.10)$$

Thus, from the equation 2.10, employing the photon of known energy hν and measuring the kinetic energy of the emitted electron and with known work function ϕ, it is possible to find the binding energy, a characteristic signature of an element. Electron traveling out through the material undergo inelastic collision with the bound electron in the material resulting into energy loss. This gives a strong background to the spectrum rather than a very sharp peak. It is due to this reason that the electrons, which come out from near the surface, give the true information about the chemical composition. Such electrons are emitted from very short distance inside the material (<100 nm) and thus XPS is known to be a surface sensitive technique where the emitted photoelectrons are detected for analysis [8].

The binding energy of an electron does not only depend upon the energy level of emission but also upon the oxidation state of the concerned atom and the local surrounding to that atom. A change in either of the two factors results in a shift of the peak for that atom in the spectrum, which is called as chemical shift. Atoms of a higher positive oxidation state exhibit a higher binding energy due to the extra coulombic interaction between the photo-emitted electron and the ion core. Similarly, presence of an electronegative atom in the surrounding of the atom in question, a net partial positive charge is imparted to that atom. Thus, emission of an electron from such an atom will require higher energy, which shifts the peak to higher binding energy. This ability to discriminate between different oxidation states and chemical environments is one of the major strengths of the XPS technique.

In this work presented here, XPS has been used to confirm the formation of Au (0) from chloroaurate ions by transmetallation against silver nanoparticles. XPS does not only give a signal for presence of Au (0) in the bimetallic film but also shows the presence of Ag^+ ions, which are formed due to the process of oxidation during the course of transmetallation. Besides, this technique has also been used to confirm the reduction of mercuric ions to mercury metal by sodium borohydride in the presence of gold nanotriangles to facilitate the process of amalgamation of gold. The Samples were prepared by drop-coating the solution on Si (111) substrate. XPS measurements were carried out on a VG Microtech ESCA 3000 instrument at a base pressure better than 1 x 10^{-9} Torr with un-monochromatized Mg Kα

radiation (1253.6 eV energy). The measurements were made in the constant analyzer energy (CAE) mode at pass energy of 50 eV and electron takeoff angle (angle between electron emission direction and surface plane) of 60°. This leads to an overall resolution of ~ 1 eV in the measurements. The chemically distinct components in the core level spectra were resolved by a non-linear least squares fitting algorithm after background removal by the Shirley method [9].

2.8 Conductivity meter.

Keithley 238 high current source measure unit has been used for all the electrical characterization. It can operate in two modes where it can functions as a current or a voltage source:

1. Source V Measure I: In this mode, the instrument functions as a voltage source and simultaneously measures the current given across the circuit. This instrument is capable of sourcing ±100μV to ±110 V. When programmed to source voltage, current measuring meter is connected in series with V source and output (Figure 2.5A).

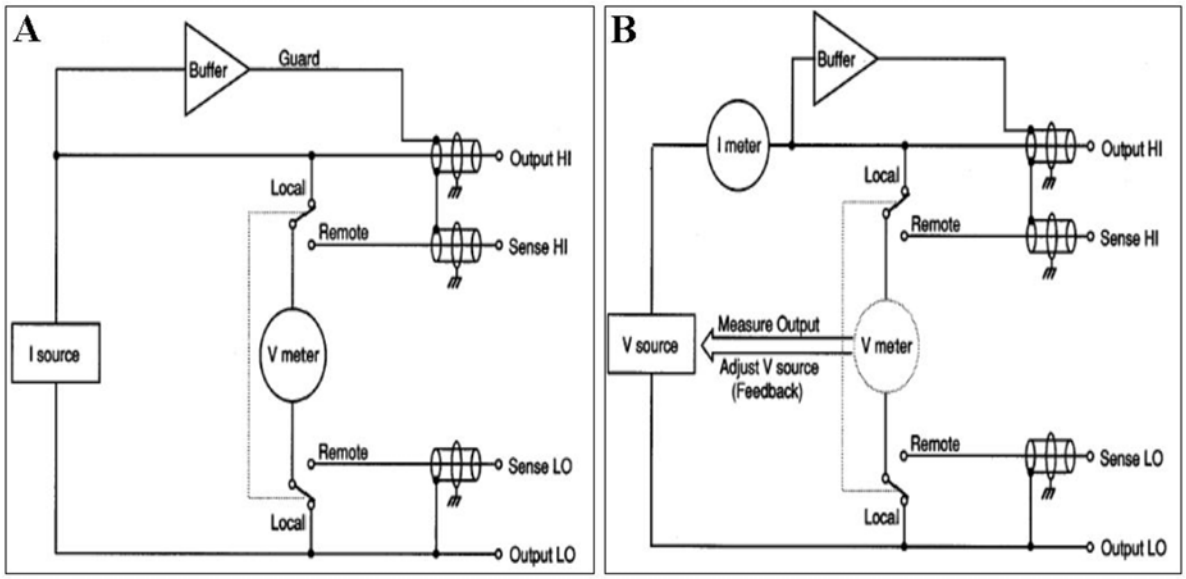

Figure 2.5 *Schematic showing the circuit diagram of conductivity meter: (A) Source I Measure V (B) Source V Measure I mode [10].*

2. Source I Measure V: Here, the instrument functions as a current source and measures the potential drop across the given circuit. This instrument is capable of sourcing ±100 fA to 1A. When programmed to source current, potential measuring meter is connected across (in parallel) with the current source and the output (Figure 2.5B).

The instrument functions in two operation modes namely DC mode and Sweep mode. The source measure unit operation (both DC and sweep modes) also consists of source delay measure (SDM) cycles. During each SDM cycles following steps occur,

1. Set the source output level.
2. Perform the delay.
3. Make the measurement.

The delay is used to allow the source to settle before the measurement is made. The total period of delay includes internal (default) delay and the user defined programmed delay. With the default delay enabled, a short delay is allowed for internal settings on the low current ranges. In dc operation a constant current or voltage is applied to the output. This operation consists of continuous series of SDM cycles. In each SDM cycle, the measured reading will be internally updated, making them available for display. In sweep operations the measure unit sweeps through the user defined list of points specifying source values and delay times for wave forms. An SDM cycle occurs in each programmed step. Each measurement taken is stored in sweep buffer.

There are six basic types of sweep waveforms available namely fixed level, linear staircase, log staircase, pulse, linear staircase pulse and log staircase pulse. The instrument is capable of being handled in 2 modes i.e. in “local mode” operated through the operating panels on the instrument or in “remote mode”. In remote mode different controls of the instrument are handled through computers, where according to our requirements programs can be written to perform the specific operation. Local mode has limitations in its application the measurement data is stored in the instruments memory, which is very limited. So in local mode it is not possible to perform the measurement for a long period. Remote sensing is a better alternative, which is achieved by interfacing the instrument with computer by standard IEEE-488 bus connector. The programs written in TEST POINT programming environment were used for various DC and sweep mode electrical measurements. Besides, another program was written to make electrical measurement at fixed voltage as a function of time, which was used to measure conductivity variation on exposure to chemical vapors.

This instrument has extensively been used in the work presented in this thesis. The electrical property measurements of the gold film fabricated using gold nanotriangles were performed as a function of number of layers on the substrate. Besides, the electrical

properties of the silver film and silver-gold bimetallic film were also studies at room temperature and as a function of varying temperature to calculate the activation energy. The electrical property of the nanogold-spider silk and nanogold-silkworm silk was also measured in order to establish the increased conductivity of the bioconjugate compared to the respective controls (untreated silk fibers). All the above systems were also studied for change in the electrical property (at fixed voltage) as a function of time during exposure and removal of various chemical vapors to establish their application in chemical vapor sensing.

2.9 X-ray diffraction.

Basic principles:

X-rays are electromagnetic radiation with typical photon energies in the range of 100 eV - 100 keV. For diffraction applications, only short wavelength x-rays in the range of a few angstroms to 0.1 angstrom (1 keV - 120 keV) are used. Because the wavelength of x-rays is comparable to the size of atoms, they are ideally suited for probing the structural arrangement of atoms and molecules in a wide range of materials. The energetic x-rays can penetrate deep into the materials and provide information about the bulk structure. X-rays are produced generally by either x-ray tubes or synchrotron radiation. In a x-ray tube, which is the primary x-ray source used in laboratory x-ray instruments, x-rays are generated when a focused electron beam accelerated across a high voltage field bombards a stationary or rotating solid target. As electrons collide with atoms in the target and slow down, a continuous spectrum of x-rays are emitted, which are termed Bremsstrahlung radiation. The high-energy electrons also eject the core electrons in atoms through the ionization process. When an electron from higher energy orbital fills the shell, a x-ray photon with energy characteristic of the target material is emitted. Common targets used in x-ray tubes include Cu and Mo, which emit 8 keV and 14 keV x-rays with corresponding wavelengths of 1.54 Å and 0.8 Å, respectively [11].

X-rays primarily interact with electrons in atoms, collide and some photons from the incident beam are deflected away from original. If the wavelength of these scattered x-rays did not change, the process is called elastic scattering where only the momentum transfer takes place. These diffracted X-rays are measured to extract information about the material, since they carry information about the electron distribution in materials. Diffracted waves from different atoms can interfere with each other and the resultant intensity distribution is

strongly modulated by this interaction. If the atoms are arranged in a periodic fashion, as in crystals, the diffracted waves will consist of sharp interference maxima with the same symmetry as in the distribution of atoms. Measuring the diffraction pattern therefore allows us to deduce the distribution of atoms in a material. When certain geometric requirements are met, X-rays scattered from a crystalline solid can constructively interfere, producing a diffracted beam. In 1912, W. L. Bragg gave the relation, which elucidates the condition for constructive interference.

$$n\lambda = 2d\sin\theta \qquad \ldots\ldots\ldots (2.11)$$

The above equation is called Bragg equation, where n denotes the order of diffraction, λ represents the wavelength, d is the interplanar spacing and θ signifies the scattering angle. The distance between similar atomic planes in a crystal, which is known as d spacing and is measured in angstroms. The angle of diffraction is called as the θ angle and measure in degrees. For practical reasons the diffractometer measures an angle twice that of the θ angle [12].

In this work, XRD has been used to show that the gold nanotriangles synthesized by biological reduction are single crystalline in nature with the flat surface comprised of (111) plane. The XRD data presented here, were carried out on a Philips PW 1830 instrument operating at a voltage of 40 kV and a current of 30 mA with Cu k_α radiation. The XRD samples were made by drop coating the sample on a glass plate.

2.10 Flow cytometry.

Basic Principles:

Flow cytometry is a technique, which has found tremendous application in the fields of cell biology and clinical medicine. It is a versatile technique which simultaneously measures and analyses several physical properties of a single particle, usually cells, as they flow in a stream of fluid through a beam of light. It is capable of obtaining information about the cell size, cell granularity and internal complexity and relative fluorescence intensity. The analysis is done by using an optical to electronic coupled system, which records the scattered incident light and emits fluorescence. A flow cytometer comprises of three components:

1. Fluidic system that transports the cell in a stream to the laser beam.

2. Optics system with a laser source which strikes the cells in a stream and suitable optical filters that direct the resulting light signals to the detector.
3. The electronic component that converts the optical signal into electronic signal, which in turn can be processed by the computer. The instruments, which also perform cell-sorting function, have another attachment to charge the cells and deflect particles for separation based on a physical property.

A particle or cell in the size range of 0.2 to 150 μm is suitable for analysis using a flow cytometer. The information can be obtained from the sample either by the laser scattering characteristic or a fluorescence label. When the laser light illuminates the stream of cells, they scatter light and if any fluorescence molecules are present, it fluoresces. Suitable lenses are positioned appropriately to collect either of the information and transmit it to the detector using filters and beam splitters. Detector produces an electronic signal, which is proportionate with the optical signal it receives from the sample.

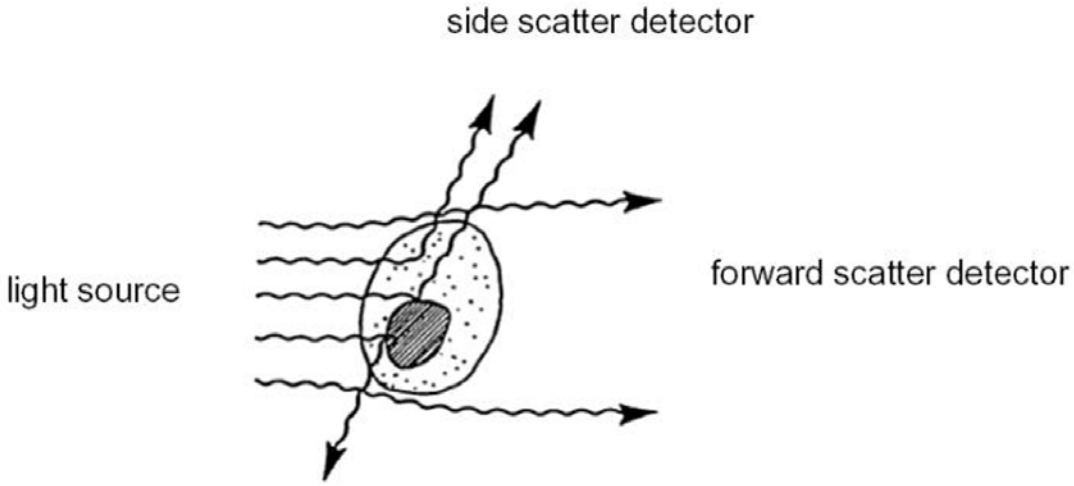

Figure 2.6 *Schematic showing the light scattering property of a cell [13].*

In the work presented in this thesis, the light scattering tendency has been used to analyse the change in the granularity of cells on exposure to gold nanotriangles. The extent of scattering gives a direct measure of particle size and the internal complexity. Factors, which govern this phenomenon, are cellular membrane, nucleus and any granular material inside the cell. Forward-scattered (FSC) light gives a measure of the cell-surface area or size and is detected just off the axis of the laser beam using a photodiode. Side-scattered (SSC) light is proportionate with the cellular granularity or internal complexity. SSC is collected approximately 90^0 to the laser beam using lenses and is directed by a beam splitter to the

detector [20]. In the experiments performed here, the SSC has been used to confirm the internalisation of the gold nanotriangles by the animal cells, which increases the cellular granularity and consequently the intensity of SSC.

2.11 Enzyme linked immunosorbent assay.

Basic Principles:

ELISA is a useful and powerful method in estimating ng/ml to pg/ml ordered materials in the solution, such as serum, urine and culture supernatant. This technique was conceptualized and developed by Peter Perlmann and Eva Engvall [14]. The basic principle of an ELISA is to use an enzyme to detect the binding of antigen (Ag) antibody (Ab). The enzyme converts a colorless substrate (chromogen) to a colored product, indicating the presence of Ag:Ab binding. An ELISA can be used to detect either the presence of Ags or Abs in a sample, depending on how the test is designed [15].

ELISA is primarily of three types namely indirect ELISA, competitive ELISA and Sandwich ELISA. In indirect ELISA, the microtiter well is coated with antigen (Ag) and primary antibody (Ab_1) is exposed which binds to Ag. A secondary antibody (Ab_2) tagged with the probe is used which binds to Ab_1 and gives signal. In competitive ELISA, the Ag sample is first exposed a known quantity of Ab_1 and this mixture is then added to microtiter well coated with same Ag. More the Ag in sample, less will be free Ab_1 in mixture to bind to Ag in the well. After washing, the well is exposed to Ab_2 tagged with probe. Thus, stronger the signal more is Ab_1 availability, indicating lesser amount of Ag in sample and viceversa.

In the work presented here, sandwich ELISA has been used to detect the expression of Tumor Necrosis Factor-α (TNF-α) by the human cells, which were exposed to gold nanotriangles. The Sandwich ELISA measures the amount of antigen between two layers of antibodies (i.e. capture and detection antibody). Here, microtiter well is coated with Ab_1 and Ag is added to it. Following washing, Ab_2 is added which recognizes a unique epitope in the same Ag. Thus, the antigen to be measured must contain at least two antigenic sites capable of binding to antibody, since at least two antibodies act in the sandwich. Either monoclonal or polyclonal antibodies can be used as the capture and detection antibodies in Sandwich ELISA systems. Monoclonal antibodies recognise a single epitope that allows fine detection and quantification of small differences in antigen. A polyclonal is often used as the capture antibody to pull down as much of the antigen as possible. The detection antibody is tagged

with an enzyme, commonly Horse-radish peroxidase (HRP) or Alkaline phosphatase (ALP), which give colored products on exposure to respective suitable colorless substrates. Thus, a positive colorimetric signal signifies the qualitative presence of the antigen in question while the absorbance value can be used to quantify the concentration of the antigen. Instead, a chemiluminescent probe can also be used to detect the signal.

2.12 References.

1) Denney, R.C; Sinclair, R. *Visible and Ultraviolet Spectroscopy. Analytical Chemistry by open learning series*, John Wiley and Sons, USA.
2) Williams, D.B. *Transmission Electron Microscopy, A textbook for Material Science*, Plenum Press. New York and London. **1996**.
3) http://www.steve.gb.com/images/science/transmission_electron_microscope.png
4) Lawes, G. *Scanning electron microscopy and X-ray microanalysis: Analytical chemistry by open learning*, John Wiley & sons, **1987**.
5) http://www.steve.gb.com/images/science/scanning_electron_microscope.png
6) http://www.che.utoledo.edu/nadarajah/webpicts/amfwht.gif
7) http://www.fz-juelich.de/isg/datapool/page/258/Fig4.jpg
8) Kaufmann, E.N. *Characterization of materials*, John Wiley & sons, **2003**.
9) Shirley, D.A. *Phys. Rev. B* **1972**, *5*, 4709.
10) Operator's manual, Keithley Model 238 Source Measure Unit.
11) Azaroff, L.V. *X-Ray diffraction*, McGraw Hill company, **1974**.
12) Cullity, B.D. *Elements of X-ray diffraction*, Addison-Wesley Publishing Co.Inc. **1978**.
13) www.petermac.org/pdf/Intro%20to%20Flow%20Cytometry%20.pdf
14) Engvall, E.; Perlmann, P. *Immunochemistry* **1971**, *8*, 871.
15) Derango, R.; Page, J. *J. Immunoassay* **1996**, *17*, 145.

Chapter III

Metal nanoparticles immobilized on a solid substrate for sensing applications

Metal nanoparticles have been assembled onto solid substrates for various applications in electronic, biological and chemical sensing and as SERS and SPR substrates. In this chapter, an attempt has been made to fabricate superstructures of metal nanoparticles onto quartz substrate to form conducting films and application of these films in chemical vapor sensing has been pursued. Films have been fabricated by simple drop coating followed by air-drying. In one approach, single crystalline, extremely flat gold nanotriangles have been used for fabrication of films of varying resistance, which were annealed to form a highly conducting film. Three layer thick film of gold nanotriangles has been used to show application in sensing methanol vapors. In yet another approach, the galvanic replacement reaction has been used to improve the conductivity of silver nanoparticles film by exposing it to aqueous solution of chloroaurate ions. The chloroaurate ions are reduced at the cost of silver atoms in silver nanoparticles, which acts as a sacrificial template, and thus form gold interconnected silver nanoparticles to reduce the resistance of the film. This Ag-Au bimetallic film formed thereby, has been used to sense ammonia and carbon di-oxide vapors.

Part of the work presented in this chapter has been published:

1) Singh, A.; Chaudhari, M. and Sastry, M. *Nanotechnology* **2006**, *17*, 2399-2405. 2) Singh, A and Sastry, M. *Chem. Mater.* (communicated)

3.1 Introduction.

Metal nanoparticles have drawn extensive interest due to their unique size, shape and composition dependent optical [1] and electronic [2] properties. However, for their application purpose, it is a major challenge to assemble these metal nanoparticles in superstructures in solution or as thin films. Thin films specially have been of more interest from the point of view of device fabrication and other applications such as surface plasmon resonance substrates [3], surface enhanced Raman spectroscopy [4], in macro and nanoscale structure fabrication [5] and biosensing [6] as well as chemical sensing [7]. Thus, different approaches have been taken up to assemble metal nanoparticles on different substrates to fabricate conducting films.

Musick *et al.* have used bifunctional cross-linkers to self-assemble gold nanoparticles onto (3-aminopropyl) trimethoxysilane (APTMS)-coated or mercaptosilane-modified glass substrate to form conductive films [8]. Brown *et al.* have used a seeding method for surface catalyzed reduction of Au^{3+} ions by NH_2OH to form conductive gold nanoparticle films on an organosilane-coated glass substrate [9]. In a slightly different approach, Doron *et al.* have demonstrated the organization of gold colloids as monolayers on the indium tin oxide (ITO) surfaces using (aminopropy1) siloxane or (mercaptopropyl) siloxane as base monolayers for adhesion of the metal nanoparticles [10]. Several other approaches such as photolithographic techniques [11], sedimentation [12], electrostatic-induced crystallization [13], convective self-assembly [14], physical confinement [15] and chemical vapor deposition [5] have also been used.

Gold nanoparticles in particular have shown some promising results as building blocks in the preparation of the electrochemical sensing devices [16]. Krasteva *et al.* have used gold-dendrimer composite films in chemical vapor sensing [17]. Ahn *et al.* have also recently demonstrated the chemical vapor sensing capability and electrical conductivity of ω-(3-thienyl) alkanethiol protected gold nanoparticle film [18] while Briglin *et al.* have used alkylamine-passivated gold nanocrystals for organic mercaptan vapor detection [19]. In yet another application, functionalized gold nanoparticle films have been used by Kim *et al.* in the sensitive detection of heavy metal ions [20]. Zamborini et al have used monolayer-protected gold clusters linked together and have used them to detect organic vapours with a decrease in the conductivity upon exposure to

vapors [21]. However, in all these reports, we note that mono and multilayer films of spherical gold nanoparticles have been fabricated. To the best of our knowledge, no attempts have been made so far to investigate the electrical behavior of anisotropic gold nanoparticles and bimetallic interconnected nanostructure thin films and their application in chemical vapor sensing has not been shown. Moreover, in all these reports, the change is the electrical transport in an environment has been explained based on the swelling of the organic layer on the nanoparticle surface, which increases the separation between the nanoparticles leading to increased resistance and decrease conductivity of the film on exposure to vapor.

In this chapter, an attempt has been made to use metal nanostructures to fabricate a film onto a solid substrate by simple drop coating method followed by air-drying. The films thus formed have been used to study their electrical transport behavior and further, they have been investigated to find applications in sensing chemical vapors. It is a well-known fact that the electrical conduction in such films is mainly by electron tunneling between the metal nanoparticles [22]. Previous studies have also shown that in the case of the capping of the nanoparticles with organic molecules in the monolayers protected clusters (MPCs), the conduction across the organic molecule barrier is by electron hopping [18,23,24]. Here, the electrical conductivity change has been studied as a function of the environment of the film and we observe that physical adsorption of a gas does change the electrical transport behavior of these films. Thus, it has been shown that these metal nanostructure films can be an attractive candidates for potential application in developing vapor sensors. The chapter has been divided into two parts, namely Part A and Part B, based on two different approaches that have been taken over to fabricate the films onto the quartz substrate.

Part A describes the use of gold nanotriangles, synthesized by a biological route, to fabricate films of varying thickness onto the quartz substrate. In our laboratory, we have shown previously the room temperature synthesis of high percentage of single crystalline gold nanotriangles by reducing chloroaurate ions using the leaf extract of the lemon grass (*Cymbopogon flexuosus*) plant [25]. The gold nanotriangles thus synthesized were flat, extremely thin with a thickness between 8-18 nm and edge length ranging 150-500 nm. We further showed that the optical properties and the size of the gold

nanotriangles could be controlled easily by controlling the rate of the reaction by varying the concentration of the reducing agent [26] or the reaction temperature [27]. Here, we have tried to exploit the extremely flat nature of the gold nanotriangles to cover the surface efficiently in order to make conducting films onto the substrate. Their electrical properties have been studied as a function of the number of layers supported with microscopic analysis and further; their application has been pursued in sensing polar vapors (methanol here). It has been also shown that the gold nanotriangle films become highly conducting in nature when the film was annealed by heating at 200 °C for two hours, showing several orders of magnitude drop in the resistance.

Part B describes the use of transmetallation reaction on to the quartz substrate surface to prepare bimetallic Ag-Au film. The sliver film was first drop coated, allowed to air-dry, followed by addition of gold salt on top of it to allow the galvanic replacement reaction to take place. Many previous reports have shown this reaction in solution where one metal nanoparticle having a lower redox potential acts as a sacrificial template for the reduction of another metal, which has a higher redox potential, from its ionic form. Liang et al have shown the formation of Pt hollow nanospheres [28] and AuPt [29] bimetallic hollow nanotubes using the Co nanoparticles as the sacrificial template. Several other reports have been shown, wherein hollow structures of different metals have been synthesized; most importantly gold hollow structures have been synthesized using silver nanoparticles as the sacrificial template for the reduction of chloroaurate ions [30]. Due to the similarity in the lattice parameters of Au and Ag, the elemental gold formed from this reaction grows epitaxially onto the silver surface, whereas solid silver nanoparticles gets oxidized to ionic silver. The reaction involved can be shown as,

$$3Ag^0 + Au^{3+} \rightarrow Au^0 + 3Ag^+$$

In our laboratory, we have shown that the similar reaction can be carried out in an organic medium as well to form hollow structures [31]. However, in this chapter, we have shown the similar reaction onto the solid support to form interconnected Ag-Au nanostructures which shows better conductivity than the control silver film and also shows sensitivity towards detection of ammonia and carbon di-oxide vapors.

Section A

Fabrication of conducting film using biologically synthesized gold nanotriangles and its application in vapor sensing

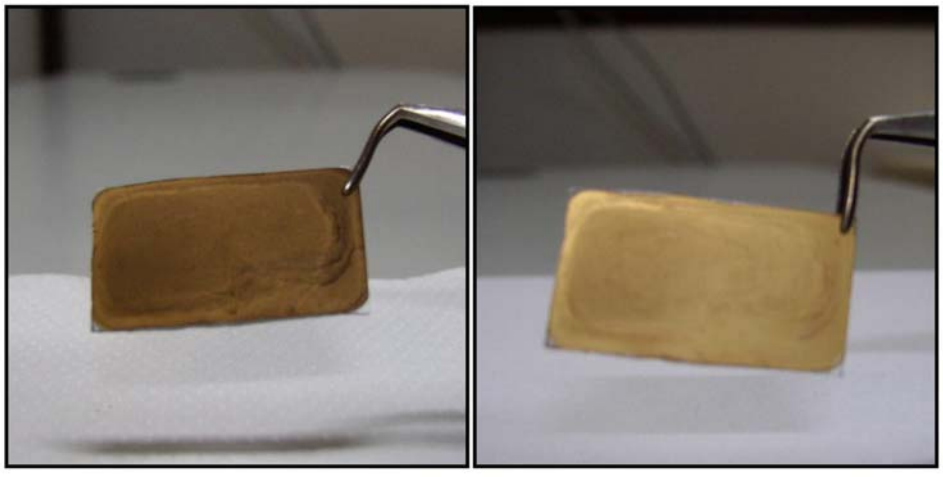

3.2.A.1 Synthesis and characterization of gold nanotriangles.

3.2.A.1.1 Experimental details:

The gold nanotriangles were synthesized using the protocol described elsewhere [22]. In a typical experiment, 100 gm of thoroughly washed and finely cut leaves of lemon grass were boiled for 5 min in 500 mL of sterile deionized water. 5 mL of the broth thus formed was added to 45 mL of 10^{-3} M aqueous solution of chloroauric acid ($HAuCl_4$). The bioreduction of the $AuCl_4^-$ ions was monitored by time dependent UV-vis-NIR spectroscopy measurement of the mixture till the saturation of the reaction. The reaction was observed to complete in 6 hours giving a brown red colored solution, which contains 1:1 ratio of triangular to spherical particles. This solution was centrifuged three times at 3000 rpm for 20 minutes, each followed by washing with deionized water. The pellet was finally suspended in 5 mL of distilled water and was used for further experiments. The centrifugation and washing steps remove majority population of the small sized spherical particles and thus the pellet contains nearly 90% population of gold nanotriangles. For some of the experiments, the synthesis process of the gold nanotriangles was altered, wherein 5 mL of the broth was added to 95 mL of 10^{-3} M aqueous solution of chloroauric acid to facilitate slow reduction, which leads to gold nanotriangles of higher aspect ratios. These nanotriangles were also purified by similar process as described above.

The purified nanoparticle solution was used for solution casting onto different substrates for various characterizations. The films were characterized by UV-vis-NIR spectroscopy and X-ray diffraction (XRD) while the nanoparticles in solution were characterized by UV-vis-NIR, transmission electron microscope (TEM) and selected area electron diffraction (SAED).

3.2.A.1.2 UV-vis-NIR measurements:

Figure 3.A.1A shows the UV-vis-NIR spectra for the as-synthesized (curve 1) as well as the purified nanoparticle solution (curve 2), which show the characteristic transverse and longitudinal plasmon absorbance peaks as reported earlier [25]. In the as-prepared solution (curve 1), the transverse plasmon absorption peak is centered around 515 nm whereas the longitudinal plasmon region shows a continuous absorption in the NIR region, suggesting that the nanoparticle solution contains gold nanotriangles of

varying edge length. However, after the purification step, it is seen that the transverse plasmon shifts from 515 nm to 540 nm, which could be due to aggregation of the spherical particles remaining in the purified solution due to extensive washing steps during purification. Washing steps will remove the capping agent, which stabilizes these biologically synthesized nanoparticles to some extent, which may lead to slight aggregation. It is also important to note that the absorption intensity of the transverse plasmon peak in purified nanoparticle solution (curve 2) is significantly less as compared

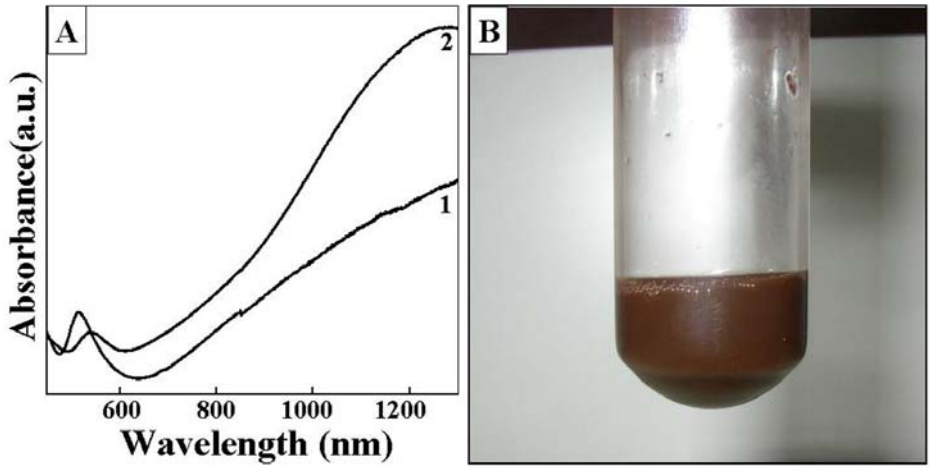

Figure 3.A.1 *A) UV-vis-NIR spectra of the as-prepared gold nanoparticle solution (curve 1) and the purified solution (curve 2) after centrifugation. B) Picture of the purified nanoparticle solution.*

to the as-prepared nanoparticle solution (curve 1) which suggests clearly that the isotropic spherical gold nanoparticles population has successfully been removed to large percentage. Yet another observation which could be made from the two curves is that the relative absorption between 800 nm to 1000 nm range decreases as compared to that at 1200 nm in the spectra of purified nanoparticle solution (Curve 2), whereas in the as-prepared solution spectra (curve 1), the absorption is fairly continuous. This could be due to the loss of the smaller size gold triangular nanoparticles, which absorb around in that region [26,27], during the process of purification. The particles, which absorb around 900 nm, are around 100 nm in edge length and may not settle down at the centrifugation speed used for purification steps.

3.2.A.1.3 TEM measurements:

Figure 3.A.2 shows the TEM image of the as prepared as well as the purified nanoparticle solution. Figure 3.A.2A shows the micrograph of the particles in the as-

synthesized solution where it can be observed that the solution contains almost 1:1 ratio of triangular to spherical gold nanoparticles. It could be seen that the triangular gold nanoparticles are fairly large in size as compared to their spherical counterpart, which make them easier to separate by centrifugation as low speeds where the spherical particle do not settle. It can also be observed that the triangular gold nanoparticles are in varying sizes, which explains the observation in the UV-vis-NIR spectra of the solution where we see a continuous absorption rather than a distinct peak in the NIR region due to longitudinal plasmon (Figure 3.A.1A, curve 1). Figure 3.A.2B shows the TEM image of

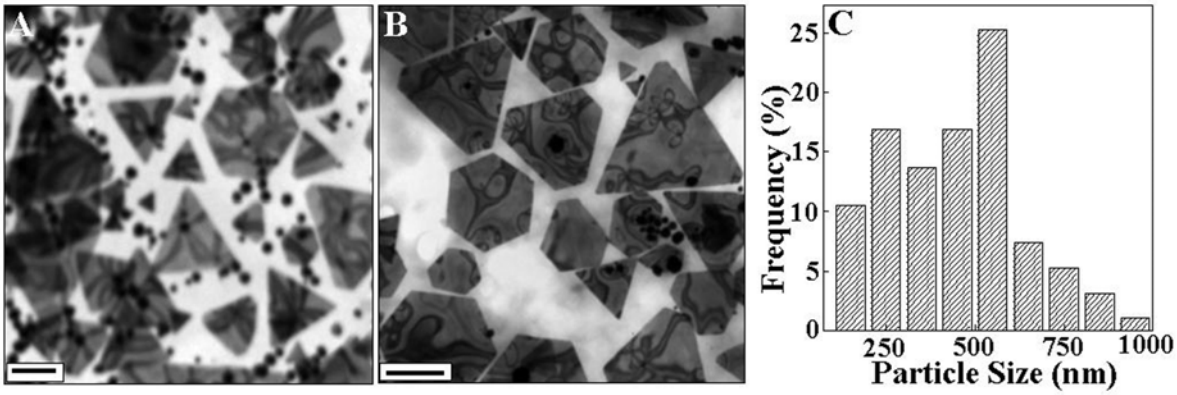

Figure 3.A.2 *TEM micrograph of the as-prepared gold nanoparticle solution (A) and the purified solution (B). The scale bar in both the micrographs correspond to 500 nm.(C) Plot showing the particle size distribution of the purified gold nanotriangles.*

the gold nanoparticles in the purified solution. It can be clearly observed that the population of the spherical has been reduced considerably as compared to the control image and thus, we succeeded in achieving almost 90% population of gold nanotriangles in the purified gold nanoparticles solution. The purified gold nanotriangles showed the particle size distribution ranging from 100 nm to 1μm with an average particle size of 440 nm (Figure 3.A.2C). The contrast seen within the surface of the triangles may have originated due to the stresses in the triangular particles arising from buckling of these thin gold sheets whose thickness have been found in the range of 8 to 20 nm.

3.2.A.1.4 SAED and XRD measurements:

SAED pattern was recorded to ascertain that the biologically synthesized gold nanotriangles are single crystalline in nature. The characteristic spot pattern seen in the Figure 3.A.3A indicates that each of these gold nanotriangles are indeed single crystalline

in nature. The boxed spots and spots circumscribed by triangles correspond to {220} and

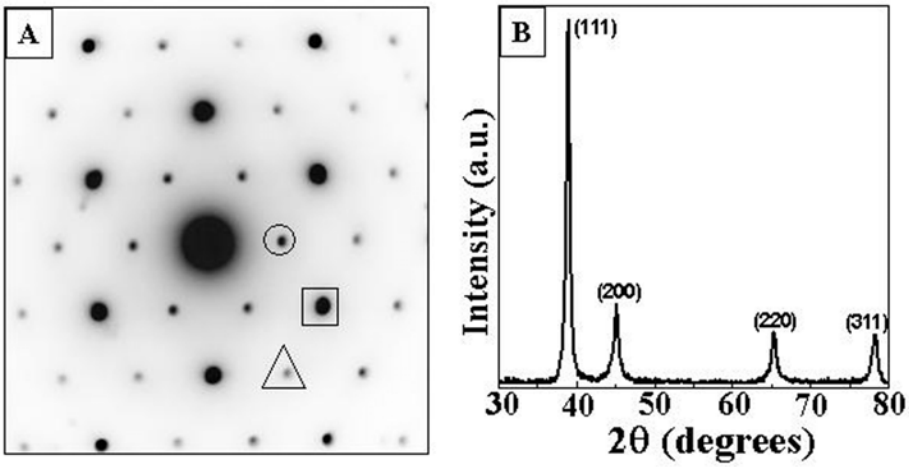

Figure 3.A.3 *(A) The SAED pattern from a single gold triangle. (B) The XRD pattern obtained from the purified gold nanoparticles solution.*

{311} Bragg reflections with lattice spacing of 1.44 and 1.23 Å respectively while the circled spots correspond to the 1/3{422} forbidden reflection with lattice spacing of 2.5 Å. The presence of the face centered cubic (fcc) forbidden 1/3{422} reflection indicates the presence of {111} stacking fault which is lying parallel to the {111} face and extending across the entire planar particle [32]. This forbidden 1/3{422} reflection has been observed in most of the reports on the flat noble metal nanostructures [29b]. The Figure 3.A.3B shows the XRD pattern obtained from the film of the purified nanoparticles solution. The Bragg reflections obtained from the gold nanotriangle film clearly correspond to the fcc crystalline structure of gold. As seen from the XRD pattern a very intense Bragg reflection for {111} lattice is observed suggesting that the <111> oriented gold nanotriangles are lying flat on the planar quartz surface. Thus, these measurements clearly ascertain that the gold nanotriangles formed from the biological synthesis of the chloroaurate ions, using the lemon grass leaf extract, are single crystalline in nature and their flat surface is highly (111) oriented.

3.2.A.2 Fabrication of the film onto the quartz substrate and electrical conductivity measurements.

3.1.A.2.1 Experimental details.

In order to make the films onto the quartz substrate for electrical measurements, the gold nanoparticle solution was dropped coated onto the substrate in known volumes

of solution (200 μL/cm^2 of the substrate; gold concentration ~ 9.2 mg/ml). Each layer was allowed to air-dry completely before addition of the subsequent layer and the process was repeated till seven-coat thick multilayer film was formed on the substrate. Under the experimental conditions of this study, the first layer of nanotriangles resulted in a surface density of ca. 1.6 X 10^{17}/cm^2; subsequent layers would therefore contain equal numbers

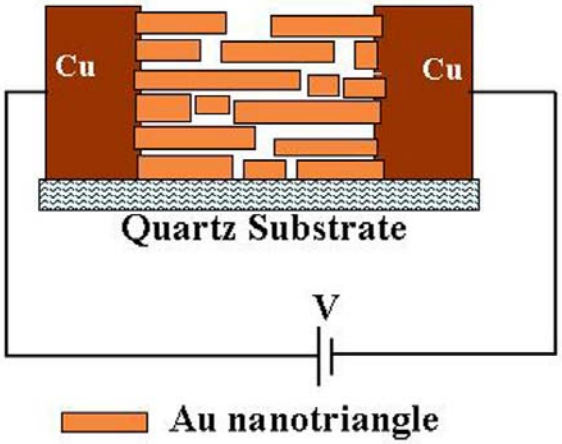

Figure 3.A.4 *The schematic shows the cross-sectional layout of the circuit used for electrical measurements.*

of triangles. Similar procedure was also adapted to coat film on silicon substrate for scanning electron microscopy (SEM) and atomic force microscopy (AFM) measurements to study the microstructure of the film. The electrical conductivity was measured after addition of each fresh coat of triangular gold nanoparticles onto the quartz substrate. Finally, the seven coat thick film was heat annealed for three cycles, each at 200°C for 1 hour with subsequent measurement of the electrical conductivity change of the film with each cycle of treatment. Copper electrodes of 100 nm thicknesses were deposited onto the substrate by vacuum deposition prior to the coating of the gold nanoparticle film for electrical conductivity measurement. In order to eliminate the effect of the electrodes, if any, on the measured conductivity, same measurements were also done on the films by painting a thick pad of silver paste at the each ends of the film to function as electrodes. Figure 3.A.4 shows the schematic of the cross-sectional view of the circuit used for all the electrical measurements.

3.2.A.2.2 UV-vis-NIR-measurements.

The UV-vis-NIR spectra were recorded as a function of the number of coats of the gold nanotriangles onto the quartz substrate. Figure 3.A.5.A shows the absorption spectra

of the purified nanoparticles film of different thickness deposited onto the quartz substrate; curve 1- one coat thick, curve 2- three coats thick and curve 3- seven coats thick. We clearly observe an increase in the absorption profile of the film with increasing thickness, which could be partially due to the increase in the triangular population on to the surface and partially due to increased scattering of light. Curve 4 in the figure 3.A.5

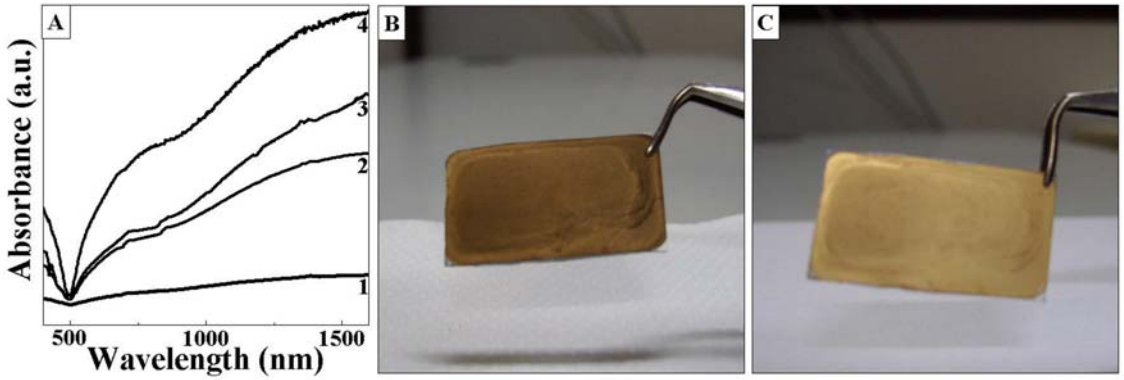

Figure 3.A.5 *(A)The UV-vis-NIR absorption spectra of the purified gold nanoparticle film onto the quartz substrate as a function of increasing number of coats. (B) and (C) show the picture of the seven coat thick film before and after heat treatment respectively.*

corresponds to the absorption profile of same seven coat thick film as in curve 3, but which was annealed by heat treatment for three cycles, each at 200°C for 1 hour.

Figure 3.A.5B & C shows the picture of the 7-layer gold nanotriangle film on quartz before and after three 1 h cycles of heat treatment at 200 ^{o}C respectively. Before heating, the film appeared blue at normal viewing and brownish yellow when viewed at an angle (3.A.5B). After heat treatment, the color changed to a characteristic golden hue when viewed at any angle (3.A.5C). Such changes in color of spherical gold nanoparticle films have been observed due to heat treatment and are a consequence of structural changes arising in the films due to annealing [14c]. The UV-vis-NIR absorption spectra recorded from the gold nanotriangle films shows a characteristic increase in absorption due to increase in film thickness (3.A.5A, curves 1-3) possibly either due to the increase in the density of particles on the surface or due to increased scattering. On heat treatment of the 7-layer gold nanotriangle film (curve 4, 3.A.5A), we observe an increase in absorption over the entire wavelength region scanned. In particular, the increase in absorbance in the NIR region is quite pronounced indicating possible aggregation of the gold nanotriangles in the film after annealing.

3.2.A.2.3 Electrical conductivity measurement.

It has been realized long back that electrical transport in such systems is by a process of electron tunneling/hopping between particles [22] and is a prime reason why the conductivity of nanoparticulate films is such a strong function of the film structure

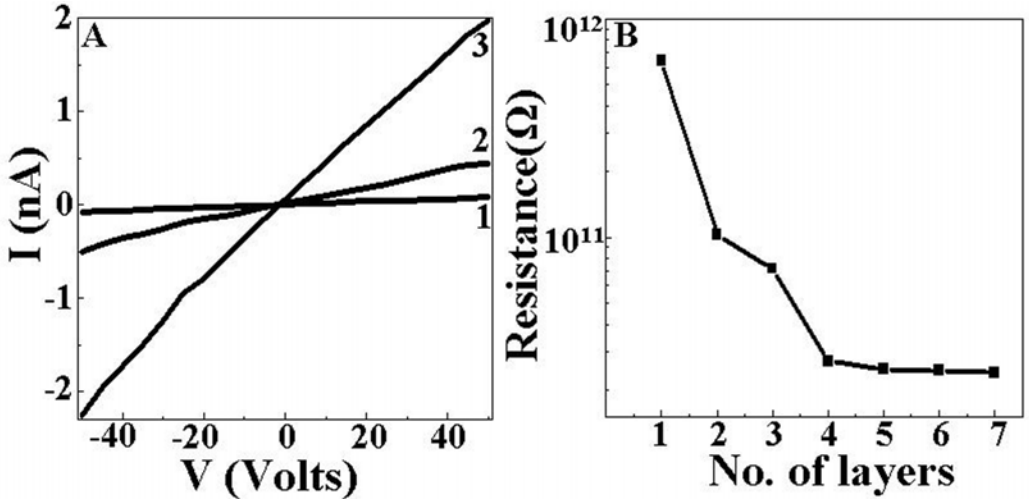

Figure 3.A.6 *(A) I-V plots of the purified gold nanoparticles film as a function of number of coats;1 (curve 1), 3 (curve 2) and 7 coats (curve 3).(B) Plot of the resistance as a function of number of coats onto the substrate.*

and surface chemistry [2b,15b]. Films of nanotriangles would be interesting candidates for electron transport studies due to their anisotropic structure and sharp vertices that could result in field enhancement effects [33]. The electrical property of the film was thus studied as a function of the number of coats of the purified gold nanoparticle on to the quartz substrate. Even though the I-V measurements were done for every subsequent coat of the gold nanoparticles on to the substrate; for simplicity, the I-V plot that have been shown correspond to those recorded from films of 1-layer, 3-layer and 7-layer thickness respectively and indicate that over this range, the films are nearly ohmic with a resistance that decreases with increasing film thickness.

Figure 3.A.6B shows a plot of the variation in resistance of the purified gold nanoparticle films as a function of number of layers deposited. A large and rapid fall in film resistance up to 4-layers is observed which is then followed by an almost steady value where the resistance values for 1, 3 and 7 coat thick films of the purified gold nanoparticles were found out to be 643, 72 and 24 GΩ respectively. We attribute this rapid fall in film resistance to increasing surface coverage of the gold nanotriangles and

the consequent fall in widths of the tunneling barriers for electrons in the film. Once full coverage is achieved, deposition of additional layers of nanotriangles does not lead to a change in the effective tunneling distance and hence, the resistance remains unaltered.

3.2.A.2.4 Heat treatment and electrical conductivity measurement.

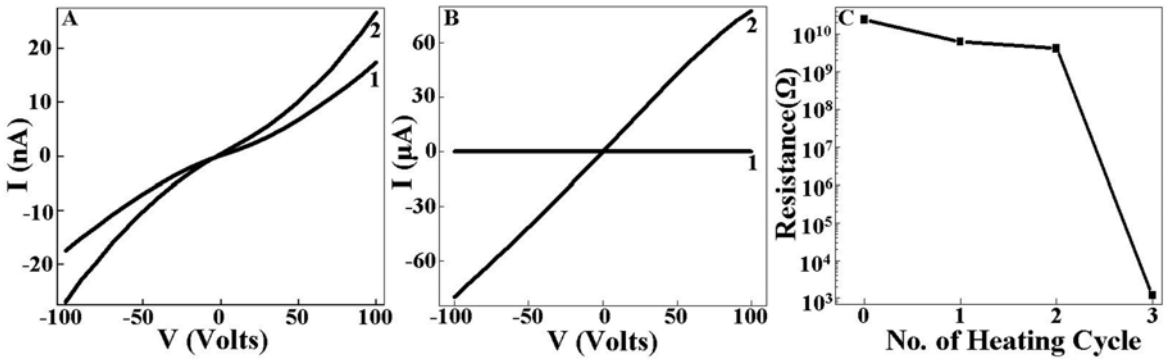

Figure 3.A.7 *(A) I-V plots of 7-coat thick film of the purified gold nanoparticles as a function of number of heat treatment cycles; one (curve 1) and two (curve 2) cycles .(B) The IV plot of the 7-coat thick film after two (curve 1) and three (curve 2) cycles of heat treatment. (C) Plot of the resistance as a function of number of heat treatment cycles of the 7-coat thick film.*

The 7-coat thick film was heat treated at 200°C for three cycles of 1 hour each and the electrical characteristics of the film was measured after each cycle of heat treatment. The curves 1 and 2 in the Figure 3.A.7A show the electrical characteristics of the 7-coat thick film after the first and second cycle of heat treatment. We observe that the conductivity of

Number of Coats	Resistance
1	643 GΩ
2	102 GΩ
3	72 GΩ
4	27 GΩ
5	25 GΩ
6	24.46 GΩ
7	24 GΩ
7-coats Heating cycle 1	6 GΩ
7-coats Heating cycle 2	4 GΩ
7-coats Heating cycle 3	1.2 kΩ

Table 3.A.1 *Resistance values as a function of number of coats and with heating cycles.*

the film increases with the duration of the heat treatment where the resistance of the film changes from 24 GΩ for untreated 7-coat thick film to 6.25 GΩ after first cycle of heat

treatment and 4.12 GΩ after second cycle of heat treatment. It is also worthwhile to note that the I-V plot for the 7-layer thick film was linear initially (curve 3, Figure 3.A.6A), does show some deviation from the linear behavior in the I-V characteristics after the heat treatment, suggesting some changes in the microstructure of the film. Figure 3.A.7B shows the I-V plot of the 7-coat thick film after the second and third cycle of heat treatment where the resistance value of the film was found to be 1.2 kΩ after the third cycle of heat treatment.

Table 3.A.1 shows the resistances of the purified nanoparticle film as a function of number of coats as well as with subsequent cycles of heat treatment. Nearly nine orders of magnitude drop in the resistance value of the film can be observed before heat treatment and after the third cycle of heat treatment, which could certainly be possible only due to the some drastic change in the microstructure of the film.

3.2.A.2.5 Microstructure analysis of the film-SEM and AFM measurement.

In order to understand the above observed changes in the electrical behavior of the film of purified gold nanoparticle solution on the quartz substrate, the microstructure

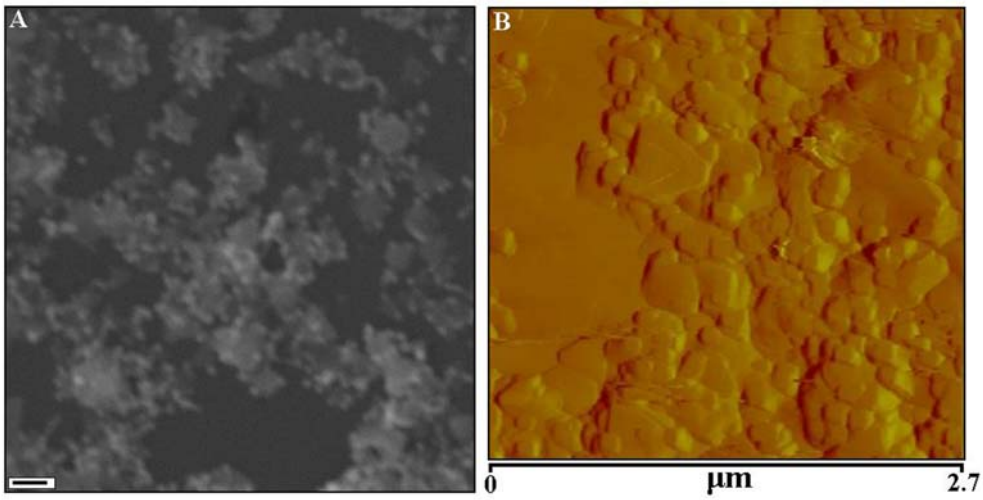

Figure 3.A.8 *(A) SEM micrograph of the 1-coat thick film of purified gold nanoparticle solution. The scale bar corresponds to 300 nm. (B) AFM micrograph of the same film taken in contact mode.*

imaging was done by SEM and AFM characterizations. Figure 3.A.8A shows the SEM image of the one coat thick film of purified gold nanoparticle solution onto the substrate where we clearly observe a mixed population of triangular and spherical nanoparticles on the surface. It is important to note that the surface coverage in this film is not very

efficient which explains the high resistance value of 643 GΩ observed by the electrical conductivity measurements (Figure 3.A.6A curve 1). The AFM micrograph of the same (Figure 3.A.8B) also confirms the similar observation and large voids can be seen in between the triangular particles with poor surface coverage, as expected.

When the same film was observed after 3-coat of the purified gold nanoparticles solution on the surface, the SEM micrograph (Figure 3.A.9A) clearly reveals that the surface coverage has built up significantly and the distance between the particles has reduced. This explains the reason behind the 9-fold drop in the resistance of this film as compared to 1-coat thick film as is shown in Table 3.A.1. It can also be observed clearly that during the process of drying of the film after every coat of the nanoparticles solution on the surface, the particles have aggregated to a great extent which could be a reason for the enhanced absorbance of this film in the NIR spectra (Figure 3.A.5A, curve 2) besides the fact that

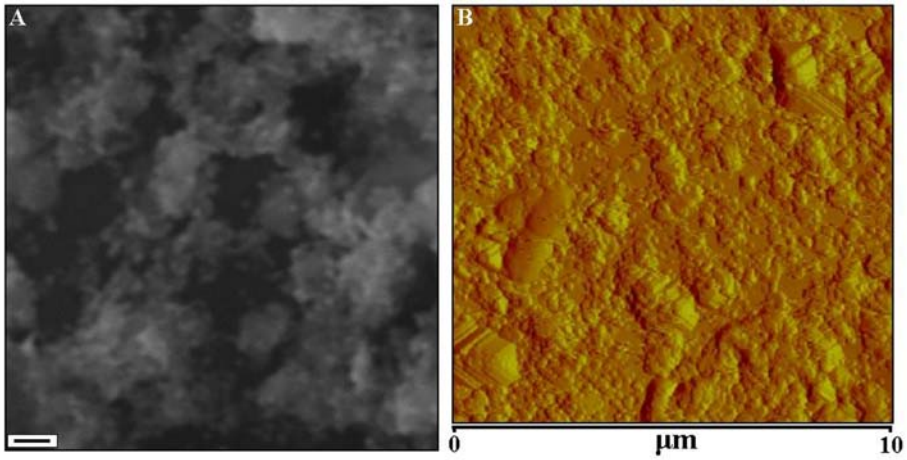

Figure 3.A.9 *(A) SEM micrograph of the 3-coat thick film of purified gold nanoparticle solution. The scale bar corresponds to 300 nm. (B) AFM micrograph of the same film taken in contact mode.*

the population of the particles increases on the surface with every coat, as has been argued above. The AFM micrograph of the same film also reveals similar features at much lower magnification and shows clearly that even over the larger area, the surface coverage is more or less similar to what has been observed from the SEM micrograph.

Figure 3.A.10 shows the 7-coat thick film of the purified gold nanoparticle solution on to the substrate. It can be clearly seen from the SEM image in the Figure 3.A.10A that the particle density on the surface of the substrate has increased

tremendously even though we still see some amount of spacing in between the cluster of the particles. The same is reflected in the I-V characteristics of the film where we see 27 fold decrease in the resistance value from 643.2 GΩ for 1-coat thick film to 24.03 GΩ for 7-coat thick film (Table 3.A.1). However, it can also be concluded that even after the complete coverage of the substrate, the resistance value of the 7-coat thick film is very high which shows that particles are not actually in contact as they appear to be. The AFM image of the same film (Figure 3.A.10B) also confirms the same observation as has been concluded from the SEM image. Thus, the 7-coat thick film was annealed by simple heat

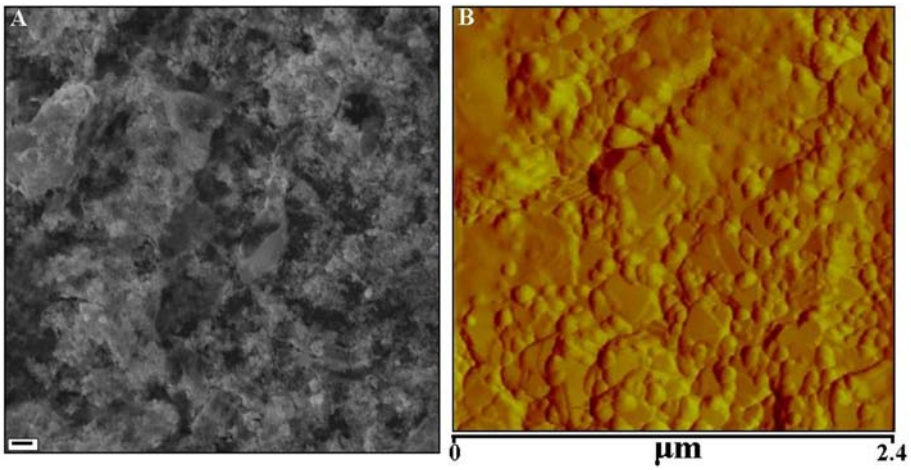

Figure 3.A.10 *(A) SEM micrograph of the 7-coat thick film of purified gold nanoparticle solution. The scale bar corresponds to 1 µm. (B) AFM micrograph of the same film taken in contact mode.*

treatment for three cycles at 200°C of 1 hour each. It has been discussed earlier that the film color changes dramatically after the annealing process which has been briefly discussed before (Figure 3.A.5).

When the film was viewed under SEM, we observe that the surface texture of the film changes completely (Figure 3.A.11A) after the third cycle of the heat treatment when compared with the one before the three cycles of heat treatment (Figure 3.A.10A). While the film structure is extremely granular for the as prepared 7-layer film with a considerable percentage of exposed substrate surface, following the heat treatment, the morphology of the gold structures becomes much more uniform and the surface coverage of gold increases dramatically. The AFM image of the same film (Figure 3.A.11B) shows the similar feature where we find a very continuous film of gold on the surface. The formation of these continuous gold filaments across the substrate surface is believed to be

responsible for the film becoming conducting after heat treatment. It is also important to note that the film does not show the existence of triangular nanoparticles on the surface of the substrate, unlike in the image of 7-coat thick film before the heat treatment (Figure 3.A.10). Similar observation was also made from the I-V profile of this film where a 9

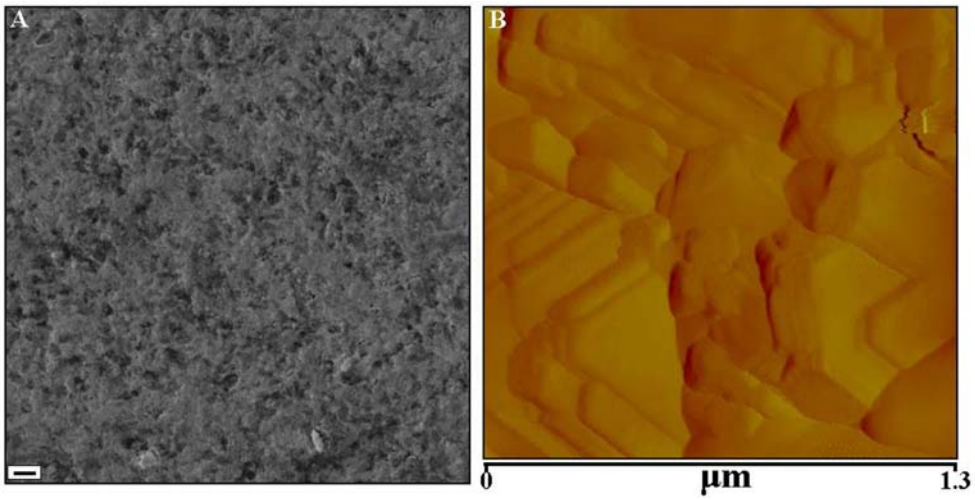

Figure 3.A.11 *(A) SEM micrograph of the 7-coat thick film of purified gold nanoparticle solution after three cycles of heat treatment. The scale bar corresponds to 3µm. (B) AFM micrograph of the same film taken in contact mode.*

orders of magnitude change in the resistance was observed to obtain the final resistance value of 1.2 kΩ (Figure 3.A.7B, curve 2). Thus, the microstructure change in the film after heat treatment is well in agreement with the conductivity data for the film.

3.2.A.3 Electrical measurement of the films in an environment.

3.2.A.3.1 Experimental details.

The film of the purified gold nanoparticle solution was checked for its efficiency to sense chemical vapors. All the vapor sensing experiments were done on the 3-coat thick film of the gold nanoparticles, which was formed by, drop coating. The film was deposited coat by coat on to the quartz substrate and the previous coat was allowed to air-dry completely before the addition of the subsequent coat. The particles density on the surface of the substrate was maintained in the same way as has been described above in section 3.2.A.2.1. The electrical measurements in a controlled environment were done using a closed glass beaker, which had an inlet for the vapors of methanol and chloroform. As a control to this experiment, similar conductivity measurements were also carried out on a 7-layer film of spherical gold nanoparticles prepared by citrate reduction

of 10^{-4} M $HAuCl_4$ solution, which results in nanoparticles of ca. 13 nm diameter. Program written in Test Point was used for time dependent conductivity measurement in an environment to estimate the response time of the film towards the vapor in question. The electrodes were fabricated for the electrical measurement by thermal evaporation of copper pieces in a vacuum coating unit as shown above in the circuit diagram in Figure 3.A.4. As an alternative method, silver paste was used to paint thick pads to function as electrodes upon drying.

3.2.A.3.2 Time dependent conductivity measurement in an environment.

The 3-coat film was challenged with an environment of methanol vapor and the electrical conductivity of the film was measured as a function of time at a fixed voltage of 10 V. Figure 3.A.12A and B show plots of the normalized variation in current in a 3-layer spherical gold nanoparticle film (curve 1 in both figures) as well as a 3-layer triangular gold nanoparticle film (curve 2 in both figures) during exposure to methanol and chloroform vapors respectively (exposures indicated by arrows in the figures). The film current was monitored during exposure to the methanol and chloroform vapors and after their removal from the vapor environment. This current was normalized with respect to the initial current before exposure (I_o) and was then plotted during the different exposure cycles to the vapors. The first observation is that the spherical gold nanoparticle film shows little electrical response to both methanol and chloroform vapor (curve 1 in Figure 3.A.12A and B). On the other hand, exposure of the gold nanotriangle film to methanol results in a rapid and large increase in the normalized conductivity (Figure 3.A.12A).

During the first methanol exposure cycle, the normalized conductivity increases by roughly three orders of magnitude while it is considerably higher at 9 orders of magnitude in the second and third exposure cycles (Figure 3.A.12A). The response time is also excellent and the normalized conductivity rises to 90 % of the peak value within 5 sec of exposure to methanol. It is also gratifying to note that following removal from the methanol vapor, the film conductivity rapidly falls (within 5 sec) to close to the starting conductivity before exposure (Figure 3.A.12A). Similar measurements were done at 0 °C in the ice bath to analyze the effect of measurement temperature on the sensitivity of the gold triangle film towards methanol vapors. We observe that at 0 °C, the film does show an increase in the conductivity when exposed to methanol vapors. However, the increase

is very small and insignificant. Thus, the measurement temperature reduces the sensitivity of the film towards methanol vapors at very low temperatures, which can be attributed to the reduced propensity of the methanol solvent to evaporate at these low temperatures.

In the case of exposure of the gold nanotriangles film to chloroform (Figure 3.A.12B), the normalized conductivity increase is much smaller than that observed for methanol with a mere doubling of the current observed during the third exposure cycle.

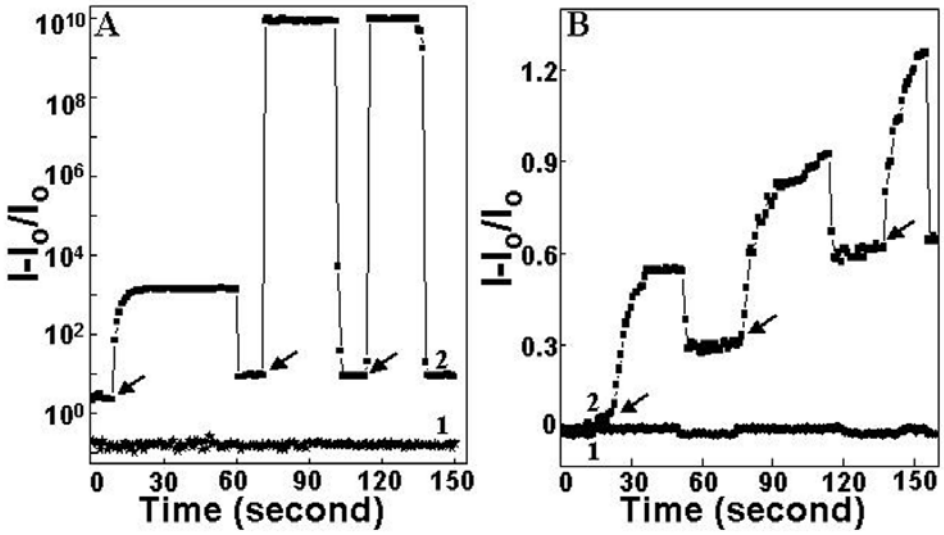

Figure 3.A.12 *(A) Normalized current variation in 3-layer thick films of spherical gold nanoparticles (curve 1) and triangular gold nanoparticles (curve 2) during exposure and removal from methanol vapor. (B) Normalized current variation in 3-layer thick films of spherical gold nanoparticles (curve 1) and triangular gold nanoparticles (curve 2) during exposure and removal from chloroform vapor.*

The response time for the gold nanoparticle film in the chloroform experiment is roughly 10 sec (Figure 3.A.12B) and thus, less rapid than that observed during methanol exposure. We did similar experiments using conducting sliver paste to fabricate the electrodes for conductivity and sensing measurements in order to ascertain that the change in the electrode does not show any change in the conductivity and sensitivity of the film towards these vapors. Also, these films with copper electrodes were stored over a period of couple of month and the sensitivity of the films was monitored towards vapor sensing. We observed that there was no change in the sensitivity of the film over this period. Thus, these films are robust and show consistent sensing response even after long periods of storage. These results indicate that the gold nanotriangles films could be

excellent candidates for the detection of polar organic vapors such as methanol with excellent response and reusability characteristics.

3.2.A.4 Discussion.

As briefly mentioned earlier, electron conduction in both the spherical gold nanoparticle film and in the nanotriangles films would be expected to occur by either electron tunneling or hopping. The observation that the spherical gold nanoparticle film does not show a detectable conductivity change even during exposure to methanol (curve 1, Figure 3.A.12A) clearly indicates that the triangular morphology of the biologically prepared gold particles significantly enhances not only electronic conduction through these films but also their sensitivity to the environment to which the films are exposed. While the reasons for this difference is not understood, we speculate that this may be due to field enhancement effects near the tips of the nanotriangles that could modify the electron tunneling conditions significantly. Presence of the polar vapors in the vicinity of the tips of the gold nanotriangles facilitates better conduction.

It has been observed before that the adsorption of the organic molecules changes the work function of the Au (111) surface by creating interface dipoles at the surface [34,35]. Besides, it has also been reported that physisorption of gas vapors significantly modify the tunneling barrier of the electron conduction by changing the work function of a discontinuous film [36,37]. It has been observed that the adsorption of the electron donor molecule (e.g., ammonia, alcohols, water) on a metal decreases the work function [38]. The result we show above agree with this fact where the adsorption of methanol (electron donor molecule) on to the film of the gold nanotriangles significantly decreases the work function of the nanoparticle film causing a 9-fold increase in the conductivity of the film (Figure 3.A.12A, curve 2). It is important to realize that the gold nanotriangles have been synthesized in a water-based protocol and thus polar solvents will have better propensity to get physisorbed onto the gold nanoparticles as compared to weakly polar and non-polar solvents. Thus, methanol vapors, being highly polar in nature are able to adsorb to the surface of the gold nanotriangles and are thus able to modulate electron conduction through the particle surface resulting in the increased conductivity. On the other hand, chloroform is weakly polar in nature and does not get adsorbed onto the surface of the gold nanotriangles as strongly as methanol.

It is also worth observing that the first exposure of the gold nanotriangle film to methanol gives a three orders magnitude change as oppose to a 9 orders of change on subsequent exposures. Also, the conductivity of the film doesn't revert to the original level on removal of vapor after the first exposure. However, removal of vapors after subsequent exposures does bring the conductivity back to the level after first exposure. This observation indicates that some molecules of methanol in the vapor fail to get desorbed from the gold nanotriangle surface after the removal of the vapor and they eventually facilitate better adsorption of other methanol molecules in the subsequent exposures. So, the first exposure to the methanol vapor results in the wetting of the gold nanoparticle film and thus, subsequent exposures show much high change in the conductivity profile of the film. Since the gold nanotriangle film conductivity returns very closely to the conductivity value measured before exposure (Figure 3.A.12), structural changes in the film leading to the conductivity change may be ruled out (i.e. no variation in the widths of the tunneling barriers). This being the case, the variation in conductivity during exposure to methanol/chloroform is most likely due to a reduction in the tunneling barrier height by the vapor due to the change in the work function of the gold nanoparticle film; this reduction is much more pronounced for polar organic vapors.

3.2.A.5 Summary.

In summary, we have demonstrated a simple method for the fabrication of conductive gold films on to the quartz substrates without any specific surface modification strategies using biologically synthesized gold nanotriangles. The films can be fabricated in any desired pattern by simple masking of the substrate. A mild heat treatment of thick films of the gold nanotriangles results in the formation of a conducting film and thus can be useful in fabricating electrodes of desired pattern. We see a 9-fold drop in the resistance of the film, which is mainly due to the change in the microstructure of the film as revealed by the SEM and AFM analysis. We also show that before the heat treatment of the film, the electron transport in the film occurs by electron tunneling between triangular particles. In this state, the film conductivity is sensitive to the presence of organic vapors such as methanol and relatively insensitive to weakly polar species such as chloroform. Thus, such films can be exciting candidates for future application in detecting polar vapors.

Section B

Fabrication of Ag-Au bimetallic film by transmetallation approach and its application in vapor sensing

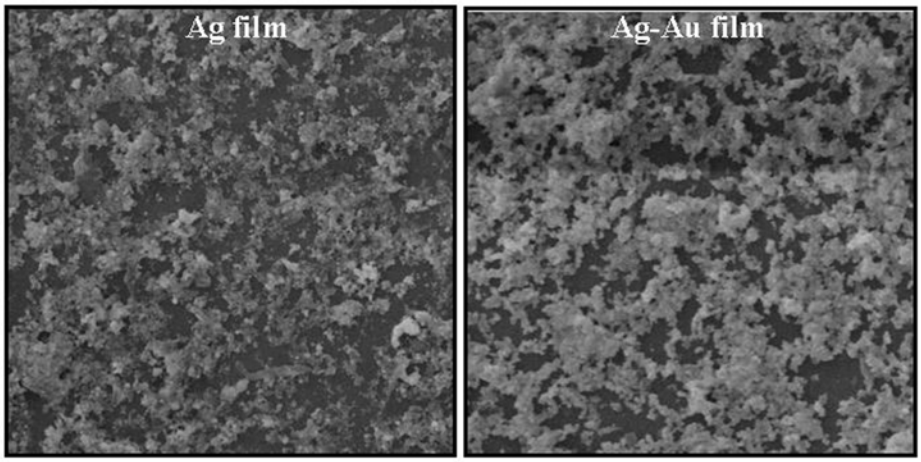

3.2.B.1 Synthesis, characterization and concentration of the tyrosine reduced silver solution.

3.2.B.1.1 Experimental details:

In a typical experiment, 10 mL of 10^{-3} M aqueous silver sulfate solution was taken along with 10 mL of 10^{-3} M aqueous solution of tyrosine and this solution was diluted to 100 mL with deionized water. To this solution, 1 mL of 10^{-1} M solution of KOH was added, and this solution (solution pH -10) was allowed to boil until the colorless solution changed into a yellow solution, indicating the formation of silver nanoparticles. The detail of this protocol has been described elsewhere [39]. Formation of the silver nanoparticles was further confirmed by the UV-vis-NIR and TEM measurements. This solution was then concentrated 10 times by low temperature evaporation of the solvent (water) under vacuum to reach a final concentration of 10^{-3} M of silver in solution, assuming 100% initial reduction. This process of concentration of the silver nanoparticles solution changes the final color of the solution from yellow to brownish yellow, which is due to slight aggregation of the silver nanoparticles upon concentration. It is important to realize that the particles don't tend to aggregate much in the process of concentration because they are prepared by a heating protocol and are found to be stable after boiling at 100ºC for 2-3 minutes. However, some aggregation is bound to take place due to the fact that the volume of the total solvent in the solution is decreased by a factor of 10.

3.2.B.1.2 UV-vis-NIR and TEM measurements:

The UV-vis-NIR spectra of the as prepared tyrosine reduced solution shows a absorption peak at 410 nm which is assigned to the transverse plasmon absorption peak for silver nanoparticles (Figure 3.B.1A, curve 1). However, after concentration of the same solution 10 times its original volume, we do see a shift in the peak, now centered around 427 nm, which clearly indicates that the particles do aggregate in the process (Figure 3.B.1A, curve 2). As above that color of the solution also changes from deep yellow to brownish yellow due to the aggregation of the particles in the concentrated solution. Figure 3.B.1B shows the TEM micrograph corresponding to the as prepared solution of tyrosine-reduced silver. Its can be clearly concluded from the image that we obtain a bimodal distribution of particles in the solution with average particle sizes of 25

and 50 nm. Inset in Figure 3.B.1B shows the higher magnification TEM micrograph of the control tyrosine reduced solution where we can very easily observe the bimodal distribution of the particles. However, to further ascertain this fact, particle size distribution (PSD) analysis was done which clearly showed that the majority of the particles are of the average size of 25 nm (Figure 3.B.1C). However, fair population of

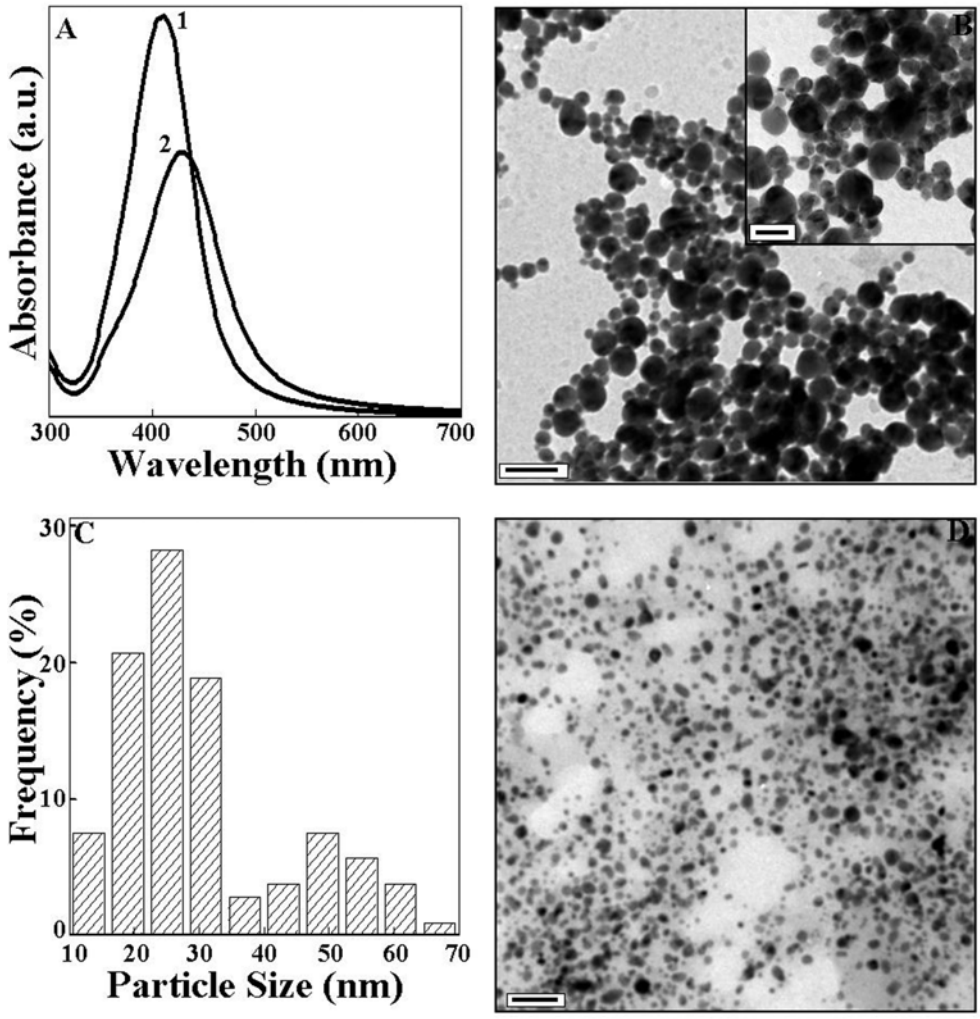

Figure 3.B.1 *(A) UV-vis-NIR spectra of the tyrosine reduced silver solution before (curve 1) and after the concentration (curve 2) process. (B) TEM micrograph of the tyrosine reduced silver nanoparticles at low magnification. Inset shows the high magnification TEM image of the tyrosine reduced silver nanoparticles. (C) Plot showing the particles size distribution of as synthesized tyrosine reduced silver nanoparticles. (D) TEM micrograph of the concentrated solution of the tyrosine reduced silver nanoparticles. The scale bars in B, inset in B and D correspond to 100, 50 and 200 nm respectively.*

the nanoparticles with average size of 50 nm can also be seen from the plot which can be observed from the TEM analysis as well (Figure 3.B.1B). Thus, PSD analysis further

shows that tyrosine reduced silver nanoparticles show bimodal particle size distribution. Figure 3.B.1D shows the low magnification TEM micrograph of the concentrated tyrosine reduced silver nanoparticles and it can be clearly seen in the image that some amount of aggregation does occur in the solution leading to fusion of spherical nanoparticles at several places. This explains the red shift in the transverse absorbance peak in the UV-vis-NIR spectra of the original solution after the process of solution concentration (Figure 3.B.1A). It was this concentrated solution of tyrosine reduced silver nanoparticles that was used to make films onto the quartz substrate.

3.2.B.2 Fabrication of Ag nanoparticle film followed by Ag-Au bimetallic film by transmetallation reaction onto the solid substrate.

3.2.B.2.1 Experimental details:

400 μL of concentrated tyrosine reduced silver nanoparticle solution was coated onto a 3 cm X 1.5 cm thick quartz substrate by drop coating and the film was allowed to air-dry naturally. This process was repeated four times to obtain a fairly uniform coating of the silver nanoparticles onto the glass substrate. This film was characterized by SEM measurements. In order to carry out the process of galvanic replacement onto the solid substrate, 10^{-2}, 5 X 10^{-3}, 10^{-3}, 5 X 10^{-4}, 10^{-4}, 5 X 10^{-5}, 10^{-5}, 10^{-6} and 10^{-7} M concentrations of chloroauric acid ($HAuCl_4$) solutions were added on separate silver nanoparticle films. The TEM analysis was done for some of the concentrations to understand the change in the microstructure of the film with varying concentration of chloroaurate ions. For preparing the TEM sample, the concentrated solution was diluted five times so as to check the formation of a very thick film. Only one layer of silver nanoparticles was coated onto the TEM grid. However, care was taken to keep the constant ratio of the silver to gold, to negate any effect due to change in the ratio. The process of solvent evaporation was slowed down during the process of transmetallation by covering the quartz slides with an inverted beaker so as to facilitate the completion of the reaction. Besides, SEM and EDX analysis was also done for the bimetallic film formed by reacting the 4-coat thick silver film with 10^{-5} M concentration solution of chloroaurate ions.

3.2.B.2.2 TEM measurements:

TEM measurements were done for bimetallic film formed by reacting the silver nanoparticle film with 10^{-3}, 10^{-4} and 10^{-5} M solutions of chloroaurate ions. The control

silver film, when seen under the TEM showed a very dense film of silver nanoparticles on the surface of the grid (Figure 3.B.2A) where-as at some places, the particles were seen to be scattered (Figure 3.B.2B) and well separated. The transmetallation reaction was carried out on this film using 10^{-3} M solution of chloroaurate ions to obtain bimetallic nanostructures on the TEM grid. After the transmetallation reaction, it was observed that the silver particle are interconnected with each other due to the deposition of gold onto the surface (Figure 3.B.2C). The high magnification image (Figure 3.B.2D) of the particles reveal this fact clearly and if observed keenly, it can be seen that these

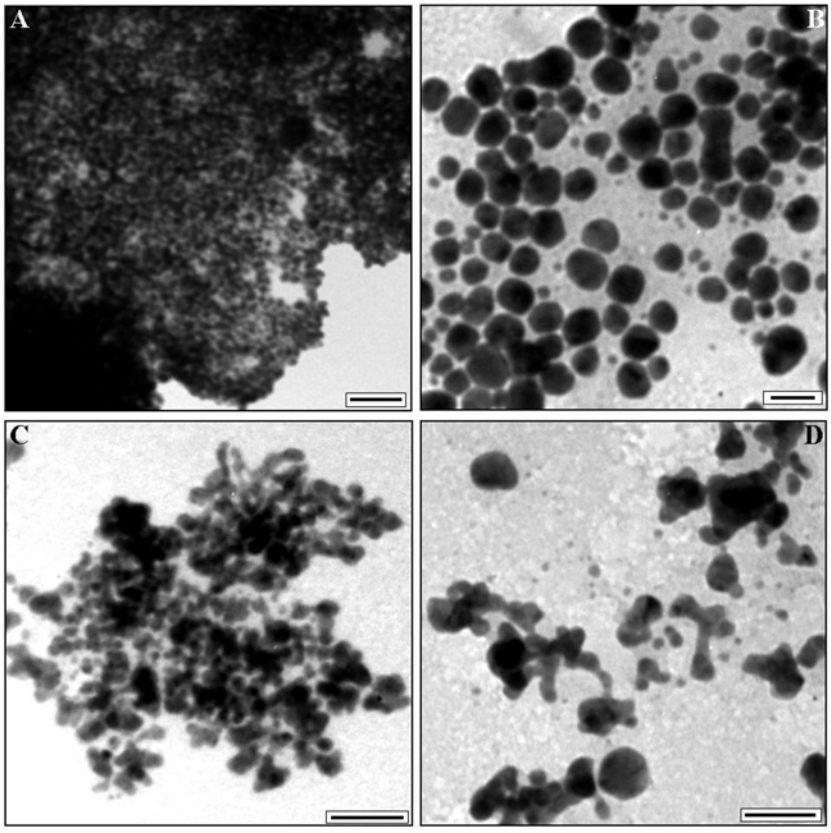

Figure 3.B.2 *(A) TEM micrograph of the 1-coat thick Ag nanoparticle film. (B) High magnification image of 1-coat thick Ag nanoparticle film. (C) TEM image of the tyrosine reduced silver nanoparticles treated with 10^{-3} M solution of chloroauric acid. (D) High magnification TEM micrograph of the tyrosine reduced silver nanoparticles treated with 10^{-3} M solution of chloroauric acid. The scale bars in A,B, C and D correspond to 100, 50, 50 and 50 nm respectively.*

elongated structures are formed due to interconnection between spherical particles and such features are completely absent in the control (Figure 3.B.2A & B). Thus, the

transmetallation reaction indeed takes place onto the surface of the silver nanoparticles, which act as the sacrificial template for the reduction of the chloroaurate ions.

When the same reaction was carried out for the tyrosine reduced silver film using 10^{-4} M solution of chloroauric acid, we observe that flower like structures are formed (Figure 3.B.3A). When the center of growth of these structures was observed carefully, it was concluded that these structures are formed on the spherical nanoparticles as in seed mediated growth. This observation suggests that other than reduction by transmetallation

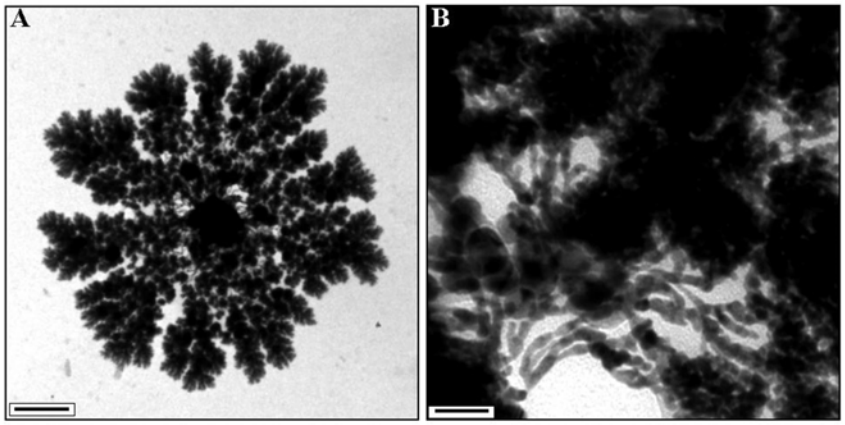

Figure 3.B.3 *(A) TEM image of the tyrosine reduced silver nanoparticles treated with 10^{-4} M solution of chloroauric acid. (B) High magnification TEM micrograph of the tyrosine reduced silver nanoparticles treated with 10^{-4} M solution of chloroauric acid. The scale bars in A and B correspond to 500 & 50 nm respectively.*

reaction, chloroauric acid solution is also reduced by some other reducing agent. It has to be remembered that the synthesis protocol of the formation of tyrosine-reduced silver uses a high concentration (10^{-4} M in final solution) of tyrosine. Thus, there are chances of the presence of some uncoordinated tyrosine molecules, which may reduce chloroaurate ions in solution and thus lead to seed mediated formation of such nanostructures. However, most importantly, we do observe interconnected nanotapes in the high magnification image, which are formed due to the reaction of the chloroaurate ions on the surface of the silver nanoparticles.

The reaction of the silver nanoparticles with the 10^{-5} M solution of chloroaurate ions shows an altogether different morphology. Here, it can be clearly seen that the silver particles have fused together with each other and the TEM image also suggest that the process of reduction of chloroaurate ions has occurred only at the surface of the silver nanoparticle (Figure 3.B.4A). When viewed at higher magnification, the reduction on the

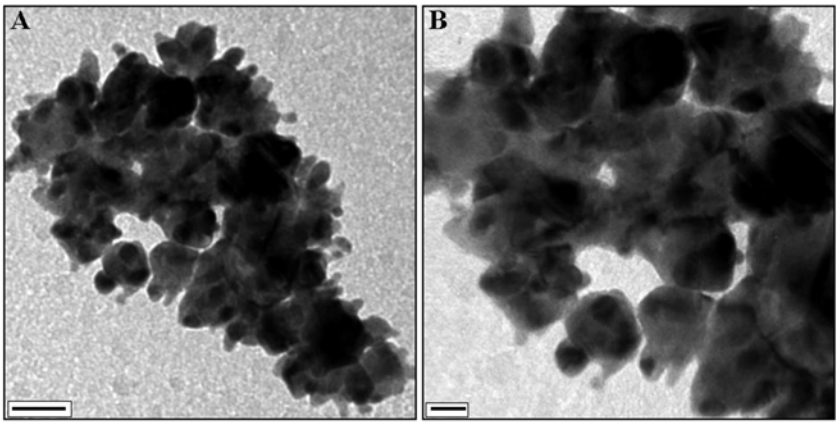

Figure 3.B.4 *(A) TEM image of the tyrosine reduced silver nanoparticles treated with 10^{-5} M solution of chloroauric acid. (B) High magnification TEM micrograph of the tyrosine reduced silver nanoparticles treated with 10^{-5} M solution of chloroauric acid. The scale bars in A and B correspond to 50 & 20 nm respectively.*

surface of the particles and the interconnection between the particles can easily distinguished (Figure 3.B.4B). Thus, at this concentration, the target of reduction of gold nanoparticles on the surface of the silver nanoparticles in order to interconnect silver nanoparticles with each other is achieved.

3.2.B.2.3 SEM and EDX measurements:

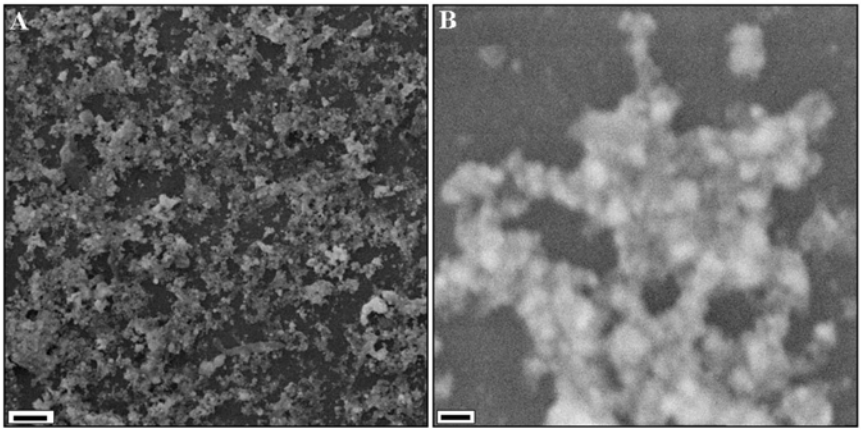

Figure 3.B.5 *(A) SEM image of the 4-coat thick film of concentrated tyrosine reduced silver. (B) High magnification SEM image of the 4-coat thick film of tyrosine reduced silver nanoparticles. The scale bars in A and B correspond to 3 μm and 300 nm respectively.*

Even though the specificity of the transmetallation reaction only at the surface of silver nanoparticles leading to their interconnection by the use of 10^{-5} M concentration of chloroaurate ions could be established from the TEM analysis, the actual picture of the same on the 4-coat thick film on the quartz substrate could not be done by TEM analysis.

Thus, SEM measurements were done for both control silver nanoparticles as well as the Ag-Au bimetallic films, formed by the transmetallation on the quartz substrate, in order to understand the actual microstructure of the film. Figure 3.B.5A shows the low magnification SEM image of the 4-coat thick film of concentrated tyrosine reduced silver nanoparticles. It can be clearly seen that the surface coverage of the substrate is poor and the silver nanoparticles lie on the surface as islands of aggregates with large separation between them. The high magnification image of the film confirms this observation where we see individual silver nanoparticles in the aggregates, which are clustered together (Figure 3.B.5B). This film was then exposed to 400 μL of 10^{-5} M concentration of chloroaurate ions and the film was allowed to air-dry slowly. SEM imaging was done for this film after the reaction with chloroaurate ions.

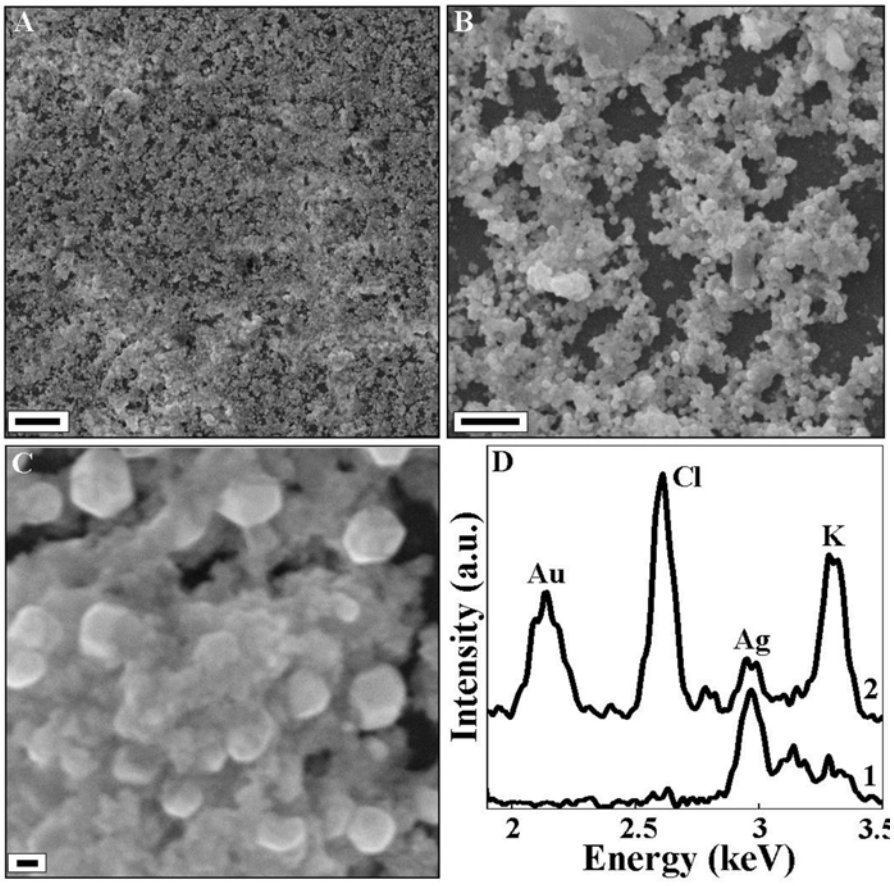

Figure 3.B.6 *(A) SEM image of the 4-coat thick film of concentrated tyrosine reduced silver after treatment with 10^{-5}M solution of chloroaurate ions. (B) High magnification SEM image of the same film. (C) High Magnification SEM image of the same film to particle level resolution. The scale bars in A, B and C correspond to10 μm, 3 μm and 200 nm respectively. (D) EDAX plot of the 4-coat thick silver nanoparticles film (curve 1) and the silver film treated with chloroaurate ions (curve 2).*

Figure 3.B.6A shows the low magnification image of same film after treatment with 10^{-5} M concentration of chloroaurate ions and it can be observed that the surface coverage of the film has improved tremendously after the treatment of the film with chloroaurate ions. When the film was viewed at higher magnification, it can be seen that the voids between the aggregates of particles are still fairly large (Figure 3.B.6B). When the same film was viewed at very high magnifications to observe the particles, we clearly see that the particles have grown in size and are profusely interconnected among themselves (Figure 3.B.6C). The EDX measurement (Figure 3.B.6D) was done for the 4-coat thick film of concentrated tyrosine reduced silver nanoparticles (curve 1) and the same film treated with 10^{-5} M concentration of chloroaurate ions (curve 2) to confirm the chemical composition of the film before and after the treatment with chloroaurate ions. The analysis from the silver film clearly indicates a strong peak of silver while no signature for gold was obtained from it (curve 1). However, the measurement from the same silver film after the treatment with chloroaurate ions clearly reveals a distinct peak of gold while the peak intensity of silver is dampened considerably (curve 2). Besides, the peaks at 2.5 and 3.3 could be assigned to Cl and K, which are contributed from $HAuCl_4$ and KOH respectively.

3.2.B.2.4 XPS measurements:

Figure 3.B.7 shows the XPS measurements performed on the 4-coat thick silver film as well as the bimetallic film prepared by transmetallation using 10^{-5} M concentration of chloroaurate ions. All the core level binding energies (BE) were shifted relative to the C1s BE of 285 eV and the spectra have been background corrected using the Shirley algorithm [40] prior to curve resolution. The Ag $3d_{5/2}$ peak obtained from the silver film was centered at 368.4 eV, which corresponds to Ag (0) oxidation state (Figure 3.B.7A). The most important factor to be considered here is that there is no signature for the presence of Ag^+ ions in the sample. This can be accounted from the fact that the tyrosine reduced silver solution was concentrated to 10 times its original volume by heating and thus, in the process, all the silver ions are expected to reduce at high temperature. On the contrary, the Ag $3d_{5/2}$ peak obtained from the bimetallic film can be deconvoluted into two distinct peaks at 368.04 and 370.2 eV, which correspond to Ag (0) and Ag (I) oxidation states respectively (Figure 3.B.7B) [41]. Thus, the Ag 3d spectrum

obtained from bimetallic film shows the presence of Ag^+ ions in the film which corroborates well with the expectation. During the course of transmetallation reaction, atomic silver is oxidized to Ag^+, thereby reducing gold ions. Thus, this observation itself confirms indirectly that transmetallation does take place when the 4-coat thick silver film

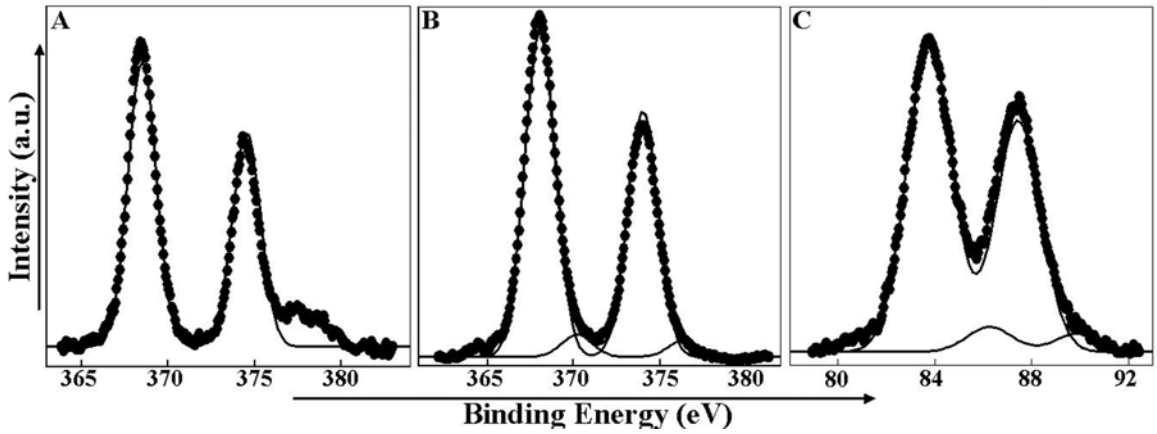

Figure 3.B.7 *(A) Ag3d core level spectra from the 4-coat thick silver film. (B) Ag3d core level spectra from the bimetallic film. (C) Au4f core level spectra from the bimetallic film.*

is exposed to chloroaurate ions. Further more, the presence of an Au $4f_{7/2}$ peak at 83.7 eV clearly shows the presence of Au (0) in the bimetallic film (Figure 3.B.7C). Besides, the Au $4f_{7/2}$ can be deconvoluted into another component at 86.3 eV, which corresponds to Au (I) oxidation state, which is formed due to partial reduction of chloroaurate ions during the process of transmetallation [41]. Thus, the XPS analysis confirms that exposure of the silver film to chloroaurate ions results in the reduction of chloroaurate ions and thus bimetallic film is formed.

3.2.B.3 Electrical conductivity measurements of the bimetallic film.

3.2.B.3.1 Experimental Details:

All the electrical measurements were done using quartz as solid substrate. 4-coat thick film of concentrated solution of tyrosine reduced silver nanoparticles were fabricated as described in section 3.2.B.2.1 and used as control for baseline resistance/conductance measurement. Similar films were then treated with varying concentrations of chloroaurate solution for transmetallation reaction using silver nanoparticles as a sacrificial template. Further, similar work was also done with chloroplatinic acid to confirm the observations made with Ag-Au bimetallic film. Pt (IV)

has a higher reduction potential compared to silver and in principle, Ag (0) should be able to reduce Pt (IV) to Pt (0).

Thick pads of silver paste was painted and allowed to dry for use as electrodes for all the measurement. In order to avoid any contribution from moisture, the film was properly dried under an IR lamp prior to use, all the measurements were redone in desiccators in a moisture free environment and the results were compared for consistency. For the time dependent electrical conductivity measurements in a controlled environment, a closed glass vessel was used with an inlet and outlet for all the vapors. As a control to these measurements, the 4-coat thick concentrated silver nanoparticles film was also challenged with the same vapors for time dependent conductivity measurement at a fixed voltage. A program written in Test Point was used for these time dependent conductivity measurements to estimate the response time of the film towards the vapor in question. The electrodes used for these measurements were fabricated by painting the silver paste at the edges of the film as was done other electrical measurements.

3.2.B.3.2 Electrical measurements:

The electrical conduction property of the films was monitored as a function of exposure to the varying concentration of the chloroaurate ions. The control 4-coat thick film of concentrated silver nanoparticles showed ohmic behavior with a resistance of 25 GΩ, which is very high for metallic nanoparticles (Figure 3.B.8A). However, when the image showing the microstructure of the film is recollected (Figure 3.A.5), the high resistance value for the film seems obvious. The image clearly shows large gaps between the aggregates of silver nanoparticles and thus the conduction across the nanoparticles is by the process of electron tunneling, which is a strong function of the distance between the particles [22]. Thus, the silver nanoparticle film shows a very high value of resistance even after 4-coats of concentrated solution coated on to the surface of the substrate.

The silver nanoparticles film was then treated with varying concentration of chloroaurate ions on the solid substrate, we see a trend in the value of the resistance of the bimetallic film after the reaction. The plot in the Figure 3.B.8B shows the value of the resistance of the bimetallic film with varying concentration of chloroaurate ions. It can be seen from the plot that the resistance of the film goes down with decreasing concentration of chloroaurate ions on the surface, attains a minimum resistance value for the film

treated with 10^{-5} M concentration of chloroaurate ions, which was found to be 8 MΩ and then again starts increasing with further decrease in the gold ion concentration. This is an unusual observation, which corroborates well with the observations made from the microstructure analysis of the bimetallic films. It can be recalled from Section 3.2.B.2.2 that for the higher concentration of the chloroaurate ions on the silver nanoparticle film, the reduction was predominantly by tyrosine and thus, the transmetallation reaction did not take place effectively. However, at lower concentrations, the transmetallation reaction occurs and it can be observed that the reduction is effectively on the surface of the silver nanoparticles, making them larger in size and interconnected to each other (Figure 3.B.4).

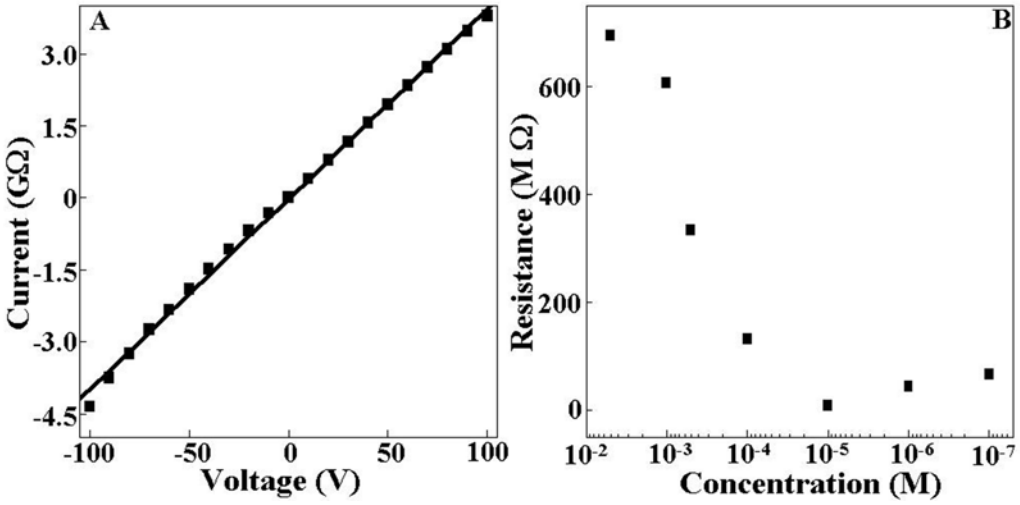

Figure 3.B.8 *(A) I-V curve of the 4-coat thick film of concentrated tyrosine reduced silver nanoparticles. (B) The value of resistances for the 4-coat thick film of concentrated tyrosine reduced silver nanoparticles after treatment with varying concentration of chloroaurate ions.*

The same was confirmed by the SEM analysis, where we clearly see interconnection between the particles in the high-magnification image (Figure 3.B.6C). However, it can be concluded that the resistance of the film is still very high which is understandable due to the fact that the separation between the Ag-Au aggregates is still very large as seen in the SEM image of the same (Figure 3.B.6B) even though the resistance of the bimetallic film had reduced 3000 fold after the transmetallation reaction. Thus, from all the above observations, it can be easily concluded that for carrying out transmetallation reaction on the solid substrate, 10^{-5} M of the chloroaurate ions is suitable for this system.

However, to further confirm this observation, similar experiments were then done using chloroplatinic acid for the transmetallation of Pt (IV) with silver nanoparticles as

sacrificial template. It can be clearly seen from the figure 3.B.9 that the concentrated silver nanoparticle film treated with chloroplatinic acid also shows a similar profile of variation in resistance with change in the concentration. As above, the resistance of the Ag-Pt bimetallic film fell with decreasing concentration of chloroplatinic acid attained a minimum for a concentration of 10^{-5} M (which showed a value of 40 MΩ) and started to rise on further decrease in the Pt ion concentration. There is almost 3 orders of magnitude decrease in the resistance of the Ag-Pt film in comparison with the control concentrated silver nanoparticles film (resistance = 25 GΩ). Thus, it was conclusively shown that the

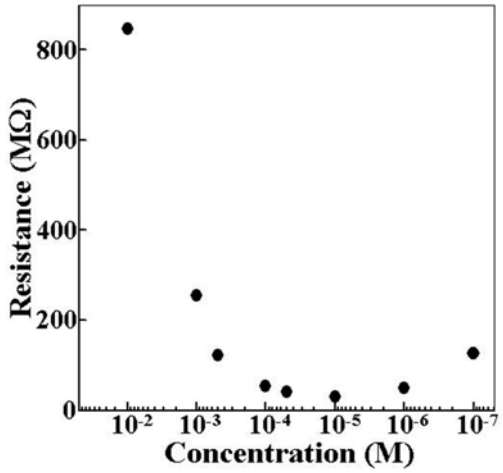

Figure 3.B.9 *The value of resistance for the 4-coat thick film of concentrated tyrosine reduced silver nanoparticles after treatment with varying concentrations of platinum ions.*

interconnection between silver nanoparticles on the surface of the substrate by transmetallation approach was best achieved using 10^{-5} M concentration of the ions of the second metal.

3.2.B.3.3 Temperature dependent conductivity measurement:

The temperature dependent conductivity measurements were done for the 4-coat thick concentrated tyrosine reduced silver nanoparticles film as well as the transmetallation film made by reacting the silver film with 10^{-5} M chloroaurate ions. Figure 3.B.10 shows the plot of the ln resistance vs 1/T in Kelvin and it can be seen from the plot that the 4-coat thick film of concentrated silver nanoparticles shows a negative value of temperature coefficient of resistance, which is characteristic for semiconductors. Thus, the measurement clearly indicated that the silver nanoparticles behaves like a semiconductor with activation energy required for electron conduction. Arrhenius-type

activated tunneling model was used to describe the electron conduction through the film where the activation energy could be calculated from the equation 1

$$\sigma(\delta,T) = \sigma_0 (e^{-\beta\delta}).e^{-E_A / k_B.T} \qquad (1)$$

where β is the electron tunneling coefficient in $Å^{-1}$, δ the average interparticle distance, E_A the activation energy and $\sigma_0 e^{-\beta\delta}$ the conductivity at $k_BT >> E_A$ [42]. The straight line fit to the data points gave the slope and the activation energy calculated was found to be 114 meV.

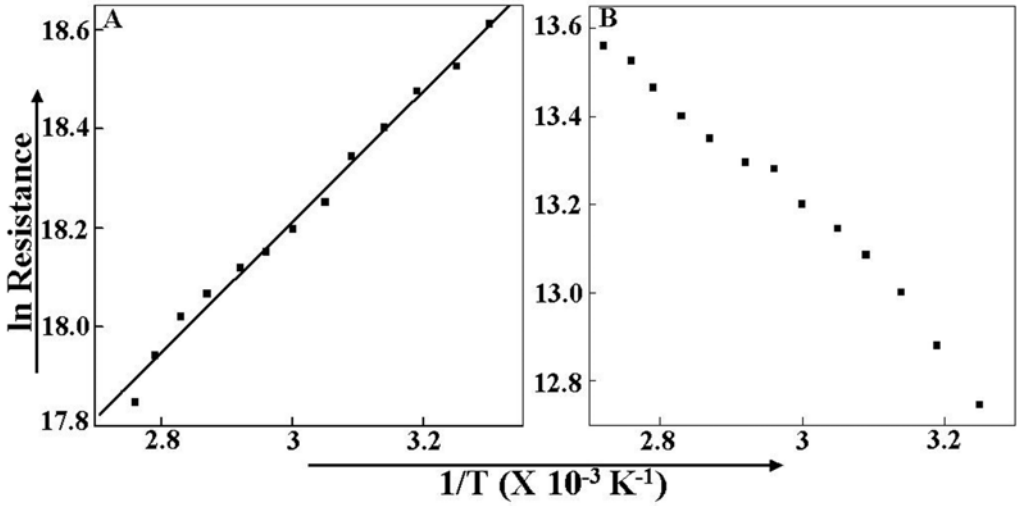

Figure 3.B.10 *Plots showing ln (resistance) vs 1/T curves of, (A) 4-coat thick film of concentrated silver nanoparticles and (B) the same film treated with 10^{-5} M concentration of chloroaurate ions. (Details discussed in the text)*

However, after the 4-coat thick film of concentrated silver nanoparticle film was treated with 10^{-5} M solution of chloroaurate ions, the temperature dependent conductivity results showed an exactly reverse property. The plot in the Figure 3.B.10B shows the ln resistance vs 1/T plot for the Ag-Au bimetallic film and reveals that with the increasing temperature, the conductivity of the film decreases. The positive value of TCR is a characteristic property of metals where we observe a similar feature and thus it can be concluded from this observation that the transmetallation reaction renders the Ag-Au film metallic in nature as oppose to the semiconducting film of silver nanoparticles to start with. Thus, as inferred from the I-V measurements, the transmetallation reaction does interconnect silver nanoparticles on the substrate and facilitate electron conduction leading to the change in the nature of the film.

3.2.B.3.4 Time dependent conductivity measurement in presence of ammonia vapor:

The microstructure of the film gave an indication of availability of a huge volume of space between the interconnected structures in the Ag-Au bimetallic film, which makes them an ideal candidate for applications in chemical vapor sensing. The films were thus checked for their application in chemical vapor sensing by performing electrical measurements in an environment of vapors of different gases. Figure 3.B.11A shows the I-V measurements of the film Ag-Au film, in sweep mode within a voltage range and finite step size, before (curve 1), during (curve 2) and after (curve 3) exposure to the ammonia vapors. The nature of the various curves themselves indicate that in the presence of the ammonia vapor in the environment, the conductivity of the Ag-Au films changes and show several fold increase. The most important feature to note from this measurement is that the conductivity of the film returns to the original value after the gas is removed from the environment (curves 1 and 3). This proves that the electrical response of the Ag-Au film in the presence of ammonia vapors is reversible in nature and that the gas is physisorbed onto the nanoparticle surface. It is also noteworthy that the film has not been exposed to any type of treatment to facilitate desorption of the ammonia gas from the surface and that the process is spontaneous at room temperature.

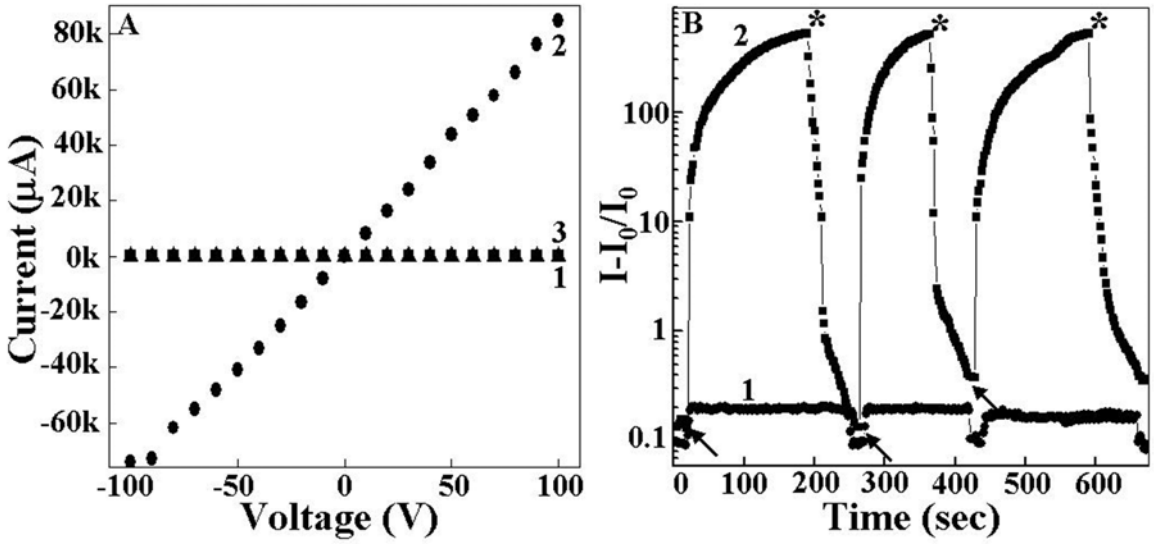

Figure 3.B.11 (A) *Plots showing change in conductivity of the Ag-Au (10^{-5} M) film before (curve 1), during (curve 2) and after exposure (curve 3) to the ammonia vapors. (B) Plots showing the normalized current vs time plot in the presence of ammonia vapor, for the 4-coat thick film of concentrated silver nanoparticles film (curve 1) and Ag-Au film (curve 2) formed by treatment with 10^{-5} M solution of chloroaurate ions.*

Figure 3.B.11B shows the time dependent change in the conductivity of the 4-coat thick concentrated silver nanoparticles film (curve 1) and the film treated with 10^{-5} M concentration of chloroaurate ions (curve 2). The symbol (→) indicates the time at which the pulse of the vapor was injected into the closed chamber while the symbol (∗) shows the point of evacuation of the ammonia vapors. The Ag-Au film shows more than 3 orders of magnitude increase in the conductivity when exposed to the ammonia vapor and it can also be appreciated that the change is very rapid and reversible. This further confirms the observation made by the I-V plot of the same film with and without ammonia vapors where we observed a similar behavior (Figure 3.B.11A). Most importantly, the decrease in the conductivity of the film is very rapid on the removal of the ammonia vapors from the measurement chamber, which reconfirms that the ammonia molecules are weakly physisorbed on the surface of the nanoparticles. It can also be observed that the response is consistent up to 3 cycles of exposure of the film to the vapor and thus indicates that the film is reusable for several exposure to the ammonia vapor. 90 % of the total increase in the conductivity was achieved within 20 seconds of exposure indicating the quick response time of the film towards the vapor. As a control to this experiment, 4-coat thick silver film was also challenged with ammonia vapor in similar conditions and we see only a 2-fold increase in the conductivity of the film, thus confirming that the bimetallic film performs much better than the silver film.

Concentration of $HAuCl_4$	Normalized Resistance Change$(R-R_0/R_0)$
10^{-3}M	69260
5X10^{-4}M	9820
10^{-4}M	4409
10^{-5}M	3400
10^{-6}M	2240
10^{-7}M	370
Silver Control	2-3

Table 3.B.1 *The change in the normalized resistance of the Ag-Au film, prepared by varying amount of chloroaurate ions, on exposure to the ammonia vapor.*

The table 3.B.1 shows the variation in the resistance value of the Ag-Au film when they are exposed to ammonia vapor, as a function of the concentration of the chloroaurate ions used to treat 4-coat thick film of concentrated silver nanoparticles film. The numbers show a decreasing trend with decreasing concentration of the chloroaurate ions which clearly shows that the extent of transmetallation if an important factor for detection of the ammonia gas and at concentration of the gold on the surface, the response is at least 2 orders of magnitude better than for the control silver film. At very low concentrations of the gold ions, the process of transmetallation will be very limited due to limiting availability of gold ions. Thus, the degree of interconnection and formation of irregular surface structures is small for the low concentration treatment with chloroaurate ions. This can be better co-related with the TEM measurements which have been discussed in Section 3.2.B.2.2 and specially the Figure 3.B.4 where it can be clearly seen in the higher magnification image that the silver nanoparticles show a rough outgrowth on its surface after treatment with 10^{-5} M concentration of chloroaurate ions. Thus, the values from the table clearly show that the bimetallic structures adsorb gas better due to increased surface deformities created by the transmetallation and thus show a greater change in the resistance value on exposure to the ammonia vapor.

3.2.B.3.5 Time dependent conductivity measurement in presence of CO_2 vapor:

The Ag-Au film was further challenged with carbon di-oxide gas, which is an important component of our atmosphere and is the major cause of global warming. Besides, it is harmful to human health and thus, its monitoring becomes all the more important. Figure 3.B.12A shows the I-V characteristic of the Ag-Au film, prepared by treating the 4-coat thick film of concentrated silver nanoparticles film with 10^{-5} M concentration of chloroaurate ions, before (curve 1), during (curve 2) and after (curve 3) the exposure to the CO_2 gas. It can be clearly observed from the nature of the curves that the film is ohmic for all the three measurements and here as well, on the exposure to the gas, the conductivity of the film goes up several orders of magnitude.

The time dependent conductivity of the film in the presence of CO_2 gas was done to see the response time and the reusability of the silver film (curve 1) as well as the Ag-Au bimetallic film (Figure 3.B.12, curve 2). The symbol ($\rightarrow$) in the plot shows the point of exposure of the film to the CO_2 vapor while the symbol ($*$) signifies the time point

when the gas was removed. It can be seen from the plot that the Ag-Au film shows a quick response to the presence of vapor with 3300-fold increase in the conductivity in the presence of the vapor. 90% of total change in the conductivity was achieved within 20 s

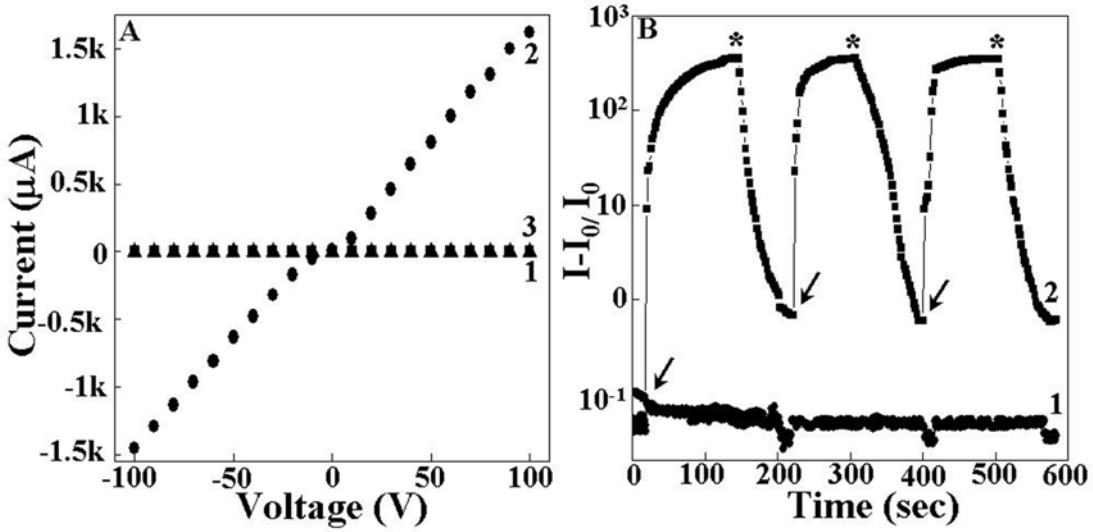

Figure 3.B.12 (A) *I-V plots showing change in conductivity of the Ag-Au (10^{-5} M) film before (curve 1), during (curve 2) and after exposure (curve 3) to the CO_2 vapors. (B) Plot showing the normalized current vs time plot in the presence of CO_2 vapor, for the 4-coat thick film of concentrated silver nanoparticles film (curve 1) and Ag-Au film (curve 2) formed by treatment with 10^{-5} M solution of chloroaurate ions.*

of exposure of the to the film. However, one observation worth mentioning is that the conductivity of the Ag-Au film does not revert back to the starting value when the gas is removed from the environment which suggests that some amount of the CO_2 gas remains adsorbed on the surface of the film even after the removal of vapors. It can also be seen that on the subsequent exposures of the film to the gas, the conductivity come all the way back to the value it had come after the first exposure, clearly suggesting that the residual gas on the surface is chemically and irreversibly bounded to the surface of the film. This feature is present in the I-V measurement in the presence of the gas too (Figure 3.B.12A) where the curve 1 & 3 do not exactly overlap, however, due to length of the scale, the information is not obvious.

It is important to mention that the film has not been given any treatment to desorb the physisorbed gas from the surface and all the measurements were done at room temperature. Besides, to eliminate any contribution from the moisture in the environment, the experiments were also performed in a dessicator in moisture free conditions and

similar results were obtained. However, the silver film (curve 1) shows a very small response of around 7-8 times on exposure to the gas, which again indicates that the bimetallic film has much better sensitivity to adsorb the gas on its surface rather than the plain silver film. Table 3.B.2 shows the change in the resistance of the bimetallic film on exposure to carbon di-oxide vapor as a function of the concentration of the gold ions and

Concentration of $HAuCl_4$	Normalized Resistance Change$(R-R_0/R_0)$
$10^{-4}M$	7055
$10^{-5}M$	3605
$10^{-6}M$	3300
$10^{-7}M$	2910
Silver Control	8

Table 3.B.2 *Change in the normalized resistance of the Ag-Au film, prepared by varying amount of chloroaurate ions, on exposure to the CO_2 vapor.*

it can be seen that the total change in the response of the film decreases with decreasing concentration. This again confirms the fact that extent of the transmetallation on the substrate's surface determines the sensitivity of the film and the fact that bimetallic film show much more propensity to adsorb the gas on the surface which might be due to the formation of the surface deformities due to the process of transmetallation. Thus, with higher concentrations of the chloroaurate ions being used for the fabrication of film, such surface features will be much more pronounced.

3.2.B.4 Discussion.

As it has been discussed in Section 3.2.A.4 of this chapter, the electrical conduction in such discontinuous films are primarily due to electron tunneling [22] which is a strong function of the bias voltage, separation between the particles [40] and the environment of the system [35]. Here, it has been observed that the initial resistance of the 4-coat thick tyrosine reduced concentrated nanoparticles film shows a very high resistance of 25.02 GΩ which could be decreased by more than 3 orders of magnitude by carrying out transmetallation on the surface of the silver nanoparticles by simple galvanic

replacement reaction. This leads to increase in the size of the particles, thereby decreasing the interparticle separation, and forming interconnects between them to facilitate easier conduction of electron. Thus, it has been shown that using optimum concentration of gold ions, films of varying resistance can be obtained. Besides, it was also seen from the temperature dependent electrical measurements that the silver film, which was semiconductor in nature, showing a negative TCR, becomes metallic in nature after the transmetallation reaction.

It has been shown previously in our lab that during the process of controlled galvanic reaction, gold is deposited on the surface of silver nanoparticles while the silver is leached out in the ionic form. This leads to a sequence of interesting nanostructures that are formed starting from porous bimetallic nanoparticles to hollow gold spheres to solid gold nanoparticles at the end of the reaction [43]. It was also seen here that during the process of the galvanic replacement on the silver nanoparticle surface, the earlier smooth surface of the nanoparticles are highly roughened and uneven. In the process, we obtain particles that have a highly uneven surface. This property was then exploited by exposing the Ag-Au film with ammonia and CO_2 gas and it was found that the Ag-Au bimetallic film shows excellent response to both the vapors by virtue of an increase in the conductivity of the film. It has been discussed in the section 3.2.A.4 that the work function of the discontinuous film is a strong function of the environment and it has been shown that the presence of the electron-donor groups on the surface decrease the work function of the film; thus increasing the conductivity [38]. In this case as well, ammonia and CO_2, both have atoms (N & O respectively), which have lone pairs and thus can donate electron. The conductivity results, which were performed in the environment containing these gases, also show the same result and thus, the practical observation corroborates well with the expected behavior of the films.

It has also been shown that the silver film shows a very small change in the conductivity when the same experiment was done, but there as well, we see and enhanced conductivity. Also, it was observed that the magnitude of change in the conductivity of the bimetallic film is a function of amount of the gold present in the film, which indirectly is the extent of the galvanic replacement reaction taken place. The films were also checked for their response time to the two vapors and it was found that the response

is quick and reversible and thus the films can be reused. In order to eliminate any possibility of change in the conductivity due to moisture content, the film was completely dried under IR-lamp and the measurements were carried out in a dessicator under a moisture free environment. However, we obtained consistent results.

3.2.B.5 Summary.

To summarize, we show that transmetallation reaction is an attractive route to fabricate porous bimetallic film on solid substrates, which finds promising application in the sensitive detection of chemical vapors. In the present work, we exploit Ag-Au bimetallic film to show that they can be used for sensing ammonia and CO_2 vapors. The response is observed in the form of an enhanced conductivity of the bimetallic film in the presence of the vapor in the environment. The control silver nanoparticles film does not show similar magnitude of response and thus, it has been shown that the bimetallic film can be an exciting option for fabrication of sensors to these chemical vapors.

3.3 Conclusions.

In conclusion, this chapter has been devoted to the use of metal nanoparticles to fabricate thin films on the surface of a solid substrate. The approach, which has been undertaken, is simple and does not involve any surface modification protocol for the substrate. The films have been made by simple drop coating of the concentrated aqueous solution of the nanoparticles on to a clean substrate followed by natural air-drying. The films were found to be very robust and were then used to investigate their potential application in chemical vapor sensing. The electrical properties of the films have been measured and the response to the changed environment was obtained in the form of changed electrical conductivity of the film in the presence of the vapors. In all the cases, the response was found to be very quick and the change in the conductivity was found to be reversible in nature, which clearly indicates that the vapors are not actually adsorbed on the surface of the nanoparticles by any kind of chemical bonding, rather its pure physisorption. Thus, we show that such metal nanoparticle films on solid substrate can be a promising candidate to design chemical vapor sensors of the future.

3.4 References.

1) (a) Norman Jr., T.J.; Grant, C.D.; Magana, D.; Zhang, J.Z.; Liu, J.; Cao, D.; Bridges, F. and Buuren, A.V. *J. Phys. Chem. B* **2002**, *106*, 7005. (b) Mulvaney, P. *Langmuir*

1996, *12*, 788 (c) Ung, T.; Liz-Marzan, L.M. and Mulvaney, P. *Colloids and Surfaces A : Physicochem. Eng. Aspects* **2002**, *202*, 119.

2) (a) Wessels, J.M.; Nothofer, H.; Ford, W.E.; von Wrochem, F.; Scholz, F.; Vossmeyer, T.; Schroedter, A.; Weller, H. and Yasuda, A. *J. Am. Chem. Soc*. **2004**, *126*, 3349. (b) Schmid, G. and Simon, U. *Chem Commun.* **2005**, 697. (c) Fishelson, N.; Shkrob, I.; Lev, O.; Gun, J. and Modestov, A.D. *Langmuir* **2001**, *17*, 403.
3) Jin, Y.; Kang, X.; Song, Y.; Zhang, B.; Cheng, G. and Dong, S. *Anal. Chem.* **2001**, *73*, 2843.
4) (a) Grabar, K.C.; Freeman, R.G.; Hommer, M.B. and Natan, M.J. *Anal. Chem.* **1995**, *67*, 735 (b) Li, X.; Xu, W.; Zhang, J.; Jia, H.; Yang, B.; Zhao, B.; Li, B. and Ozaki, Y. *Langmuir* **2004**, *20*, 1298.
5) (a) Jeon, N.L.; Uzzo, R.G.; Xia, Y.; Mrksich, M. and Whitesides, G.M. *Langmuir* **1995**, *11*, 3024 (b) Potochnik, S.J.; Pehrsson, P.E.; Hsu, D.S.Y. and Calvert, J.M. *Langmuir* **1995**, *11*, 1841.
6) (a) Cao, Y.C.; Jin, R. and Mirkin, C.A. *Science* **2002**, *297*, 1536 (b) Niemeyer, C.M. *Angew. Chem. Int. Ed.* **2001**, *40*, 4128 (c) Kamat, P.V. *J. Phys. Chem. B.* **2002**, *106***,** 7729 (d) Shenton, W.; Davis, S.A. and Mann, S. *Adv. Mater*. 1999, *11*, 449.
7) (a) Osterloh, F.; Hiramatsu, H.; Porter, R. and Guo, T. *Langmuir* **2004**, *20*, 5553 (b) Murray, B.J.; Walter, E.C. and Penner, R.M. *Nano Lett.* **2004**, *4*, 665 (c) Du, X.; Wang, Y.; Mu, Y.; Gui, L.; Wang, P. and Tang, Y. *Chem. Mater.* **2002**, *14*, 3953.
8) Musick, M.D.; Keating, C.D.; Keefe, M.H. and Natan, M.J. *Chem. Mater.* **1997**, *9*, 1499.
9) Brown, K.R.L.; Lyon, A.; Fox, A.P.; Reiss, B.D. and Natan, M.J. *Chem. Mater.* **2000**, *12*, 314.
10) Doron, A.; Katz, E. and Willner, I. *Langmuir* **1995**, *11*, 1313.
11) (a) Dressick, W.J.; Dulcey, C.S.; Georger Jr, J.H. and Calvert, J.M. *Chem. Mater*. **1993**, *5*, 148. (b) Vargo, T.G.; Gardella Jr, J.A.; Calvert, J.M. and Chen, M.S. *Science* **1993**, *262*, 1711.
12) Blaaderen, A.V.; Ruel, R. and Wiltzius, P. *Nature* **1997**, *385*, 321.

13) (a) Decher, G *Science* **1997**, *277*, 1232 (b) Zheng, H.; Lee, I.; Rubner, M.F. and Hammond, P.T. *Ad*v. *Mater*. **2002**, *14*, 569 (c) Hua, F.; Shi, J.; Lvov, Y. and Cui, T. *Nano Lett.* **2002**, *2*, 1219.

14) (a) Ye, Y.H.; LeBlanc, F.; Hache, A. and Truong, V. *Appl. Phys. Lett*. **2001**,*78*, 52 (b) Zhang, J.; Alsayed, A.; Lin, K.H..; Sanyal, S.; Zhang, F.; Pao, W.J.; Balagurusamy, V.S.; Heiney, P.A. and Yoah, A.G. *Appl. Phys. Lett.* **2002,** *81*, 3176 (c) Prevo, B.G.; Fuller III, J.C. and Velev, O.D. *Chem. Mater.* **2005**, *17*, 28.

15) (a) Yin, Y.; Lu, Y.; Gates, B. and Xia, Y. *J. Am. Chem. Soc.* **2001**, *123*, 8718 (b) Yang, S.M. and Ozin, G.A. *Chem. Commun.***2000**, 2507.

16) (a) Xiao, Y.; Patolsky, F.; Katz, E.; Hainfeld, J.F. and Willner, I. *Science* **2003**, *299*, 1877 (b) Wang, J.; Xu, D.; Kawde, A. and Polsky, R. *Anal. Chem.* **2001**, *73*, 5576.

17) Krasteva, N.; Besnard, I.; Guse, B.; Bauer, R.E.; Müllen, K.; Yasuda, A. and Vossmeyer, T. *Nano Lett.* **2002**, *2*, 551.

18) Ahn, H.; Chandekar, A.; Kang, B.; Sung, C.; Whitten, J.E. *Chem. Mater.* **2004**, *16*, 3274.

19) Briglin, S.M.; Gao, T.; Lewis N.S. *Langmuir* **2004**, *20*, 299.

20) Kim, Y.; Johnson, R.C.; Hupp J.T. *Nano Lett.* **2001**, *1*, 165-167.

21) Zamborini, F.P.; Leopold, M.C.; Hicks, J.F.; Kulesza, P.J.; Malik, M.A.; Murray, R.W. *J. Am. Chem. Soc.* **2002**, *124*, 8958.

22) Hill, R.M. *Proc. Roy. Soc. A*, **1969**, *309*, 377.

23) Wohltjen, H.; Snow, A.W. *Anal. Chem.* **1998**, *70*, 2856.

24) Wuelfing, W.P.; Green, S.J.; Pietron, J.J.; Cliffel, D.E.; Murray, R.W. *J. Am. Chem. Soc.* **2000**, *122*, 11465.

25) Shankar, S.S.; Rai, A.; Ankamwar, B.; Singh, A.; Ahmad, A. and Sastry, M. *Nature Mater.* **2004**, *3*, 482.

26) Shankar, S.S.; Rai, A.; Ahmad, A. and Sastry, M. *Chem. Mater.* **2005**, *17*, 566.

27) Rai, A.; Singh, A.; Ahmad, A. and Sastry, M. *Langmuir*, **2006**, *22*, 736.

28) Liang, H.P.; Zhang, H.M.; Hu, J.S.; Guo, Y.G.; Wan L.J.; Bai, C.L. *Angew. Chem., Int. Ed.*, **2004**, *43*, 1540.

29) Liang, H.P.; Guo, Y.G.; Zhang, H.M.; Hu, J.S.; Wan L.J.; Bai, C.L. *Chem. Commun.* **2004**, 1496.

30) (a) Sun, Y.; Xia, Y. *J. Am. Chem. Soc.* **2004**, *126*, 3892 (b) Sun, Y.; Mayers, B. T.; Xia, Y. *Adv. Mater.* **2003**, *15*, 641 (c) Sun, Y.; Xia, Y. *Nano Lett.* **2003**, *3*, 1569 (d) Jin, Y.; Dong, S. *J. Phys. Chem. B* **2003,** *107*, 12902 (e) Sun, Y.; Mayers, B.T.; Xia, Y. *Nano Lett.* **2002**, *2*, 481 (f) Chen, J.; Saeki, F.; Wiley, B.J.; Cang, H.; Cobb, M.J.; Li, Z.Y.; Au, L.; Zhang, H.; Kimmey, M.B.; Li, X.D.; Xia, Y. *Nano Lett.* **2005**, *5*, 473.

31) Selvakannan, PR.; Sastry, M. *Chem. Commun.* **2005**, 1684.

32) (a) Germain, V.; Li, J.; Ingert, D.; Wang, Z.L.; Pileni, M.P. *J. Phys. Chem. B* **2003**, *107*, 8717 (b) Salzemann, C.; Lisiecki, I.; Urban, J.; Pileni, M.P. *Langmuir* **2004**, *20*, 11772.

33) Kelly, K.L.; Coronado, E.; Zhao, L.L.; Schatz, G.C. *J. Phys. Chem. B* **2003**, *107*, 668.

34) Crispin, X.; Geskin, V.; Crispin, A.; Cornil, J.; Lazzaroni, R.; Salaneck, W.R.; Brédas J. *J. Am. Chem. Soc.* **2002**, *124*, 8131.

35) De Renzi, V.; Rousseau, R.; Marchetto, D.; Biagi, R.; Scandolo, S.; del Pennino, U. *Phys. Rev. Lett.* **2005**, *95*, 46804.

36) Grigor'ev, E.I.; Vorontsov, P.S.; Zav'yalov, S.A.; Chvalun, S.N. *Tech. Phys. Lett.* **2002**, *28*, 845.

37) Wilker, S.; Henning, D.; Lober, R. *Phys. Rev. B* **1994**, *50*, 2548.

38) Asscher, M.; Rosenzweig, Z. *J. Vac. Sci. Technol. A* **1991**, *9*, 1913.

39) Selvakannan, PR.; Swami, A.; Srisathiyanarayanan, D.; Shirude, P.S.; Pasricha, R.; Mandale, A. B.; Sastry, M. *Langmuir* **2004**, *20*, 7825.

40) Shirley, D. A. *Phys. Rev. B.* **1972**, 5, 4709.

41) Wagner, C.D; Riggs, W.M.; Davis, L.E.; Moulder, J.F.; Muilenberg, G.E. *Handbook of X-ray photoemission spectroscopy, Perkin Elmer Corp. Publishers, Eden Prairie*, MN, **1979**.

42) (a) Wuelfing, W.P.; Murray, R.W. *J. Phys. Chem. B* **2002**, *106*, 3139. (b) Wessels, J.M.; Nothofer, H.G.; Ford, W.E.; Wrochem, F.V.; Scholz, F.; Vossmeyer, T.; Schroedter, A.; Weller, H.; Yasuda, A. *J. Am. Chem. Soc.* **2004**, *126*, 3349.

43) Shukla, S.; Priscilla, A.; Banerjee, M.; Bhonde, R.R.; Ghatak, J.; Satyam, P.V.; Sastry, M. *Chem. Mater.* **2005**, *17*, 5000.

Chapter IV

Metal nanoparticles on a soft scaffold for sensing applications

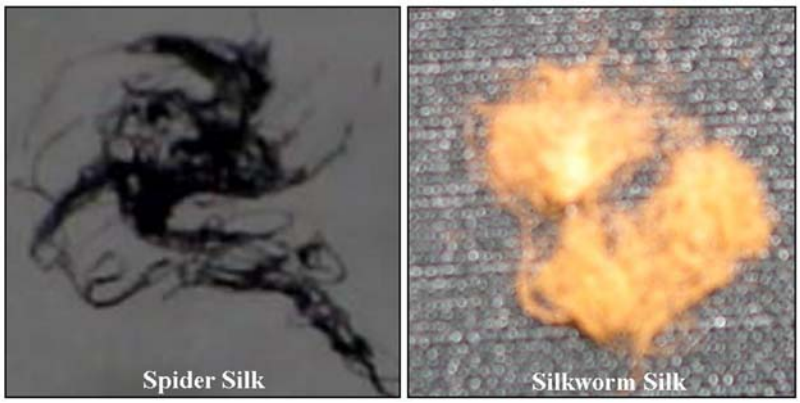

Spider and silkworm silks are well known natural biopolymer which are primarily composed of amino acids polypeptide chain. This chapter shows the use of the these biological templates as active scaffolds for *in situ* reduction of chloroaurate ions on their surface and subsequent immobilization of the formed gold nanoparticles. Amino acids have been shown to independently reduce gold ions in solution and this fact has been exploited in the presented work. Results show a concentration dependent density of decoration of the spider silk with gold nanoparticles on their surface. The electrical conductivity measurements were done thereafter showing that the immobilization of the gold nanoparticles impart electron conduction ability to the otherwise non-conducting spider silk fibers. Besides, based on the prior knowledge that the spider silk shows reversible supercontraction in polar environment, it has been shown that the nanogold-spider silk bioconjugate can be used to sense polar vapors with varying degree of response based on the polarity of the solvent. Silkworm silk, which does not show any such ability, have been used to make nanogold-silkworm silk bioconjugate and showed no response on exposure to the polar vapors.

Part of the work presented in this chapter has been published:

1) Singh, A.; Hede, S. and Sastry, M. *Small* **2006** (accepted).

4.1 Introduction.

Spider silk, a natural semicrystalline biopolymer, has been of tremendous interest to scientists and researchers across the world due to their unusual mechanical properties [1], high resilience, tensile strength [2] and elasticity [3]. Thus, a number of attempts have been made to understand the structure and composition of spider silk and a recent review article by Lewis [4] gives a good account of our present understanding towards the molecular level complexity of the spider silk protein. Spider silk is basically made up of fibroin protein (M_r ~ 200,000-300,000) which in turn is composed of two proteins namely spidroin I and spidroin II [5]. These proteins are primarily composed of 42% glycine and 25% alanine as major amino acids. It has been shown that the backbone of the fiber, in a simplified manner, can be viewed as a block co-polymer with poly-Ala blocks (approximately 8 monomers) and Gly-rich domain (24-35 monomers), with Gly-Gly-X as most rich motif in spidroin I [5]. When fibroins are spun into fibers, the poly-alanine blocks form the β-sheet crystals that cross links the fibroins into a polymer network imparting stiffness, strength and toughness to the fiber [1b]. Spiders make silk of different types, numbers, composition and properties depending on the species, diet, environment and the metabolic status [6]. Being a natural polymer with unusual strength, primary research on spider silk has mainly been focused on studying its mechanical properties and it has been viewed as a promising candidate for making lightweight composite materials [7]. Several attempts have been made towards using genetic manipulations to alter the composition of the silk in order to improve upon the mechanical properties of the fiber [8].

However, one area which has not been exploited till date to its full potential is the use of the spider silk fibers as a template for immobilizing and patterning inorganic nanostructures, which could generate a new class of composite materials with multifunctionality, exploiting the mechanical property of silk fiber and the surface chemistry of the nanomaterials. One of the first attempts towards achieving this goal was made by Mayes, Vollrath and Mann where they showed that the *Nephila edulis* spider silk is an excellent template for immobilization of magnetite particles on the surface without any apparent change in the mechanical property of the spider silk [9]. Huang *et al* have used the spider silk as a template to form hierarchically ordered hollow mesoporous

silica fibers by removing the template by calcination after the immobilization of the silica particles [10]. In another interesting report, He and Kunitake have combined a sol-gel process with silk threads in achieving porous filaments of titania and zirconia after removal of the template and thereafter, use of these nanoporous filaments in the entrapment of gold nanoparticles [11]. However, in all the above attempts, spider silk has been used as a passive template for immobilization of the nanostructures. In the past few years, some endeavors have been made on using the derivatives of silk fibers as an active template for *in situ* reduction and immobilization of nanostructures. In one of the works, Zhou *et al* have used aqueous solution of silk fibroin proteins to reduce gold ions to colloidal gold, which results in the formation of core-shell gold nanoparticles-silk fibroin bioconjugate at room temperature [12]. In a recent report, Foo *et al* have shown an innovative way of preparing nanocomposites of silica and spider silk [13]. They have prepared a bioengineered chimeric fusion protein which consists of two components; first component is R5 peptide of silaffin protein which is known to induce and regulate the precipitation of silica [14] and the second component is self-assembling domain based on the consensus repeat in the major ampullate spidroin protein 1 (MaSp 1) which is known for highly stable β-sheet structure with good mechanical property. Thus, they show that these molecular level manipulations can be an attractive option to fabricate such nanocomposites with exotic properties for various applications.

This chapter of the thesis has been devoted to studying the possibility using spider silk as an active scaffold for the *in situ* reduction of gold ions and immobilization of the thus-formed gold nanoparticles on its surface. It has been previously shown that certain amino acids have the capability of reducing gold ions to form nanoparticles [15] and their subsequent ability to function as capping agents in order to stabilize the surface of the formed nanoparticles by interaction of gold nanoparticles with the amine group of the protein [16]. The known literature on the composition of the spider silk clearly indicates that it is primarily made of proteins, which have amino acids as the building blocks. Thus, in principle, spider silk should be able to reduce gold ions to form gold nanoparticles and immobilize them subsequently on their surface. This rationale has been exploited in the present work to prepare nanogold-spider silk bioconjugate at room temperature without any modification in the composition of the spider silk. Besides, it

has been also shown that this nanogold-spider silk bioconjugate can be used as an excellent candidate for sensing polar solvents with a varying degree of response which was found to be directly related to the polarity of the vapor used. The well-known property of supercontraction [17], which is a hallmark of spider silk, was used here to study the variation in electrical conduction of the nanobioconjugate in the presence of polar vapors [18].

The phenomenon of supercontraction is well known in the spider silk, has extensively been studied in the past [17] and it has been shown that the spider silk tends to reversibly contract in the presence of polar environment [18]. This contraction is primarily due to breaking of the hydrogen bond and re-orientation and coiling of the molecular chain [19]. When viewed at molecular level, all silk have three repetitive sequences- dominant proteins in the major (MaSp1) [20], minor (MiSp1) [21] and cocoon silk of silkworm (*Bombyx mori*) [22]. However, the supercontracting fibers differ from non-supercontracting fibers in mainly two aspects- crystalline region in MaSp1of supercontracting fibers fold into β-sheet with poly (Ala) [23] repeats while other have poly(Gly-Ala). Besides, a significant number of leucine residues are found only in supercontracting fibers and not in non-supercontracting ones. It has also been reported that there is a highly conserved amino acid sequence in supercontracting silk of *Nephila clavipes* but absent in non-supercontracting fibers, which imparts them this property [22]. In the present work, we have used *Pholcus phalangioides* (family Pholcidae) spider silk to modulate the electrical conductivity of the gold nanoparticle sheath surrounding the fibers and thus constructing a polar vapor sensor based on a similar supercontracting property. The nanobioconjugate system shows a varying conductivity response to different polar vapors depending on their relative polarity. As a control to elucidate and confirm that the response of the nanobioconjugate comes from its ability to contract, silkworm silk has been used which does not contract in polar environment [18a]. Its contraction has only been reported in powerful swelling agents such as an aqueous solution saturated with sodium thiocyanate [24] or else an increase in cross-sectional area on wetting with water [25]. Thus, the nanogold-silkworm silk bioconjugate serves as an ideal control to the presented work, which indirectly confirms that any change in the

response of the nanogold-spider silk bioconjugate in the presence of polar vapor would be due to inherent property of the spider silk to supercontract in such an environment.

4.2 Spider/Silkworm silk processing and fabrication of nanobioconjugates.

4.2.1 Experimental Details.

The spider silk was harvested from the spider *Pholcus phalangioides* (family Pholcidae), which was reared in a clean and dust-free environment and fed with houseflies. The web was collected 2 days after its formation and was thoroughly washed with isopropyl alcohol several times along with sonication to remove dust particles from the surface. The cleaned spider web was then allowed to air-dry thoroughly. This was followed by a careful separation of the entangled webs using a fine forceps with special care not to break the web into small pieces. By this method, webs were separated into very fine fibrils. The separated fibers of the spider silk were then treated with 10^{-1} and 10^{-3} M concentrations of aqueous solution of chloroauric acid for 48 hours to facilitate the reduction of chloroaurate ions on the surface of the spider silk. It is important to note that on exposure to the aqueous solution of chloroaurate ions, the separated fine fibrils of spider silk tend to get entangled again within itself, which probably was due to the phenomenon of supercontraction [18]. However, they are again well separated when allowed to dry. The spider silk fibers change their color from buff white (Figure 4.1A) to ruby red after the chloroauric acid treatment, thus confirming the reduction of the chloroaurate ions on their surface (Figure 4.1B). The nanobioconjugate was then washed thoroughly with water so as to remove any unreduced chloroaurate ions or unbound gold nanoparticles.

The nanobioconjugate was then characterized by Scanning Electron Microscopy (SEM), Energy Dispersive Analysis of X-ray (EDAX) and Atomic Force Microscopy (AFM). The bare as well as nanogold-spider silks were carefully lifted onto a Si (111) wafer and were allowed to adhere to the surface using isopropyl alcohol. For the AFM analysis, the spider silk was treated with 1 N HCl solution followed by sonication to separate the fibers into very small sized fibrils, which were picked up on the substrate. In a similar fashion, silkworm silk was also harvested from the cocoon stage of silkworm reared in a clean environment. The silkworm silk was cleaned in isopropyl alcohol and

exposed to 10^{-1} and 10^{-3} M aqueous solution of chloroauric acid. It was observed that the silkworm silk reduces the chloroaurate ions much faster than the spider silk and we observe that the silkworm silk web turns golden-orange in color (Figure 4.1C) unlike spider silk which turns ruby red (Figure 4.1B). It is worth mentioning here that in the case

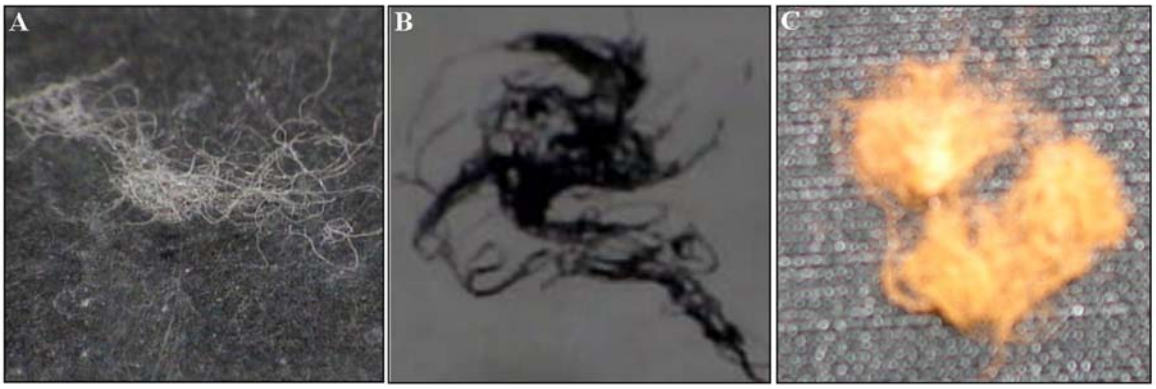

Figure 4.1 *(A) The picture of bare spider silk washed with isopropyl alcohol. (B) The picture of the nanogold-spider silk nanobioconjugate prepared by treatment with 10^{-1} M aqueous solution of chloroauric acid. (C) The picture of the nanogold-silkworm silk nanobioconjugate prepared by treatment with 10^{-1} M aqueous solution of chloroauric acid.*

of silkworm silk, reduction of the chloroaurate ions occur ex-surface as well where it was observed that the chloroauric acid solution, in which the silk worm silk was immersed, turns golden-orange in color. The UV-vis-NIR and TEM analysis of the solution was done to characterized the particles formed in the solution due to reduction by the silkworm silk. This was not observed in the solution where spider silk was immersed and there the reduction of the gold ions was found to be confined only to the surface of the fiber. Simultaneously, cleaned silk fibers were also exposed to an aqueous solution of borohydride reduced gold nanoparticles that yielded similar ruby red colored spider silk fibers. The aqueous solution of borohydride-reduced gold nanoparticles was prepared by reducing aqueous chloroauric acid (10^{-4} M) with sodium borohydride as described earlier [26]. This procedure gives a ruby-red solution containing spherical gold nanoparticles of dimensions 65 ± 7 Å. Spider as well as silkworm silk fibers, which were treated with chloroauric ions or borohydride reduced gold, were washed three times with Milli-Q® water prior to all the measurements.

4.2.2 SEM measurements of bare as well as the nanogold-spider silk bioconjugate.

The bare spider silk as well as the nanogold-spider silk bioconjugate prepared by treatment of clean fibers with 10^{-1} and 10^{-3} M aqueous solution of chloroauric acid were

imaged under SEM to obtain the information about the topology of the samples. Figure 4.2 shows the SEM image of the bare spider silk (A and B) as well as the nanogold-spider silk bioconjugate (C and D) prepared by the exposure of clean spider silk fibers to 10^{-1} M aqueous solution of chloroauric acid. The bare spider silk fiber shows a smooth surface texture at low (Figure 4.2A) as well as high (Figure 4.2B) magnification with a thickness varying from 3 to 10 μm depending on the separation of the fibers. It can also be seen that the surface of the spider silk fiber is clean and does not show dust particles anywhere. The nanogold-spider silk bioconjugate prepared by using 10^{-1} M aqueous solution of chloroaurate ions show a highly irregular texture due to the deposition of a continuous sheet of gold particles on its surface (Figure 4.2C & D). The presence of the gold on its surface was ascertained from EDAX analysis discussed later. It can also be seen that the sheet of gold particles on the surface does show some porous formation on the surface, which indicates that the gold particles do not cover the entire surface of the fiber. However, when compared to the bare spider silk fiber, the thickness of the nanobioconjugate does not change much, which shows that the covering of gold particles on the surface of spider silk fiber is not very thick. It is important to mention here that the treatment of spider silk fiber with this concentration of chloroaurate ions renders the nanobioconjugate fragile and brittle, probably due to dense loading of gold nanoparticles on the surface.

Figure 4.3 A and B show representative SEM images of the nanogold-spider silk nanobioconjugate prepared by treating the spider silk with 10^{-3} M aqueous solution of chloroauric acid. The low magnification image (Figure 4.3A) shows clearly that the spider silk fiber is covered with gold nanoparticles on its surface and it can be easily concluded that the surface of the fiber is not completely covered with the gold nanoparticles as is observed in the spider silk treated with 10^{-1} M solution (Figure 4.2C & D). When the fiber was viewed at a higher magnification (Figure 4.3B), the surface of spider silk fiber showed irregular shaped gold nanoparticles of different sizes all over. These particles were found to be of varying sizes and well separated from each other. Also, it is worth mentioning that the nanobioconjugate prepared at this concentration of chloroaurate ions is very strong and retains its natural elasticity unlike the one prepared using 10^{-1} M concentration of chloroaurate ions. Thus, they are easy to maneuver for their

use in chemical vapor sensing applications and for this reason, they were used for all the electrical property measurements. The particle size distribution analysis (Figure 4.3C) shows that the average size of the particles on the surface of the spider silk is around 275 nm and from the size distribution plot, it can be easily concluded that some particles were

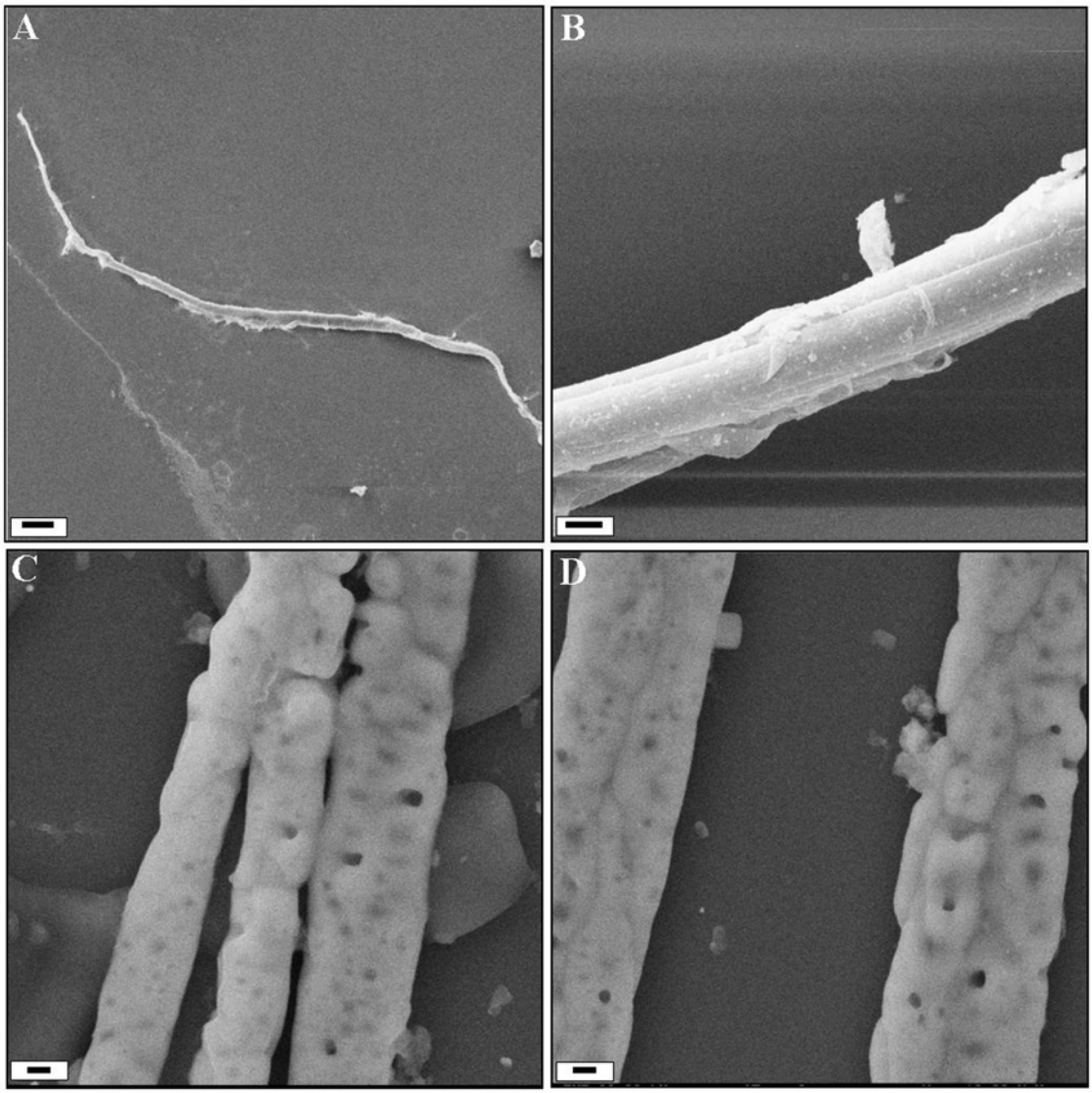

Figure 4.2 *(A & B) Representative SEM images recorded from a spider silk fiber at different magnifications. The scale bar in Figure A and B correspond to 30 and 3 μm respectively. (C & D) Representative SEM images at different magnifications recorded from a spider silk fiber after exposure to 10^{-1} M aqueous solution of chloroauric acid for 48 h. The scale bars in both the images correspond to 1μm.*

found to be as big as 1 μm. However, nearly 70% of the total particles population lies in the range of 200-300 nm and the population of large sized particles is fairly low. Besides,

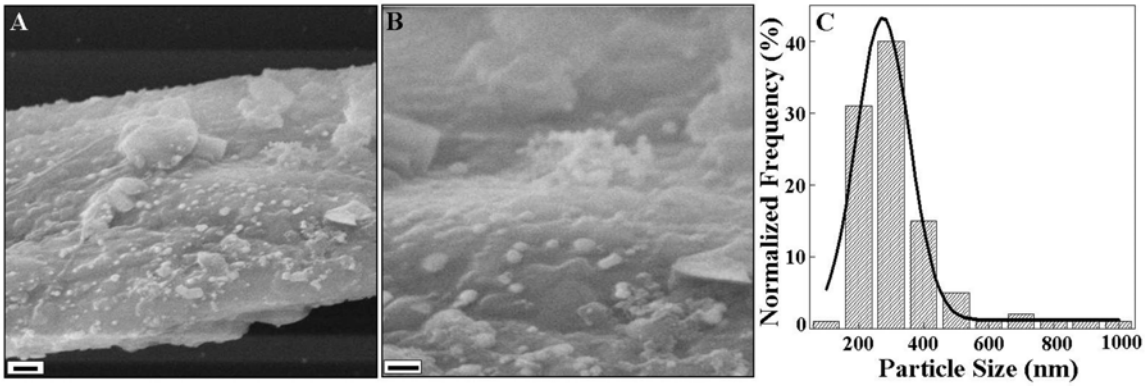

Figure 4.3 *Representative SEM images of spider silk fiber at (A) low and (B) high magnification after exposure to 10^{-3} M aqueous solution of chloroauric acid for 48 h. The scale bars in A and B correspond to 300 and 100 nm respectively. (C) Particle size distribution analysis plot.*

immobilization of borohydride reduced gold nanoparticles was also attempted by immersing the clean spider silk fiber in the solution of reduced gold nanoparticles. However, it was observed that though the particles do bind to the surface, they were not very stable and there was a loss in the color of the fiber and subsequently the particles during the washing steps. Thus, the best result in fabricating the nanobioconjugate was obtained only when the cleaned spider silk fibers itself were used as an active scaffold for concomitant reduction and immobilization of the gold nanoparticles.

4.2.3 EDAX measurements.

EDAX analysis was performed from the surface of the bare spider silk as well as nanogold-spider silk bioconjugate in order to confirm the presence of the gold. The bare spider silk showed a strong signature of C, N and O from its surface owing to the presence of the protein while no signature was obtained corresponding to the energy value for gold (Figure 4.4, curve 1). In addition to this, a strong peak is observed around 1.04 keV which may correspond to Na and/or Cu which have been shown to occur naturally in silk fiber along with K and Ca [27]. Figure 4.4, curve 2 shows the EDAX plot captured from the surface of the nanobioconjugate prepared by exposing the cleaned spider silk surface to 10^{-1} M solution of chloroauric acid; a strong signal for the presence of gold along with the C and O signature from the underlying fibers are observed (the Au signal comes from the surface of the nanobioconjugate shown in the Figure 4.2C). It is clear from the above that exposure of spider silk fibers to chloroaurate ions results in their reduction and that the gold nanoparticles thus formed are trapped on the surface of the fibers. Silk fibroin proteins are implicated in the chloroaurate ion reduction here and

have clearly not lost their reducing power when spun in the form of silk fibers. It is believed that the surface immobilization of the particles is due to the interaction of the

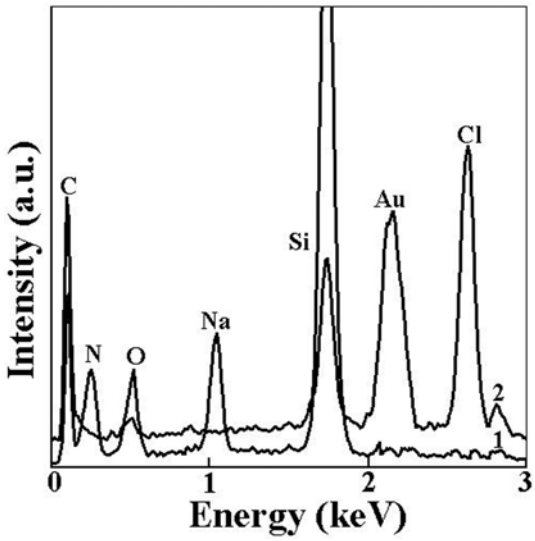

Figure 4.4 *EDAX plot recorded from the surface of the bare spider silk (curve 1) and the spider silk treated with 10^{-1} M aqueous solution of chloroauric acid (curve 2).*

gold nanoparticles with the amine groups in the fibroin protein, as has been shown by our group in previous works [15, 16b]. This is confirmed by the observation that the nanogold-spider silk bioconjugate material is stable even after repeated washing with Milli-Q® water. However, some places on the silicon wafer showed gold nanoparticles broken off from the surface of the spider silk as well.

4.2.4 AFM measurements.

The spider silk fibers were further separated into even finer fibers by treatment of the clean fibers with 1 N solution of HCl. The spider silk was then sonicated for 30 minutes which resulted into very fine fibers which were then taken on the Si (111) wafer for analysis. Figure 4.5A shows the low magnification image of the bare spider silk where it can be seen that the fibers have uniform surface as was confirmed by the SEM images earlier (Figure 4.2 A & B). The high magnification image (Figure 4.5B) of the same shows the surface texture much more clearly in the upper panel while the lower panel gives the line profile across the lines drawn in the upper panel. The height of the spider silk fiber was found to be ca. 18 nm while the thickness was 130 nm. Also it can be seen that due to the acid treatment, spider silk fibers show dendrites like structure, a feature which is completely absent in the SEM images (Figure 4.2 A & B), and thus these

finer fibers seem to be generated due to the better separation of a larger sized spider silk fiber. These very fine fibers were found to be entangled with the thicker fibers at all the places. When the corresponding SEM images of bare spider silk fibers were observed, it

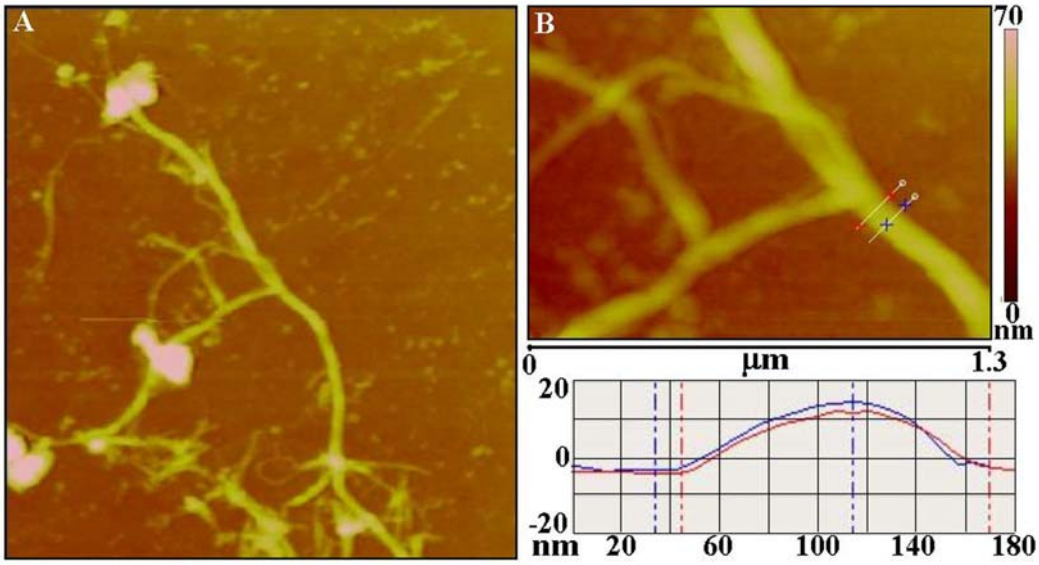

Figure 4.5 *(A) A low magnification AFM image of bare spider silk treated with 1 N HCl. (B) The high magnification image showing the line profile of the bare fiber in lower panel where the height along the line was 18 nm while the thickness was found to be 130 nm.*

was found that the fibers were around 3-4 µm in thickness and thus, from the AFM analysis, it is confirmed that the spider silk fiber can indeed be separated into much finer fibers by using acid treatment.

4.2.5 UV-vis-NIR and TEM measurements of particles formed in solution during nanogold-silkworm silk bioconjugate preparation.

It was observed that other than the reduction of the chloroaurate ions on the surface, silkworm silk fibers also reduce the chloroaurate ions in the solution which turns the solution golden-orange in color. The particles thus formed were anticipated to be of large sizes due to the fact that they tend to settle down naturally at the bottom of the beaker. The UV-vis-NIR spectra of the solution (Figure 4.6A) shows a characteristic transverse plasmon peak for gold nanoparticles at 580 nm, which indeed is shifted towards higher wavelength c.f. spherical gold nanoparticles synthesized by borohydride reduction (absorbance peak around 520 nm), indicating the probability of large sized particles. It can also be observed that the absorption peak is very broad, which is

indicative of polydisperse particles. Moreover, it can be clearly seen that the spectra shows a definite and continuous absorption in the NIR wavelength region, which might

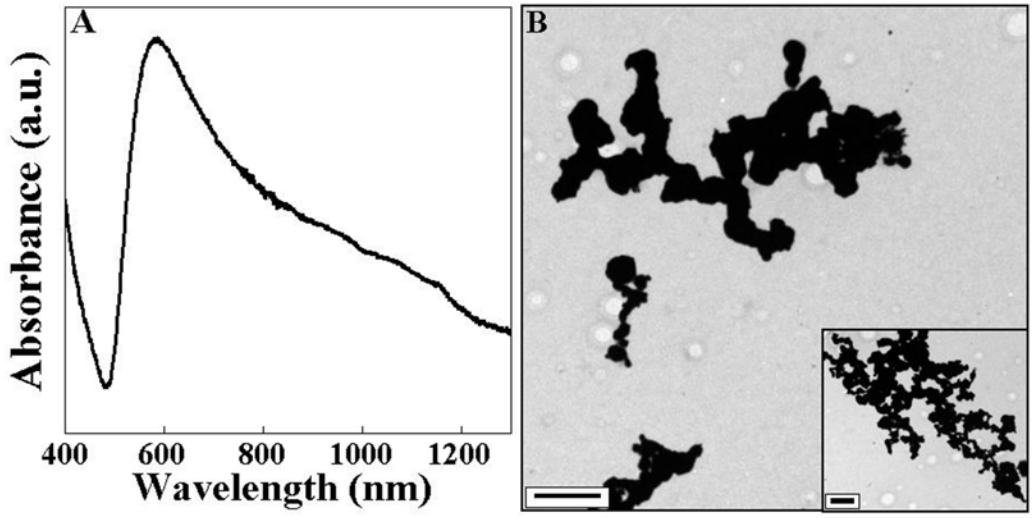

Figure 4.6 *(A) UV-vis-NIR spectra of the solution of gold nanoparticles reduced by silkworm silk, ex-surface. (B) Representative TEM micrograph of the gold particles. The inset shows a high magnification image. The scale bars correspond to 1μm each.*

be due to some anisotropy in the formed gold nanostructures. The TEM analysis shows a perfect corroboration with the UV-vis-NIR spectra and it can be seen that 1-7 μm-sized particles are formed in the process of this reduction. The particles were highly irregular and anisotropic in nature and seem to be formed due to clustering of particles. It can be seen from the contrast generated from these particles that they are indeed very thick and so the selected area electron diffraction (SAED) pattern could not be recorded from the sample.

4.3 Electrical property measurements.

4.3.1 Experimental details.

The nanogold-spider silk bioconjugate was thoroughly washed in Milli-Q® water and dried. This nanobioconjugate was then picked up and placed in the gap between two copper electrodes vacuum deposited onto a glass slide. The separation between the electrodes was made 2 mm by masking during the process of the metal deposition in vacuum system. The ends of the nanobioconjugate were fixed to the copper electrode using fine droplets of silver paste in order to ascertain a better contact. The silver paste was allowed to dry completely prior to measurements. The picture of the entire layout can be seen in the Figure 4.7A, the white arrow indicating the spider silk across the gap,

touching the two electrodes at the either sides. In order to check the effect of electrode separation on the conductivity change of the web, another electrode was fabricated by making a fine cut between a uniformly deposited film of copper. A single fiber of spider silk was placed between the gaps and was imaged under SEM (Figure 4.7B). The SEM image showed that the separation between the two electrodes was about 45-60 μm as indicated by the white arrow in the image and a single fiber of spider silk can be seen spanning across it. However, electrical properties showed no change in either of the two measurements and thus the possibility of an effect of electrode separation on the conductivity was ruled out. Further, only a pad of silver paste was used to immobilize the fiber on to the glass substrate at either ends and the conductivity was checked using small cleaned copper strips for contact at both the ends. The conductivity profile of the nanobioconjugate does not change even with change in the electrode material. All the electrical property measurements were done at room temperature in an open environment

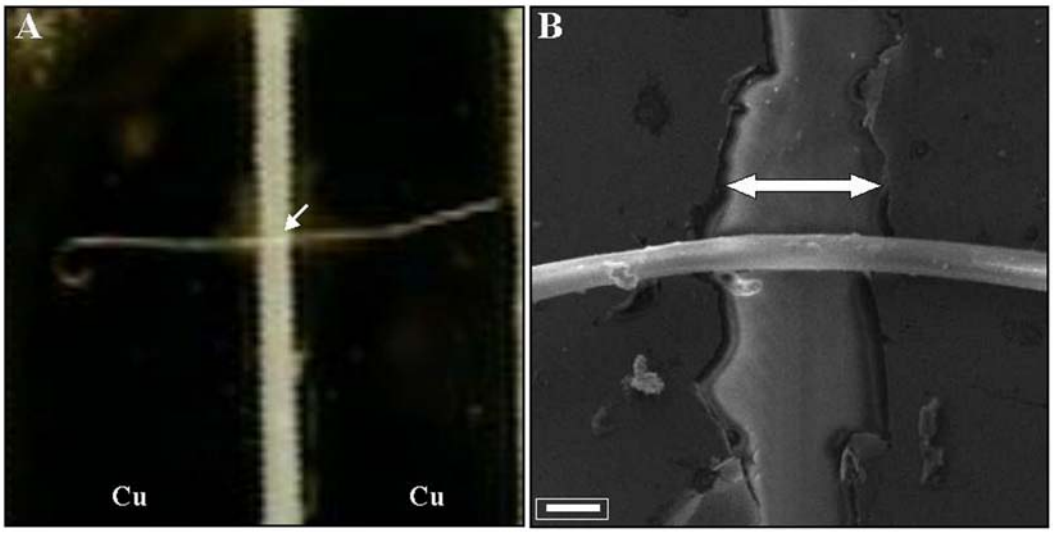

Figure 4.7 *(A) The lay out of the Cu electrode with 2 mm separation for electrical conductivity measurement. White arrow indicates the single fiber of bare spider silk. (B) A fine separation Cu electrode with bare spider silk control fiber across it. The scale bar corresponds to 30 μm White arrow shows the separation between the two copper electrodes.*

and the data was cross checked under a moisture-free environment. All the environment dependent conductivity measurements as a function of time at fixed voltage of 50V were done in a closed chamber at room temperature, with an inlet and outlet for the chemical vapors.

4.3.2 Electrical conductivity measurement at varying voltage.

The electrical conductivity measurements were performed for the nanogold-spider silk bioconjugate. Figure 4.8A, curve 1 shows the I-V characteristics recorded from the nanobioconjugate. It is evident from the curve that within this voltage range of measurement, the electronic conduction is fairly ohmic with some amount of non-linearity. The resistance of the nanogold-spider silk bioconjugate was measured from the slope of the I-V curve to be ca.1300 MΩ. The high resistance of the bioconjugate indicates that the electron conduction in the fiber is by electron tunneling/hopping which is an activated process [28]. The electronic conduction in such cases is a strong function of the interparticle distance [29], the applied bias voltage and the local environment [30]. Curve 2 in Figure 4.8A corresponds to the I-V characteristics of the nanogold-spider silk bioconjugate during exposure to methanol vapor. It is clear that exposure of the nanogold-spider silk fibers to vapors of a polar solvent such as methanol results in considerable changes in the I-V characteristics and that there is enhanced electronic conduction in the fibers.

Previous studies show that physisorption of gas vapors significantly modify the tunneling barrier for electron conduction by changing the work function of a discontinuous film [31]. It has been shown that the adsorption of the electron donor molecule (e.g., ammonia, alcohols, water) on a metal decreases the work function [32]. This fact fits in well with the experimental observation where it is seen that the presence of methanol vapor reduces the work function for electron conduction across the gold nanoparticles. As in the case of the nanogold-spider silk fibers in air (Figure 4.8A, curve 1), the electronic conduction in the voltage range + 20 to – 20 V is ohmic. The resistance of the nanogold-spider silk fiber during exposure to methanol falls to 29 MΩ from the original value of 1300 MΩ and thus appears to be an excellent candidate for application in vapor sensing. Curve 3 in Figure.3A corresponds to the I-V characteristics of the nanogold-spider silk bioconjugate after removing the methanol vapor. This I-V curve superimposes excellently on that recorded from the nanobioconjugate material before methanol exposure indicating that the changes in the fibers consequent to methanol exposure are fully reversible. This measurement was done using the nanogold-spider

bioconjugate prepared using 10^{-3} M $HAuCl_4$ aqueous solution where the SEM study revealed the presence of well-separated gold nanoparticles on the surface of the fibers.

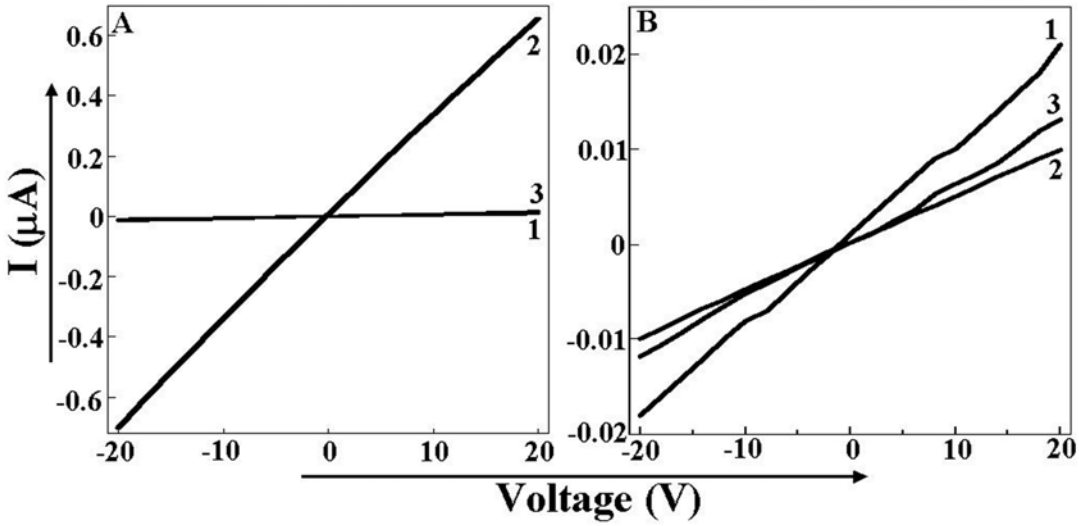

Figure 4.8 *(A) I-V plot of the nanogold-spider silk bioconjugate before (curve 1), during (curve 2) and after (curve 3) exposure to methanol vapors. (B) I-V plot of the nanogold-spider silk bioconjugate before (curve 1), during (curve 2) and after (curve 3) exposure to chloroform vapors.*

Figure 4.8B shows the I-V plot of the nanogold-spider silk bioconjugate on exposure to the chloroform vapors. Curves 1, 2 and 3 in Figure.4.8B correspond to I-V characteristics recorded from the nanogold-silk bioconjugate fibers before, during and after exposure to the chloroform vapor, respectively. It is to be noted that for exposure to chloroform vapor, fresh nanobioconjugate was used. The resistance of this nanobioconjugate fiber was determined from the I-V curve (curve 1) to be 1050 MΩ. During exposure to chloroform vapor (curve 2), it is seen that electronic conduction in the fibers falls and in this respect is different from the behavior observed in the fibers during exposure to methanol (Figure 4.8A, curve 2 & 3). The resistance of the nanogold-spider silk fiber during exposure to chloroform was determined from curve 2 to be 2020 MΩ. The fall in the resistance of the nanobioconjugate might be due to the absorption of the weakly polar chloroform molecule by the spider silk leading to the swelling of the fiber, which will result in an increase in the separation between the gold nanoparticles on the surface. As discussed before, the electron conduction decreases with increasing interparticle spacing, and this can be seen from the result, where for the applied voltage, we get a decrease in conductivity of the bioconjugate. After removal of the

nanobioconjugate fiber from chloroform, it is observed that the I-V characteristics of the fiber (Figure 4.8B, curve 3) do not return to that recorded before chloroform exposure (Figure 4.8 B, curve 1) – there is clearly an irreversible change in the structure of the nanogold-spider silk fiber by chloroform vapor where some amount of chloroform vapor remains absorbed even after removal of the vapors from the environment. As a control experiment, the conductivity of the spider silk was measured in the absence of gold nanoparticles on the surface and was found to be extremely small and insignificant. On exposure to methanol and chloroform vapors, no change was observed in the conductivity of the uncoated spider web.

4.3.3 Time dependent electrical conductivity measurement at fixed voltage.

Time dependent conductivity measurement was performed for the nanogold-spider silk as well as nanogold-silkworm silk as control in order to see the response time and recycling efficiency of the nanobioconjugates. Figure. 4.9A shows the normalized current vs time plot of the exposure of nanogold-spider silk bioconjugate prepared by treatment of thoroughly washed spider silk with 10^{-1} M $HAuCl_4$. As can be clearly seen from the profile of the curve, the arrow indicates the point of exposure of the nanogold-spider silk bioconjugate to methanol. The curve clearly shows that the nanogold-spider silk bioconjugate show a very quick response to the polar methanol vapors and we get a

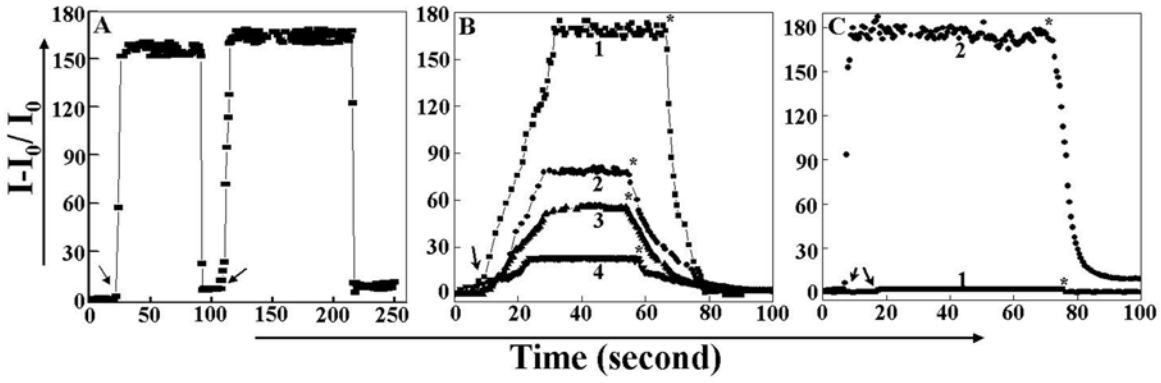

Figure 4.9 *(A) Normalized current vs time plot of the exposure of the nanogold spider silk bioconjugate to the methanol vapors. (B) Normalized current vs time plot for the exposure of the nanogold spider silk bioconjugate to methanol (curve 1), ethanol (curve 2), 2-propanol (curve 3) and n-butanol (curve 4) vapors. (C) Normalized current vs time plot for the exposure of the nanogold silkworm silk (curve 1) and nanogold spider silk (curve 2) to methanol vapors.*

change in the current by more than 150 fold (90 % of the total response) within 10 seconds of exposure of the bioconjugate to the vapors. The curve finally saturates and the

conductivity drops back almost to the original level on removal of the vapour. This cycle of exposure and removal was repeated and similar data was observed for the second cycle as well which indicates clearly that the nanogold-spider silk bioconjugate has an excellent cycling efficiency for the methanol vapors. Thus, the nanogold-spider silk bioconjugate is able to sense the methanol vapors efficiently with a response time of around 10 seconds for 90% of the total response. Besides, it also shows excellent cycling efficiency and reusability with consistent conductive response over repeated exposure and removal of the vapors. A similar experiment was done by using the bioconjugate prepared by treating the thoroughly washed spider silk to 10^{-3} M $HAuCl_4$, which gave low electrical conductivity with a change of around 40 fold only (data not shown). Thus, enriching the surface of the spider silk with gold nanoparticles results in better electrical conductivity as well as sensitivity of the nanogold-spider silk bioconjugate towards exposure to methanol vapors.

Figure 4.9B corresponds to normalized current vs time plot of the nanogold-spider silk bioconjugate to vapors with varying polarity. It is well known that in the alcohol chain starting from methanol onward, the polarity of the solvent decreases with increasing chain length. The values of the Snyder polarity index for methanol, ethanol, 2-propanol and n-butanol are 6.6, 5.2, 4.3 and 3.9 respectively [32]. When the nanogold spider silk bioconjugate is exposed to these solvents of varying polarity, we observe that the change in the conductivity response is in accordance with the polarity of the solvent. Curve 1 shows the conductivity response towards the methanol vapor while curves 2, 3 and 4 correspond to nanogold-spider silk bioconjugate exposed to ethanol, 2-propanol and n-butanol vapors respectively. The arrow ($\rightarrow$) indicates the point of exposure of the bioconjugate to the different vapors while the star ($*$) indicates the time of their removal. The change in the conductivity is about 170 fold when the bioconjugate is exposed to the methanol vapors which decreases to nearly 75-fold on exposure to ethanol vapors, 60-fold for 2-propanol vapors and 25-fold for n-butanol vapors. Thus, we find that the nanogold spider silk bioconjugate is able to distinguish the vapors on the basis of the polarity of the solvents.

Figure 4.9C compares the response of the nanogold spider silk bioconjugate on the exposure to methanol vapors against that of the nanogold-silkworm silk bioconjugate.

Curve 1 shows the change in the conductivity of the nanogold silkworm silk bioconjugate on exposure to methanol vapor. The arrow (→) indicates the point of exposure of the bioconjugate to the methanol vapor while the star (∗) indicates the time of removal. It can be clearly seen from the curve that the nanogold silkworm bioconjugate does not show any significant change in the conductivity profile on exposure as compared to the nanogold spider silk bioconjugate (curve 2) which shows the characteristic 170-fold change in the conductivity. Spider silk is known to respond to polar environments wherein these vapors cause the amorphous protein matrix of the spider silk to contract, thus causing a reduction in the interparticle distance of gold nanoparticles. However, silkworm silk does not show such a behavior and thus does not show any change in the conductivity profile on exposure to the highly polar methanol vapors. These results clearly indicate that the nanogold-spider silk bioconjugate can be an attractive candidate for the fabrication of vapor sensor for polar vapors where the response is in accordance to the polarity of the vapor.

4.3.4 Temperature dependent electrical conductivity measurement at fixed voltage.

It has been discussed above that the electrical conduction across the nanogold-spider silk bioconjugate is due to electron tunneling which is an activated process with a finite work function for electron conduction. Temperature dependent electrical conductivity measurements were performed for the nanogold-spider silk bioconjugate to work out the activation energy for electron conduction by monitoring the change in the resistance of the nanobioconjugate with temperature. Figure 4.10A and B shows the temperature dependent measurements from the nanobioconjugates prepared by treatment of clean spider silk with 10^{-3} and 10^{-1} M concentration of chloroaurate ions respectively. Figure.4.10A shows a plot of the ln(resistance) vs 1/T (temperature) curve obtained from a freshly prepared nanogold-spider silk fiber prepared using 10^{-3} M concentration of chloroaurate ions. This measurement was done in the temperature range 27 to 37 ^{o}C. – care was thus taken to perform these measurements in a temperature range in which there would be no alteration to the structure of the silk fibers. It is seen that the fiber resistance is exponentially dependent on the inverse temperature and that there is a change in slope of the curve beyond a certain temperature.

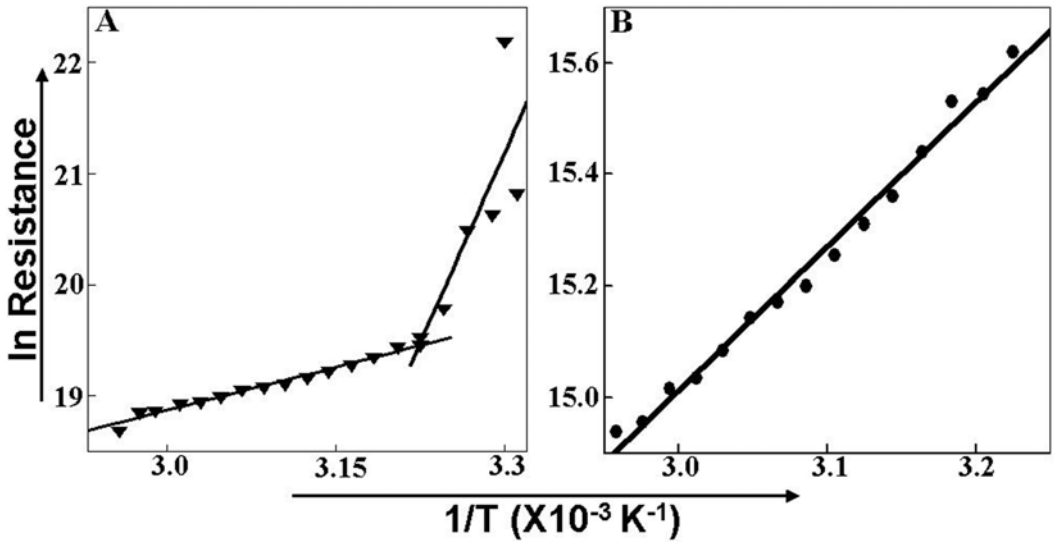

Figure 4.10 *ln (R) vs 1/T plot for the nanobioconjugates prepared by using 10^{-3} (A) and 10^{-1} M concentration of chloroaurate ions.*

An Arrhenius-type activated tunneling model was used to describe the electron conduction through the nanobioconjugate where the activation energy could be calculated from the equation 1

$$\sigma(\delta, T) = \sigma_0 (e^{-\beta\delta}).e^{-E_A / k_B.T} \qquad (1)$$

where β is the electron tunneling coefficient in $Å^{-1}$, δ the average interparticle distance, E_A the activation energy and $\sigma_0 e^{-\beta\delta}$ the conductivity at $k_BT >> E_A$ [29]. From a linear fit to the ln(R) vs 1/T plot in the high temperature region, one obtains the activation energy for tunneling from the slope of the linear fit. The activation energy was estimated from the slope and was found to be 1.7 eV. Similar measurement was also done for the nanobioconjugate prepared by the use of 10^{-1} M concentration of chloroaurate ions and the activation energy was worked out to be 0.22 eV. Thus, it can be concluded that enriching the surface of the spider silk with the gold nanoparticles increases the particles density as can be seen from the corresponding SEM image (Figure 4.2C & D), thereby reducing the interparticle distance. Thus, the electron conduction across the nanogold-spider silk bioconjugate is facilitated.

4.4 Discussion.

It is clear from the above preliminary conductivity measurements that the nanogold-spider silk nanobioconjugate material shows significant increase in electron

transport during exposure to strongly polar vapors while the variation is much smaller in the case of weakly polar molecules. The increase in conductivity of the nanogold-spider silk fibers may be rationalized in terms of contraction of the fiber during exposure to methanol. It is well known that spider silks contract when exposed to polar environments [18] and in the case of the nanogold-silk fiber biocomposite, this leads to reduction in the separation between the gold nanoparticles on the spider silk fiber surface. The current flowing through assemblies of nanoparticles separated by a dielectric by a process of tunneling is exponentially dependent on the separation between the nanoparticles [33]. As a control, the nanogold silkworm silk bioconjugate does not show any appreciable response to the exposure to the methanol vapor. Silkworm silk does not show any contraction on exposure to the polar vapors [18a] and thus, in their case, there is no significant change in the conductivity of the fibers on exposure to the methanol vapors. Thus, reduction of the interparticle separation on the surface of the nanogold-spider silk bioconjugate during contraction in a polar environment would result in an increase in the electronic conduction (or reduction in resistance) as is observed for the fibers exposed to methanol which does not happen in the case of nanogold silkworm silk bioconjugate. That this contraction is large and reversible in the nanogold-spider silk bioconjugate suggests potential application in vapor sensors. The small fall in the nanogold-spider silk fiber conductivity during exposure to chloroform suggests a marginal (irreversible) expansion of the fiber. In order to ascertain that the nanogold spider silk bioconjugate exposed prior to chloroform still shows similar response on exposure to methanol, the nanobioconjugate was exposed to chloroform and allowed it to stay at the room temperature for 15 minutes. This nanobioconjugate was then exposed to the methanol vapors and a similar response as well as the cycling behavior observed in this case as well, as was observed before in chloroform-unexposed nanobioconjugate (Figure 4.9A). Thus, it was confirmed that the prior exposure of the bioconjugate to the chloroform vapors does not show any marked change in its sensitivity to the methanol vapor.

4.5 Conclusion.

In conclusion, it has been illustrated that the spider silk can be used as an active template for the spontaneous reduction of gold ions and the consequent one-step formation of gold nanoparticle-loaded spider silk nanobioconjugates. It has also been

shown that the environment dependent expansion/contraction of the spider silk fiber can be used to modulate electron transport between the nanoparticles, thus providing the basis for a novel vapor sensor. The nanogold-spider bioconjugate shows an excellent response time of around 10 seconds to show almost 150 fold (90% of total change) change in conductivity on exposure to the methanol vapor while it showed poor irreversible response when exposed to the chloroform vapors. Also, the nanogold-spider bioconjugate shows excellent cycling efficiency for exposure to methanol vapors and give consistent response up to 4 cycles of exposure and subsequent removal of vapour. It has also been shown that the nanobioconjugate shows a varying response to the exposure of polar vapors of varying polarity and the response was found to be in direct proportion to the polarity of the vapor used. On the contrary, as-harvested spider silk fibers give poor conductivity and show insignificant change in the conductivity when exposed to these vapors. Thus, nanogold-spider bioconjugate can be a promising candidate towards the development of materials for vapor sensing applications.

4.6 References.

(1) (a) Tirrell, D.A. *Science* **1996**, *271*, 39. (b) Gosline, J.M.; Guerette, P.A.; Ortlepp, C.S.; Savage, K.N. *J. Exp. Biol.* **1999**, *202*, 3295.

(2) van Hest, J.C.M.; Tirrell, D.A. *Chem. Commun.* **2001**, 1897.

(3) Vollrath, F.; Edmonds, D.T. *Nature* **1989**, *340***,** 305.

(4) Lewis, R.V. *Chem. Rev.* **2006**, *106*, 3762.

(5) (a) Xu, M.; Lewis, R.V. *Proc. Natl. Acad. Sci. USA* **1990**, *87*, 7120. (b) van Beek, J.D.; Hess, S.; Vollrath, F.; Meier, B.H. *Proc. Natl. Acad. Sci. USA* **2002**, *99*, 10266.

(6) Work, R.W.; Young, C.T.; *J. Arachonol*. **1987**, *15*, 65.

(7) Kubik, S. *Angew. Chem. Int. Ed.* **2002**, *41*, 2721.

(8) (a) Fahnestock, S.R.; Yao, Z.; Bedzyk, L.A. *Rev. Mol. Biotechnol.* **2000,** *74*, 105. (b) Scheller, J.; Gührs, K.; Grosse, F.; Conrad, U. *Nature Biotechnol.* **2001**, *19*, 573. (c) Lazaris, A.; Arcidiacono, S.; Huang, Y.; Zhou, J.; Duguay, F.; Chretien, N.; Welsh, E.A.; Soares, J.W.; Karatzas, C.N. *Science* **2002**, *295*, 472.

(9) Mayes, E.L.; Vollrath, F.; Mann, S. *Adv.Mater.* **1998**, *10*, 801.

(10) Huang, L.; Wang, H.; Hayashi, C.Y.; Tian, B.; Zhaoc, D.; Yan, Y. *J. Mater. Chem.* **2003**, *13*, 666.

(11) He, J.; Kunitake, T.; *Chem. Mater.* **2004,** *16*, 2656.

(12) Zhou, Y.; Chen, W.; Itoh, H.; Naka, K.; Ni, Q.; Yamane, H.; Chujo, Y.; *Chem. Commun.* **2001**, 2518.

(13) Foo, C.W.P.; Patwardhan, S.V.; Belton, D.J.; Kitchel, B.; Anastasiades, D.; Huang, J.; Naik, R.R.; Perry, C.C.; Kaplan, D.L. *Proc. Natl. Acad. Sci. USA* **2006**, *103*, 9428.

(14) (a) Brott, L.L.; Pikas, D.J.; Naik, R.R.; Kirkpatrick, S.M.; Tomlin, D.W.; Whitlock, P.W.; Clarson, S.J.; Stone, M.O. *Nature* **2001**, *413***,** 291. (b) Sumper, M.; Kroger, N. *J. Mater. Chem.* **2000**, *14***,** 2059. (c) Patwardhan, S.V.; Clarson, S.J.; Perry, C.C. *Chem. Commun.* **2005**, *9***,** 1113.

(15) (a) Mandal, S.; Selvakannan, PR.; Phadtare, S.; Pasricha, R.; Sastry, M. *Proc. Indian Acad. Sci.* (*Chem. Sci.*) **2002**, *114*, 513. (b) Selvakannan, PR.; Mandal, S.; Phadtare, S.; Pasricha, R.; Sastry, M. *Langmuir* **2003**, *19*, 3545. (c) Selvakannan, PR.; Mandal, S.; Phadtare, S.; Gole, A.; Pasricha, R.; Adyanthaya, S.D.; Sastry, M. *J. Colloid Interface Sci.* **2004**, *269*, 97.

(16) (a) Ooka, A.A.; Kuhar, K.A.; Cho, N.; Garrell, R.L. *Biospectroscopy* **1999**, *5*, 9. (b) Joshi, H.; Shirude, P.S.; Bansal, V.; Ganesh, K.N.; Sastry, M. *J. Phys. Chem. B* **2004**, *108*, 11535. (c) Zhong, Z.; Patskovskyy, S.; Bouvrette, P.; Luong, J.H.T.; Gedanken, A. *J. Phys. Chem. B* **2004**, *108*, 4046. (d) Fujiki, Y.; Tokunaga, N.; Shinkai, S.; Sada, K. *Angew. Chem. Int. Ed.* **2006**, *45*, 4764.

(17) (a) van Beek, J.D.; Kümmerlen, J.; Vollrath, F.; Meier, B.H. *Int. J. Biol. Macromol.* **1999**, *24*, 173. (b) Savage, K.N.; Guerette, P.A.; Gosline, J.M. *Biomacromolecules* **2004,** *5*, 675. (c) Eles, P.T.; Michal, C.A. *Macromolecules* **2004,** *37*, 1342. (d) Liu, Y.; Shao, Z.; Vollrath, F. *Nat. Mater.* **2005**, *4*, 901.

(18) (a) Pérez-Rigueiro, J.; Viney, C.; Llorca, J.; Elices, M. *Polymer* **2000**, *41*, 8433. (b) Um, I.C.; Kweon, H.Y.; Park, Y.H.; Hudson, S. *Int. J. Biol. Macromol.***2001**, *29*, 91. (c) Lee, K.G.; Kweon, H.Y.; Yeo, J.H.; Woo, S.O.; Lee, Y.W.; Cho, C.; Kim, K.H.; Park, Y. H. *Int. J. Biol. Macromol.***2003**, *33*, 75. (d) Dicko, C.; Knight, D.; Kenney, J.M.; Vollrath, F. *Macromolecules* **2004,** *5*, 758.

(19) Shao, Z.; Young, R.J.; Vollrath, F. *Int. J. Biol. Macromol.* **1999**, *24*, 295.

(20) Xu, M., Lewis, R.V. *Proc. Natl. Acad. Sci. U.S.A.* **1990**, *87*, 7120.

(21) Colgin, M.A.; Lewis, R.V.; *Protein Sci.* **1998**, *7*, 667.

(22) Yang, Z.; Liivak, O.; Seidel, A.; LaVerde, G.; Zax, D.B.; Jelinski, L.W. *J. Am. Chem. Soc.* **2000**, *122*, 9019

(23) Simmons, A.H.; Michal, C.A.; Jelinski, L.W. *Science*, **1996**, *271*, 84.

(24) Mellon, E.F.; Korn, A.H.; Hoover, S.R. *J. Am. Chem. Soc.* **1949**, *71*, 2761.

(25) Kawahara, Y.; Shioya, M., Takaku, A. *J. Appl. Polym. Sci.* **1996**, *59*, 51.

(26) Chang*a*, Q.; Lakowicz, J.R.; Rao, G. *Analyst* **1997**,*122*, 173.

(27) Zhou, L.; Terry, A.E.; Huang, Y.; Shao, Z.; Chen, X. *Acta Chim. Sinica* **2005**, *63*, 1379. (b) Zhou, L.; Chen; X.; Shao, Z.; Zhou, P.; Knight, D.P.; Vollrath, F. *FEBS Lett*. **2003**, *554*, 337.

(28) Hill, R.M. *Proc. Roy. Soc. A*, **1969**, *309*, 377.

(29) (a) Wuelfing, W.P.; Murray, R.W. *J. Phys. Chem. B* **2002**, *106*, 3139. (b) Wessels, J.M.; Nothofer, H.G.; Ford, W.E.; Wrochem, F.V.; Scholz, F.; Vossmeyer, T.; Schroedter, A.; Weller, H.; Yasuda, A. *J. Am. Chem. Soc.* **2004**, *126*, 3349.

(30) De Renzi, V.; Rousseau, R.; Marchetto, D.; Biagi, R.; Scandolo, S.; del Pennino, U. *Phys. Rev. Lett.* **2005**, *95*, 46804.

(31) (a) Grigor'ev, E.I.; Vorontsov, P.S.; Zav'yalov, S.A.; Chvalun, S.N. *Tech. Phys. Lett.* **2002**, *28*, 845. (b) Wilker, S.; Henning, D.; Lober, R. *Phys. Rev. B* **1994**, *50*, 2548.

(32) http://home.planet.nl/~skok/techniques/hplc/eluotropic_series_extended.html

(33) Krasteva, N.; Besnard, I.; Guse, B.; Bauer, R.E.; Mullen, K.; Yasuda, A.; Vossmeyer, T. *Nano Lett.* **2002**, *2*, 551.

Chapter V

Metal nanoparticles in solution for mercury ion detection

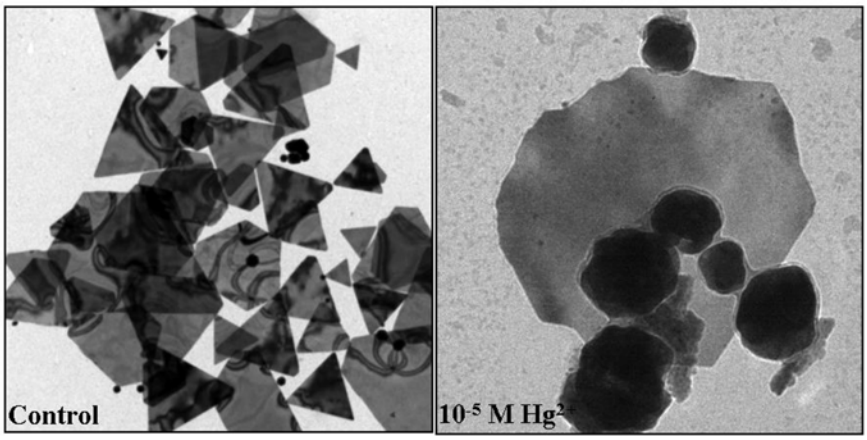

Mercury ions have been known to cause severe ailments to human beings in various vital organs. Thus, attempts have been made to develop protocols for their accurate detection at lowest possible concentration. In the present work, we have developed a simple protocol for detection of mercuric ions in water samples using biologically synthesized gold nanotriangles. It has been shown that the reduction of mercuric ions in the presence of gold nanotriangles damages the structural integrity of the triangles by the well know process of amalgamation. This leaves a signature in the optical properties of the triangles and can be sensitively picked up by UV-vis-NIR spectroscopy. Transmission electron microscopy (TEM) and atomic force microscopy clearly show the loss of the structural integrity of the gold nanotriangles while high resolution TEM (HRTEM) elucidates the underlying mechanism of action of the metallic mercury on gold triangles. This technique shows that mercuric ions can be easily detected in water samples in concentrations as low as 10^{-18} M.

Part of the work presented in this chapter has been published:

Singh, A and Sastry, M. *Nature Nanotechnology* (communicated).

5.1 Introduction.

Mercury is a severe pollutant of the environment that is known to exist in air, water and soil. It persists in the environment in three different forms namely elemental, methyl mercury and as other compound (organic and inorganic) and all the three forms have been proved to be hazardous to human health [1]. The outcome of mercury poisoning in different forms have shown different symptoms; however, in general its poisoning causes malfunctioning of several vital organs such as kidney, heart, nervous system, respiratory system and muscles. The major source of mercury pollution is manufacturing, burning coal and volcanic eruptions [1], coal burning being the major contributor. Once the mercury is disposed into the air or soil, it is washed away by rain to contaminate the soil and water. All different forms are oxidized to form stable mercuric (II) ions, which serve as the major water and soil contaminant. The problem is extended further when a class of bacteria transforms these mercuric ions into methyl mercury [2], which is a neurotoxin. All these forms of mercury are taken up by various marine organisms from water or by the plants through soil and thus enter the complex food chain, leading to their biomagnification and accumulation in various other life forms. Thus, it is very important to continuously monitor mercury levels in the environment.

Several techniques have been developed over the years and have shown to sensitively detect precise levels of mercury in the environment. Some of these are electro-thermal atomic absorption spectroscopy (ETAAS) [3], cold vapour atomic absorption spectroscopy (CVAAS) [4], cold vapour-inductively coupled plasma-mass spectrometry (CV-ICP-MS) [5], atomic fluorescence spectrometry (AFS) [6], neutron activation [7] , high performance liquid chromatography (HPLC) [8], thermometric continuous flow sensor system [9], surface plasmon resonance spectroscopy [10] and voltammetry [11]. Attempts have been made towards precise detection of low levels of mercury from various possible sources such as air [6b,12], human hair [7], water [13], soil [8b,14], urine [15], fishes [16] , wine/liquor [17], fungicides [18] and other biological samples [19]. Several different approaches have been developed by the researchers across the globe to improve upon the lowest detection limit of mercuric compounds especially the mercuric (II) ions in aqueous based systems. Coronado *et al* have reported two ruthenium complex based colorimetric probes (N719 and N749), which have shown to sensitively

detect mercury (II) up to concentration of 20 ppb in aqueous solution [20]. In yet another report, Nolan *et al* have developed a fluorescein-based sensor, which selectively detects mercuric (II) ions in water as low as 2 ppb, the maximum allowable limit in drinking water as per EPA standards [21]. Takahashi *et al* have reported the use of dye compounds for developing test strips for rapid detection of mercury levels in water that are effective up to 10 ppb [22].

Mercury metal has a strong tendency to form amalgam with other metals and in particular, its amalgamation process with gold has been extensively studied since very early [23]. Owing to this fact, gold has been exploited extensively to detect mercury from various types of samples. In one of the early reports, McNerney *et al.* have used a gold thin film to detect metallic mercury in the air using the increase in resistance of the film as a measure of mercury concentration [24a]. Chaurasia *et al.* have used a similar approach by electron beam assisted deposition of gold film onto the glass slides for amperiometric detection of mercury [24b]. In yet another report, Ping *et al.* have used gold film sensors to detect mercury levels in water and urine after digesting the sample with Fenton's reagent [25]. In a different approach, Leong *et al.* have shown a method of detecting micro-amounts of mercury from soil and rock sample where they use gold trap to absorb mercury vaporized from the sample by heating followed by its colorimetric detection [26]. Recently the optical detection of mercuric (II) ions has gained attention due to the simplicity in approach and also due to the fact that it does not involve any sophisticated instrumentation and sample processing. Kim *et. al.* have used 11-mercaptoundecanoic acid functionalized gold nanoparticles which tend to aggregate in presence of divalent ions (such as lead, cadmium and mercury) and thus could be detected optically as well as by hyper-Rayleigh scattering (HRA) [27]. However, this process is cumbersome and involves gold nanoparticles surface modification protocols. Thus, people have been looking for simpler alternative methods for rapid and accurate optical detection of mercury in water samples.

It is a well-known fact that anisotropic structures of gold nanoparticles show very interesting optical properties and thus, researchers have synthesized gold nanoparticles of various shapes such as cubes [28], rods [29], disks [30], stars [31] and triangles [32]. Owing to their unusual optical properties, these nanoparticles are now being looked upon

for a variety of interesting applications. Sastry and coworkers have shown that due to their strong optical absorbance in the NIR region of the electromagnetic spectrum, gold nanotriangles are a potential candidate as optical coatings material [33]. In a very recent report, Rex *et al.* have used gold nanorods for sensitive optical detection of mercuric (II) ions down to the limit of 6.6 X 10^{-13} g/L. They have exploited the unusual change in the optical properties of gold nanorods due to the change in their aspect ratio during the process of amalgamation as a method to detect mercuric (II) ions in aqueous systems [34].

In the present work, we have used biologically synthesized gold nanotriangles to develop a protocol for rapid, selective and specific detection of mercuric (II) ions in aqueous solution down to lower limit of 10^{-18} M. In our lab, the room temperature biosynthesis of gold nanotriangles in high yields using lemongrass plant extract as the reducing and shape-stabilizing agent has been demonstrated [32b]. The optical absorption spectrum of the gold nanotriangles can be precisely tailored by controlling the reduction rate either by varying the amount of the reducing agent [33] or the reaction temperature [35]. Since the optical property of the anisotropic nanostructures strongly depends on their size [36], controlled reduction gives wonderful control over the size of the nanotriangles and subsequently their optical properties. This process results in the formation of a high percentage of thin, flat, single crystalline gold nanotriangles with edge lengths in the range of 100 nm to 1 μm with an average particle size of 440 nm (particle size distribution plot given in Chapter III, Figure 3.A.2C). The thickness of the nanotriangles varies between 8 and 18 nm. The anisotropic nature of these gold nanotriangles results in extremely strong absorbance of the longitudinal SPR component in the near infrared region apart from a distinct peak at around 530 nm characteristic of the transverse SPR component. In this work, it has been shown that reduction of mercuric (II) ions in the presence of gold nanotriangles disrupts the morphology of the gold nanotriangles, which affects the absorption profile of the gold nanotriangles. It has been observed that reduction of higher concentrations of mercuric (II) ions completely transforms the morphology of the gold nanotriangles besides changing the topology of the surface and thus results a loss in the longitudinal SPR band in the NIR region of the spectrum. The underlying possible reactions during this process have already been

reported [34]. Transmission electron microscopy images and subsequent atomic force microscopy measurements reveal that even though the morphology of a large percentage of gold nanotriangles remain intact when mercuric (II) ions are reduced in lower concentrations, the optical absorption profile shows a significant and clearly detectable change. The HRTEM analysis reveals the possible mechanism of action of metallic mercury, which leads to loss in the structural integrity of the gold nanotriangles, thus leaving a strong signature in the optical absorption spectra. This method enables the sensitivity of detection as low as 10^{-18} M. The specificity and selectivity of this protocol has been confirmed by carrying out the same reaction in presence of lead (II) ions where we observe that they do not show much change in the optical spectrum even at concentration as high as 10^{-6} M. Thus, we present a rapid and selective method for detecting ultra-low levels of mercuric (II) ions in aqueous samples.

5.2 Ultra-low level optical detection of mercury in water samples using biogenic gold nanotriangles.

5.2.1 Synthesis, purification and exposure of gold nanotriangles to mercury.

5.2.1.1 Experimental details.

The synthesis of the gold nanotriangles was accomplished according to the procedure described elsewhere [32b]. The lemon grass (*Cymbopogon flexuosus*) broth was prepared by boiling 100 gm of freshly cut and thoroughly washed leaves of the plant in 500 mL water for 5 min. 5 mL of this broth was then added to 45 mL of 10^{-3} M aqueous solution of chloroaurate ions and the reduction process was monitored by time dependent UV-vis-NIR spectroscopy measurements. The process of bioreduction is completed in 6 hours giving a brown-red colored solution, which contains 1:1 mixture of spherical to triangular nanoparticles. Thereafter, the larger size triangular nanoparticles were separated from the smaller spherical nanoparticles by using 3 cycles of centrifugation at 3000 rpm for 20 minutes each. The pellet obtained was washed with deionized water after every cycle of centrifugation. Finally, the pellet obtained was suspended in 5 mL of deionized water for all further experimentation. The centrifugation and washing steps remove a majority population of the small size spherical nanoparticles and thus the pellet contains nearly 90% population of gold nanotriangles. This stringent washing protocol also ensures the removal of any unreduced chloroaurate ions from the

solution. Atomic absorption spectroscopy results show that the final concentration of elemental gold in the purified concentrated triangular gold solution was 2.4 mM.

4 mL of this concentrated solution was then diluted to 40 mL and 4 mL aliquots were made to which mercuric (II) ions were added in different concentrations to achieve desired final concentration. 10^{-2} M stock solution of $HgCl_2$ was used for various serial dilutions and gold nanotriangles were exposed to mercuric ions of concentrations, 10^{-3} M, 10^{-6} M, 10^{-9} M, 10^{-12} M, 10^{-15} M and 10^{-18} M. 5 mg of sodium borohydride was added to each aliquot (2.6 mM final concentration) to reduce the mercuric ions in the presence of the gold nanotriangles. The final solutions were then kept for 10 minutes at room temperature and were subsequently subjected to various characterizations. The solutions were characterized by UV-vis-NIR spectroscopy, transmission electron microscopy (TEM), atomic force microscopy (AFM), high resolution TEM (HRTEM), energy dispersive analysis of X-ray (EDAX) and X-ray photoelectron spectroscopy (XPS). As a control, the triangular gold nanoparticle solution exposed only to mercuric ions in the absence of sodium borohydride were also analyzed under TEM to ensure the effect of the ions themselves on the morphology and structural integrity of gold nanotriangles, if any.

5.2.1.2 UV-vis-NIR spectroscopy.

The UV-vis-NIR spectra were recorded for all the different solutions to observe the changes owing to various treatments compared to control spectra. Figure 5.1A gives the spectra of the control solution (curve 1) of the purified gold nanotriangles; it shows the two characteristic surface plasmon resonance (SPR) peaks obtained for the gold nanotriangles where the peak at 530 nm corresponds to the transverse plasmon component while the continuous absorbance in the NIR region corresponds to the longitudinal plasmon component of the gold nanotriangles [32b]. The strong absorbance in the NIR region as compared to the visible wavelength peak confirms that the gold nanoparticle solution has been enriched with gold nanotriangles after the process of centrifugation. Curve 2 in the same figure shows the spectrum of the gold nanotriangles in the presence of 2.6 mM concentration of sodium borohydride, in order to confirm the effect of the reducing agent itself on the gold nanotriangle solution. It can be clearly see that the two spectra overlap perfectly and are indistinguishable, indicating that there is no

apparent effect of the reducing agent, on its own, on the absorption profile of the gold nanotriangles solution.

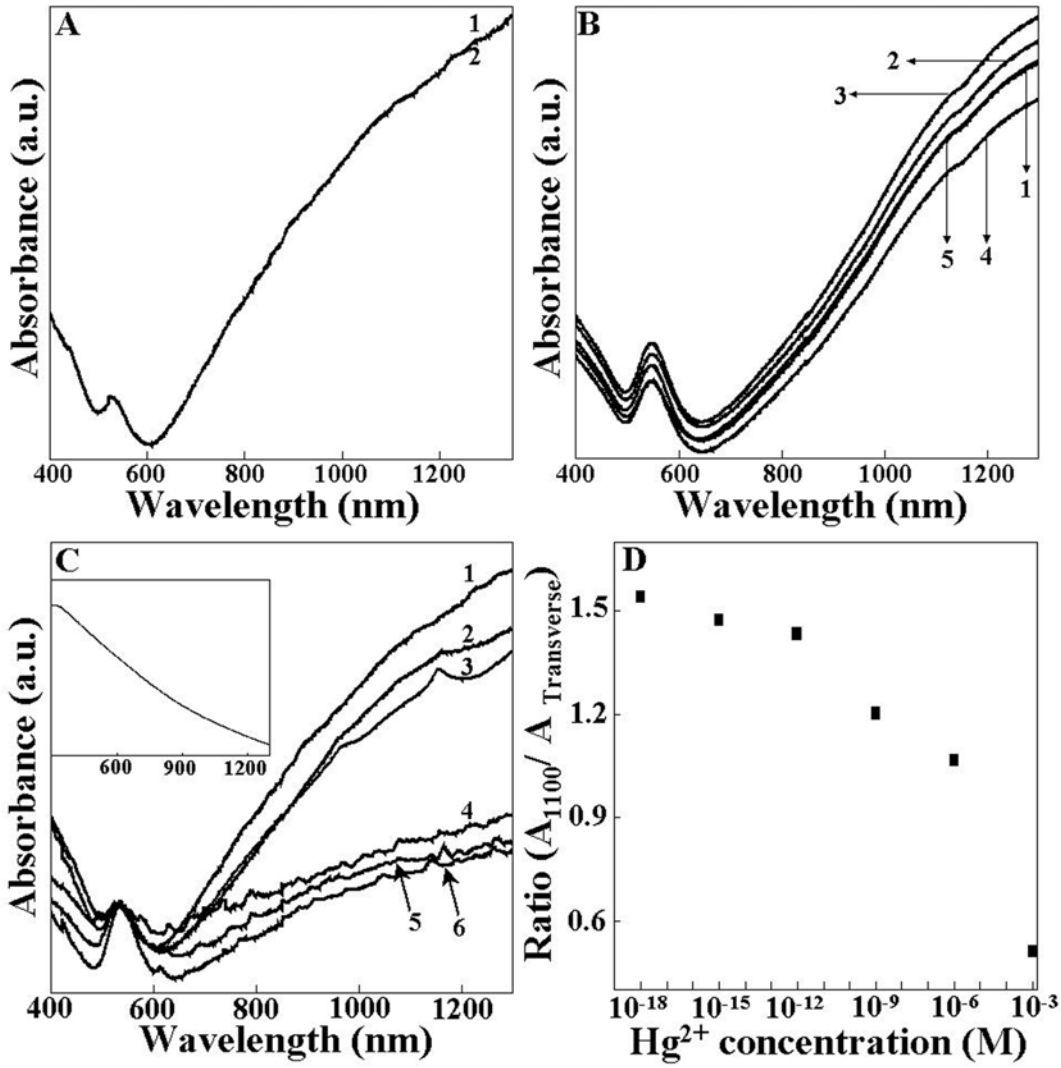

Figure 5.1 *(A) UV-vis-NIR spectra of the gold nanotriangle without (curve 1) and with addition of 2.6mM solution of sodium borohydride (curve 2). (B) UV-vis-NIR spectra of the gold nanotriangle solution control (curve 1) and on exposure to mercuric ions only at concentration of 10^{-3}, 10^{-6}, 10^{-9} and 10^{-12} M (curves 2-5 respectively). (C) UV-vis-NIR spectra of the gold nanotriangles treated with mercuric (II) ions in the presence of 2.6 mM sodium borohydride; curves 1-6 correspond respectively to control, 10^{-18} M, 10^{-15} M, 10^{-12} M, 10^{-9} M and 10^{-6} M mercuric (II) ions. The inset shows the curve corresponding to gold nanotriangles treated with 10^{-3} M mercuric (II) ions in presence of the reducing agent. (D) Plot of the absorbance ratio of $A_{1100nm}/A_{transverse}$ vs concentration of the mercuric ions in the gold nanotriangles solution in the presence of reducing agent.*

Figure 5.1B shows the absorption spectra of the gold nanotriangles in the presence of the mercuric ions but in the absence of the reducing agent i.e. 2.6 mM concentration of sodium borohydride. Curves 1 corresponds to the control gold

nanotriangles solution while curves 2-5 correspond to same concentration of the gold nanotriangles in the presence of 10^{-3}, 10^{-6}, 10^{-9} and 10^{-12} M concentration of mercuric ions respectively. Even though the curves show a changed intensity of absorbance, upon normalization it is seen that there is no change in the relative intensity of the longitudinal to the transverse absorption, which suggests that the mercuric ions do not have any effect on the morphology of the triangular gold nanoparticles. Thus, independently, it was confirmed that the mercuric ions or the reducing agent alone have no effect on the structural integrity of the gold nanoparticles. However, when the gold nanotriangles were exposed to mercuric ions in the presence of the reducing agent, the absorption spectra of the gold nanotriangles changes drastically (Figure 5.1C). Curve 1 gives the spectrum of the as-prepared gold nanotriangle solution while curves 2-6 correspond to the reaction mixture containing same concentration of triangular gold nanoparticles with 10^{-18}, 10^{-15}, 10^{-12}, 10^{-9} and 10^{-6} M concentration of the mercuric ions respectively along with 2.6 mM concentration of sodium borohydride. It is important to note that the dilutions in all the solutions were maintained identical while performing the experiments as well as during the UV-vis-NIR measurements and so any change in the intensity of absorbance could be directly attributed to the reaction. The curves in Figure 5.1C show a prominent fall in the intensity of absorption of the gold nanotriangles in the NIR region and the intensity loss is found to be in direct proportion to the concentration of the mercuric ions to which the gold triangles were exposed (concentration of gold nanotriangles and the reducing agent being constant in all the cases). The presence of the NIR absorption band in the spectra is due to the anisotropic nature of the gold nanoparticles in the solution [32b] and thus any change in the intensity of the NIR peak would be a direct measure of the loss in the anisotropic property of the nanotriangles. Thus, its can be clearly concluded from the spectra that higher the intensity of the mercuric ions in the solution, higher will be the loss in the intensity of the NIR peak. The same was found to hold good for the gold nanotriangles solution, which was exposed to 10^{-3} M concentration of mercuric ions in the presence of the reducing agent where we observe a complete loss in the intensity of the NIR peak (Inset, Figure 5.1C).

The picture becomes clearer when the ratio of the absorbance values at NIR wavelengths (here taken to be at 1100 nm) to that of transverse plasmon wavelength was

plotted against the concentration of the mercuric ions present in the solution. It was seen that there is a gradual decrease in the ratio with increasing concentration of mercuric ions in the solution in the presence of the reducing agent (Figure 5.1D). This plot thus, shows that there is a significant loss in the intensity of absorption at the NIR wavelength when mercuric ions are reduced in the presence of gold nanotriangles. This point onwards, the reduced mercuric ions will be addressed as mercury metal for simplicity, a fact which has been confirmed by XPS analysis (discussed later in the chapter). Thus, the UV-vis-NIR measurements give an indication that the metallic mercury changes the absorption profile of the gold nanotriangles, a property that is a strong function of the shape of the nanoparticles. Thus, it gives an indirect evidence of loss of the structural integrity of the gold nanotriangles in the presence of metallic mercury. However, in order to get a direct evidence of the process, electron microscopic analysis was performed.

5.2.1.3 Transmission electron microscopy measurements.

Figure 5.2A shows a representative low magnification TEM micrograph of the as-prepared, purified gold nanotriangles. These triangles are extremely thin in nature (as was confirmed by AFM analysis discussed later) with an average edge length of around 500 nm. Most importantly, it can be seen that the population of spherical gold nanoparticles is very small in the purified gold nanotriangle solution showing that centrifugation and

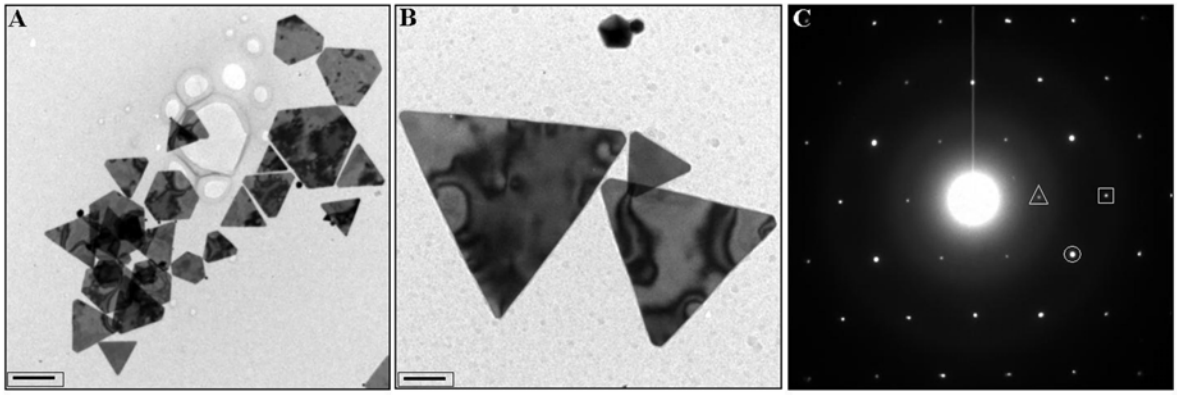

Figure 5.2 *(A) Low magnification TEM micrograph of purified gold nanotriangles. (B) High magnification image of the particles in A. The scale bars in A and B correspond to 500 and 100 nm respectively. (C) SAED pattern from one of the triangles (details in text, section 5.2.1.3).*

washing steps effectively remove the spherical particles. This corroborates well with the corresponding UV-vis-NIR curve (Figure 5.1, curve 1), which shows a very strong absorption in the NIR region with a weak absorption corresponding to the transverse

plasmon band. Figure 5.2B shows the high magnification image of the same gold nanotriangle solution, which shows contrast within the triangles and is believed to arise from the stresses in the nanoparticle due to buckling of the thin nanosheets. Figure 5.2C shows a selected area electron diffraction (SAED) pattern from one of the gold triangles and clearly shows that the triangles are single crystalline. The spots could be indexed based on the face-centered cubic (fcc) crystal lattice structure of gold. The circled and boxed spots correspond to {220} and {311} Bragg reflections with the lattice spacing of 1.44 and 1.23 Å respectively, while the spots circumscribed in the triangle corresponds to the 1/3{422} forbidden Bragg reflection with a lattice spacing of 2.5 Å. The presence of this forbidden Bragg reflection is a common feature in the flat nanostructures of noble metals [37]. This shows the occurrence of {111} stacking faults parallel to the {111} face and extending across the entire planar particle. These purified gold nanotriangles solution was then exposed to the mercuric ions as well as mercury metal in varying concentrations and the TEM measurements were performed to observe the effect on the structure of the gold nanotriangles.

Figure 5.3A shows a representative TEM micrograph of the gold nanotriangles that were exposed to 10^{-3} M concentration of mercuric ions alone (without reduction) and it is clearly evident from the image that there is no apparent change in the structure of the gold nanotriangles when compared with the control (Figure 5.2A & B). This result corroborates well with UV-vis-NIR data where we do not observe any change in the absorption profile of gold nanotriangles in the presence of the mercuric ions at this concentration (Figure 5.1B, curve 2). Thus, from the above observations, it can be concluded that mercuric ions by themselves are incapable of bringing about any change in the morphology of the gold nanotriangles. Figure 5.3B and C show the low and high magnification images of the nanotriangles after reaction with the 10^{-3} M concentration of the mercury metal respectively and it can be clearly seen in both the images that the triangular morphology of the gold nanoparticles is completely lost. The gold nanotriangles have been completely transformed into spherical particles of high contrast unlike the untreated gold nanotriangles, which were extremely thin and showed low contrast (Figure 5.2A & B). Here as well, the contrast may be compared with the gold nanotriangles in Figure 5.3A where the transparency of the thin gold nanotriangles can be

appreciated from the fact that a small triangle lying beneath a larger triangles can be clearly seen. This shows that the mercuric ions by themselves do not show any change in the contrast of the triangles. Thus, it can be concluded that the amalgamation process has transformed the gold nanotriangles into spheroids and thus, the complete loss of the NIR absorption in the UV-vis-NIR spectra of the same solution could be explained (inset, Figure 5.1C).

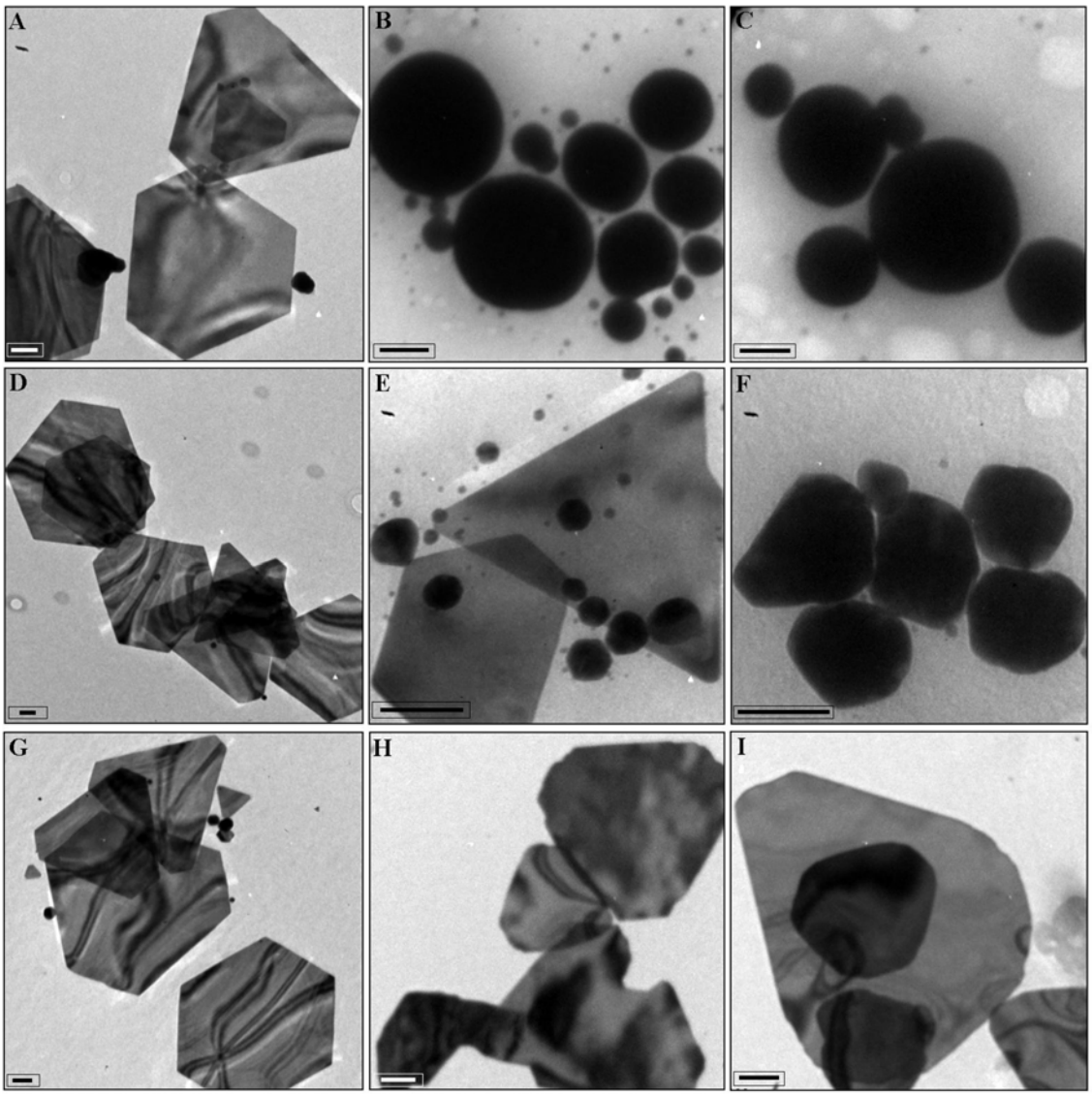

Figure 5.3 *The three rows correspond respectively to TEM images of the gold nanotriangles treated with 10^{-3}, 10^{-6} and 10^{-9} M concentrations of mercuric ions. The first image in each row (A, D and G) respectively corresponds to the presence of unreduced 10^{-3}, 10^{-6} and 10^{-9} M concentrations of mercuric ions. The second and third image (B & C, E & F, H & I) respectively shows the low and high magnification TEM micrograph of the solutions in the presence of reduced 10^{-3}, 10^{-6} and 10^{-9} M concentrations of mercury metal. The scale bar in all the images corresponds to 100 nm.*

Figure 5.3D and G show the TEM micrograph of gold nanotriangles treated with 10^{-6} and 10^{-9} M concentration of mercuric ions respectively in the absence of the reducing

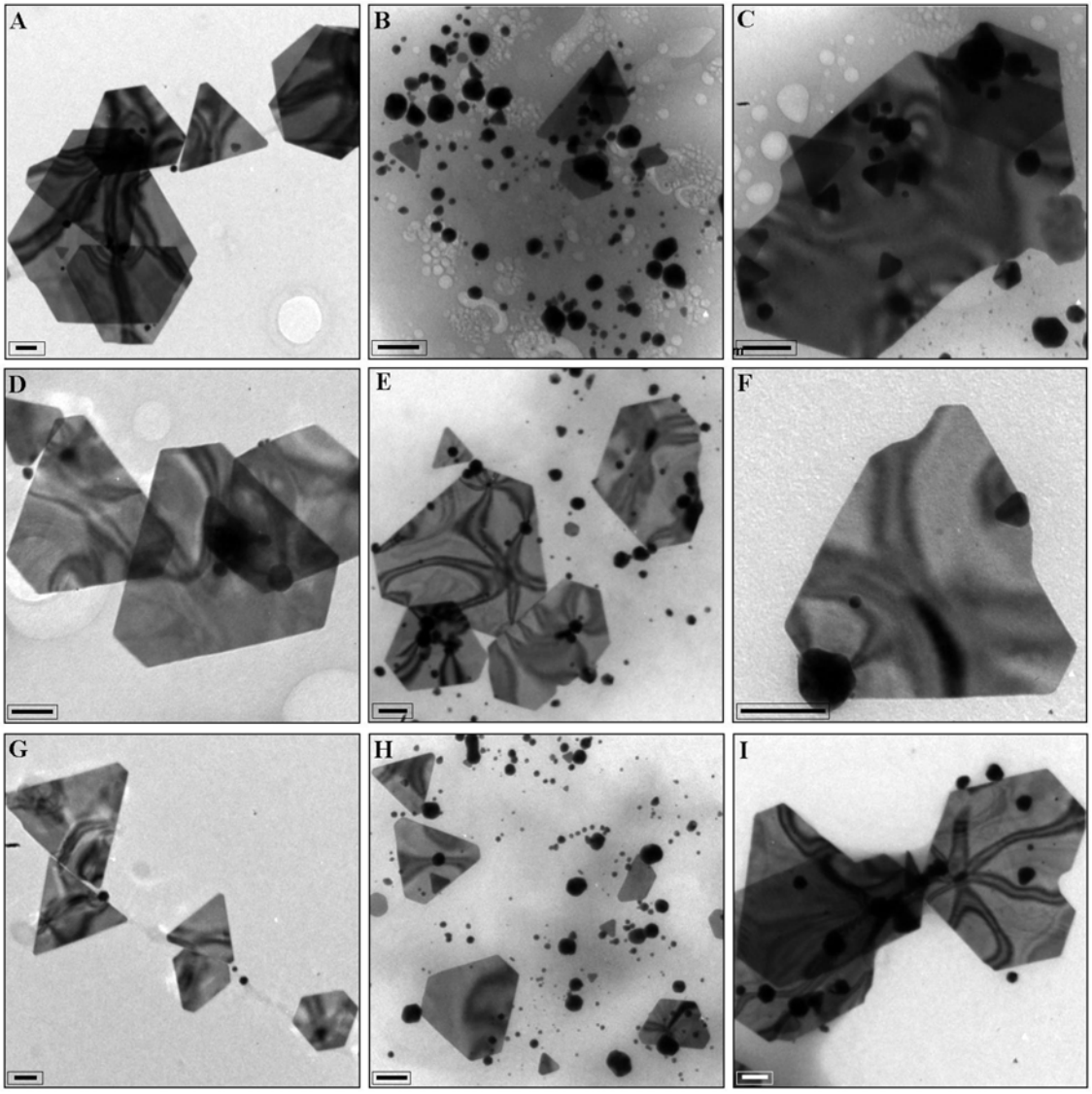

Figure 5.4 *The three rows correspond respectively to TEM images of the gold nanotriangles treated with 10^{-12}, 10^{-15} and 10^{-18} M concentrations of mercuric ions. The first image in each row (A, D and G) respectively corresponds to the presence of unreduced 10^{-12}, 10^{-15} and 10^{-18} M concentrations of mercuric ions. The second and third image (B & C, E & F, H & I) respectively shows the low and high magnification TEM micrograph of the solutions in the presence of reduced 10^{-12}, 10^{-15} and 10^{-18} M concentrations of mercury metal. The scale bar in all the images corresponds to 100 nm.*

agent. No change in the morphology of the gold nanotriangles is observed, which has been concluded earlier from the UV-vis-NIR spectra of the same solutions (Figure 5.1B, curve 3 & 4 respectively). Thus, the TEM micrographs prove the conclusion of the UV-

vis-NIR spectra. Figures 5.3E & F show respectively the low and high magnification TEM images of the particles in the gold nanotriangles treated with 10^{-6} M concentration of mercury metal. In this case, some particles do show triangular morphology and some flat nanostructures with a high contrast as seen in the images. Besides, its worthwhile to note that a large population of high contrast spherical particles are also seen which were absent in the control purified gold nanotriangle solution. At this point of time, we speculate that these high contrast spherical particles are formed due to the breaking of the amalgamated gold nanotriangles. Similarly, the TEM micrographs corresponding to the gold nanotriangle solution exposed to 10^{-9} M concentration of mercury metal also shows flat structures which are highly damaged and show a changed contrast (Figure 5.3H & I). When the UV-vis-NIR spectra of these solutions (i.e. gold nanotriangles treated with 10^{-6} and 10^{-9} M concentration of mercury metal) are seen again (Figure 5.1C, curves 6 & 5 respectively), it can be clearly seen that in both the spectra, the NIR absorption peak is highly damped which gave an indirect indication of the loss of structural integrity of the gold nanotriangles, a fact that is proved by the TEM analysis.

Further, it was observed that the mercuric ions at low concentrations of 10^{-12}, 10^{-15} and 10^{-18} M also do not show any effect on the morphology of the gold nanotriangles (Figure 5.4A, D & G respectively). However, the gold nanotriangles which are exposed to 10^{-12} M concentration of metal mercury show that even though the contrast on the flat particles does not show a significant change, the triangular gold nanoparticles are damaged at all the places while the population of the spherical nanoparticles is very high, indicating that the gold nanotriangles break into spherical particles even at this concentration of mercury metal (Figure 5.4B & C). The high magnification image shows a once triangular nanoparticle, which is now disrupted. However, it may also be noted that not the entire population of the gold nanotriangles is damaged at this concentration; even then a significant change in the absorption profile can be seen in the NIR region (Figure 5.1C, curve 4) suggesting that the majority of the gold nanotriangles are damaged, which was confirmed from the TEM analysis. It is also important to note that the larger sized gold nanotriangles are found to be more prone to damage than the smaller triangles, suggesting that the strain on the triangles due to the process of amalgamation is more pronounced in the larger sized gold nanotriangles.

When the gold nanotriangles were exposed to the 10^{-15} M concentration of mercury metal, it is observed that the surface contrast of the gold nanotriangles is same as the control; however, the triangles are damaged in this case as well (Figure 5.4E & F). A similar observation can be made for the triangles of the solution exposed to the 10^{-18} M concentration of mercury metal (Figure 5.4H & I). However, it is important to mention that at these low concentrations of 10^{-15} and 10^{-18} M, a very small population of the gold nanotriangles actually show damaged morphology, yet, a significant change is seen in the UV-vis-NIR spectra of the solutions (Figure 5.1C, curve 3 & 2 respectively). Thus, the TEM analysis of the various solutions gives clear information that the process of amalgamation of the gold nanotriangles leads to their breaking, which causes a loss in the NIR absorption profile of these nanoparticles, as shown in the UV-vis-spectra described earlier.

5.2.1.4 Atomic force microscopy measurements.

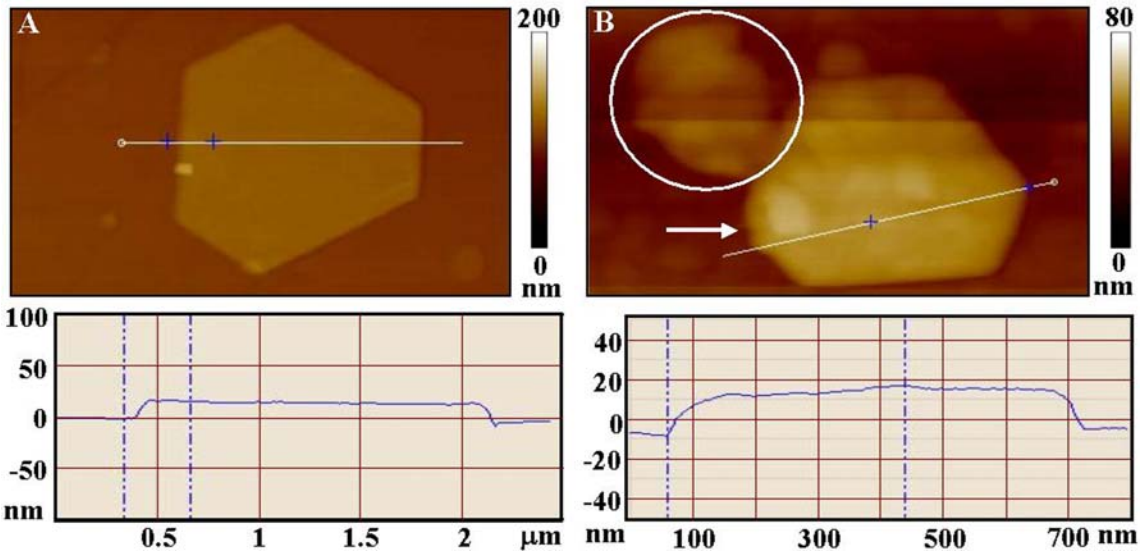

Figure 5.5 *(A) AFM analysis of the control untreated gold nanotriangles. Upper panel shows a hexagon while the lower panel shows its line profile. The thickness was found to be 16.5 nm. (B) AFM image (upper panel) of gold nanotriangle treated with 10^{-15} M concentration of mercury metal and its line profile (lower panel). The circled particle is a damaged nanotriangle while the arrow indicates damaged edge of the hexagon. The thickness of the hexagon was found to be 23.5 nm.*

AFM measurements were performed to confirm the surface texture of the gold nanotriangles treated with the mercury metal. Figure 5.5A shows a representative AFM micrograph (upper panel) and the line profile (lower panel) of the control solution, which

has not been subjected to any treatment. The truncated triangle (or hexagon) seen in the image was found to be of 1.7 μm in length and the line profile shows that its thickness is 16.5 nm. However, an analysis of a larger population of the gold nanotriangles shows that their thickness ranges between 15 to 25 nm. The most important information drawn from the AFM measurement was that the surface of the untreated gold nanotriangles is perfectly flat without any surface corrugation or irregularities. When the gold nanotriangles were treated with 10^{-15} M concentration of mercury metal (Figure 5.5B), it is observed that the surface of the gold nanotriangles is essentially flat here as well as in the control, proving that the process of amalgamation does not impact the flat surface of the gold nanotriangles. This observation corroborates well with the TEM analysis where it was seen that the surface texture of the gold nanotriangles do not change even though the morphology is transformed on exposure to the low concentrations (10^{-15} & 10^{-18} M) of mercury metal. The thickness of this nanotriangle was found to be 23.5 nm, which is within the range of the thickness of the control gold nanotriangles population. The size of this nanoparticle was found to be 1.4 μm. Thus, the AFM analysis suggests that the amalgamation of the gold nanotriangles does not leave an effect on the flat surface and thus the site of action of the mercury metal is probably at the edges and tips of the particles which are likely defect points in the single crystalline gold nanotriangles [38] and thus, would be more prone to the process of amalgamation. In order to ascertain this hypothesis, HRTEM measurements were performed along with spot EDX analysis.

5.2.1.5 High-resolution transmission electron microscopy and energy dispersive X-ray measurements.

Figure 5.6A shows a representative HRTEM micrograph of a single triangle showing the tip and edge where it can be seen that the edges and the tips of the gold nanotriangles were found to be very uniform and smooth with no deformation. Figure 5.6B shows the edge of an untreated gold nanotriangle in control where it can be seen that the surface of the edge is very uniform. The lattice spacing between the planes was found to be 2.36 Å, which corresponds to {111} planes for face-centered cubic gold. Figure 5.6C shows the EDX analysis of the gold nanotriangles in the control where it can be seen that the profile gives a very strong signal for gold apart from copper, which comes from the underlying copper grid. The peaks at low energy in the plot correspond to

the presence of C, N and O, which possibly arise from the biomolecules that stabilize the surface of the gold nanotriangles.

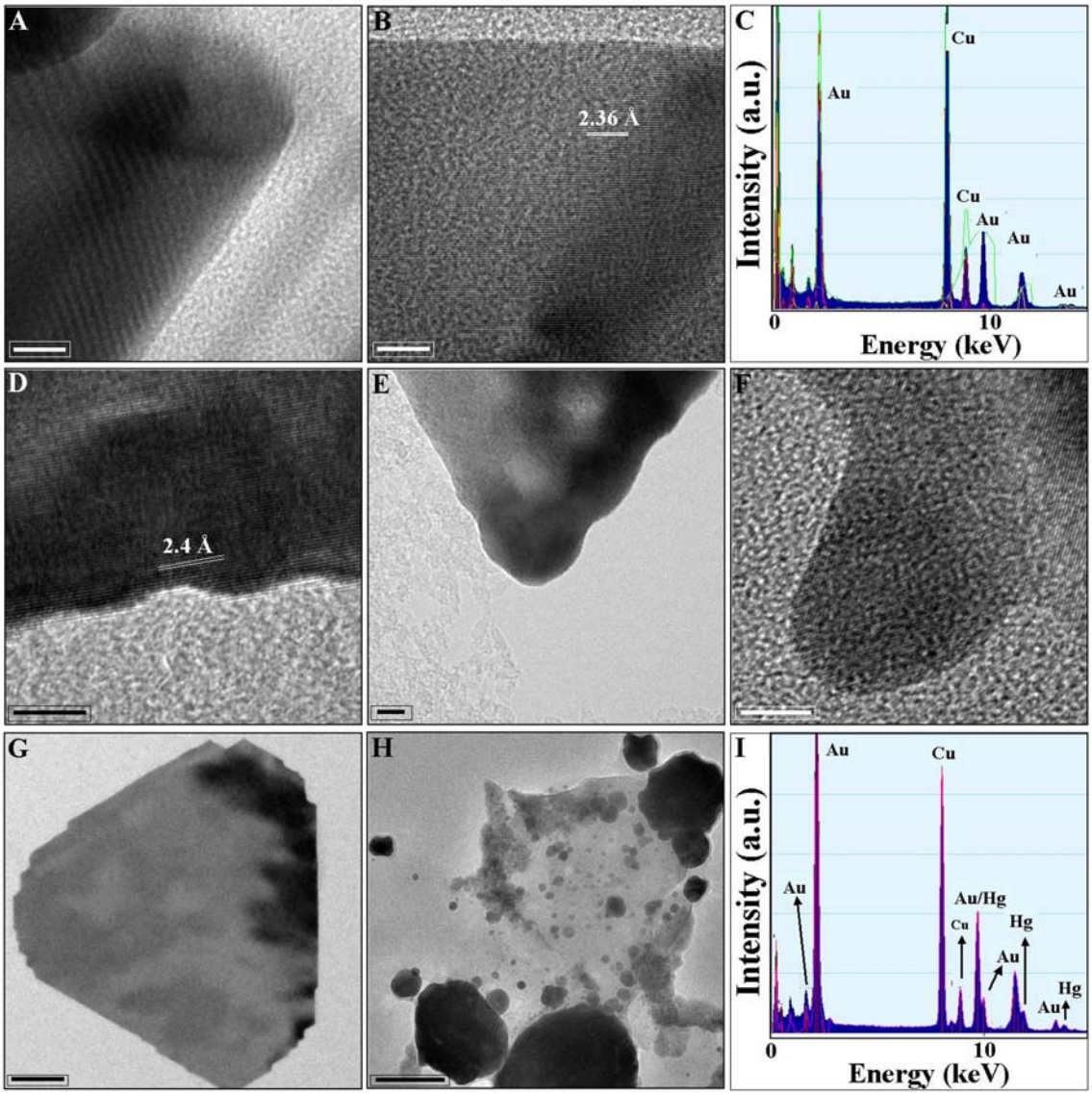

Figure 5.6 *(A & B) HRTEM image of the gold nanotriangle control showing uniform edges and tips. The scale bar corresponds to 5 nm in both images. (C) The spot EDX profile from an as prepared gold nanotriangle. (D & E) HRTEM image of the edge and tip of gold nanotriangles exposed to* 10^{-15} *M concentration of mercury metal. (F) HRTEM image of an edge of gold nanotriangle showing the budding off of amalgamated gold from the triangle edge. The scale bars in D, E and F correspond to 5 nm. (G) HRTEM image of a gold nanotriangles exposed to* 10^{-5} *M concentration of mercury metal. (H) HRTEM image of the spherical amalgamated gold nanoparticles. The scale bars in G and H correspond to 100 nm. (I) EDX profile from the spherical gold nanoparticles shown in H.*

Figure 5.6D shows a representative HRTEM image of a gold nanotriangle treated with 10^{-15} M concentration of mercury metal. It can be seen that the edge of the triangle is

wavy and irregular. The contrast near the edge of the triangle was also found to be higher than towards the center of the particle and the lattice spacing was found to be 2.4 Å. The higher contrast near the edge might be due to the amalgamation of the gold nanotriangles, which also leads to a slight change in the lattice spacing between the lattice planes near the particle's edge. Figure 5.6E shows the tip of one of the mercury treated gold triangles where it can be clearly observed that the tip is blunt with a damaged and wavy edge. Besides this, the triangular particle shows areas of high contrast along the edge and it can also be seen that at all the places of high contrast, the surface of the edge appears to be projecting out. Our earlier speculation that the amalgamation process occurs near the edges and tips rather than at the flat surfaces, leading to the breaking off of amalgamated gold, was confirmed when it was seen that some of the particles showed a finger like projection near the edge at some places (Figure 5.6F). The picture depicts a snapshot of an intermediate step between the amalgamation and breaking off of the amalgamated gold from the tip where the small projection appears to bud off the surface. The EDX analysis from the projected area showed the presence of mercury along with gold whereas the center of the flat surface of the same triangle did not even show traces of mercury. Thus, this confirms conclusively that the process of amalgamation of the gold nanotriangles takes place at the edges and tips, which are the sites of lattice defects and thus, the propensity of metallic mercury to amalgamate these regions is expected to be higher.

Figure 5.6G shows a low magnification HRTEM image of a gold nanotriangle from the solution, which has been exposed to 10^{-5} M solution of metallic mercury and shows that the entire population of particles is damaged with broken edges and high contrast at the edges. When the spherical nanoparticles in the solution formed due to breaking up of the gold nanotriangles were checked, it was found that they contain a high percentage of mercury along with gold. Figure 5.6H shows the cloud of small sized particles, which have been formed as a process of amalgamation of gold nanotriangles and are absent in the case of the control. These particles vary in size and show a high content of mercury. The EDX profile recorded from these particles showed the presence of 11.3 % of mercury in them by weight (Figure 5.6I).

Scheme 1 shows the possible events occurring during the process of amalgamation of the gold nanotriangles at the edges and the tips leading to the breaking off of the amalgamated spherical nanoclusters. The process leads to damage of the nanotriangles from the edges and the tips. The scheme shows that in the absence of a reducing agent, the triangle morphology of the gold nanoparticles is intact and thus, the optical properties do not change. However, as shown in the lower panel, in the presence

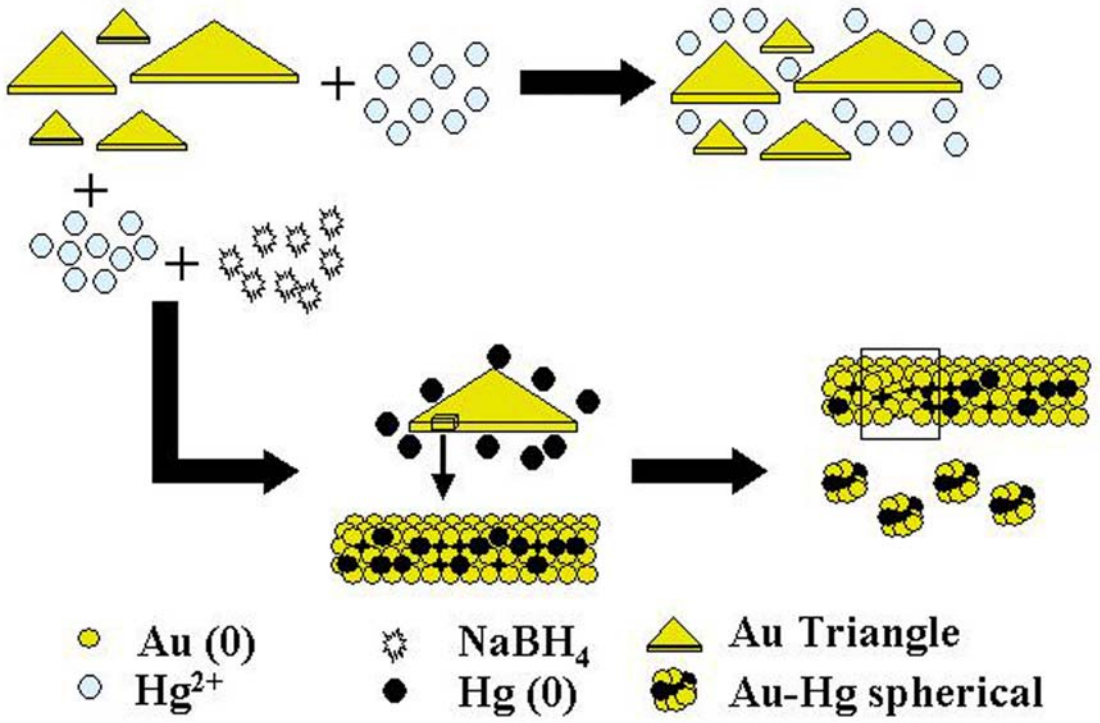

Scheme 5.1 *Schematic showing the probable events occurring during the process of amalgamation of gold nanotriangles. The area enclosed by rectangles in the lower part of the scheme shows the site of damage of gold nanotriangles due to breaking off of amalgamated gold nanoclusters.*

of the reducing agent, the mercury atoms amalgamate with gold triangles at the edges and tips which might lead to strain on the triangular structure, distorting its geometry. It is this distortion in the geometry, which leads to the breaking off of the amalgamated sites of the triangle in the form of gold nanoclusters. The area enclosed in the rectangle in the scheme shows such damaged site which has formed in the process. In order to confirm that sodium borohydride indeed forms mercury atoms from ions by the process of reduction, XPS analysis was done for a low and a high concentration of mercuric ions in solution containing gold nanotriangles.

5.2.1.6 X-ray photoelectron spectroscopy measurements.

Figure 5.7 shows the XPS plots for the gold nanotriangle control as well as the solution exposed to 10^{-3} and 10^{-15} M concentration of mercuric ions in the presence of the reducing agent. All the core level binding energies (BE) were shifted relative to the respective C1s BE of 285 eV and the spectra have been background corrected using the Shirley algorithm [39] prior to curve resolution. The Au $4f_{7/2}$ peak in the control sample could be decomposed into two chemically distinct peaks at 83.5 and 85.7 eV, which correspond to Au (0) and Au (I) oxidation states respectively (Figure 5.7A). The relatively small amount of Au (I) present on the surface of the gold nanotriangles contributes towards the high binding energy component and is believed to stabilize the gold nanotriangles electrostatically in solution [40].

The gold nanotriangles exposed to 10^{-3} M concentration of mercuric ions in the presence of 2.6 mM concentration of sodium borohydride as reducing agent showed a strong signal for mercury (Figure 5.7B). The BE of the high intensity Hg $4f_{7/2}$ peak was found to be 100.6 eV corresponding to the Hg (0) oxidation state, which confirms that mercury metal is indeed formed due the reduction of mercuric ions by sodium borohydride. Besides, we also observe a low binding energy peak at 98.2 eV that could be either due to amalgamation of sodium contributed from sodium borohydride or copper substrate, which was used for the measurement [40]. This sample was also checked for the presence of gold and it was found that at this high concentration of mercury, the gold signal is very weak, as can be seen in the Figure 5.7C. If the TEM micrograph of this sample is observed (Figure 5.3B & C), it can be clearly seen that the gold nanotriangles are not seen at all and they have been deposited with a very thick layer of mercury on the surface, giving a very strong contrast. It is well known that XPS is a surface sensitive technique and thus, the signal of gold inside the spheroidal nanostructures is not readily detected.

On the contrary, gold nanotriangles exposed to 10^{-15} M concentration of mercuric ions in the presence of the reducing agent shows a very strong signal of gold (Figure 5.7D) as expected from the TEM observations. The TEM micrograph of the corresponding sample (Figure 5.4E & F) shows that a good population of gold nanotriangles remains intact in this solution and those, which are damaged, also don't

show the presence of mercury in the surface, as is confirmed from EDX analysis. Thus, a very intense signal of gold can be seen from this sample. The spectra of Au4f spectrum

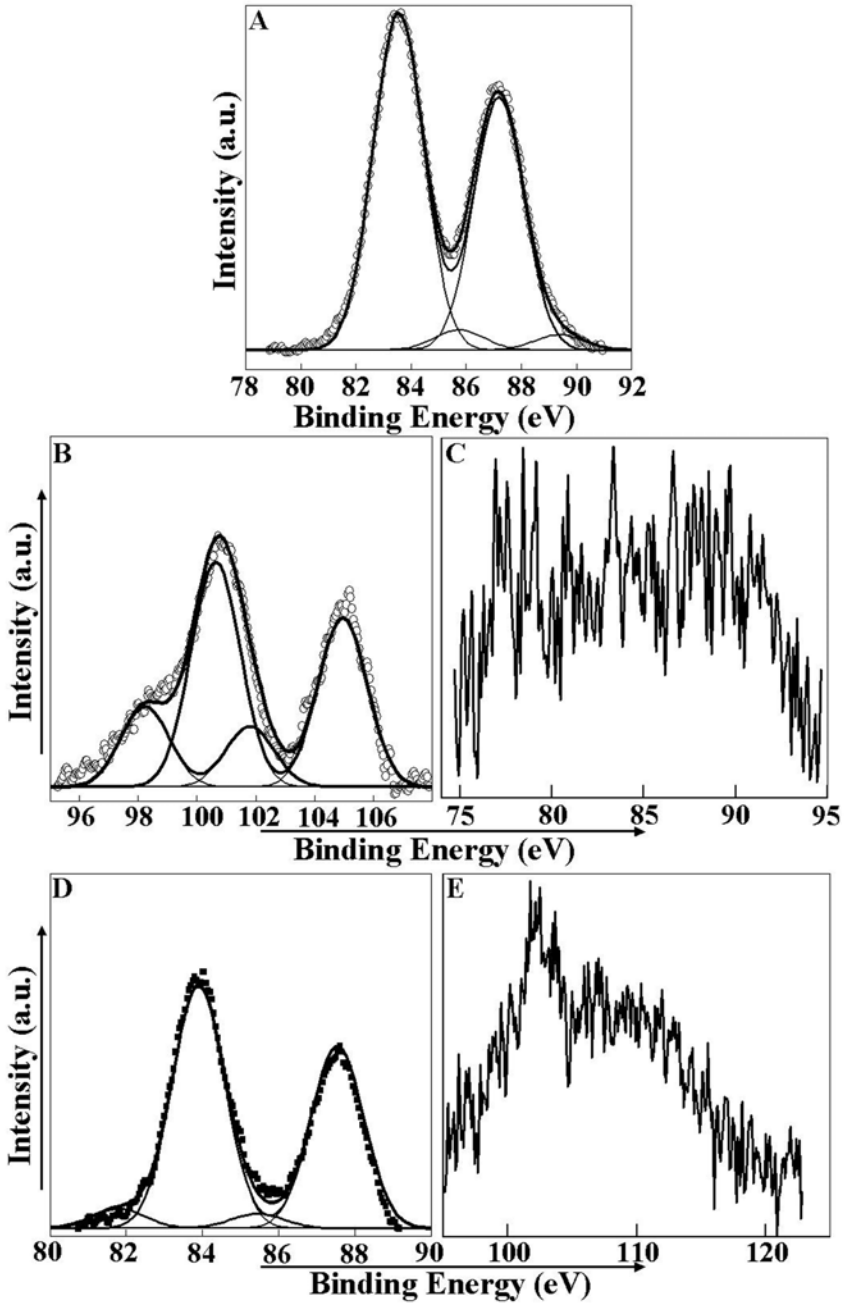

Figure 5.7 *(A) Au4f core level spectrum from the purified gold nanotriangles control. (B) Hg4f core level spectrum from the triangles treated with 10^{-3} M concentration of mercuric (II) ions in presence of 2.6 mM sodium borohydride. (C) Au4f core level spectrum from the triangles treated with 10^{-3} M concentration of mercuric (II) ions in presence of 2.6 mM sodium borohydride. (D) Au4f core level spectrum from the triangles treated with 10^{-15} M concentration of mercuric (II) ions in presence of 2.6 mM sodium borohydride. (E) Hg4f core level spectrum from the triangles treated with 10^{-15} M concentration of mercuric (II) ions in presence of 2.6 mM sodium borohydride.*

can be deconvoluted into two components at binding energies 82.1 and 83.9 eV. The high intensity peak at 83.9 corresponds to Au (0) oxidation state while the low binding energy component could be due to the gold amalgam [40]. The electronegativity of mercury is 1.9 while that of gold is 2.54 and thus mercury is electropositive in comparison with gold, which leads to a shift in the $Au4f_{7/2}$ peak to lower binding energies. It is important to note that no high binding energy peak corresponding to the presence of Au (I) is seen here which may be due to the fact that any amount of unreduced gold would get reduced to Au (0) in the presence of sodium borohydride. Figure 5.7E shows the shift corrected Hg 4f core level spectra from the sample and we can see that the signal here is very weak which suggests that the amount of mercury on the gold is very small. This is obvious due to the fact that a very low concentration of mercuric (II) ions (10^{-15} M) was added to this sample. Thus, from the XPS analysis, it is concluded that the addition of sodium borohydride indeed results in the reduction of mercuric ions to mercury metal, which in turn amalgamates the gold nanotriangles to distort their morphology.

5.2.2 Exposure of gold nanotriangles to lead.

5.2.2.1 Experimental details.

The as-prepared gold nanotriangle solution was centrifuged, purified and concentrated by the same protocol discussed in section 5.2.1.1. 4 mL of the concentrated purified gold nanotriangle solution was diluted to 40 mL and 4 mL aliquots were made to which lead (II) ions were added in different concentration to achieve desired final concentration. 10^{-2} M stock solution of $PbCl_2$ was used for the serial dilutions and the gold nanotriangles were exposed to lead ions of concentrations 10^{-3}, 10^{-6}, 10^{-9} and 10^{-12} M. 2.6 mM concentration of sodium borohydride was added to each aliquot to reduce the lead ions in the presence of the gold nanotriangles. The final solutions were then kept for 10 minutes at room temperature and were subsequently used for various characterizations. The solutions were characterized by UV-vis-NIR spectroscopy and TEM analysis.

5.2.2.2 UV-vis-NIR spectroscopy.

UV-vis-NIR spectroscopy was done for all the concentrations of lead ions exposed to gold nanotriangles in the presence of 2.6 mM concentration of sodium borohydride to monitor change in the optical properties of the gold nanotriangles. This

experiment was done with view to check the interference of lead with the results obtained for mercuric ions. It is a well know fact that lead is another severe water pollutant and it

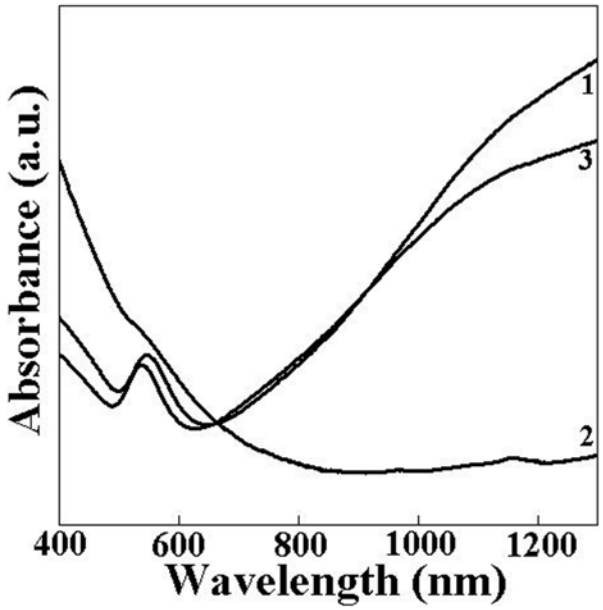

Figure 5.8 *UV-vis-NIR spectra of purified gold nanotriangles control (curve 1), control with 10^{-3} M (curve 2) and 10^{-6} M (curve 3) concentration of $PbCl_2$ in presence of 2.6 mM sodium borohydride.*

was necessary to check for the effect of lead on the gold nanotriangles. Figure 5.8 shows the UV-vis-NIR spectra of the control solution (curve 1), gold nanotriangles exposed to 10^{-3} M (curve 2) and 10^{-6} M (curve 3) in the presence of 2.6 mM concentration of sodium borohydride. It can be seen from the spectra that the gold nanotriangles exposed to 10^{-3} M concentration of lead metal show a complete loss of the NIR absorption peak while the spectrum corresponding to the solution exposed to 10^{-6} M concentration of lead metal shows a slight dampening in the NIR peak. Thus, from the spectra, it is obvious that at 1 mM concentration of lead, the presence of lead will interfere with the results of mercury detection. However, at 1 μM concentration, the change is almost equivalent to that obtained for gold nanotriangles exposed to 10^{-18} M concentration of mercury metal (Figure 5.1C, curve 2). When viewed from the point view of practical application, such high concentrations of lead in water samples are rarely encountered. It was seen that below 1 μM concentration of lead metal, the absorption profile of the gold nanotriangles overlap with that of control spectra suggesting no change in the morphology of the gold nanotriangles. Thus, the protocol can be used to detect mercuric ions in real life samples

where the actual concentrations of mercuric and lead ions is very small and thus the optical signal, if any, will be only from the presence of mercuric ions in the sample.

5.2.2.3 TEM measurements.

TEM analysis was done for the gold nanotriangles exposed to 1 mM and 1 μM concentration of lead metal in order to understand the reason behind the loss in the optical intensity of the NIR peak of gold nanotriangles in both the case (Figure 5.8, curve 2 & 3 respectively). The triangles which were treated with 1 mM solution of lead (II) chloride in the presence of the reducing agent showed that the morphology of the triangle remains intact (Figure 5.9A), though they are covered with metallic lead on the surface which results in the loss of the spectral signal of in the NIR region. It can be seen from the image that the structural integrity of the gold nanotriangles remain intact on exposure to 1 mM concentration of lead metal but the surface texture is highly roughened due to deposition of lead. It is well known that in core-shell type structure, the deposition of one metal over the other results into the loss of the spectral signature of the latter [41] and a similar phenomenon is observed here as well where the surface deposition of lead leads

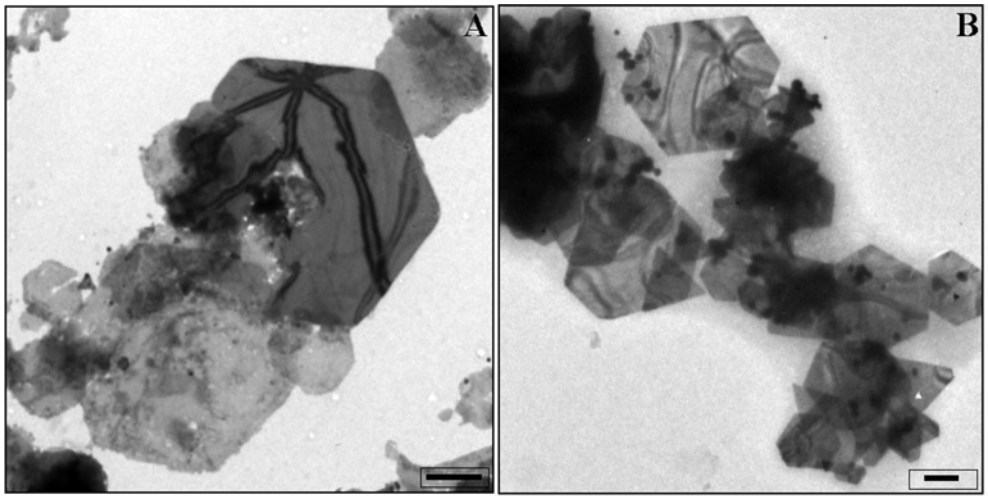

Figure 5.9 *(A) TEM image of purified gold nano triangle treated with 10^{-3} M lead (II) ions in the presence of 0.026 M sodium borohydride. (B) TEM image of purified gold nanotriangle treated with 10^{-6} M lead (II) ions in the presence of 2.6 mM sodium borohydride. The scale bars in A and B correspond to 1μM and 100 nm respectively.*

to the loss in the signature of gold in UV-vis-NIR spectra (Figure 5.8, curve 2). The picture becomes much more clear when the TEM micrograph of the gold nanotriangles exposed to 1 μM concentration was observed, where we see that the triangles are entirely intact at all the place (Figure 5.9B); however, they are seemed to be covered with a dense

cloud of metallic lead which causes a slight dampening in the NIR spectra of the gold nanotriangles. Thus, the TEM measurements clearly show that alloy formation does not take place in the case of exposure of gold nanotriangles to lead metal and that the same occurs on exposure to mercury only due to the strong amalgamation tendency of the mercury metal.

5.3 Discussion.

The above results conclusively show that biogenically prepared gold nanotriangles can be used as an optical beacon for the detection of mercuric ions in water samples with high specificity and selectivity. The strong tendency of mercury metal to amalgamate gold has been exploited in the work to induce injury to the gold nanotriangles, which leads to the partial loss in anisotropy, leaving a signature in the optical absorption spectra. The single crystalline gold nanotriangles are extremely thin as shown by the AFM measurements and thus, addition of any foreign atom to their crystal lattice tends to cause a strain on the nanostructure, resulting into the distortion of geometry and eventual loss of the morphology.

In one of our previous reports, it has been shown that the formation of adlayers of halide ions on these triangles induces a shape transformation [35] depending on the strength of binding and interaction of the halide ions with the crystallographic planes of gold fcc structure. There, it has been shown that the bromide and iodide ions, which bind strongly to the {110} plane of gold nanotriangles (comprising the edges and tip) induce a shape transformation while chloride does not show any such behavior. The propensity of mercury metal to interact strongly with gold nanotriangles at the edges and the tips brings about similar structural transformations. The propensity of amalgamation at the edges and tips is probably due to the fact that they are the sites of structural defects in the triangular lattice. The optical property of gold nanotriangle shows two distinct absorption peaks; the transverse plasmon peak at around 530 nm and another longitudinal plasmon peak, which is a function of the aspect ratio of the nanotriangles and thus strongly depends on the structural integrity of the nanostructure. It is observed that the amalgamation leads to the breaking off of the gold nanotriangles, a process initiated at the edges and tips of the nanotriangles. The HRTEM analysis reveals a slight change in the lattice parameter of the {111} plane from 2.36 Å to 2.40 Å at the edges of the triangles treated with mercury

metal. Also, in one of the HRTEM images, it is observed that the edge of one of the gold nanotriangle shows a finger like projection, a snapshot of the budding off of amalgamated gold atoms from the edge of the nanotriangle, leading to breaking off of the structure eventually. The EDX analysis of that projected structure reveals a high content of mercury along with gold, which confirms the fact that the event is an outcome of amalgamation. Thus, amalgamation of gold nanotriangles leaves them damaged and broken with corrugated edges.

This process is also confirmed indirectly due to presence of small sized spherical nanoparticles, which were absent in the control sample, and their EDX analysis reveals a high content of mercury along with gold. Thus, they are probably the broken off product of the amalgamation process. As discussed above, the longitudinal plasmon peak arises due to the anisotropy of the structure and thus, the change in the structural morphology is shown in the NIR absorption peak in the form of dampening, which is found to be in proportion with the concentration of the mercury metal. It is important to mention that at lower concentrations i.e. 10^{-15} and 10^{-18} M, a good population of the gold nanotriangles is intact in morphology but still a significant change in seen in the optical spectra. Thus, this indicates that the NIR optical absorption sensitively depends on the structural integrity. The same protocol was also checked for sensitivity towards lead metal and it was seen that only at concentrations as high as 10^{-6} M, a significant change is recorded. Thus, this indirectly shows that the structural transformation is brought about solely due to the strong amalgamating tendency of mercury metal. It has also been shown that the reducing agent (2.6 mM sodium borohydride) and mercury ions by themselves show no change in the optical absorption of the gold nanotriangles, ruling out any change from their individual contribution.

5.4 Conclusion.

The chapter describes the use of anisotropic gold nanotriangles with exotic optical properties as candidates for sensitive and specific detection of mercuric ions in the water samples at concentrations as low as 10^{-18} M. The protocol is extremely simple, cost-effective and free of any sample processing. Besides, it takes only 30 minutes to sensitively detect the presence of mercury in a water sample. Here, mercuric ions have been reduced externally into mercury metal, in the presence of gold nanotriangles, which

leads to amalgamation of the thin sheets of gold at the edges and tips. The salient observation here is that mercury metal does not get incorporated into the crystal lattice of the gold nanotriangles but tends to break off the amalgamated sites leading to structural damage and changed optical properties. This change in the optical property has been used as a method to estimate the concentration of mercuric ions in the sample. The protocol does not show similar sensitivity to lead ions where the change is seen only at concentrations as high as 10^{-6} M and thus, the protocol holds valid for real life samples where the high concentration interference of the lead is not possible. Thus, this can be a simple and fast method for sensitive detection of the mercury in the water samples and thus can be of immense application in monitoring the mercury levels in the aquatic systems.

5.5 References.

(1) http://www.epa.gov/mercury/exposure.htm

(2) (a) Wood, J.M.; Kennedy, F.S.; Rosen, C.G. *Nature* **1968**, *220*, 173. (b) Hamdy, M.K.; Noyes, O.R. *J. Appl. Microbiol.* **1975**, *30*, 424.

(3) Karadjova, I.; Mandjukov, P.; Tsakovsky, S.; Simeonov, V.; Startis, J.A.; Zachariadis G.A. *J. Anal. At. Spectrom.* **1995**, *10*, 1065.

(4) (a) McMullin, J. F.; Pritchard, J. G.; Sikondari, A. H. *Analyst*, **1982**, *107*, 803. (b) Liang, L.; Bloom, N.S. *J. Anal. At. Spectrom.* **1993**, *8*, 591.

(5) Karunasagar, D.; Arunachalam, J.; Gangadharan, S. *J. Anal. At. Spectrom.* **1998**, *13*, 679.

(6) (a) Bloxham, M. J.; Hill, S. J.; Worsfold, P. J. *J. Anal. At. Spectrom.* **1996**, *11*, 511. (b) Sällsten, G.; Nolkrantz, K. *Analyst* **1998**, *123*, 665.

(7) Pritchard, J. G.; Saied, S. 0. *Analyst* **1986**, *111*, 29.

(8) (a) Evans, O.; McKee, G.D. Analyst 1988, 113, 243. (b) Hempel, M.; Hintelmann, H.; Wilken, R. *Analyst*, **1992**, *117*, 669.

(9) Pirvutoiu, S.; Surugiu, I.; Dey, E. S.; Ciucu, A.; Magearu, V.; Danielsson, B. *Analyst* **2001**, *126*, 1612.

(10) Morris, T.; Szulczewski, G. *Langmuir* **2002**, *18*, 5823.

(11) Salaün, P.; van den Berg, C. M. G. *Anal. Chem.* **2006,** *78*, 5052.

(12) (a) Crisp, S.; Meddle, D.W.; Nunan, J.M.; Smith, A.F. *Analyst* **1981**, *106*, 1318. (b) Mazzolai, B.; Mattoli, V.; Raffa, V.; Tripoli, G.; Accoto, D.; Menciassi, A.; Dario, P. *Sens. Actuators. A* **2004**, *113*, 282.

(13) (a) Kuswandi, B.; Narayanaswamy, R. *Sens. Actuators B* **2001**, *74*, 131. (b) Métivier, R.; Leray, I.; Lebeau, B.; Valeur, B. *J. Mater. Chem.* **2005**, *15*, 2965. (c) Zimmerman, R.; Basabe-Desmonts, L.; van der Baan, F.; Reinhoudt, D. N.; Crego-Calama, M. *J. Mater. Chem.*, **2005**, *15*, 2772.

(14) Fayad, P. B.; Amyot, M.; Sauvé, S. *J. Environ. Monit.* **2004**, *6*, 903.

(15) Lindstedt, G. *Analyst* **1970**, *95*, 264.

(16) (a) Louie, H.W. *Analyst* **1983**, *108*, 1313. (b) Yoon, S.; Albers, A. E.; Wong, A. P.; Chang, C. J. *J. Am. Chem. Soc.* **2005**, *127*, 16030.

(17) Li, Y.; Zheng, C.; Ma, Q.; Wu, L.; Hua, C.; Hou, X. *J. Anal. At. Spectrom.* **2006**, *21*, 82.

(18) (a) Sporek, K.F. *Analyst* **1956**, *81*, 474. (b) Sporek, K.F. *Analyst* **1956**, *81*, 478.

(19) (a) Konishi, T.; Takahashi, H. *Analyst* **1983**, *108*, 827. (b) Kan, M.; Willie, S.N.; Scriver, C.; Sturgeon, R.E. Talanta 2006, 68, 1259.

(20) Coronado, E.; Galán-Mascarós, J. R.; Martí-Gastaldo, C.; Palomares, E.; Durrant, J. R.; Vilar, R.; Gratzel, M.; Nazeeruddin, M. K. *J. Am. Chem. Soc.* **2005**, *127*, 12351.

(21) Nolan, E.M., Lippard, S.J. *J. Am. Chem. Soc.* **2003**, *125*, 14270.

(22) Takahashi, Y.; Kasai, H.; Nakanishi, H.; Suzuki, T. M. *Angew. Chem. Int. Ed.* **2006**, *45*, 913.

(23) (a) Britton, G.T.; Mcbain, J.W. *J. Am. Chem. Soc.* **1926**, *48*, 593. (b) Sunier, A.A.; Gramkee, B.E. *J. Am. Chem. Soc.* **1929**, *51*, 1703. (c) Sijnier, A.A.; White, C.M. *J. Am. Chem. Soc*. **1930**, *52*, 1842. (d) Sunier, A.A.; Weiner, L.G. *J. Am. Chem. Soc.* **1931**, *53*, 1714. (e) Mees, G. *J. Am. Chem. Soc.* **1938**, *60*, 870.

(24) (a) McNerney, J.J.; Buseck, P.R.; Hanson, R.C. *Science* **1972**, *178*, 611. (b) Chaurasia, H. K.; Huizinga, A.; Voss, W. A. G. *J. Phys. D : Appl. Phys.* **1975**, *8*, 214.

(25) Ping, L.; Dasgupta, P.K. *Anal. Chem.* **1989**, *61*, 1230.

(26) Leong, P.C.; Ong, H.P. *Anal. Chem.* **1971**, *43*, 940.

(27) Kim, Y.; Johnson, R.C.; Hupp, J.T. *Nano Lett.* **2001**, *1*, 165.

(28) Sau, T.K.; Murphy, C.J. *J. Am. Chem. Soc.* **2004**, *126*, 8648.

(29) Jana, N.R.; Gearheart, L.; Murphy, C.J. *J. Phys. Chem. B* **2001**, *105*, 4065.

(30) Hanarp, P.; Kall, M.; Sutherland, D. S. *J. Phys. Chem. B.* **2003**, *107*, 5768.

(31) Nehl, C.L.; Liao, H.; Hafner, J.H. *Nano Lett.* **2006**, *6*, 683.

(32) (a) Shao, Y.; Jin, Y.; Dong, S. *Chem. Commun.* **2004**, 1104. (b) Shankar, S.S.; Rai, A.; Ankamwar, B.; Singh, A.; Ahmad, A.; Sastry, M. *Nat. Mater.* **2004**, *3*, 482.

(33) Shankar, S.S.; Rai, A.; Ahmad, A.; Sastry, M. *Chem. Mater.* **2005**, *17*, 566.

(34) Rex, M.; Hernandez, F. E.; Campiglia, A. D. *Anal. Chem.* **2006**, *78*, 445.

(35) Rai, A.; Singh, A.; Ahmad A.; Sastry M. *Langmuir* **2006**, *22*, 736.

(36) Kelly, KL.; Coronado, E.; Zhao, L.L.; Schatz, G.C. J. Phys. Chem. B **2003,** *107*, 668.

(37) (a) Germain, V.; Li, J.; Ingert, D.; Wang, Z.L.; Pileni, M.P. *J. Phys. Chem.* B **2003**, *107*, 8717. (b) Salzemann, C.; Lisiecki, I.; Urban, J.; Pileni, M.P. *Langmuir* **2004**, *20*, 11772.

(38) Lofton, C.; Sigmund, W. *Adv. Funct. Mater.* **2005**, *15*, 1197.

(39) Shirley, D. A. *Phys. Rev. B.* **1972**, 5, 4709.

(40) Wagner, C.D; Riggs, W.M.; Davis, L.E.; Moulder, J.F.; Muilenberg, G.E. *Handbook of X-ray photoemission spectroscopy, Perkin Elmer Corp. Publishers, Eden Prairie*, MN, **1979**.

(41) Mulvaney, P. *Langmuir* **1996**, *12*, 788.

Chapter VI

Cytotoxicity studies and cellular internalization of gold nanotriangles in animal cell lines

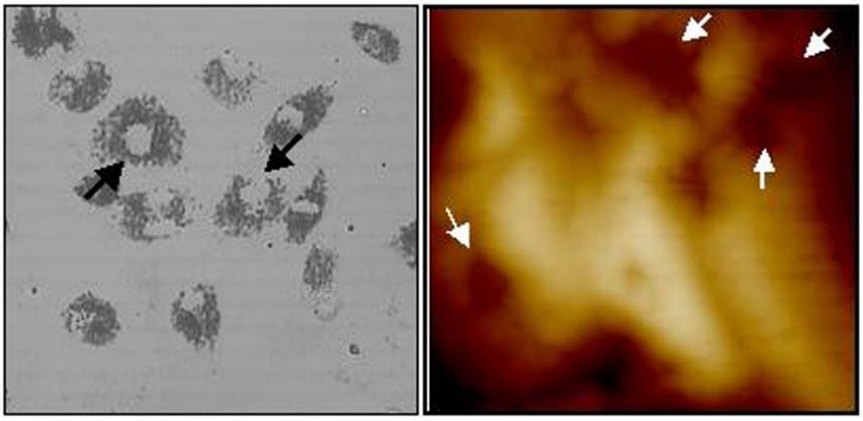

This chapter discusses the use of biogenic gold nanotriangles to study the cytotoxicity and biocompatibility of biologically synthesized nanomaterial on animal cells. Cancerous as well as non-cancerous cells were used to study the dose dependent viability of the cells on exposure to the triangles. Besides, it was observed that the gold nanotriangles are internalized inside the cells and are compartmentalized in the cytoplasm. Thus, it has been shown that the biologically synthesized gold nanotriangles are indeed biocompatible and thus are promising candidates as scaffolds for delivery of drug, genes or growth factors inside the cells.

6.1 Introduction.

Nanotechnology is revolutionizing human life in a big way in the past decade. Metal nanomaterials have specially been investigated for several applications in the field of catalysis [1], fuel cells [2], heavy metal detection [3], photonic band-gap materials [4], single electron transistors [5], non-linear optical devices [6], surface-enhanced Raman spectroscopy [7], chemical sensing [8], biology and medicine [9]. They have also used with interest in biomedical applications due to the fact that colloidal gold and silver have been known to possess potential curative abilities since ancient times for many diseases. They have been reported as Aurum potable (drinking gold) and luna potable (drinking silver) in ancient literature and have been considered as elixirs by alchemists since 1570 [10]. Colloidal gold has been the candidate of prime interest to the researchers and several works have lead to its potential application in the field of biodiagonostics [11], therapeutics [12], drug delivery [13], bioimaging [14], immunostaining [15] and biosensing [16]. Thus, the future use of gold nanostructures for various biological and clinical applications has been envisioned [17].

Owing to the fact that metal nanoparticles have found a strong niche in the world of nanotechnology, there has been a constant conscience effort to develop recipes for synthesis of metal nanostructures of varying size, shapes and properties. Till date, synthesis of rods [18], disks [19], triangular prisms [20], multipods [21], cubes [22] and nanoshells [23] have successfully been reported using several physical and chemical methods. However, recently biological synthesis of metal nanostructures has gained tremendous popularity due to the environmental friendly green chemistry approach. After the first report on the use of a microorganism (*Pseudomonas stutzeri* AG259) by Klaus et al. [24] for synthesizing silver nanoparticles intracellularly, there have been numerous attempts to use biological materials. Till date, reports are available on successful use of several bacteria [25], S-layer [26], fungi [27], algae [28] and plant systems [29] for the synthesis of metal nanostructures. However, precision over synthesis of nanoparticles of an anisotropic shape using biological systems has been an unrealized dream for a long time. Shao et al. had used aspartic acid for synthesis of gold nanotriangles [29g]. Yet, the major break-through was the report by Sastry and coworkers on synthesis of large population of gold nanotriangles by a room temperature method, using leaf extract of lemon grass plant (*Cymbopogon flexuosus*) [29h]. The nanotriangles thus formed show very interesting optical properties with a strong absorbance

in the near-IR (NIR) region owing to their anisotropic shape [29h, 30]. Sastry and coworkers have shown that the NIR optical absorbance peak of these gold nanotriangles can be tuned at will by controlling the rate of reduction varying the amount of reducing agent [31] or the temperature of the reaction [32]. It is due to this strong optical absorbance in the NIR region due to which these triangles have been shown to have potential application in the field of optical coatings to block high-energy radiations [31]. Besides, one of its futuristic applications, which can be envisaged, is in the hyperthermic treatment of tumorous cancer.

However, the biocompatibility of the gold nanotriangles is a key issue to be addressed before its use in any clinical or biological application. One of the important aspects to be considered here should be the cytotoxicity of the gold nanotriangles owing to their size [33], shape [34], chemical composition [35], property [34] or interaction with cell surface [36], which have been known to affect the biocompatibility of a material. The initial studies on cytotoxicity of nanomaterials have been mainly focused on aerosols and their intake and concentration in the lungs [37]. Later, the toxicity effects of heavy metals [35] and quantum dots [38] were studied in great details. However, with a proved potential in the biomedical field, gold has also be used as a system to study the biocompatibility and cytotoxicity effect. There are numerous reports on the cytotoxicity studies gold (I) [39] and gold (III) [39b,c, 40] precursors; apart from the gold nanoparticles itself [41].

Although, a lot of work has been done to ascertain the cytotoxicity levels and biocompatibility issues related with gold nanoparticles, Sastry and coworkers gave the first detailed account of the immunological response of cells on exposure to the gold nanoparticles and elucidated the mode of internalization [42]. They have reported that the gold nanoparticles synthesized by sodium borohydride reduction do not show any visible cytotoxicity upto 100 μM concentration in macrophages, which are actively phagocytotic cells. Furthermore, it has been shown that they do not elicit any stress-induced production of proinflammatory cytokines TNFα or IL-1β in the macrophages. At higher concentrations, the gold nanoparticles inhibit the secretion of reactive oxygen species (ROS) and reactive nitrite species (RNS) and thus indicate that they have much to offer in the gold nanoparticle based biomedical applications. It has been observed that the gold nanoparticles are internalized inside the cells by the mechanism of pinocytosis and are compartmentalized in the lysosomes to arrange in the perinuclear space without entering the nucleus. Thus, this report, in

particular, has rationalized the attempts from different groups across the world on the use of gold nanoparticles for various biomedical applications.

In the work presented in this chapter, an attempt has been made to perform similar experiments on the *biogenic anisotropic gold nanostructures*. Biological synthesis has been looked upon as an environmentally benign replacement to the toxic chemical methods for synthesis of nanostructures. It is believed that the biogenic nanostructures will be biocompatible too and thus, will have immense application in the biological and clinical aspects. However, no sincere attempt has been made to scientifically confirm this hypothesis. The following sections are devoted to address these issues using gold nanotriangles. The gold nanotriangles were synthesized by the reduction of chloroaurate ions using the leaf extract of lemon grass plant. Selectively, small sized gold nanotriangles were synthesized for this work, which have NIR absorbance maxima centered around 950 nm. This was done with the anticipation that these triangles could be an excellent candidate for hyperthermic treatment of cancer cells if the optical properties are tuned such that the live cells are transparent to that wavelength [43]. The cytotoxicity studies were performed on cancerous as well as non-cancerous human cell lines, which reveal that gold nanotriangles do not show any cytotoxicity to the exposed cells upto 800 μM concentrations for 24 h. The flow cytometry results and phase contrast microscopy images confirm that the gold nanotriangles are indeed internalized inside the cells.

6.2 Synthesis and purification of small sized gold nanotriangles.

6.2.1 Experimental details.

The gold nanotriangles were synthesized as described elsewhere [29h]. In a typical experiment, lemon grass (*Cymbopogon flexuosus*) broth was prepared by boiling 100 gm of freshly cut and thoroughly washed leaves of the plant in 500 mL water for 5 min. 1, 1.4, 1.8, 2.2, 2.6 and 3 mL of this broth was then added to 10 mL of 10^{-3} M aqueous solutions of chloroaurate ions and the reduction process was monitored by UV-vis-NIR spectroscopy measurements. The varying amount of broth helps in controlling the rate of chloroaurate ion reduction. It has been observed that higher the amount of the broth (reducing agent), higher is the rate of reduction and thus, smaller is the size of nanotriangles formed. The optical absorption of these test solutions helped in choosing the concentration of the broth, which form gold nanotriangles with NIR optical maxima around 950 nm. It was observed that when

3 mL of broth was taken in 10 mL of 10^{-3} M chloroaurate ions, we obtain solution with desired optical absorption characteristics. The process was scaled up by making 5 batches of the solutions, where 30 mL of the broth was added to 100 mL of 10^{-3} M chloroaurate ions in each batch to maintain the same ratio as in the test solution. The solution gives a ruby-red color rather than the typical brown-red color obtained for the solution prepared by standard procedure, indicating that it contains more of spherical nanoparticles rather than the triangular ones. The triangular nanoparticles were purified from the solution by two rounds of centrifugation at 3000 rpm for 30 minutes each, followed by two rounds at 2000 rpm for 30 minutes. The pellet was thoroughly washed with deionized water after each round of centrifugation and was finally resuspended in 5 mL of deionized water by sonication for 10 minutes. The pellets from all the batches were pooled together to get the final solution of purified gold nanotriangles, which was characterized by UV-vis-NIR and transmission electron microscopy (TEM). Simultaneously, atomic absorption spectroscopy of the solution was also done, which revealed that the concentration of gold in the final solution was 2.4 mM.

6.2.2 UV-vis-NIR spectroscopy.

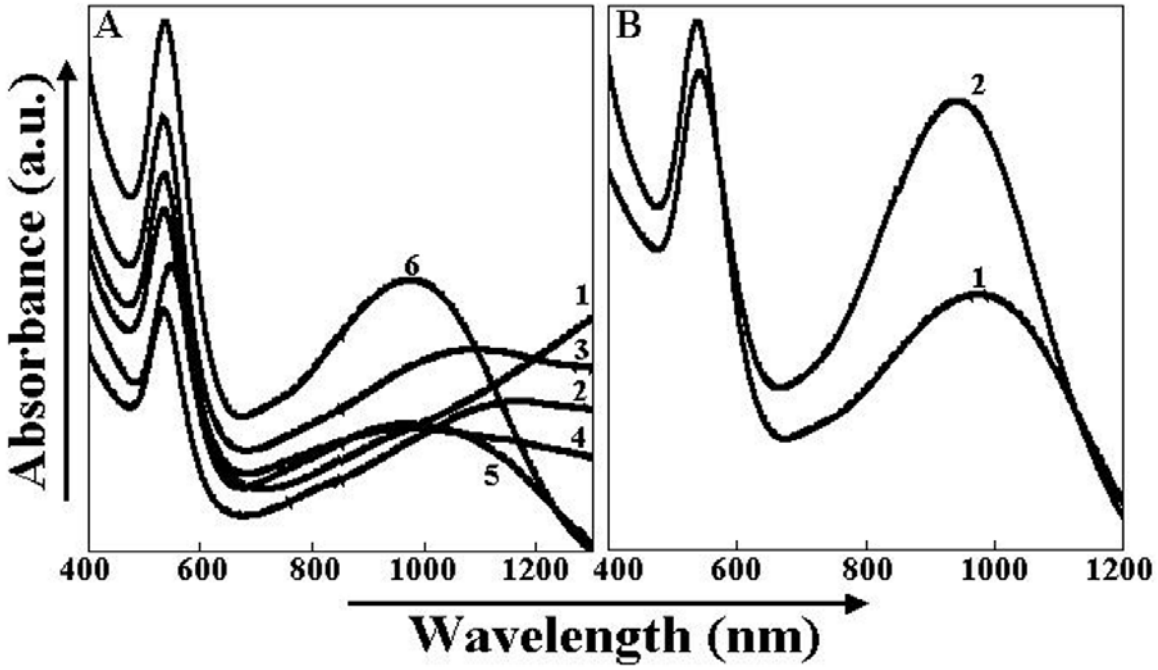

Figure 6.1 *(A) UV-vis-NIR spectra of the gold nanotriangle solutions. Curves 1-6 correspond to 1, 1.4, 1.8, 2.2, 2.6 and 3 mL of broth respectively in 10 mL of 10^{-3} M chloroaurate ions. (B) UV-vis-NIR spectra of as-synthesized solution (curve 1) and purified gold nanotriangle solution (curve 2).*

The test solutions were analyzed by UV-vis-NIR spectroscopy and Figure 6.1A shows the optical spectra of the different gold nanoparticle solutions obtained. Curves 1-6 show the absorption spectra of the as-synthesized gold nanotriangle solution using 1, 1.4, 1.8, 2.2, 2.6 and 3 mL of broth respectively in 10 mL of 10^{-3} M concentration of chloroaurate ions. The position of the absorption maxima in the NIR region (longitudinal plasmon peak) clearly shows a blue shift with increasing concentration of the lemon grass broth (reducing agent) in the solution. Besides, a transverse plasmon peak is observed in the visible region centered at 530 nm in all the curves. Also, the plot clearly reveals that curve 6 shows the NIR plasmon centered at 950 nm, which corresponds to the gold nanoparticle solution synthesized using 3 mL of lemon grass broth. As has been discussed in the section 6.2.1, this recipe for synthesis of gold nanotriangles was used for all the further analysis. The reason behind choosing the solution with NIR optical absorption maxima at 950 nm is that the human cells are optically transparent at this wavelength and thus, the gold nanotriangles in this solution can serve as excellent candidates for hyperthermic treatment of cancerous cells.

Figure 6.1B shows the UV-vis-NIR spectra of the as-synthesized gold nanoparticle solution (curve 1) prepared by reducing 100 mL of 10^{-3} M concentration chloroaurate ions using 30 mL of the lemon grass broth. It can be clearly concluded from the nature of the curve that the absorption characteristic of the gold nanoparticle solution remains essentially the same when the reaction was carried out using 100 mL of initial volume of chloroaurate ions (compared to curve 6, Figure 6.1). However, it is worthwhile mentioning that this does not hold true for larger volumes, where we observe change in the absorption profile of the final solution. Therefore, it was necessary to prepare 5 small batches of 100 mL each rather than one batch of 500 mL of chloroaurate ions with corresponding amount of the lemon grass broth as per the ratio followed. Curve 2 in Figure 6.1B corresponds to the purified gold nanotriangles after the centrifugation. It can be seen from the intensity of the longitudinal to transverse plasmon peak that the triangular nanoparticle population has increased in the solution after centrifugation, as compared to the as-synthesized solution (curve 1). Thus, the as-synthesized solution was indeed enriched in the population of gold nanotriangles after centrifugation. However, some spherical gold nanoparticles do remain in the solution along with the triangles, as can be realized from the intense peak at 535 nm in the optical spectrum from the purified solution (curve 2). The TEM analysis in the following section will reveal

that the triangles synthesized by this recipe are small in size and thus, it is very difficult to separate them completely from the spherical particles by the use of centrifugation based purification.

6.2.3 TEM analysis.

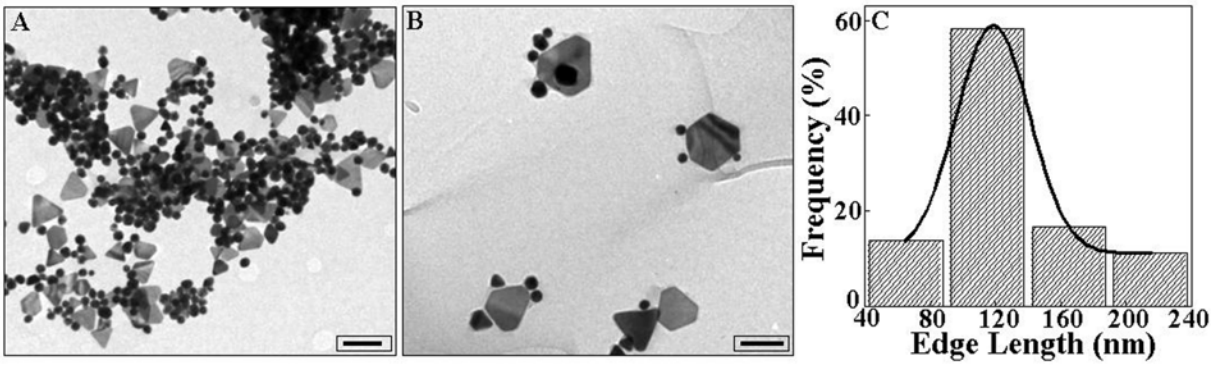

Figure 6.2 *(A) Representative TEM image of as-synthesized gold nanotriangles. (B) Representative TEM image of the purified gold nanotriangles. The scale bars in A and B correspond to 200 and 100 nm. (C) Particle size distribution plot of the gold nanotriangles. The average edge length was found to be 113 nm.*

The as-synthesized and purified gold nanotriangle solutions were analyzed by TEM imaging. Figure 6.2A shows the TEM micrograph of the as-synthesized gold nanotriangles, which clearly shows a large population of spherical gold nanotriangles along with the triangles. However, the most important observation to be made here is that the triangles synthesized by this method (increasing the amount of reducing agent) are much smaller in size as compared to those formed by the standard method described elsewhere [29h]. Figure 6.2B shows the representative TEM micrograph obtained for the purified gold nanotriangles. The image clearly indicates that the population of gold spherical particles has reduced considerably in the solution after the purification step and the relative population of triangles has improved significantly. Figure 6.2C shows the particles size distribution plot for the gold nanotriangle synthesized by the modified protocol. It is observed that nearly 60% population of the gold nanotriangles is in the size range 80-120 nm as opposed to the average size of 440 nm observed for the gold nanotriangles synthesis of standard method (Chapter 3, Figure 3.A.2C). This observation corroborates well with the optical absorption spectra of the solution, which showed that the NIR peak was centered around 950 nm (Figure 6.1B, curve 2). Thus, TEM imaging and particle size distribution analysis clearly indicates that the gold

nanotriangles, which have absorbance maxima at 950 nm, are predominantly those that have an edge length ranging between 80-120 nm.

6.3 Cytotoxicity studies using gold nanotriangles.

6.3.1 Experimental details.

The cytotoxicity studies were performed in the cancerous (RAW264.7 macrophages & MCF-7 human breast cancer cell line) as well as non-cancerous (NIH 3T3 mouse embryonic fibroblast cell line) cells. The RAW264.7 macrophages were cultured in RPMI-1640 culture medium while the MCF-7 and NIH 3T3 cells were cultured in Dulbecco's modified Eagle's medium (DMEM). Both the culture mediums were supplemented with 10% fetal calf serum (FCS), 100 units/mL penicillin, 100 μg/mL streptomycin, and 2 mM glutamine and the cells were incubated in a humidified atmosphere of 5% CO_2 and 95% air at 37 °C. Actively growing cells were seeded with density around $1X10^5$ cells/well in a 96-well tissue culture plate. The cells were treated with different concentrations of gold nanotriangles (5, 25, 50, 100, 200, 400 and 800 μM) for 24 h. The control cells were not treated with gold nanotriangles and were kept in the same volume of phosphate buffer saline (PBS, p^H-7.4) for the same period of time. After the end of the exposure time, the cell viability was checked using the 3-(4,5-dimethylazol-2-yl)-2,5- diphenyl-tetrazolium bromide (MTT) assay [44]. The MTT assay is based on the optical detection of the purple colored formazan at 570 nm, which is formed by the enzymatic reduction of yellow tetrazolium MTT. All experiments were performed 3 times in quadruplets, and their average has been shown as cell-viability percentage in comparison with the control experiment. The gold triangles untreated controls were considered to be 100% viable.

6.3.2 MTT assay.

The cytotoxicity of gold nanotriangles under *in vitro* conditions in RAW264.7 macrophage cells was examined in terms of the effect of gold nanoparticles on cell proliferation by the MTT assay. Figure 6.3A shows the histogram plot of MTT assay results for cell viability studies performed on RAW264.7 macrophage cell line after exposing to varying concentrations of gold nanotriangles. The white bars correspond to the gold precursor (aqueous solution of $HauCl_4$) while the gray bars correspond to the % cell viability at the given concentration of gold nanotriangles. The plot clearly shows 75 % cell viability for the cells that were treated with 800 μM concentration of gold nanotriangles for 24 h. On

the contrary, the LD_{50} (lethal dose 50 i.e. the concentration of the material in question which causes death of 50 % of cell population) is achieved in the case of gold precursor at the concentration as low as 50 μM. Thus, it can be easily concluded from this result that the gold salt precursor ($AuCl_4^-$ ions) is highly toxic to the cells while the biogenic gold nanotriangles do not show acute toxicity even at high concentrations. This result become even more important when it is compared with the result of the same experiment using chemically synthesized spherical gold nanoparticles [42]. The borohydride-reduced gold nanoparticles show nearly 80 % cell viability at the exposure to 100 μM concentration for 24 h. Thus, it can be conclusively inferred that biogenic gold nanotriangles are more biocompatible than chemically synthesized gold nanoparticles and can be looked upon as promising candidate for biomedical applications.

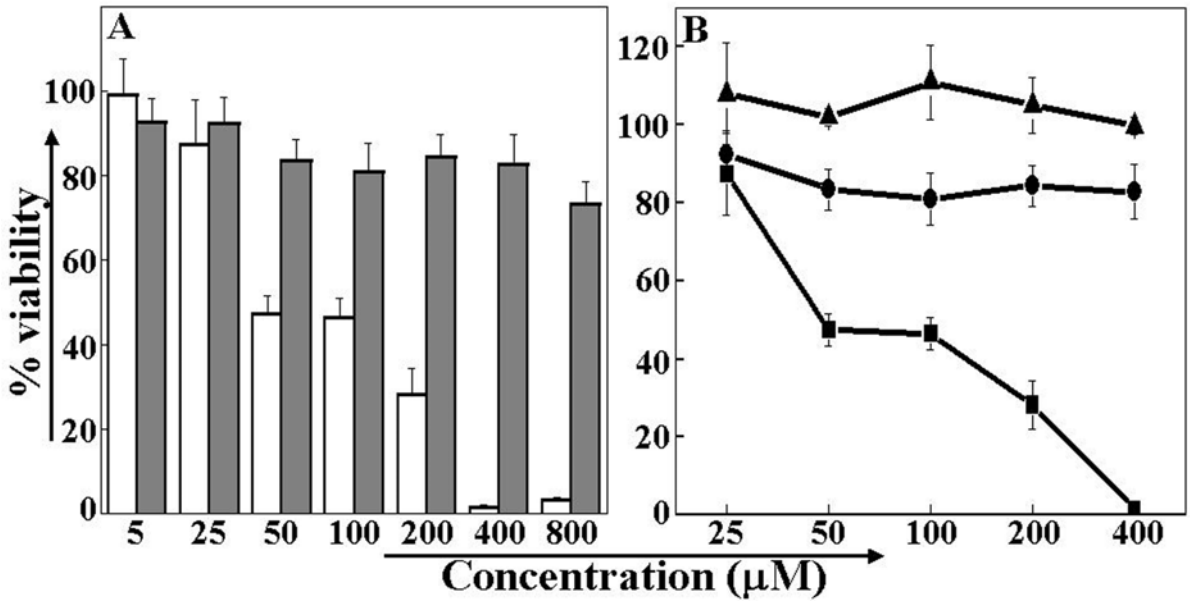

Figure 6.3 *(A) MTT assay showing cell viability during exposure of RAW264.7 cells to varying concentration of gold nanotriangles for 24 h. The white and gray bars correspond to exposure of cells to gold salt precursor and gold nanotriangles respectively. (B) MTT assay showing cell viability during exposure of gold nanotriangle to cancerous MCF-7 (▲), non-cancerous NIH 3T3 (●) and exposure of gold salt precursor to non-cancerous NIH 3T3 (■) for 24 h.*

Figure 6.3B shows the MTT assay results for cell viability studies performed on cancerous MCF-7 (▲) and non-cancerous NIH 3T3 (●) cells after 24 h exposure to gold nanotriangles. Simultaneously, NIH 3T3 cells were also exposed to gold salt precursors (■) and checked for cell viability after 24 h. The percent viability of the cells has been calculated considering the respective untreated cells to have 100 % viability. The MCF-7 cells show

almost 100 % viability after exposure to 400 μM concentration of gold nanotriangles for 24 h. It is also seen that the viability at lower concentrations is nearly 110 %, which suggests that the gold nanotriangles have some growth proliferating effects on the MCF-7 cells. When the gold nanotriangles were exposed to the non-cancerous NIH 3T3 fibroblast cells, it was observed that the cells show 83 % viability for 400 μM concentration of the gold nanotriangles after exposure for 24 h. When these non-cancerous cells were exposed to the gold salt precursor, the LD_{50} was attained at the concentration of 50 μM and at 400 μM concentration, almost all the cells were found dead. Thus, these results suggest that the gold nanotriangles do not show any cellular toxicity to non-phagocytotic cancerous as well as non-cancerous cells while the gold salt precursor showed acute toxicity to the cells.

6.3.3 Studies on stress induction by gold nanotriangles.

6.3.3.1 Experimental details.

The RAW264.7 cells were seeded at the cell density of 1 X 10^6 cells/well in the 6-well tissue culture plates and grown overnight. The cells were treated with 250 μM concentration of gold nanotriangles for 24 hours. Simultaneously, the cells treated with 5 μM concentration of bacterial lipopolysacchride (LPS) were taken as the positive control for this experiment while the untreated cells served as the standard control. The culture supernatants in all the cases were assayed for the proinflammatory cytokines TNF-α (tumor necrosis factor-α) by enzyme-linked immunosorbent assay (ELISA) using the Opt-EIA kits (BD Biosciences). The ELISA experiments were performed as per the instructions given by the manufacturer. The RAW264.7 macrophage cells were chosen for this experiment due to the fact that macrophages are primary immune effector cells and thus, there would be maximum probability of particle internalization by them through active phagocytosis. Therefore, they are the most suitable candidates for study of stress induction.

6.3.3.2 Enzyme-linked immunosorbent assay.

Macrophages are one of the primary immune effector cells and are known to be actively phagocytotic in nature. Thus, in addition to the cytotoxicity studies on exposure to the gold nanotriangles, the immonological response of the RAW264.7 macrophages cells was analyzed by enzyme linked immunosorbent assay. Here, the proinflammatory cytokine, TNF-α production was analyzed at the protein level to check the stress induction in the cells on exposure to gold nanotriangles. Figure 6.4 shows the histogram of the results from the

ELISA analysis for the untreated control cells, bacterial LPS treated positive control and the cells treated with 250 μM concentration of gold nanotriangles. It can be clearly seen that the untreated control cells did not show any sign of stress and the production of TNF-α cytokine

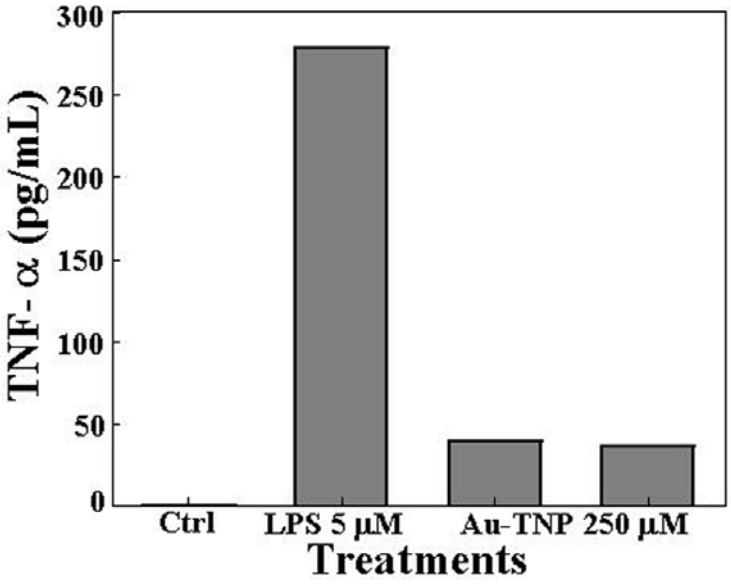

Figure 6.4 *The ELISA analysis using RAW264.7 macrophage cells showing the expression of TNF-α in control, lipopolysaccharide (LPS) treated and gold nanotriangles (Au-TNP) treated cells.*

was negligible. However, the macrophage cells, which were exposed to 250 μM concentration of gold nanotriangles, show 35 pg/mL concentration of the cytokine. Thus, it can be concluded that exposure of the gold nanotriangles does cause some stress to the macrophages, even though the cells are viable after 24 hours of incubation. The cells that were incubated with bacterial LPS showed a significant amount of TNF-α production, which is expected as bacterial LPS in known to cause stress to the cells. Thus, the ELISA analysis suggests that the exposure of gold nanotriangles to the macrophage cells indeed induces stress on the cells and elicits immunological response in the form of production of the proinflammatory cytokine TNF-α. However, the cytokine produced was much smaller in concentration compared to the positive LPS treated control.

6.4 Cellular internalization of gold nanotriangles.

6.4.1 Experimental details.

The NIH 3T3 fibroblast cells were treated with 50, 100 and 250 μM concentration of gold nanotriangles and incubated for 24 h in a humidified atmosphere of 5% CO_2 and 95% air at 37 °C. Thereafter, the cells were washed thoroughly in phosphate buffer saline (PBS,

p^H- 7.4) to remove any surface bound or uncoordinated gold nanotriangles. These cells were then checked for change in their cellular granularity using flow cytometry. Besides, the cells were also imaged under inverted phase contrast microscope to confirm that the gold nanotriangles are internalized inside the cells. The advantage of using gold nanotriangles is that they are much bigger in size when compared with spherical nanoparticles or quantum dots, which have been used earlier for such studies. Thus, they can be easily viewed under a simple inverted phase contrast microscope at 60X magnification. The control untreated and the cells treated with 100 μM concentration of gold nanotriangles were also analyzed by atomic force microscopy (AFM) to observe any change in the surface texture of the cells on exposure.

6.4.2 Flow cytometry analysis.

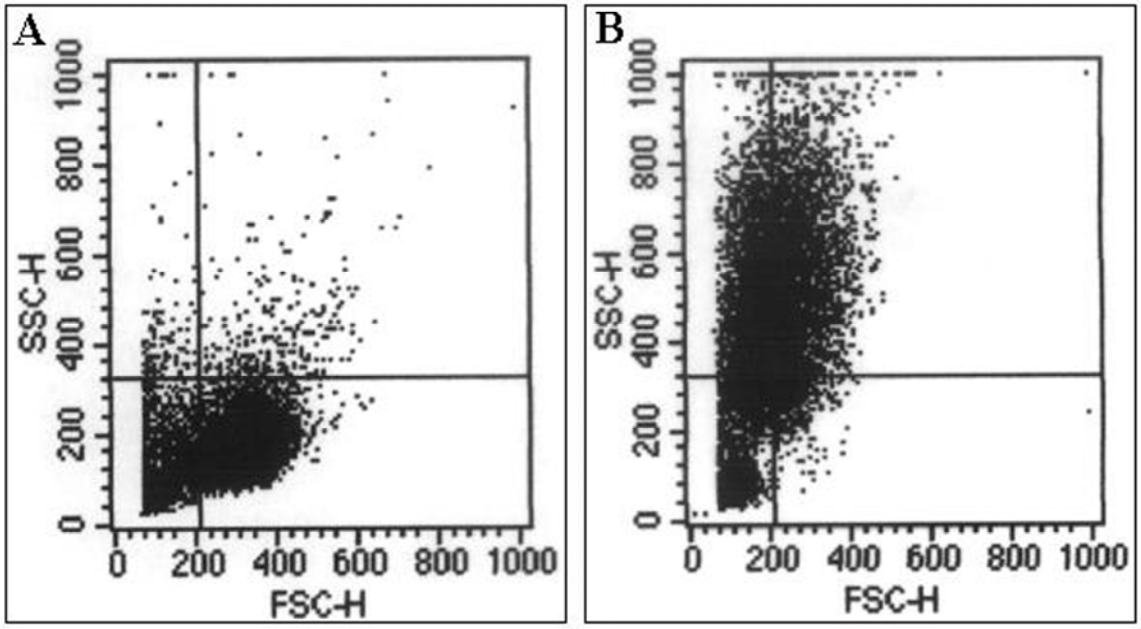

Figure 6.5 *The flow cytometry analysis of (A) untreated control NIH 3T3 fibroblast cells and (B) fibroblast cells treated with 50 μM concentration of gold nanotriangles for 24 h.*

The NIH 3T3 fibroblast cells were analyzed using a flow cytometer to find any change in the cellular granularity after exposure to the gold nanotriangles. In principle, if the gold nanotriangles are internalized by the cells, the granularity inside the cells should increase, which could be picked up by analyzing the side scatter plot. Figure 6.5 shows the forward and side scatter (FSC/SSC) plots obtained for the untreated control cells (Figure 6.5A) and the cells treated with 50 μM concentration of gold nanotriangles (Figure 6.5B).

Thus, Figure 6.5A reveals the granularity of the untreated control cells, which shows only one type of cells predominantly. However, when the FSC/SSC plot for the cells treated with 50 μM concentration of gold nanotriangles is observed (Figure 6.5B), we see that the majority of the cells show an increased side scatter profile as compared to the control (Figure 6.5A). Thus, in the FSC/SSC plot of the treated cells, we have two types of cell populations; one, which show FSC/SSC profile corresponding to that of the control cells and the others, which show an increased side scatter plot. The population of cells of the former types is the one that do not show uptake of gold nanotriangles, and thus, the granularity of the cells do not change when compared with the control cells (Figure 6.5A). This may be due to the fact that at a given time, not all cells in the population will have phagocytotic activity and so not all cells are able to take up the gold nanotriangles in the vicinity.

It is known that the increase in the side scatter profile of a cell is a direct measure of the increased granularity inside that cell. Thus, the FSC/SSC plot of the treated cells clearly indicates that the cellular granularity inside a majority of cells increases after the treatment with gold nanotriangles. This gives an indirect indication that the gold nanotriangles are internalized inside the fibroblast cells and are localized in the cytoplasmic space, thereby increasing the cellular granularity. It is important to realize that there is a streak of dots, which are diverging from the original cell population as compared to the control and show varying degree of side scatter. This shows that different cells show different degree of uptake of the gold nanotriangles and thus, a graded variation in the side scatter is obtained. This can be accounted for based on the fact that all cells in a population do not show same degree of phagocytotic activity and thus, the cellular uptake of gold nanotriangles will not be uniform in all the cells. However, to further confirm this observation, the untreated controls as well as the experimental treated fibroblast cells were observed under inverted phase contrast microscope, for direct visual evidence.

6.4.3 Inverted phase contrast microscopic analysis.

The non-cancerous NIH 3T3 cells were treated with 100 and 250 μM concentration of gold nanotriangles for 24 h and imaged under inverted phase contrast microscope at 60X magnification. The untreated cells were taken as control for this experiment. Figure 6.6A shows the control fibroblast cell. It can be seen that the cells are either attached to the surface of the culture plate and can be seen in their elongated and flat morphology or are detached

from the substrate and dispersed in the culture medium, showing a spherical morphology. Figure 6.6B shows the fibroblast cells treated with 100 μM concentration of gold nanotriangles. It can be seen that the cells show a lot of particulate matter within the cytoplasm while the round nucleus of the cells do not show them. This proves that the gold nanotriangles do get internalized inside the cells and compartmentalize in the cytoplasmic space. This also confirms that the gold nanotriangles do not enter the nucleus of the cells. The arrows in the image shows the cells with the gold nanotriangles showing the contrast in the cytoplasmic region while the nuclear region does not show any contrast.

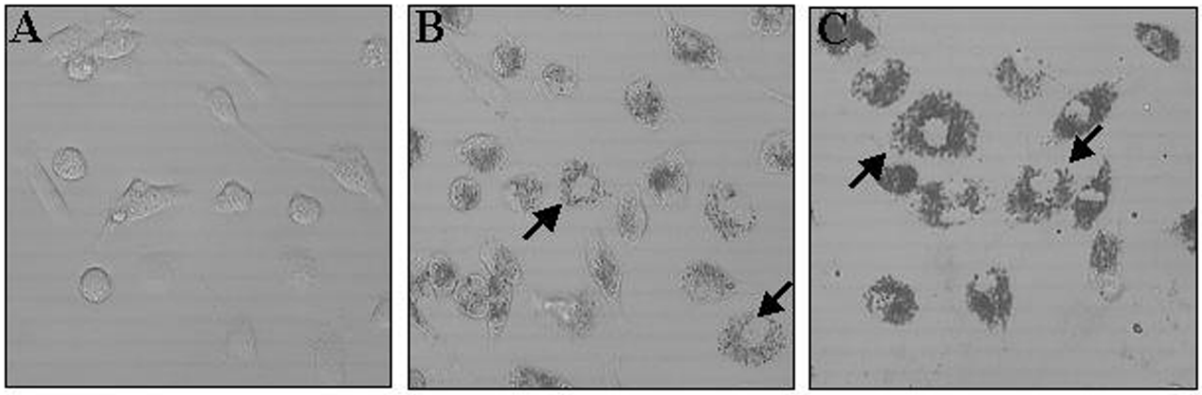

Figure 6.6 *(A) Control untreated NIH 3T3 fibroblast cells. (B) Fibroblast cells treated with 100 μM concentration of gold nanotriangles. (C) Fibroblast cells treated with 250 μM concentration of gold nanotriangles.*

Figure 6.6C shows the fibroblast cells treated with 250 μM concentration of gold nanotriangles. The image shows a highly dense contrast in the cytoplasmic region of the cells indicating that the cellular uptake of gold nanotriangles is much higher. Thus, it can be concluded that the amount of uptake of the gold nanotriangles by the cells is concentration dependent. Also, at this concentration, the nuclear region of low contrast is seen prominently and confirms the observation that the gold nanotriangles are confined in the cell cytoplasmic space and do not enter the nucleus. Another important observation that can be made from the images in Figure 6.6 A and B is that the density of the particles in the different cells in not uniform; some cells show high uptake of gold nanotriangles while several others show lower concentration of gold nanotriangles. This observation confirms the graded side scatter population of the cells obtained in the flow cytometry analysis (Figure 6.5B), which is primarily due to non-uniform density of the gold nanotriangles in the cytoplasm of the fibroblast cells.

6.4.4 Atomic force microscopy analysis.

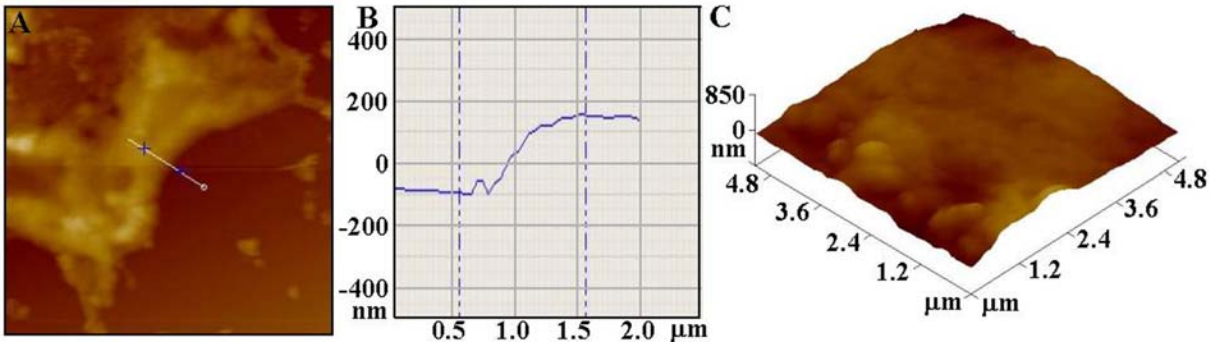

Figure 6.7 *(A) AFM micrograph of untreated NIH 3T3 fibroblast cell. (B) Line profile showing the height of the cell in A. The height of the cell was found to be 245 nm. (C) 3D profile of the untreated fibroblast cells showing a smooth topology.*

Figure 6.7A shows the atomic force microscopy image of the untreated NIH 3T3 fibroblast cells showing their elongated and flat morphology on attachment to the substrate. The height of the cell was calculated across the line drawn at the edge of the cell and it was found to be 245 nm (Figure 6.7B). The 3D profile of the untreated fibroblast cell has been shown in the Figure 6.8C, which shows a smooth and uniform surface with no deformity. However, the fibroblast cells that were treated with 100 µM concentration of gold nanotriangles showed a very rough surface texture (Figure 6.8A). The AFM micrograph reveals the presence of pits on their surface, which have been indicated in the image by white arrows. The 3D profile of the same image has been shown in the Figure 6.8B where the surface pits can be observed much more prominently corresponding to the surface features indicated in the 2D image (Figure 6.8A). The size of pits was found to be 300 to 400 nm, which might have formed due to entry of the gold nanotriangles into the cells at these sites.

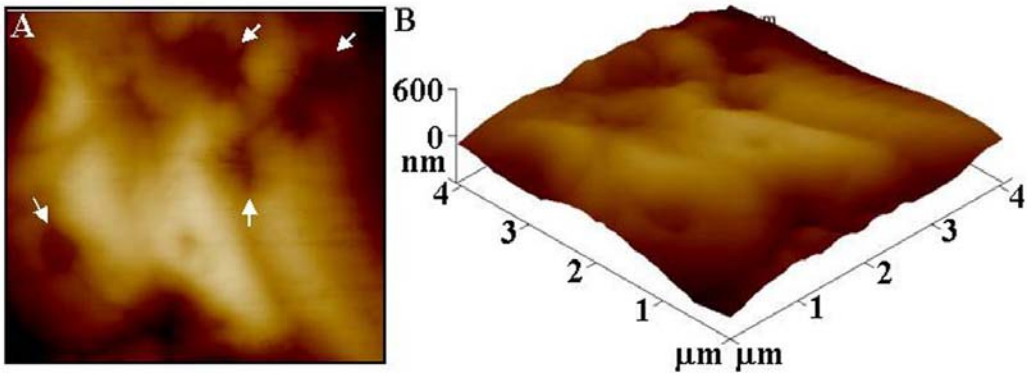

Figure 6.8 *(A) The height mode AFM image of the NIH 3T3 fibroblast cells treated with 100 µM concentration of gold nanotriangles. The arrows indicate the surface deformities of the cells. (B) 3D profile of the 2D image shown in A, showing the pits at the surface of the fibroblast cells.*

The observations made above clearly indicate that exposure of the fibroblast cells to the gold nanotriangles renders their surface highly rough and irregular and the 3D profile shows the presence of pits on the surface. The conclusions drawn by phase contrast microscopy clearly proves that the fibroblast cells internalize the gold nanotriangles and compartmentalize them in the cytoplasmic space. Thus, the pits that are seen at the surface of the fibroblast cell in Figure 6.8 could be the sites of the entry of the gold nanotriangles into the cell. It is very difficult to predict whether the entry of the gold nanotriangles is activated or it is a passive mode of entry, where the sharp triangles cut through the surface of the cells. However, the latter argument seems unlikely due to the fact that the cytotoxicity studies show 80 % viability of the NIH 3T3 fibroblast cells on treatment with 100 μM concentration of gold nanotriangles (Figure 6.3B). Thus, such high cell viability will be difficult to explain if the gold nanotriangles are cutting through to enter the cells, which will cause damage to the cellular integrity. The other possibility could be the entry of the gold nanotriangles by pinocytosis (cell drinking), which is also unlikely because the size of the gold nanotriangles is too large. It has been reported in literature that the particles that are smaller than 100 nm in size enter in the cell by pinocytosis while the particles bigger than that enter through phagocytosis (cell eating) [45]. Thus, the entry of the gold nanotriangles might be due to phagocytosis. However, this possibility could only be confirmed by further experimentation.

6.5 Discussion.

The work presented in this chapter discusses the cytotoxicity and biocompatibility issues of the biogenic gold nanotriangles synthesized by using lemon grass extract. Gold is a noble metal and thus, gold nanoparticles have been of prime interest in the biomedical applications. Biogenic nanostructures have been considered to have better biocompatibility than the chemically or physically synthesized nanostructures. However, there is a dearth of scientific research to prove this assumption. An attempt has been made to address these issues in this work. Another highlight of this work is that the anisotropic gold nanotriangles with highly unusual optical properties have been used to carry out the work, which may find future application in hyperthermic treatment of cancer cells. The results of the cytotoxicity studies suggest that the gold nanotriangles do not cause any harm to the cancerous (RAW264.7 and MCF-7) as well as non-cancerous (NIH 3T3) cells upto 800 μM concentration after 24 h of exposure. The possibility of induction of stress by these gold

nanotriangles has been studied by ELISA analysis, which suggests that they cause some stress-induced production of TNF-α cytokines. The flow cytometry analysis and inverted phase contrast microscopy imaging suggests that the gold nanotriangles are internalized inside the cells and are compartmentalized in the cytoplasmic space but do not enter inside the nucleus of the cells. The comparative AFM analysis of the control untreated fibroblast cells and fibroblast cells treated with gold nanotriangles reveals that the surface of the treated cells is highly irregular. The surface of the control untreated cells was found to be very smooth and regular as opposed to the treated ones, which showed pits of the sizes of 300 to 400 nm. It is speculated that these surface pits are the sites of entry of the gold nanotriangles into the cells. The exact mechanism of entry of the gold nanotriangles inside the cells has been fully understood. However, phagocytosis might be the process operative in this case. The average size of the gold nanotriangles has been calculated to be 113 nm and thus, they are too big to be taken inside by pinocytosis. Phagocytosis has been reported to be the process by which particles bigger than 100 nm enter inside the cells.

6.6 Conclusions.

In conclusion, it has been shown in this chapter that the biogenic gold nanotriangles show biocompatibility better than the chemically synthesized nanoparticles. The nanotriangles have been found to be non-toxic to the animal cells at high concentrations, though they do elicit some immunological response. They have been shown to be internalized by the cells and are confined in the cytoplasmic space but do not enter into the cells. Thus, these biogenic gold nanotriangles could be an excellent scaffold for delivery of drugs, genes or growth factors inside the cells. Besides, since these nanoparticles show a strong and tunable NIR absorption, they can serve as excellent candidates for hyperthermic treatment of cancer cells.

6.7 References.

1) (a) Haruta, M.; Daté M. *Appl. Catal. A* **2001**, *222*, 427. (b) Zhong, C.J., Maye, M.M. *Adv. Mater*. **2001**, *13*, 1507. (c) Roucoux, A.; Schulz, J.; Patin, H. *Chem. Rev.* **2002,** *102,* 3757. (d) Lewis. L.N. *Chem. Rev.***1993**, *93*, 2693. (e) Daniel, M.; Astruc, D. *Chem. Rev.* **2004**, *104*, 293.

2) Fichtner, M. *Adv. Eng. Mater.* **2005**, *7*, 443.

3) (a) Kim, Y.; Johnson, R.C.; Hupp, J.T. *Nano Lett.* **2001**, *1*, 165. (b) Liu, J.; Lu, Y. *J. Am. Chem. Soc.* **2004**, *126*, 12298. (c) Obare, S.O.; Hollowell, R.E.; Murphy, C.J. *Langmuir* **2002**, *18*, 10407.

4) Moran, C.E.; Steele, J.M.; Halas, N.J. *Nano Lett*. **2004**, *4*, 1497.

5) a) Simon, U. In *Nanoparticles: From Theory to Application*, Schmid, G., Ed. Wiley-VCH, Weinheim, **2004**. b) *Nanomaterials: Synthesis, Properties, and Applications*, edited by Edelstein, A.S. and Cammarata, R.C., Institute of Physics Publishing, Bristol, U.K., **1996**.

6) a) Maier, S.A.; Brongersma, M.L.; Kik, P.G.; Meltzer, S.; Requicha, A.A.G.; Atwater, H.A. *Adv. Mater.* **2001**, *13*, 1501. b) Maier, S.A.; Brongersma, M.L.; Kik, P.G.; Atwater, H.A. *Phys. Rev. B*, **2002**, *65*, 193408. c) Wang, Y. *Acc. Chem. Res.* **1991**, *24*, 133. (b) Yoffe, A.D. *Adv. Phys.* **1993**, *42*, 173.

7) Li, X.; Xu, W.; Zhang, J.; Jia, H.; Yang, B.; Zhao, B.; Li, B.; Ozaki, Y. *Langmuir* **2004**, *20*, 1298.

8) (a) Wohltjen, H.; Snow, A.W. *Anal. Chem.* **1998**, **70**, 2856. (b) Evans, S.D.; Johnson, S.R.; Cheng, Y.L.; Shen, T. *J. Mater. Chem.* **2000**, *10*, 183. (c) Han, L.; Daniel, D.R.; Mayer, M.M.; Zhong, C.-J. *Anal. Chem.* **2001**, *73*, 4441. (d) Krasteva, N.; Besnard, I.; Guse, B.; Bauer, R.E.; Muellen, K.; Yasuda, A.; Vossmeyer, T. *Nano Lett.* **2002**, *2*, 551. (e) Vossmeyer, T.; Guse, B.; Besnard, I.; Bauer, R.E.; Muellen, K.; Yasuda, A. *Adv. Mater.* **2002**, *14*, 238. (f) Zamborini, F.P.; Leopold, M.C.; Hicks, J.F.; Kulesza, P.J.; Malik, M.A.; Murray, R.W. *J. Am. Chem. Soc.* **2002**, *124*, 8958. (g) Zhang, H.-L.; Evans, S.D.; Henderson, J.R.; Miles, R.E.; Shen, T.-H. *Nanotechnology* **2002**, *13*, 439. (h) Grate, J.W.; Nelson, D.A.; Skaggs, R. *Anal. Chem.* **2003**, *75*, 1868. (i) Krasteva, N.; Guse, B.; Besnard, I.; Yasuda, A.; Vossmeyer, T. *Sens. Actuators B* **2003**, *92*, 137.

9) (a) Glomm, W.R. *J. Dispersion Sci. Technol.* **2005**, *26*, 389. (b) Salata, O.V. *J. Nanobiotechnology* **2004**, *2*, 3. (c) West, J.L.; Halas, N.J. *Curr. Opin. Biotechnol.* **2000**, *11*, 215. (d) Katz, E.; Willner, I. *Angew. Chem. Int. Ed.* **2004**, *43*, 6042.

10) (a) Antonii, F. Panacea Aurea–Auro Potabile, Bibliopolio Frobeniano, Hamburg, **1618**. (b) Kunckels, J. Nuetliche Observationes oder Anmerkungen von Auro und ArgentoPotabili, Schutzens, Hamburg **1676**. (c) Helcher, H. H. Aurum Potabile oder Gold Tinstur, J. Herbord Klossen, Breslau and Leipzig **1718**. (d) Lloyd, J.U. *Elixirs and*

Flavoring Extracts: Their History, Formulae, and Methods of Preparation, New York: William Wood and Company, **1892**.

11) Rosi, N.L.; Mirkin, C.A. *Chem. Rev.* **2005,** *105*, 1547.

12) (a) Shaw III, C.F. *Chem. Rev.* **1999,** *99,* 2589. (b) Pissuwan, D.; Valenzuela, S.M.; Cortie, M.B. *Trends Biotechnol.* **2006**, *24*, 62.

13) (a) Emerich, D.F.; Thanos, C.G. *Biomol. Eng.* **2006**, *23*, 171. (b) Niemeyer C.M. *Angew. Chem. Int. Ed.* **2001**, *40*, 4128. (c) Sanford, J.C.; Smith, F.D.; Russell, J.A. *Methods Enzymol.* **1993**, *217*, 483.

14) (a) Sharma, P.; Brown, S.; Walter, G.; Santra, S.; Moudgil, B. *Adv. Colloid Interface Sci.* **2006**, *123-126*, 471. (b) Bielinska, A.; Eichman, J.D.; Lee, I.; Baker, J.R., Jr.; Balogh, L. *J. Nanopart. Res.* **2002**, *4*, 395.

15) Roth, J. *Histochem. Cell Biol.* **1996**, *106*, 1.

16) Olofsson, L.; Rindzevicius, T.; Pfeiffer, I.; Kall, M.; Hook, F. *Langmuir* **2003**, *19*, 10414.

17) Alivisatos, A.P. *Sci. Am.* **2001**, *285*, 59.

18) (a) Busbee, B D.; Obare, S.O.; Murphy; C.J *Adv. Mater.* **2003**, *15*, 414. (b) Chang, S.-S.; Shih, C.-W.; Chen, C.-D.; Lai, W.-C.; Wang, C.R.C. *Langmuir* **1999**, *15*, 701. (c) Chemseddine, A.; Moritz, T. *Eur. Inorg. Chem.* **1999**, 235. (d) Jana, N.R.; Gearheart, L.; Murphy, C.J. *Chem. Commun.* **2001**, 617. (e) Kim, F.; Song, J.H.; Yang, P. *J. Am. Chem. Soc.* **2002**, *124*, 14316. (f) Tang, Z.; Kotov, N.A.; Giersig, M. *Science* **2002**, *297*, 237. (g) Xia, Y.N.; Yang, P.D.; Sun, Y.G.; Wu, Y.Y.; Mayers, B.; Gates, B.; Yin, Y.D.; Kim, F.; Yan, Y.Q.; *Adv. Mater.* **2003**, *15*, 353.

19) (a) Chen, S.; Fan, Z.; Carroll, D.L. *J. Phys. Chem. B* **2002**, *106*, 10777. (b) Hao, E.; Kelly, K.L.; Hupp, J.T.; Schatz, G.C. *J. Am.Chem. Soc.* **2002**, *124*, 15182. (c) Maillard, M.; Giorgio, S.; Pileni, M.-P. *Adv. Mater.* **2002**, *14*,1084. (d) Puntes, V.F.; Zanchet, D.; Erdonmez, C.K.; Alivisatos, A.P. *J. Am. Chem. Soc.* **2002**, *124*, 12874. (e) Maillard, M.; Huang, P.; Brus, L. *Nano Lett.* **2003**, *3*, 1611.

20) (a) Jin, R.; Cao, Y.; Mirkin, C.A.; Kelly, K.L.; Schatz, G.C.; Zheng, J.G. *Science* **2001**, *294*, 1901. (b) Chen, S.; Carroll, D.L. *Nano Lett.* **2002**, *2*, 1003. (b) I. Pastoriza-Santos, L.M. Liz-Marźan, *Nano Lett.* **2002**, *2*, 903. (c) Y. Sun, B. Mayers, Y. Xia, *Nano Lett.* **2003**, *3*, 675. (d) Yang, J.; Fendler, J.H. *J. Phys. Chem* **1995**, *99*, 5505. (e) Jin, R.; Cao, Y.; Hao, E.; Metraux, G.; Schatz, G.C.; Mirkin, C.A. *Nature* **2003**, *425*, 487.

21) (a) Lee, S.-M.; Jun, Y.-W.; Cho, S.N.; Cheon, J. *J. Am. Chem.Soc.* **2002**, *124*, 11244. (b) Chen, S.; Wang, Z.L.; Ballato, J.; Foulger, S.H.; Carroll, D.L. *J. Am. Chem. Soc.* **2003**, *125*, 16186. (c) Manna, L.; Milliron, D.J.; Meisel, A.; Scher, E.C.; Alivisatos, A.P. *Nature Mater.* **2003**, *2*, 382. (d) Manna, L.; Scher, E.C.; Alivisatos, A.P. *J. Am. Chem.Soc.* **2000**, *122*, 12700. (e) Hao, E.; Bailey, R.C.; Schatz, G.C.; Hupp, J.T.; Li, S. *Nano Lett.* **2004**, *4*, 327.

22) (a) Sun, Y.; Xia, Y. *Science* **2002**, *298*, 2139. (b) Ahmadi, T.S.; Wang, Z.L.; Green, T.C.; Henglein, A.; El-Sayed, M.A. *Science* **1996**, *272*, 1924.

23) (a) Oldenburg, S.J.; Jackson, J.B.; Westcott, S.L;. Halas, N.J. *Appl. Phys. Lett.* **1999**, *75*, 897. (b) Jackson, J.B.; Halas, N.J. *J. Phys. Chem. B* **2001**, *105*, 2743. (c) Graf, C.; Blaaderen, A.v. *Langmuir* **2002**, *18*, 524. (d) Pordan, E.; Nordlander, P. *Nano Lett.* **2003**, *3*, 543. (e) Oldenburg, S.J.; Averitt, R.D.; Westcott, S.L.; Halas, N.J. *Chem. Phys. Lett.* 1998, *288*, 243. (f) Jin, Y.; Dong, S. *J. Phys. Chem. B* **2003**, *107*, 12902.

24) Klaus, T.; Joerger, R.; Olsson, E.; Granqvist, C.G. *Proc. Natl. Acad. Sci. USA* **1999**, *96*, 13611.

25) (a) Ahmad, A.; Senapati, S.; Khan, M.I.; Kumar, R.; Sastry, M. *Langmuir* **2003**, *19*, 3550. (b) Ahmad, A.; Senapati, S.; Khan, M.I.; Ramani, R.; Srinivas, V.; Sastry, M. *Nanotechnology* **2003**, *14*, 824. (c) Beveridge, T.J.; Murray, R.G.E. *J. Bacteriol* **1980**, *141*, 876. (d) Beveridge, T.J.; Hughes, M.N.; Lee, H.; Leung, K.T.; Poole, R.K.; Savvaidis, I.; Silver, S.; Trevors, J.T. *Adv. Microb. Physiol.* **1997**, *38*, 178. (e) Joerger, R.; Klaus, T.; Granqvist C.-G. Adv. Mater. **2000**, *12*, 407. (f) Klaus-Joerger, T.; Joerger, R.; Olsson, E.; Granqvist, C.-G. *Trends Biotechnol.* **2001**, *19*, 15. (g) Konishi, Y.; Nomura, T.; Tsukiyama, T.; Saitoh, N. *Trans. Mater. Res. Soc. Jpn.* **2004**, *29*, 2341.

26) (a) Pum, D.; Sleytr, U.B. *Trends Biotechnol.* **1999**, *17*, 8. (b) Sleytr, U.B.; Messner, P.; Pum, D.; Sara, M. *Angew. Chem. In.t Ed.* **1999**, *38*, 1035.

27) (a) Mukherjee, P.; Ahmad, A.; Mandal, D.; Senapati, S.; Sainkar, S.R.; Khan, M.I.; Ramani, R.; Parischa, R.; Ajayakumar, P.V.; Alam, M.; Sastry, M.; Kumar, R. *Angew. Chem. Int. Ed.* **2001**, *40*, 3585. (b) Mukherjee, P.; Senapati, S.; Mandal, D.; Ahmad, A.; Khan, M.I.; Kumar, R.; Sastry, M. *Chembiochem* **2002**, *3*, 461. (c) Kowshik, M.; Ashtaputre, S.; Kharrazi, S.; Vogel, W.; Urban, J.; Kulkarni, S.K.; Paknikar, K.M. *Nanotechnology* **2003**, *14*, 95. (d) Mukherjee, P.; Ahmad, A.; Mandal, D.; Senapati, S.;

Sainkar, S.R.; Khan, M.I.; Ramani, R.; Parischa, R.; Ajayakumar, P.V.; Alam, M.; Sastry, M.; Kumar, R. *Angew. Chem. Int. Ed.* **2001**, *40*, 3585. (e) Mukherjee, P.; Ahmad, A.; Mandal, D.; Senapati, S.; Sainkar, S.R.; Khan, M.I.; Parischa, R.; Ajayakumar, P.V.; Alam, M.; Kumar, R.; Sastry, M. *Nano. Lett.* **2001**, *1*, 515. (f) Senapati, S.; Ahmad, A.; Khan, M.I.; Sastry, M.; Kumar, R. *Small* **2005**, *1*, 517.

28) Hosea, M.; Greene, B.; Mcpherson, R.; Henzl, M.; Alexander, M.D.; Darnall, D.W. *Inorg. Chim. Acta.* **1986**, *123*, 161.

29) (a) Gardea-Torresdey, J.L.; Parsons, J.G.; Gomez, E.; Peralta-Videa, J.; Troiani, H.E.; Santiago, P.; Yacaman, M.J. *Nano Lett.* **2002**, *2*, 397. (b) Gardea-Torresdey, J.L.; Gomez, E.; Peralta-Videa, J.R.; Parsons, J.G.; Troiani, H.; Yacaman, M.J. *Langmuir* **2003,** *19,* 1357. (c) Shankar, S.S.; Rai, A.; Ahmad, A.; Sastry, M. *J. Colloid Interface Sci.* **2004**, *275*, 496. (d) Shankar, S.S.; Ahmad, A.; Sastry, M. *Biotechnol. Prog.* **2003,** *19,* 1627. (e) Armendariz, V.; Herrera, I.; Peralta-Videa, J.R.; Jose-Yacaman, M.; Troiani, H.; Santiago, P.; Gardea-Torresdey, J.L. *J. Nano. Res.* **2004**, *6*, 377. (f) Ankamwar, B.; Damle, C.; Ahmad, A.; Sastry, M. *J. Nanosci. Nanotech.* **2005**, *5*, 1665. (g) Shao, Y.; Jin, Y.; Dong, S. *Chem. Commun.* **2004**, 1104. (h) Shankar, S.S.; Rai, A.; Ankamwar, B.; Singh, A.; Ahmad, A.; Sastry, M. *Nat. Mater.* **2004**, *3*, 482.

30) Hao, E.; Schatz, G.C.; Hupp, J.T. J. Fluores. **2004**, *14*, 331.

31) Shankar, S.S.; Rai, A.; Ahmad, A. and Sastry, M. *Chem. Mater.* **2005**, *17*, 566.

32) Rai, A.; Singh, A.; Ahmad, A. and Sastry, M. *Langmuir*, **2006**, *22*, 736.

33) Service, R.F. *Science* **2000**, *290*, 1526.

34) (a) Lam, C.W.; James, J.T.; McCluskey, R.; Hunter, R.L. *Toxicol.Sci.* **2004**, *77*, 126. (a) Warheit, D.B.; Laurence, B.R.; Reed, K.L.; Roach, D.H.; Reynolds, G.A.M.; Webb, T.R. *Toxicol. Sci.* **2004**, *77*, 117.

35) (a) Goyer, R.A. *Am. J. Clin. Nutr.* **1995**, *61*, 646. (b) Sakurai, T.; Kaise, T.; Matsubara, C. *Chem. Res. Toxicol.* **1998**, *11*, 273.

36) Hoshino, A.; Fujioka, K.; Oku, T.; Suga, M.; Sasaki, Y.F.; Ohta, T.; Yasuhara, M.; Suzuki, K.; Yamamoto, K. *Nano Lett.* **2004**, *4*, 2163.

37) Videira, M.A.; Botelho, M.F.; Santos, A.C.; Gouveia, L.F.; Lima, J.J.P.D.; Almeida, A.J. *J. Drug Targeting* **2002**, *10*, 607.

38) (a) Derfus, A.M.; Chan, W.C.W.; Bhatia, S.N. *Nano Lett.* **2004**, *4*, 11. (b) Kirchner, C.; Liedl, T.; Kudera, S.; Pellegrino, T.; Javier, A. M.; Gaub, H.E.; Stolzle, S.; Fertig, N.; Parak, W. J. *Nano Lett.* **2005**, *5*, 331. (c) Chang, E.; Thekkek, N.; Yu, W.W.; Colvin, V.L.; Drezek, R. *Small* **2006**, *2*, 1412.

39) (a) Grootveld, M.; Blake, D.R.; Sahinoglu, T.; Claxson, A.W.; Mapp, P.; Stevens, C.; Allen, R.E.; Furst, A. *Free Radical Res. Commun.* **1990**, *10*, 199. (b) Gleichmann, E.; Kubicka-Muranyi, M.; Kind, P.; Goldermann, R.; Goerz, G.; Merk, H.; Rau R. *Rheumatol. Int.* **1991**, *11*, 219. (c) Griem, P.; Gleichmann, E.*Z. Rheumatol*. **1996**, *55*, 348.

40) (a) Mirabelli, C.K.; Johnson, R.K.; Sung, C.M.; Faucette, L.F.; Muirhead, K.; Crooke, S.T. *Cancer Res.* **1985**, *45*, 32. (b) Cossu, R.; Matovic, Z.; Radanovic, C.; Ponticelli, G. *Farmaco* **1994**, *49*, 301. (c) Svensson, A.; Moller, H.; Bjorkner, B.; Bruze, M.; Leden, I.; Theander, J.; Ohlsson, K.; Linder, C. *BMC Dermatol*. **2002**, *2*, 2.

41) (a) Goodman, C.M.; McCusker, C.D.; Yilmaz, T.; Rotello, V.M. *Bioconjugate Chem.* **2004**, *15*, 897. (b) Connor, E.E.; Mwamuka, J.; Gole, A.; Murphy, C.J.; Wyatt, M.D. *Small* **2005**, *1*, 325. (c) Bhattacharya, R.; Mukherjee, P.; Xiong, Z.; Atala, A.; Soker, S.; Mukhopadhyay, D. *Nano Lett.* **2004**, *4*, 2479. (d) Tsoli, M.; Kuhn, H.; Brandau, W.; Esche, H.; Schmid, G. *Small* **2005**, *1*, 841.

42) Shukla, R.; Bansal, V.; Chaudhary, M.; Basu, A.; Bhonde, R.R.; Sastry, M. *Langmuir* **2005,** *21,* 10644.

43) Hirsch, L.R.; Stafford, R.J.; Bankson, J.A.; Sershen, S.R.; Rivera, B.; Price, R.E.; Hazle, J.D.; Halas, N.J.; West, J.L. *Proc. Natl. Acad. Sci. USA* **2003**, *100*, 13549.

44) Mosmann, T. *J. Immunol. Methods* **1983**, *65*, 55.

45) (a) Kruth, H. S.; Jones, N. L.; Huang, W.; Zhao, B.; Ishii, I.; Chang, J.; Combs, C. A.; Malide, D.; Zhang, W. Y. *J. Biol. Chem.* **2005**, *280*, 2352. (b) Ferencik, M. *Handbook of Immunochemistry: Phagocytosis*; Chapman and Hall: London, U.K., 1993; p 387.

Chapter VII

Conclusions

This chapter describes the salient features of the work undertaken in this thesis and discusses the possible avenues for future work.

7.1 Summary of the work.

Nanotechnology is becoming an integral part of all application-oriented research that is being carried out in various fields. One of the important challenges is to exploit the unusual electronic, optical and surface properties of the nanostructured materials to our benefit for a variety of potential applications. The work undertaken in this thesis has emphasized on the use of some unusual properties of metal nanostructures for potential applications in chemical vapor sensing and solution based mercury ions detection. Furthermore, cytotoxicity studies of the biogenic gold nanotriangles have been performed, since they are the prime materials used for a majority of the work presented in the thesis.

The work in this thesis has been devoted towards exploitation of the electrical properties of the metal nanostructures on an insulating substrate. The electronic conduction of the material at nanoscale largely depends on the local environment in the vicinity of the particles. Thus, the presence of an electron donor or acceptor ligand in the microenvironment results in a large impact on the electrical conduction behavior of the metal nanoparticles. A part of this thesis has been focused on immobilization of biogenic gold nanotriangles on quartz substrates to fabricate conducting films of varying resistances. The electrical properties of the film have been studied as a function of number of layers of gold nanotriangles on the surface. Besides, the anisotropic nature and subsequent unique electrical property of the nanoparticulate film has been used to detect polar vapors, methanol being the vapor for case study. The film shows nine orders of magnitude increase in the electrical conductivity on exposure to the methanol vapors and a response time of 10 s. The drastic increase in the electrical conductivity of the film in the presence of the methanol vapors has been attributed to the field enhancement effect at the tips of the gold nanotriangles in the presence of vapors in the vicinity.

As an extension to the previous work, Ag-Au bimetallic film with high porosity has been fabricated on the quartz substrate by a transmetallation approach. The electrical properties of the films have been studies as a function of concentration of chloroaurate ions used for the bimetallic film fabrication. The microstructure analysis of the films had been done which reveals that the bimetallic particles formed on the surface of the substrate are interconnected with pores in between them. This film of high porosity was then utilized for detection of ammonia and carbon di oxide vapors, studying the change in the electrical

conduction behavior of the film on exposure to the vapor. The film shows excellent sensitivity to the vapors, quick response time and a very uniform cycling behavior. Thus, this film has been proposed to be a promising candidate for developing metal nanoparticle based chemiresistor to detect these gases.

Soft templates have also been exploited in this work, where the spider and silkworm silk has been used as active scaffolds for immobilization of gold nanoparticles on the surface. Spider silk and silkworm silk are two natural polymers composed largely of proteinaceous material, which have been extensively studied in the past for their mechanical properties and tensile strength. Spider silk has been known to show super-contraction in the presence of polar vapors, which has been exploited here to our benefit. Spider and silkworm silk has been used to reduce chloroaurate ions to form nanoparticles and subsequently immobilize them on their surface using free amine moieties. The gold nanoparticles-decorated spider silk bioconjugate was used for electrical measurements. Based on the prior knowledge of super contraction property of the spider silk, the bioconjugate was exposed to vapors of varying polarity to obtain a graded electrical response based on the vapor polarity. It has been observed that higher the polarity of the vapor, higher is the increase in electrical conductivity of the bioconjugate. The phenomenon has been explained based on the fact that exposure to polar vapors causes super contraction of the gold nanoparticles decorated spider silk, thereby increasing the electrical conductivity.

Besides the electrical property, the optical property of the gold nanotriangles has been exploited for the solution-based detection of mercuric ions with atto-molar level sensitivity. Gold nanotriangles show a strong absorption peak in the NIR region of the electromagnetic spectrum owing to their anisotropic nature. This NIR absorption is known to be strongly dependent on the shape of the gold nanotriangles. These triangles, synthesized by reduction of chloroaurate ions using lemon grass leaf extract, are single crystalline and extremely thin in nature with the thickness ranging between 15-25 nm. Thus, they are highly prone to damage or disintegration under slight stress in the crystal structure. The strong tendency of mercury metal to amalgamate gold is an age-old phenomenon, which forms the basis of this work. The mercuric ions present in water were reduced in presence of gold nanotriangles using sodium borohydride to form mercury metal, which subsequently amalgamates the gold nanotriangles. The amalgamation process leads to disintegration of the gold nanotriangles

into small spherical particles, leaving a signature in the optical spectra as loss in NIR absorption intensity. It is this optical signature, which is picked up for quantitative analysis of the mercuric ion concentration in the sample. The HRTEM analysis reveals that the amalgamation process is initiated at the edges and tips of the gold nanotriangles, breaking them off into small particles by budding.

Biogenic methods for synthesizing nanostructured materials are being investigated to replace the toxic chemical methods. However, it is immensely important to analyze the cytotoxicity levels and biocompatibility of these biogenic materials before envisaging their biomedical applications. Gold nanotriangles are an integral part of this thesis from the material point of view and thus, it becomes necessary to investigate their cytotoxicity levels. Besides, the exotic properties offered by them makes them a promising candidate for various applications. Their strong NIR absorption tendency can be utilized for hyperthermic treatment of cancerous cells. With these aspects in mind, a study was undertaken to analyze the cytotoxicity levels of these nanotriangles, their tendency to elicit immunological responses and their capability to enter inside the cell without disrupting the cellular integrity. It has been shown that the biogenic gold nanoparticles are non-cytotoxic upto 800 μM concentration despite the fact that per particle load of gold will be much more due to their larger size. They are internalized inside the cells and are confined in the cytoplasmic space but fail to break through in the nucleus. The possible mechanism of entry could be by the phenomenon of phagocytosis, a process reported for uptake of particles bigger than 100 nm. Gold nanoparticles have also shown the capability to induce immunological response in the cells, though the cells are viable on exposure for 24 hours. Thus, these particles can be of immense use in the metal nanoparticles based formulation for biomedical applications.

7.1 Scope for future work.

The thesis illustrates the potential application of metal nanostructures in chemical vapor sensing. The results provided in the work show a huge promise towards the fabrication of metal nanoparticle based sensors for detecting chemical vapors. However, a key issue which could not be pursued in this work was the selectivity of these metal nanoparticle films. It would be really interesting to modify the surface of these nanoparticles prior to film fabrication to impart them selectivity towards a particular gas. Another issue of importance is

to work out the minimum detection limit of these films, which have been used for sensing various gases.

The work undertaken to fabricate spider silk bioconjugate shows great potential for detecting polar vapors based on their polarity. However, one aspect that will be interesting to pursue is the study of the force of contraction of these bioconjugates on exposure of different vapors. These bioconjugates can be used as linear motors to perform tasks based on their contraction-relaxation tendency, if these physical values are known. Besides, it would be interesting to study the minimum vapor detection limit of this system because the contraction-relaxation of the spider silk fiber is a macroscopic phenomenon.

The work performed to study the cytotoxicity limits and biocompatibility of the gold nanotriangles requires detailed study. Use of a phagocytotic and pinocytotic inhibitor during the exposure of gold nanotriangles to cells will illustrate the mechanism of entry of these nanoparticles in the cells. Besides, much more work could be done to study the immunological response of the cells in great details. A detailed account on cytokine profiling of the cell during exposure to gold nanotriangles will open up a new arena in the field of nanotechnology based biomedical research.

List of Publications

1) *Biological synthesis of triangular gold nanoprisms.*

S. Shiv Shankar, Akhilesh Rai, Balaprasad Ankamwar, **Amit Singh**, Absar Ahmad, Murali Sastry, **Nature Materials**, 3, 482-488, **2004**.

2) *Role of Halide Ions and Temperature on the Morphology of Biologically Synthesized Gold Nanotriangles.*

A.Rai, **Amit Singh**, A. Ahmad, M. Sastry **Langmuir**, *22*, 736, **2006**.

3) *Construction of Conductive Multilayer Films of Biogenic Triangular Gold Nanoparticles and their Application in Chemical Vapor Sensing.*

Amit Singh, M. Chaudhary, M. Sastry **Nanotechnology**, *17*, 2399, **2006**.

4) *Spider silk as an active scaffold for immobilization of gold nanoparticles and their application in vapour sensing.*

Amit Singh, Shantesh Hede, M. Sastry **Small** (accepted).

5) *Fabrication of Ag-Au nanoparticle film on to a substrate using transmetallation reaction and its potential application in vapor sensing.*

Amit Singh, M. Sastry **Chemistry of Materials**. (communicated).

6) *Optical Detection of Ultra-low levels of mercuric (Hg^{2+}) ions in water sample using biogenic gold nanotriangles.*

Amit Singh, M. Sastry **Nature Nanotechnology** (communicated).

7) *Separation of gold nanoclusters from triangles by a competitive complexation with Octadecyl Amine monolayers at the air-water interface.*

Renu Pasricha, **Amit Singh**, M. Sastry (manuscript under preparation).

8) *Assembly of silver nanoparticles at liquid-liquid interface, synthesis of Ag-Au bimetallic film and subsequent application in vapor sensing.*

Renu Pasricha, **Amit Singh**, M. Sastry (manuscript under preparation).

9) *Cytotoxicity study of biologically synthesized gold nanotriangles and understanding its internalization process in animal cells.*

Amit Singh, Ravi Shukla, R.R. Bhonde, M. Sastry (manuscript under preparation).

10) *Synthesis of silver nanoparticles using curcumin: synthesis of multifunctional nanoparticles.*

Ravi Shukla, **Amit Singh**, R.R. Bhonde, M. Sastry (manuscript under preparation)